Institut für Angewandte Photophysik

Fachrichtung Physik

Fakultät Mathematik und Naturwissenschaften

Technische Universität Dresden

Inverted Organic Light Emitting Diodes

Optical and Electrical Device Improvement

DISSERTATION

zur Erlangung des akademischen Grades

Doktor der Naturwissenschaften

(Doctor rerum naturalium)

vorgelegt von

Dipl. Phys. Michael Thomschke

geboren am 16.11.1980 in Hoyerswerda

Dresden 2012

TECHNISCHE UNIVERSITÄT DRESDEN

Eingereicht am: 07.09.2012

1.   Gutachter: Prof. Dr. Karl Leo
2.   Gutachter: Prof. Dr. Wolfgang Brütting

Verteidigt am: 12.02.2013

Abstract

This study focuses on the investigation of the key parameters that determine the optical and electrical characteristics of inverted top-emitting organic light emitting diodes (OLED). A co-deposition of small molecules in vacuum is used to establish electrically doped films that are applied in n-i-p layered devices. The knowledge about the functionality of each layer and parameter is important to develop efficient strategies to reach outstanding device performances.

In the first part, the thin film optics of top-emitting OLEDs are investigated, focusing on light extraction via cavity tuning, external outcoupling layers (capping layer), and the application of microlens films. Optical simulations are performed to determine the layer configuration with the maximum light extraction efficiency for monochrome phosphorescent devices. The peak efficiency is found at 35%, while varying the thickness of the charge transport layers, the semitransparent anode, and the capping layer simultaneously. Measurements of the spatial light distribution validate, that the capping layer influences the spectral width and the resonance wavelength of the extracted cavity mode, especially for TM polarization. Further, laminated microlens films are applied to benefit from strong microcavity effects in stacked OLEDs by spatial mixing of external and to some extend internal light modes. These findings are used to demonstrate white top-emitting OLEDs on opaque substrates showing power conversion efficiencies up to $30\,\mathrm{lm/W}$ and a color rendering index of 93, respectively.

In the second part, the charge carrier management of n-i-p layered diodes is investigated as it strongly deviates from that of the p-i-n layered counterparts. The influence of the bottom cathode material and the electron transport layer is found to be negligible in terms of driving voltage, which means that the assumption of an ohmic bottom contact is valid. The hole transport and the charge carrier injection at the anode is much more sensitive to the evaporation sequence, especially when using hole transport materials with a glass transition temperature below $100\,°\mathrm{C}$. As a consequence, thermal annealing of fabricated inverted OLEDs is found to drastically improve the device electronics, resulting in lower driving voltages and an increased internal efficiency. The annealing effect on charge transport comes from a reduced charge accumulation due to an altered film morphology of the transport layers, which is proven for electrons and for holes independently. The thermal treatment can further lead to a device degradation. Finally, the thickness and the material of the blocking layers which usually control the charge confinement inside the OLED are found to influence the recombination much more effectively in inverted OLEDs compared to non-inverted ones.

Kurzfassung

In dieser Arbeit werden die optischen und elektrischen Eigenschaften von invertierten top-emittierenden organischen Leuchtdioden (OLED) untersucht. Dabei handelt es sich um Dünnschichtsysteme mit dotierten Schichten, welche teilweise durch Ko-Verdampfung organischer Moleküle im Vakuum entstehen. Mit dem Wissen über die Funktionalität der Einzelschichten und ihrer Parameter können Strategien zur Bauteilverbesserung entwickelt werden.

Im ersten Teil der Arbeit werden die mikrooptischen Eigenschaften untersucht, wobei der Resonatorcharakter und die Lichtauskopplung mittels externer Deckschicht bzw. Mikrolinsen im Vordergrund stehen. Die gleichzeitige Schichtdickenvariation der Ladungsträgertransportschichten, der halbdurchlässigen Anode und der Deckschicht in der optischen Simulation monochromer OLEDs führt auf ein maximale Auskoppeleffizienz von 35%. Die Messung der winkelabhängigen Lichtabstrahlung bestätigt den Einfluss der Deckschicht auf die mikrooptischen Resonanzeigenschaften, wie spektrale Emissionsbreite und Peak-Wellenlänge, besonders für Licht mit TM Polarisation. Die deutlich stärkeren Resonanzeigenschaften in gestapelten OLEDs lassen sich mit Hilfe auflaminierter Mikrolinsenfolien nutzen, um auskoppelbare und interne Lichtmoden zu mischen. Diese Erkenntnisse werden benutzt, um Weißlicht-emittierende OLEDs zu demonstrieren, welche bis zu 30 lm/W Leistungseffizienz bzw. einen Farbwiedergabeindex von 93 erreichen.

Im zweiten Teil wird das Ladungsträgerverhältnis in invertierten OLEDs mit n-i-p Struktur untersucht, welches sich deutlich von dem herkömmlicher p-i-n OLEDs unterscheidet. Der Einfluss der Grundkathode und der Elektronentransportschicht ist kaum von Bedeutung, wodurch der untere Kontakt als ohmsch angenommen werden kann. Die Lochinjektion an der Anode bzw. der Lochtransport stellt sich besonders bei der Nutzung von organischen Materialien mit Glasübergangstemperaturen $<100\,°C$ als sehr sensibel hinsichtlich der Schichtfolge heraus. Ein nachträgliches Heizen von invertierten OLEDs hat eine deutliche Verringerung der Betriebsspannung, sowie in einigen Fällen eine Erhöhung der Effizienz zur Folge. Der Einfluss des Heizschrittes auf den Transport von Ladungsträgern ist sowohl für Elektronen, als auch für Löcher nachgewiesen und wird durch Morphologieänderungen der Transportschichten verursacht. Ebenso kann eine temperaturbedingte Zersetzung der OLED beobachtet werden. Die Untersuchung der Blockerschichten, welche für das Ladungsträgerverhältnis in der OLED mitverantwortlich sind, zeigt den Einfluss des Materials und der Schichtdicke auf die Rekombination der Ladungsträger wesentlich stärker als bei nicht-invertierten OLEDs.

CONTENTS

PUBLICATIONS

REFEREED ARTICLES

2012 Michael Thomschke, Sebastian Reineke, Björn Lüssem, and Karl Leo
"Highly Efficient White Top-Emitting Organic Light-Emitting Diodes Comprising Laminated Microlens Films", Nano Letters **12**, 424 (2012).

2011 Tobias Schwab, Michael Thomschke, Simone Hofmann, Mauro Furno, Karl Leo, and Björn Lüssem
"Efficiency Enhancement of Top-Emitting Organic Light-Emitting Diodes Using Conversion Dyes", Journal of Applied Physics **110**, 083118 (2011).

2011 Matthias Schober, Merve Anderson, Michael Thomschke, Johannes Widmer, Mauro Furno, Reinhard Scholz, Björn Lüssem, and Karl Leo
"Quantitative description of charge-carrier transport in a white organic light-emitting diode", Physical Review B **84**, 165326 (2011).

2011 Simone Hofmann, Michael Thomschke, Björn Lüssem, and Karl Leo
"Top-emitting organic light emitting diodes", Optics Express **19**, A1250 (2011).

2011 Vipul Gohri, Simone Hofmann, Sebastian Reineke, Thomas Rosenow, Michael Thomschke, Marieta Levichkova, Björn Lüssem, and Karl Leo
"White top-emitting organic light-emitting diodes employing a heterostructure of down-conversion layers", Organic Electronics **21**, 2126 (2011).

2011 Jonghee Lee, Simone Hofmann, Michael Thomschke, Mauro Furno, Yong Hyun Kim,Björn Lüssem, and Karl Leo
"Highly efficient bi-directional organic light-emitting diodes by strong micro-cavity effects", Applied Physics Letters **99**, 073303 (2011).

2011   Jonghee Lee, Simone Hofmann, Michael Thomschke, Mauro Furno, Yong Hyun Kim, Björn Lüssem, and Karl Leo
"Increased and balanced light emission of transparent organic light-emitting diodes by enhanced microcavity effects", Optics Letters **36**, 2931 (2011).

2011   Michael Thomschke, Simone Hofmann, Selina Olthof, Merve Anderson, Hans Kleemann, Matthias Schober, Björn Lüssem, and Karl Leo
"Improvement of voltage and charge balance in inverted top-emitting organic electroluminescent diodes comprising doped transport layers by thermal annealing", Applied Physics Letters **98**, 083304 (2011).

2011   Jonghee Lee, Simone Hofmann, Mauro Furno, Michael Thomschke, Yong Hyun Kim, Björn Lüssem, and Karl Leo
"Influence of organic capping layers on the performance of transparent organic light-emitting diodes", Optics Letters **36**, 1443 (2011).

2011   Jonghee Lee, Simone Hofmann, Mauro Furno, Michael Thomschke, Yong Hyun Kim, Börn Lüssem, and Karl Leo
"Systematic investigation of transparent organic light-emitting diodes depending on top metal electrode thickness", Organic Electronics **12**, 1383 (2011).

2010   Simone Hofmann, Michael Thomschke, Patricia Freitag, Mauro Furno, Björn Lüssem, and Karl Leo
"Top-emitting organic light-emitting diodes: Influence of cavity design", Applied Physics Letters **97**, 253308 (2010).

2009   Michael Thomschke, Robert Nitsche, Mauro Furno, and Karl Leo
"Optimized efficiency and angular emission characteristics of white top-emitting organic electroluminescent diodes", Applied Physics Letters **94**, 083303 (2009).

2008   Sebastian Scholz, Qiang Huang, Michael Thomschke, Selina Olthof, Philipp Sebastian, Karsten Walzer, Karl Leo, Steffen Oswald, Cathrin Corten, and Dirk Kuckling
"Self-doping and partial oxidation of metal-on-organic interfaces for organic semiconductor devices studied by chemical analysis techniques", Journal of Applied Physics **104**, 104502 (2008).

REFEREED CONFERENCE PAPERS

2011 Michael Thomschke, Patricia Freitag, Simone Hofmann, Mauro Furno, Sebastian Reineke, Björn Lüssem, and Karl Leo
"Top-emitting OLEDs for lighting applications", Proc. of IEEE Optoelectronics and Communications Conference (OECC), **16th** 504 - 505 (2011).

2010 Michael Thomschke, Mauro Furno, Björn Lüssem, and Karl Leo
"Highly efficient inverted top-emitting organic electroluminescent devices with doped charge transport layers", Proc. of SPIE, **7722**, (2010).

2010 Mauro Furno, Rico Meerheim, Michael Thomschke, Simone Hofmann, Björn Lüssem, and Karl Leo
"Outcoupling efficiency in small-molecule OLEDs: from theory to experiment", Proc. of SPIE **7617**, 761716 (2010).

2008 Robert Nitsche, Matthias Kurpiers-Guenther, Michael Thomschke, Matthias Schober, and Karl Leo
"Combined Electrical and Optical Simulation of OLED Devices", SID Symposium Digest of Technical Papers **39**, 411 (2008).

PATENT APPLICATIONS

2007 Michael Thomschke, Robert Nitsche, and Karl Leo
"Organisches, Weißlicht nach oben emittierendes Bauelement", Patent Application DE 10 2007 028821 (2007).

1 INTRODUCTION

In 1959, Richard P. Feynman gave a lecture about manipulating single atoms and described possible applications like sub-microscopic computers in the nano-scale. This talk, "There is a plenty of room at the bottom" [1] was a remarkable forward-looking contribution which inspired people and predicted things that finally entered our daily life in the beginning of the 21st century. Billions of transistors on a single chip, electronics in general, miniaturized in mobile phones, television or electronic paper are state of the art. In the last decades, organic chemistry offered molecular solid-state semiconductors with outstanding properties. In the sense of Feynman, there is a plenty of possibilities especially with these new materials that serve as components in an incredibly huge construction kit for organic electronic devices. Nanometer thick multilayered devices, deposited on flexible substrates or printed micro-structured electronic circuits are going to revolutionize our imagination of electronics again. Emerging applications like organic light emitting diodes (OLED) and organic solar cells are going to face the need for energy efficient lighting and a cost effective usage of renewable energy sources.

Since the breakthrough for efficient OLEDs in the 1980s [2, 3], this technology has already entered the consumer market with brilliant active-matrix OLED displays inside hand-held devices. Some companies announced the mass production of large area screens as well as displays of micro-size in the next years. OLED lighting still faces the problem of hardly achieving high luminous flux per area combined with long device lifetimes and high power efficiency. Stable organic emitter materials, device encapsulation and the scalability to large areas are challenges manufacturers have to deal with. Furthermore, rather expensive glass substrates with transparent electrode materials like indium tin oxide (ITO) need to be replaced by alternative materials to reduce the production costs. One possibility to overcome this problem is the top-emitting OLED architecture which can be deposited onto opaque and flexible substrates such as metal foils. Recent advancements by Novaled and OSRAM show that top-emitting OLEDs on metal foil substrates can reach promising high efficiencies of $36\,\mathrm{lm/W}$ and $32\,\mathrm{lm/W}$, respectively [4, 5].

So-called inverted OLEDs comprising a reversed layer sequence can be important for lighting and display applications as well but they feature two general difficulties of optical and electrical nature. Within this work, both issues are addressed in Chapters 4 and 5, respectively.

On the one hand, state-of-the-art top-emitting OLEDs make use of metal contacts thus showing resonator-like emission characteristics as narrow spectral bandwidth and angular dependent emission color [6, 7]. These optical properties originate from microcavity effects which strongly alter the light outcoupling in top-emitting OLEDs. Investigations of these optical device properties are described in Section 4.2 for monochrome electroluminescence. Additionally, approaches to suppress and to benefit from these microcavity effects are presented in Section 4.3 with the aim of demonstrating white light emission.

Figure 1.1: *High quality white light emitting OLED on metal substrates demonstrated by OSRAM in November 2011. The luminous efficiency is 32 lm/W at a brightness of 1000 cd/m^2. Image taken from [5].*

On the other hand, inverted OLED structures are required for high performance active matrix OLED displays [8]. These are preferentially based on n-channel thin-film-transistor (TFT) backplanes because of the superior mobilities for electrons in silicon. As a consequence, the TFT driving circuitry can be realized beneath the active OLED pixel which leads to higher display resolution but provides the cathode as bottom contact [9]. As charge injection and transport across the thin film device depends on the layer sequence, inverted OLEDs exhibit inferior device performances compared to non-inverted ones [10, 11]. From the electrical point of view, several OLED architectures have been suggested [12, 13]. This work focuses on OLEDs using doped charge transport layers where the electronic behavior of inverted (n-i-p) OLED architectures is discussed in Chapter 5. Finally, if inverted OLEDs have electrical properties equivalent or identical to their non-inverted counterparts, the freedom of layer sequence might be advantageous for multilayered emission zones in white OLEDs where the transport properties usually determine the sequence of the different emitter systems.

2 PHYSICS AND APPLICATIONS OF ORGANIC DYES

This chapter familiarizes the reader with the fundamentals of organic molecules and organic thin films. The functionality of a complex multilayer system like an OLED is determined by the electronic and optical properties of this material class. The second part of this chapter introduces the working principle of p-i-n OLEDs and briefly explains optical processes in multilayered systems with embedded emitter molecules.

2.1 DISORDERED ORGANIC SOLIDS

2.1.1 ORGANIC MOLECULES

Organic molecules represent the major constituent in organic light-emitting devices (OLED) and for this reason they determine almost the complete characteristics of these optoelectronic devices. Beside polymers, smaller oligomers and in particular polycyclic aromatic hydrocarbons of low molecular weight play a major role in highly efficient state-of-the-art OLEDs [14]. The molecular structure and the chemical bonds are mainly determined by the electronic configuration of the basis: the carbon atom. Therein, only the electrons in the outer 2s and the 2p orbitals can contribute to chemical bonds. When forming an aromatic molecule like for example benzene, these s and p electrons are sp^2 hybridized [15]. The resulting s and, without loss of generality, the p_x and the p_y orbitals lie in the plane of the molecule with an angle of 120° one to another. They form the σ-bonds between the carbon atoms. The remaining p_z orbitals are oriented perpendicular to the plane of the sp^2 orbitals and overlap with each other, forming the π-bonds which results in a delocalized electron density below and above the molecule (conjugation). Figure 2.1 illustrates the σ- and the π-bonds in our example: the benzene molecule.

In contrast to the strong σ-bonds, the weak overlap of the π-electrons corresponds to a lower energetic splitting of the occupied binding π-orbital and the unoccupied antibinding π^*-orbital. This leads to the characteristic absorption
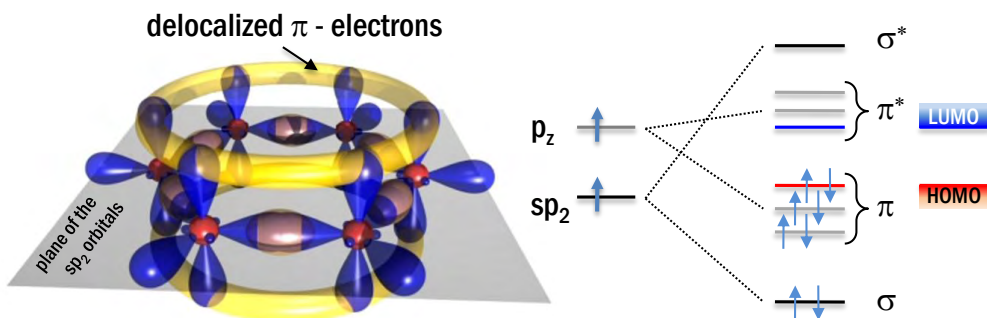
Figure 2.1: Molecular orbitals of benzene in the Hückel scheme (left) and a diagram of the orbital energies (right), illustrating the HOMO and LUMO states, taken from [16, 17].
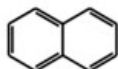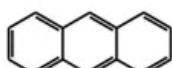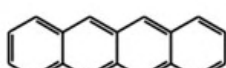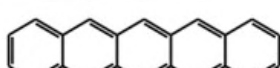
bands of these molecules that typically occur in the visible range from 1.6 - 3.3 eV. In organics, the π-orbital forms the highest occupied molecular orbital (HOMO) and the π^*-orbital the lowest unoccupied molecular orbital (LUMO) [18]. This means that the energetically lowest electron transitions are π-π^* transitions that for example depend on the size of the molecule. In Table 2.1, the influence of the number of phenyl rings can be directly compared to the absorption peak of the molecule. Here, the large variety of application possibilities becomes apparent. By simply changing the chemical structure, the photophysical properties like absorption and emission are easily tunable by adjusting the optical bandgap.

Furthermore, the π-electron system roughly determines most physical properties of organic solids formed by these molecules, for example by means of their intermolecular van der Waals interactions [19].

These intermolecular forces are much weaker than the intramolecular interactions forming and stabilizing the molecules. The properties of molecular solids are therefore mainly determined by the properties of the individual molecules. This fact can be easily illustrated by comparing the Coulomb potential of a single molecule and a molecular solid as they are depicted in Figure 2.2. In a single molecule, the effective electronic potential well is formed by the superposition of the nuclei and the electron potentials. The nuclei therein form the broad part of the well while the deep core levels are still localized at each nucleus [20]. The upper atomic orbitals overlap and form molecular orbitals that are delocalized over the whole molecule.

In the solid, both occupied and unoccupied molecular orbitals are usually located on the individual molecules, keeping the electronic structure of each

Table 2.1: *Dependence of the molecular size, i.e. the number of phenyl rings on the absorption peak of the molecules in solution, adapted from [19].*

molecule	structure	absorption peak (nm)
benzene		254
naphthalene		311
anthracene		375
tetracene		471
pentacene		582

molecule nearly unchanged. In contrast to inorganic semiconductors, where covalent bonds form the solid state and lead to delocalized electronic states, organic semiconductors show a small overlap of neighboring electronic wavefunctions which also represents the limitation for a bandstructure model. As a consequence, this localization of electronic wavefunctions, especially with respect to the geometry of a single molecule, has a large influence on the charge transport in organic solids.

Organic chemistry offers a large variety of compounds which can be tailored to show certain electrical and photophysical properties in the single molecule and further in the organic solid [21]. The morphology of the solid state can further be influenced by the kind of formation of the solid, e.g. film deposition or crystal growth.

2.1.2 CHARGE TRANSPORT IN ORGANIC SEMICONDUCTORS

In general, organic solids appear in three different forms: as single crystals, poly crystals or as glasses [19]. The spatial overlap of the electronic π-orbitals in the solid is strongly determined by the orientation of the corresponding adjacent molecules. As a first consequence, the transport of charge carriers is very anisotropic in organic crystals [22]. Two general models account for this strong influence of the solid state structure on the transport properties. On the one hand, charge carrier transport in highly purified organic crystals can be described by coherent Bloch-type band states exhibiting mobilities up
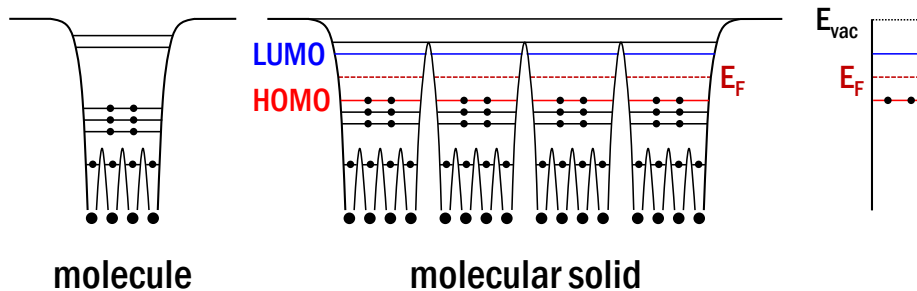
Figure 2.2: *Electronic structure of a single molecule and an organic solid represented by potential wells. In the simplified picture (right) of the energy levels in the solid E_{vac} denotes the vacuum level and E_F the Fermi level, reproduced from [20].*

to several $100\,\mathrm{cm^2/Vs}$ at low temperatures which is comparable to inorganic semiconductors [23, 24]. Nevertheless, actual organic crystals exhibit mobilities in the range of $1\,\mathrm{cm^2/Vs}$ at room temperature.

In disordered organic solids, the mobility is even lower (10^{-5} - $10^0\,\mathrm{cm^2/Vs}$) and in typical conjugated molecular materials the mean free path for charge carriers is in the range of the lattice constant which is due to the small orbital overlap of adjacent molecules [25]. It can be shown that an increased disorder of the molecular solid leads to a broadening of energetic bandwidth of the density of electronic states (DOS) and to an increased localization of charge carriers [26, 27].

The transport of charge carriers in organic molecular solids is always accompanied with ionic molecular states. When an electron is removed from a neutral molecule, a localized hole is left which has a certain hopping probability to reach an electronic state of an adjacent molecule. The analogue process holds for an electron which is brought to a neutral molecule, occupying a state in the LUMO region. In disordered solids like organic semiconductor films used within this work, thermally activated hopping has proven to adequately describe the charge carrier transport. This hopping transport mechanism in the presence of an external electric field is illustrated in Figure 2.3(a). There are some variations of this model, investigating different assumptions for the DOS and the spatial distribution of the molecular sites which in the end influence the hopping rates. One of the simplest and most convenient was proposed by Bässler [28]. Later, this model has been extended and was applied to describe multilayered OLED devices [29, 30]. Several approaches have been developed to describe the hopping processes, e.g. the percolation approach [31–33] or the multiple trapping and release model [34]. The Bässler model accounts for energetic and structural disorder. It has proven to fit very well with experimental data, observed in organic field effect transistors (OFETs) and can also be used

to model OLED devices. The hopping rates are of the Miller-Abrahams type [35] whereas the energetic distribution of the electronic states contributing to transport are described by a gaussian, given by

$$\Gamma(\epsilon) = (2\pi\sigma^2)^{-1/2} \exp\left(-\frac{\epsilon^2}{2\sigma^2}\right), \qquad (2.1)$$

with the energetic width of the distribution σ and the energy ϵ, relative to the center of the DOS. The temperature dependence of the carrier mobility ensues from Monte Carlo simulation results and is of the non-Arrhenius-type. The hopping rate not only depends on the energetic barrier height of neighboring sites but also on the external electric field F.

In most experiments, the field dependence of the observed charge carrier mobility follows the so-called Poole-Frenkel form

$$\mu = \mu_0 \exp(\beta\sqrt{F}), \qquad (2.2)$$

where μ_0 is the zero-field mobility, F the electric field and β the field enhancement factor.

Assuming a highly disordered solid with field dependent hopping rates under high field strengths ($F > 10^5 \, \mathrm{V/cm}$), the mobility has the form

$$\mu(T, \Sigma, F) = \mu_0 \exp\left[\left(-\frac{2\sigma}{3k_BT}\right)^2\right] \exp\left\{C\left[\left(\frac{\sigma}{k_BT}\right)^2 - \Sigma^2\right]F^{1/2}\right\}. \qquad (2.3)$$

Here, the parameter C describes the intersite distance while σ and Σ determine the energetic and positional disorder, respectively. A detailed description and the derivation can be found in literature [19, 36]. From the prefactor $exp(-1/T^2)$ in Equation 2.3 it becomes clear that the mobility is increasing with increasing temperature.

From the experimental point of view, the macroscopic current density j is connected to an externally applied field F via Ohm´s law

$$j = \hat{\sigma}F \qquad \text{with} \qquad \hat{\sigma} = e(n\mu_n + p\mu_p), \qquad (2.4)$$

where $\hat{\sigma}$ is the conductivity of a material that includes the physical processes that contribute to the transport of charge carriers. As shown in Equation 2.4, $\hat{\sigma}$ can be described by the charge carrier densities n for electrons and p for holes, respectively. The carrier mobility is μ while e stands for the elementary charge. The accuracy of an experimental determination of μ always depends on the method and the sample properties like the electrodes, the purity of the material and the deposition parameters. There are several techniques to measure the mobility in organic semiconductors [37] from which the most common are the

time-of-flight method [38, 39], the field effect transistor method [40–42], and the space-charge-limited-current (SCLC) method [36].
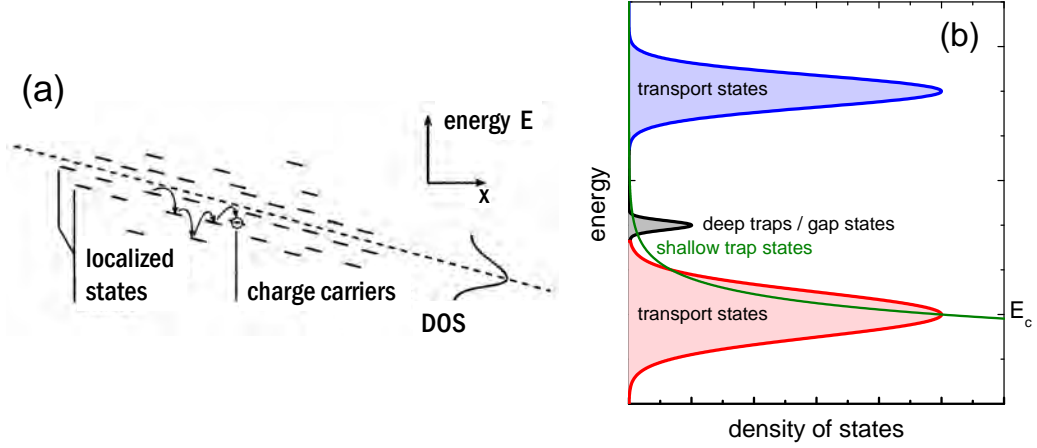

Figure 2.3: *Illustration of the hopping transport in disordered organic semiconductors (a) under an external electric field. The density of states (DOS) divides into the transport states, deep trap or gap states and shallow trap states, respectively. Figure (a) is taken from [19], Figure (b) reproduced from [43].*

Looking into real organic solids, we find defects, impurities, dopants or other disturbances of the lattice. All these disturbing sites introduce trap states for charges that can significantly alter the charge transport in organic materials. These traps can be divided into shallow traps and deep traps as depicted in Figure 2.3(b). Their occupation follows in both cases the Fermi statistics. Especially at low temperatures, the transport is limited by traps [19]. They can build up to a huge space charge in the organic material which hinders the free charges from moving by coulomb interactions.

With a total density of traps N_t and the energy $k_B T_t$ that characterizes the trap distribution, an exponential relation, given by

$$n_t(E) = \left(\frac{N_t}{k_B T_t} \right) \exp \left(\frac{E - E_c}{k_B T_t} \right) \tag{2.5}$$

can be assumed for shallow traps in disordered organic materials. Applying this distribution to describe the transport, two regimes in the current-voltage characteristic can be described [43, 44]. Below a critical voltage V_c, the charge transport is of ohmic nature and follows

$$j = n_0 q\mu \frac{V}{L}, \tag{2.6}$$

with the equilibrium electron density n_0, the layer thickness L and the single charge q. Above V_c, the current is described by the so-called trap-filled-limited (TFL) regime. The current density is given by the general form

$$j = N_c q\mu_n \left(\frac{\epsilon_0 \epsilon_r}{qN_t}\right)^r \frac{V^{r+1}}{L^{2r+1}} C(r), \tag{2.7}$$

with $C(r) = r^r (2r+1)^{r+1}(r+1)^{-r-2}$, $r = T_t/T$ and the effective density of states $N_c = 2.5 \times 10^{19}\,\text{cm}^{-3}$ in the conduction band [43].

If r=1, this equation describes the regime of space-charge-limited currents (SCLC). Assuming ohmic contacts, an unipolar current, and thus no recombination, the current density j follows the so-called *Mott-Gurney law*

$$j_{MG} = \frac{9}{8} \epsilon_0 \epsilon_r \mu \frac{V^2}{L^3}, \tag{2.8}$$

where V is the applied voltage, L the layer thickness, $\epsilon_0 \epsilon_r$ the permittivity and μ the mobility of the organic layer. With the temperature-dependent zero-field mobility μ_0 and the Poole-Frenkel relation from Equation 2.2, it was found empirically that Equation 2.8 has to be modified to

$$j_{PF} = \frac{9}{8} \epsilon_0 \epsilon_r \mu_0 \exp\left(0.89\sqrt{\beta\frac{V}{L}}\right) \frac{V^2}{L^3} \tag{2.9}$$

accounting for the Frenkel-effect [45].

2.1.3 CHARGE INJECTION AND INTERFACES

The current flow through an organic layer can either be limited by the process of charge injection into the molecular solid or by the transport properties of the organic semiconductor itself. In the latter case, the current through an organic semiconductor is limited by its mobility, determined by the density and localization of the electronic states. Space-charges that build up at the contacts or at internal interfaces or trapped charges determine the current via coulomb interactions. The resulting inhomogeneous charge carrier density leads to a bending of the transport levels as depicted in Figure 2.4(a). In the case of injection limitation, charge carriers have to overcome such a high energetic barrier at the contact that it is not possible to provide enough charge carriers to build up space-charges in the organic semiconductor. The current is therefore limited by the contact and the electric field F is homogenous between the electrodes. As a consequence, the current does not depend on the thickness

of the organic semiconductor. In Figure 2.4, the cases of space-charge-limited current (a) and injection-limited current (b) are compared.
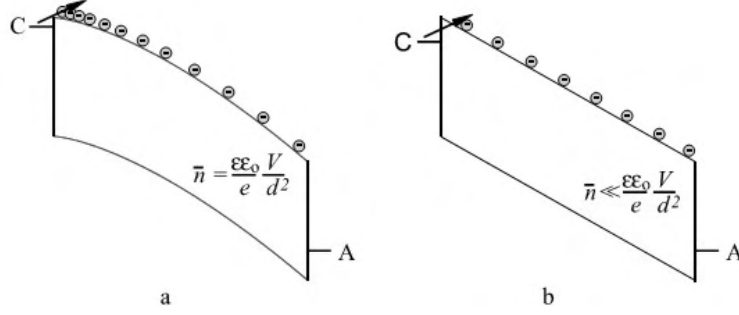

Figure 2.4: *Space-charges limit the current coulomb interaction and form an inhomogeneous charge carrier density that bend the transport levels (a) while an injection limitation leads to constant charge density as no space charge can build up (b), taken from [19].*

A large number of investigations on the injection mechanisms from an electrode into an organic semiconductor have been done in the past. In particular, metal-organic interfaces have been intensively studied by photoelectron spectroscopy or related methods [46, 47]. It has to be pointed out that the density of free charge carriers strongly influences the interface energetics [48]. In numerous experiments, the currents are limited by the contact interfaces and some models have been proposed to describe the current injection into organic solids. Thermionic and tunnel injection are the two most commonly used mechanisms.

Thermionic injection

Thermionic injection originates from the description of electron emission currents in vacuum tubes and is described by the Richardson-Schottky-model. The injection is restricted to the first monolayer and thermally activated. The injection current is given by [49]

$$j_{RS}(T, F, \Delta) = AT^2 \exp\left[-\frac{\Delta - \sqrt{\beta_{RS}F}}{k_B T}\right] \tag{2.10}$$

with the Richardson constant $A = 4\pi q m_{eff} k_b^2 / h^3$, where m_{eff} is the effective electron mass and the barrier height Δ. The field-induced lowering of the injection barrier by the Schottky-effect is taken into account by $\beta_{RS} = e^3/4\pi\epsilon\epsilon_0$.

20

Tunnel injection

The second approach to describe charge carrier injection is a tunneling mechanism proposed by Fowler and Nordheim [50] which accounts for high injection barriers and low temperatures. This tunnel process is temperature independent and follows [51–53]

$$j_{FN}(F, \Delta) = \frac{A}{\Delta} \left(\frac{eF}{\alpha k_B} \right)^2 \exp \left[-\frac{2\alpha \Delta^{3/2}}{3eF} \right], \qquad (2.11)$$

where $\alpha = 4\pi \sqrt{2m_{eff}}/h$.

Both injection mechanisms are illustrated in Figure 2.5 and represent boundary cases while in reality a superposition of them is more likely. For organic semiconductors, especially disordered ones, these models are rather limited because of the absence of transport bands. Therefore, the models have to be extended to include charge injection into a system of localized states [53–56].
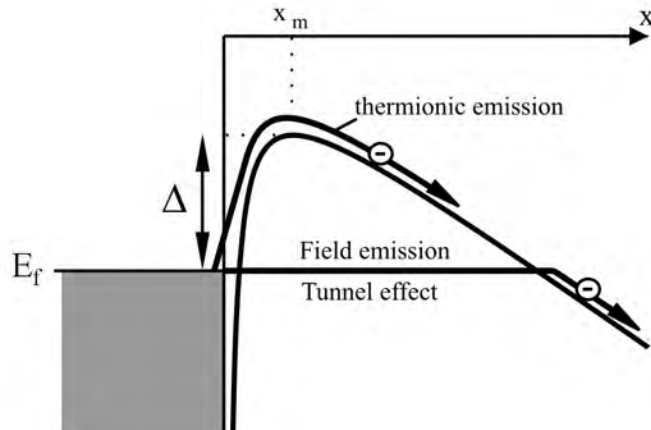
Figure 2.5: Illustration of thermally activated (thermionic) injection and temperature independent tunnel injection at an energy barrier of the height Δ. x_m denotes the width of the barrier and E_f the Fermi-energy, taken from [19].

Metal-Organic interfaces

Originally, the energy levels at metal-organic (MO) interfaces were considered to align with respect to the vacuum level. Therefore, it is convenient to treat the boundary like an ideal Mott-Schottky metal-semiconductor interface as depicted in Figure 2.6(a). From several investigations in the past [47, 57–60] it is known that such idealization does not hold for MO interfaces as interface dipoles can shift the vacuum level by several eV and significantly alter the

corresponding energetic barriers. These dipoles can originate from a charge transfer across the interface, rearrangement of the surface electron cloud of the metal, chemical interactions of the metal and the adsorbate, or metal induced interface states [20, 48]. Furthermore, the surface roughness of the metal contact as well as the organic semiconductor being either intrinsic or doped have a significant influence on the local DOS of the transport level. Limketkai and Baldo [61, 62] found an increased energetic disorder at MO interfaces. They proposed two main consequences for disorder and doping at such an interface. On the one hand, a broader DOS next to the interface due to a higher degree of disorder leads to an injection barrier with respect to the narrow DOS being present far from the interface. On the other hand, doping enhances the interface dipole and can lead to enhanced injection into the first layer of molecules.
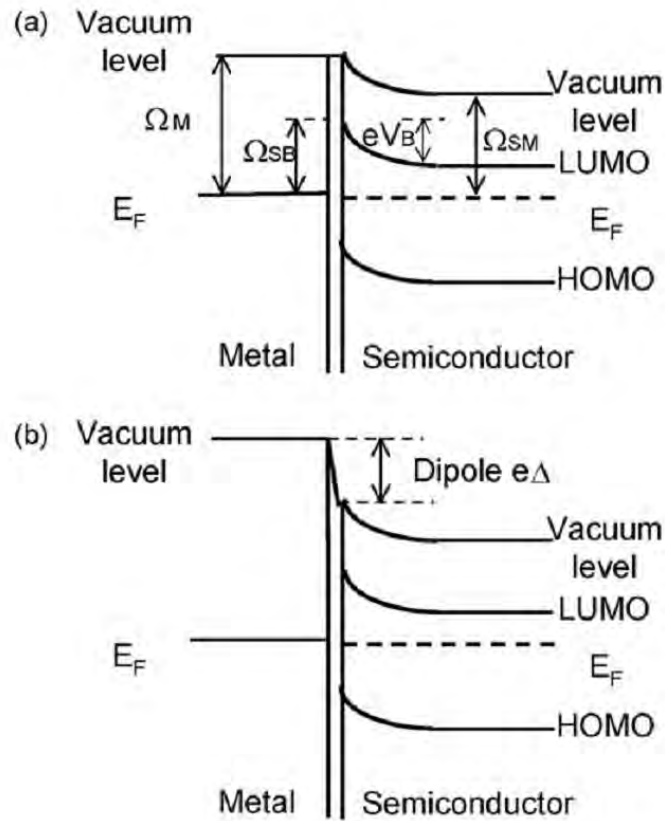

Figure 2.6: *Schematical representation of an ideal (a) and a realistic (b) Mott-Schottky contact for a n-type semiconductor. The ideal Schottky barrier height Ω_{SB} is given by the difference of the work functions of the metal Ω_M and the semiconductor Ω_{SM}, taken from [46].*

For the understanding of organic electronic devices it is worth pointing out the different behavior of metal-organic and organic-metal interfaces [47]. The energetics at these interfaces strongly depend on the two adjacent materials [20].

ORGANIC-ORGANIC INTERFACES

As motivated above, charge carriers which are already injected have to overcome additional barriers inside an organic multilayered system. Many material combinations have been investigated by ultraviolet photoelectron spectroscopy (UPS) to determine the energy level alignment [63]. In contrast to MO interfaces, most organic-organic interfaces show a vacuum level alignment which can simply be understood by the "closed-shell nature" [60] of the molecules as no charge transfer between different molecular solids is expected. As a consequence, the energetic position and distribution of the electronic transport levels determine the charge transport across such interfaces via the resulting energy offset or barrier. This holds for electron transport via adjacent LUMO- as well as for hole transport over the HOMO-levels. An overview about metal-organic and organic-organic interfaces has been published by Braun et al. [64].

2.1.4 ELECTRICAL DOPING

Previously, the current through an organic film has been discussed by assuming the existence of free charge carriers in the film. In addition to the influences of an electric field, the temperature or the injection efficiency, the charge transport should also be determined by the carrier concentration in the material. In the non-equilibrium case, charge carriers can be injected from the contacts, photogenerated or released by a high electric field as it is suggested in case of the field effect. The other possibility is the release of intrinsic carriers in the thermal equilibrium by impurities or dopants. The pendant to p- and n-doping in inorganic semiconductors is the co-deposition of an organic host material and an accepting or donating material, respectively. The principle of both cases is depicted in Figure 2.7. In the case of p-type doping, the LUMO of the dopant has to be energetically located below or near the HOMO of the host material, whereas a donor in n-doped films is supposed to have a HOMO above the LUMO of the host material. In case of p-type doping, a charge transfer complex (CTC) $[M^+A^-]$ between a host molecule M and an acceptor molecule A is formed. When this CTC dissociates, i.e. an electron departs from the host molecule, a free hole is generated. This process can be illustrated by:

$$MMMAM \rightleftharpoons MM[M^+A^-]M \rightleftharpoons MM^+MA^-M \leftrightharpoons M^+MMA^-M. \quad (2.12)$$
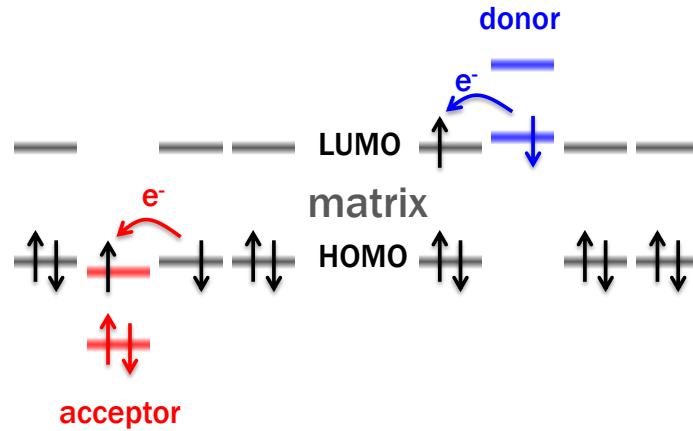
Figure 2.7: Illustration of the doping mechanisms in organic semiconductors. An acceptor molecule takes an electron from the host molecule (left) while a donor molecule releases an electron, after [65].

The process of electrical doping in organic semiconductors is still under current research. Material combinations, doping efficiency or the influence on the film morphology are of great interest [66]. Figure 2.8 shows the measured field-effect mobility, depending on the doping concentration in pentacene. The p-type dopants F_4-TCNQ and F6-TCNNQ strongly influence the crystalline order of the pentacene films and decrease the charge carrier mobility, while the conductivity increases.

It can be shown that doped disordered organic semiconductors exhibit an increased energetic disorder as well as a broadened distribution of the density of states. On the one hand, doping increases the carrier concentration and lifts the Fermi level while on the other hand, deep traps of the opposite polarity are created. The increased carrier concentration leads to an increased conductivity but the creation of traps decreases the hopping rate. Further, the mobility becomes strongly field dependent with increasing dopant concentration [67].

Acceptor-doping

P-type doping of organic semiconductors could be shown by exposition to oxidizing gases, by inorganic oxidizing agents or by organic acceptor molecules. One of the first and probably the most famous molecular acceptor is F_4-TCNQ. In 1998, Blochwitz and Pfeiffer [68] could show an increase in current through an OLED device by several orders of magnitude when doping vanadyl-phthalocyanine (VOPc) films with F_4-TCNQ. Later, the hole transport materials m-MTDATA, 1-TNATA, 2-TNATA and in our case MeO-TPD were used as host for F_4-TCNQ. In Figure 2.9, the conductivity of doped and
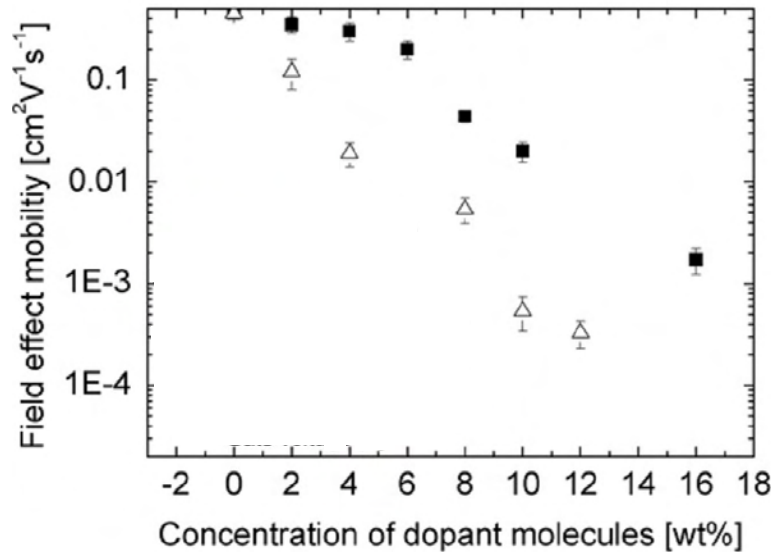
Figure 2.8: *Field-effect mobility of pentacene films in organic thin film transistors (OTFT), doped by either F_4-TCNQ (closed rectangles) or F6-TCNNQ (open triangles) at different doping concentrations. The reduced mobility is directly correlated to a loss in the crystalline order of the pentacene film. Adopted from [66].*

undoped organic films is compared. MeO-TPD, doped with 2% of F_4-TCNQ exhibits a conductivity of 5×10^{-6} S/cm and a hole mobility of 1×10^{-4} cm^2/Vs [65]. In NPB, Re_2O_7 has been shown [69] to work as a p-type dopant as well. Additionally, we use F6-TCNNQ (F6TNAP) [70] as acceptor molecule, which shows improved processability and equivalent doping efficiency compared to F_4-TCNQ.

Donor-doping

As donating materials, alkaline metals like lithium (Li) and cesium (Cs) or the alkaline compounds CsN_3 [72], Cs_2O [73], Cs_2CO_3 [69] or CsOH [74] have been used. Due to the requirement of a very low ionization potential of the donor, the realization of n-doping is very difficult as such materials are very reactive and therefore sensitive against oxygen. Thus, only a few molecular n-dopants are known / published which are for example BEDT-TTF [75], AOB [76], Pyronin B [77, 78], $Ru(terpy)_2$, $Cr(bpy)_3$, $Cr(TMB)_3$ [79, 80] or N-DMBI [81]. In this work, we use the highly reactive Cs and the molecular donor $W_2(hpp)_4$ [82].

In general, electrical doping leads to the following improvements, regarding organic devices:

25
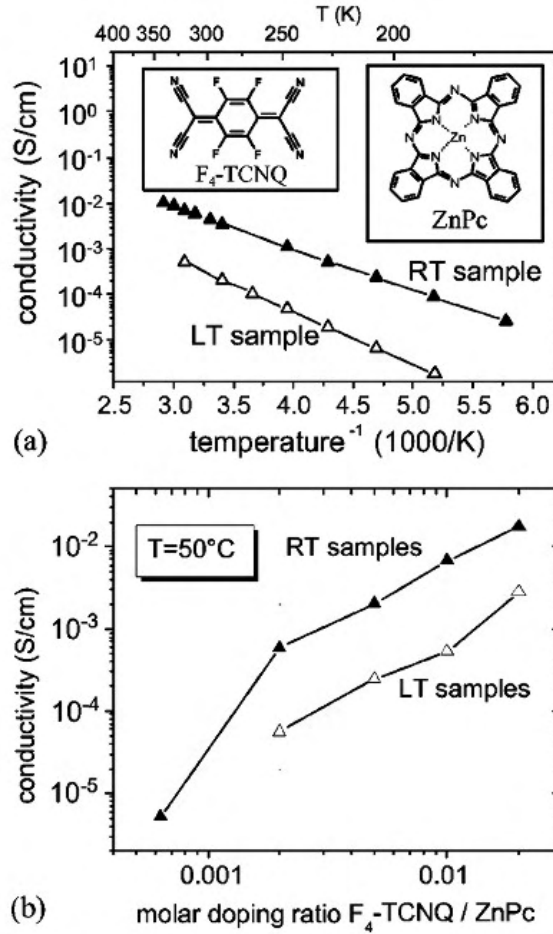
Figure 2.9: Conductivity of 30 nm thick zinc-phthalocyanine (ZnPc) films doped with F_4-TCNQ. Figure (a) shows the Arrhenius plot for samples at room temperature (RT) and at -100 °C (LT) and Figure (b) the conductivity depending on the molar doping ratio, taken from [71].

- The conductivity of a doped organic layer increases significantly and ohmic losses are strongly reduced. This leads to nearly field-free doped transport layers under device operation.

- The space charge regions at the electrodes become very thin ($\approx 2\,\text{nm}$) [48] which results in a very efficient charge injection by tunneling. Thus, the contact resistance is minimized, showing ohmic behavior and the injection is not depending on the work function of the electrode material.

- This results in a free choice of transport layer thickness and contact material which is beneficial for designing OLEDs comprising an optical cavity.

One important fact which should not be neglected is the ability of dopants to diffuse more or less freely inside an organic matrix material. Especially metal dopants are known to be highly volatile which can reduce the device lifetime and the efficiency. It can be shown, that for example Li tends to diffuse $70 \pm 10\,\text{nm}$ into the underlying layer when evaporated onto BCP films [83].

2.1.5 LUMINESCENCE FROM ORGANIC DYES - EXCITED STATES

Two main processes lead to excited states in organic dyes. The first one is photoexcitation. It is realized by the absorption of an incoming photon which induces a transition from the ground state to an excited state of the molecule. Due to conservation of energy, the excitation energy equals the photon energy $h\nu$. The second process to create excited molecular states is the recombination of charge carriers.

The probability of any transition between two electronic states is described within the quantum mechanical framework by the response of an electronic system, perturbed by an electromagnetic field. For the process of spontaneous emission, Fermi´s golden rule correlates the emission rate Γ between initial state $|i\rangle$ and final state $|f\rangle$

$$\Gamma \propto |M_{if}|^2 \rho(\nu_{if}), \tag{2.13}$$

with the transition matrix element $M_{if} = \langle f|M|i\rangle$ where M is the electric dipole operator and $\rho(\nu_{if})$ the photonic mode density at the location of the radiating molecule for the transition frequency ν_{if}. This relation describes the interaction of emitting molecules with the optical field inside an OLED cavity.

In the molecule, the majority of electronic excitations is accompanied with an increased average distance of the atoms compared to the ground state. Considering the conservation of momentum, transitions between states of the same atomic distances have the highest probability. This is called Franck-Condon-principle. In quantum mechanics, this principle describes selection rules for transitions where the transition probability is proportional to the overlap of the two (initial and final state) corresponding nuclear wavefunctions. Considering photon absorption by a diatomic molecule, the absorption process always occurs at higher energies than the related emission processes, as illustrated in Figure 2.10. This Franck-Condon red-shift between absorption and emission originates from the much higher lifetime of the excited state compared to the non-radiative intrastate relaxation of the vibrational modes [53].

Figure 2.10: Typical absorption and fluorescent emission spectrum of a molecule in solution, demonstrating the Franck-Condon shift due to non-radiative intrastate relaxations (orange arrows). The two exemplary potential curves on the top illustrate the different average coordinates of the nuclei, reprinted from [15].
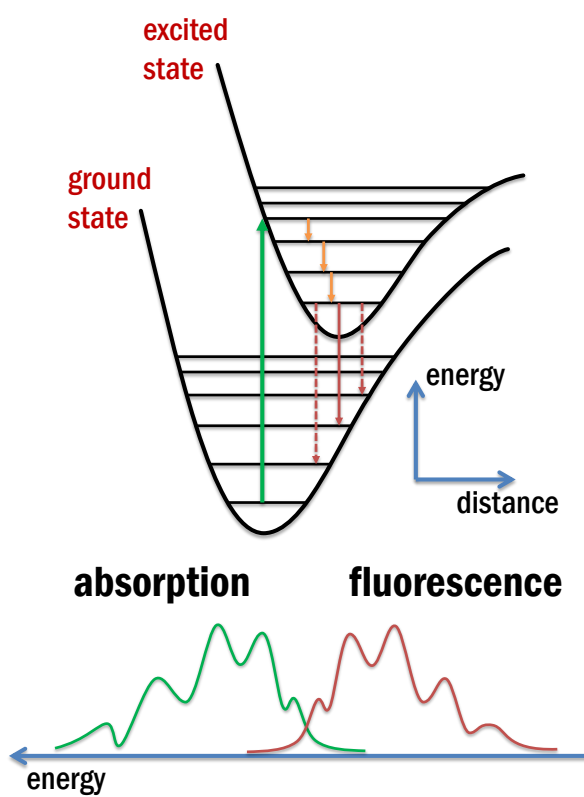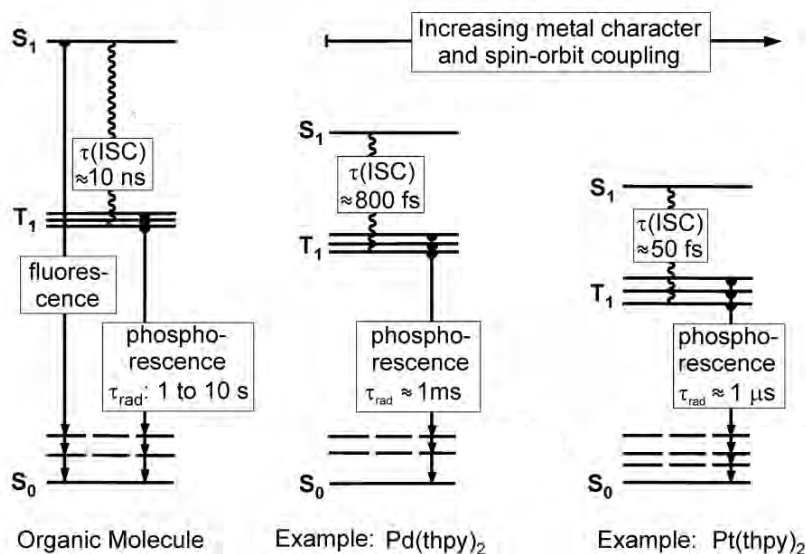
Figure 2.11: *Comparison of the photophysical properties like intersystem crossing lifetime τ(ISC) and radiative lifetime τ_{rad} of a typical organic molecule (left) and the two triplet emitters Pd(thpy)$_2$ and Pt(thpy)$_2$ (middle and right), taken from [84].*

It has to be distinguished between the singlet ground state S_0, the excited singlet states S_1 and S_2 and the excited triplet states T_1 and T_2. For singlet states the total spin is S=0 whereas for triplet states S=1. There are spin-allowed and spin-forbidden transitions.

Fluorescence is the radiative decay from S_1 to S_0 which conserves the spin. It is a very fast process with a rate constant of about $10^9\,\mathrm{s}^{-1}$ [85] which corresponds to lifetimes in the nanosecond regime. The radiative transition between T_1 and S_0 is called phosphorescence and non-spin-conservative. The selection rules do not allow phosphorescence for the majority of organic dyes and non-radiative transitions are the dominating relaxation paths from T_1 to the ground state. The reason is the long triplet lifetime ($\tau_{triplet} = 10^{-6} - 10^2\,\mathrm{s}$) which increases the probability for non-radiative decay. These radiationless transitions between states of the same multiplicity are called internal conversion (IC) while transitions of different multiplicity are known as intersystem crossing (ISC) [86].

To increase the radiative rate from the triplet state, heavy-atoms such as Ir and Pt have been used to design highly efficient phosphorescent emitter molecules [87] with strong spin-orbit coupling. These show radiative rates of $10^{13}\,\mathrm{s}^{-1}$ [36]. Figure 2.11 illustrates the important transitions in typical organic dyes compared to emitter molecules incorporating heavy metal atoms.

2.2 Organic electroluminescent diodes

2.2.1 Device architectures

A typical OLED is a multilayered system of organic thin films between two highly conductive electrodes. Geometrically, the device area is infinitely large compared to the total thickness of the organic layers which is in the range of 0.1 - 1 μm. As area light source, the optical properties of the electrodes, the substrate, and the organics define the light propagation.

There are two main device types which are labeled by their emission direction with respect to the substrate: bottom- and top-emitting OLEDs (Figure 2.12(a), (c) and (d)). The intermediate type which emits in both directions is the transparent OLED, shown in Figure 2.12(b) [88–90]. Here, the cathode as well as the anode and the substrate have to be highly transparent. Such devices offer new possibilities in design and lighting applications that are almost "invisible" and can make use of microcavity effects to achieve high efficiencies [91].
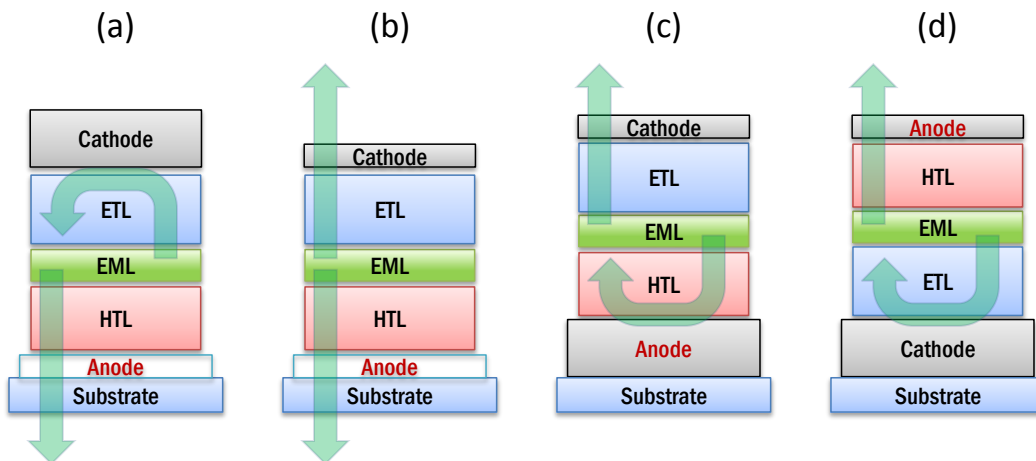
Figure 2.12: Typical single unit OLED layer structures: (a) conventional bottom-emitting, (b) transparent, (c) top-emitting and (d) inverted top-emitting OLED.

As depicted in Figure 2.12(a), bottom-emitting OLED devices feature a transparent substrate like glass and a transparent conductive electrode like indium tin oxide (ITO) that is directly coated onto the substrate. The organic materials are deposited in layers onto this transparent electrode and the OLED is finalized with a thick metal film acting as backside mirror and electrode, simultaneously. There is a large variety of organic layer sequences depending on the used materials and their related functionality. As ITO is still the

most popular material for transparent electrodes in bottom-emitting OLEDs, it influenced the sequence of the organic layers. The reason is the work function of ITO which is in the range of 3.7 eV- 4.7 eV [48, 92, 93] depending on chemical pre-treatment and the cleaning procedure. Enabling good hole injection, ITO acts as anode in common OLED structures and is coated with the hole injection and hole transport layers.

In contrast, top-emitting OLED devices based on small molecules can be made on every kind of substrate that is physically and chemically suitable for the deposition of thin layers. The only requirement is a sufficiently smooth surface, meaning that the surface roughness should be far below the organic layer thickness. Furthermore, porous surfaces can lead to decreased device stability in terms of operational lifetime because of possible confinement and adsorption of water, organic solvents, oxygen or other harmful materials that may diffuse from the substrate into the OLED layers and cause device degradation. As a top-emitting OLED emits light away from the substrate, the latter one can also be opaque like for example metal foils. If the substrate is electrically conductive, it may also act as an electrode. The easiest way to provide electrodes is to use metal layers. Especially the electrode layer at the bottom next to the substrate has to be highly reflective and smooth to avoid optical losses and electrical shortcuts. Thick metal layers or dielectric mirrors have been suggested for this purpose [94]. On the opposite side, the top electrode has to be transparent and conducting at the same time. Transparent conductive oxides like indium tin oxide (ITO) or zinc oxide doped with aluminium (ZAO) or gallium (GZO) may provide such properties [95, 96], but their deposition is rather complicated and may destroy the underlying organic layers [97]. Since the first demonstrations of top- or surface-emitting organic LEDs made use of ITO as transparent top contact [98, 99], thin metal layers turned out to be suitable as top electrodes as well. The preferred materials are highly conductive with considerably low absorbance like silver (Ag), aluminium (Al) or ytterbium (Yb). For thicknesses in the range of 10 - 40 nm, such metal electrodes provide sufficient transverse electric conductivities (20 nm Ag: 1 - 5 $\Omega/\square$) [100, 101] and an optical transmittance in the range of 10 - 70%. Hence, due to the fairly high reflectivity, such thin metal layers act as semitransparent mirrors.

2.2.2 WORKING PRINCIPLE AND THE P-I-N CONCEPT

In 1998, Bharathan et al. [102] and in 2002, Huang et al. [103] introduced electrically doped transport layers, forming a p-i-n layered OLED device structure. Ever since, this device architecture showed to have the potential to reach driving voltages at the thermodynamic limit [104], superior lifetimes, high quantum efficiencies [105, 106], and record luminous efficacies [14]. These im-

provements result from the properties of electrically doped charge transport layers which are: reduced ohmic losses, efficient tunneling injection, and flat-band conditions under operation [103]. As a consequence, p-i-n structured OLEDs do not necessarily need additional injection layers like MoO_3 [107], LiF [108] or plasma treatment of the anode [109]. Charge carriers can easily tunnel trough the few nanometer thick depleted regions of the transport layers adjacent to the electrodes. The energy levels in a typical bottom-emitting p-i-n OLED have been measured by using ultraviolet photoelectron spectroscopy which revealed the diagram in Figure 2.13. Due to the charge carrier concentrations of about 10^{18} cm^{-3} in the doped layers, the LUMO and the HOMO are shifted towards the Fermi-level. The complete built-in potential drops across the emission layer (EML) [110].
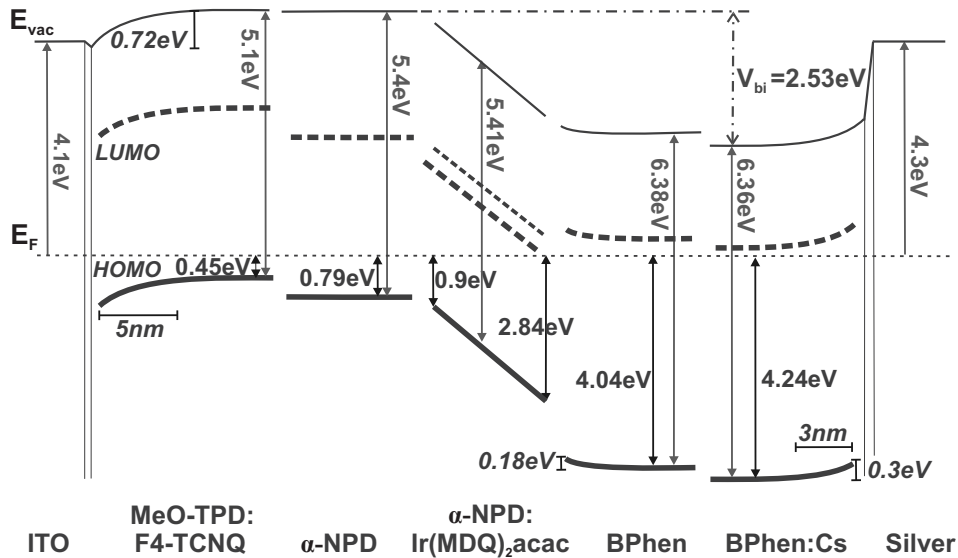

Figure 2.13: Energy levels of a typical bottom-emitting p-i-n OLED based on the phosphorescent orange emitter Ir(MDQ)$_2$(acac), doped into α-NPD. The hole transport layer is MeO-TPD, doped with F$_4$-TCNQ which establishes an ohmic contact to the ITO electrode. The electron transport is realized with BPhen, doped with cesium. The electron blocking layer is made of α-NPD while intrinsic BPhen acts as hole blocking layer. The built-in voltage V$_{bi}$ is found to be 2.53 V, taken from [110].

If a voltage is applied at the contacts, the high conductivity of the doped materials leads to a negligible potential difference across the transport layers. Thus, the external field drops completely over the intrinsic layers. When the built-in voltage is reached, electrons can be injected over the LUMO of the electron-transporting materials and holes over the HOMO of the hole-

transporting materials into the EML. There, recombination takes place by electrons and holes which meet on one and the same molecule.

An example of a current-voltage characteristic is depicted in Figure 2.14, in which the influence of a shunt resistance parallel to the OLED is illustrated. Before the built-in voltage is reached, a strong increase in the current over several orders of magnitude shows the drift-diffusion dominated region determined by the trap density. This second region can be described analytically with the Shockley equation for p-n junctions and Schottky diodes

$$j(V) = j_0 \left[\exp\left(\frac{eV}{nk_bT} - 1 \right) \right],$$ (2.14)

where j_0 is the saturation current, e the elementary charge, k_b the Boltzmann constant, T the temperature and n an ideality factor which is in the range of 1.8 - 2 at room temperature for p-i-n homojunctions [80]. Recently [111], it has been found that the ideality factor can be used as indicator for the kind of charge carrier recombination. At low bias, a non-radiative trap-assisted recombination is dominant whereas a bimolecular Langevin process [112] describes emissive recombination.

In the high voltage regime, the current is assumed to be limited by space charges. This assumption is not valid in general and depends on the intrinsic layer properties. Nevertheless, the I-V curve above 2.8 V in Figure 2.14 illustrates the region where emissive recombination takes place and the high carrier density leads to interactions of excited molecules with charge carriers.

RECOMBINATION OF CHARGE CARRIERS

After the charge carriers are injected and transported across the organic layers, Langevin-type recombination, assisted by attractive Coulomb interaction leads to excited molecular states in the emission layer [112, 113]. The recombination efficiency γ is given by the ratio

$$\gamma = \frac{j_{low}}{j_{high}} \leq 1$$ (2.15)

of the hole and the electron currents where j_{low} is the lower and j_{high} the higher one [43]. This ratio accounts for the charge carrier balance in the emissive region of the OLED. The whole recombination process is illustrated in Figure 2.15.
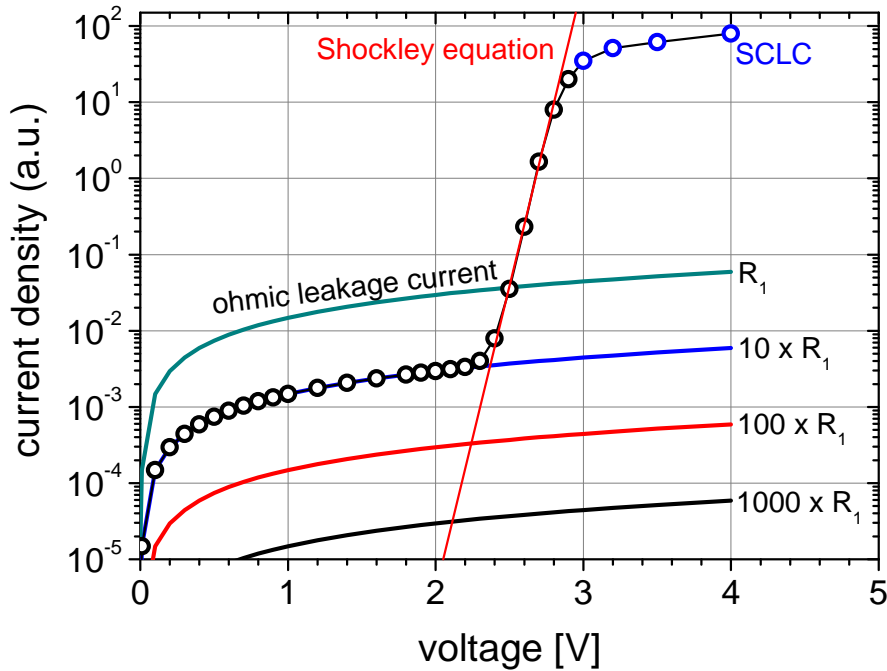
Figure 2.14: Typical S-shaped current-voltage characteristic of p-i-n structured OLED (circles) with an exemplary change of the leakage current, induced by the shunt resistance R_1. The Shockley equation can be used to describe the drift-diffusion dominated part of the I-V curve between 2.4 and 2.8 V while the space-charge limited current region is reached above 3 V in this example.

Exciton dynamics

Once excitons are created, their corresponding energy can be transferred via several channels as depicted in Figure 2.16. Further, one has to distinguish between singlet and triplet excitons because of their different lifetimes (see Section 2.1.5). Singlet excitons tend to decay immediately via fluorescence while triplets have a longer lifetime. The important energy transfer mechanisms are described by Förster- [114] and Dexter-type [115] transfers. The Förster energy transfer is dominated by dipole-dipole-interaction, i.e. it is based on Coulomb interaction. The effective radius can be up to 10 nm. The Dexter-type energy transfer originates from exchange interactions of the charge density distributions of a donor and an acceptor molecule (compare Figure 2.16). It depends on the spatial overlap of the corresponding orbitals and is therefore only effective in a range of 1 - 1.5 nm [43].

Both types of energy transfer enable excitons to migrate across organic layers randomly with respect to their lifetime. The gradient of the exciton density
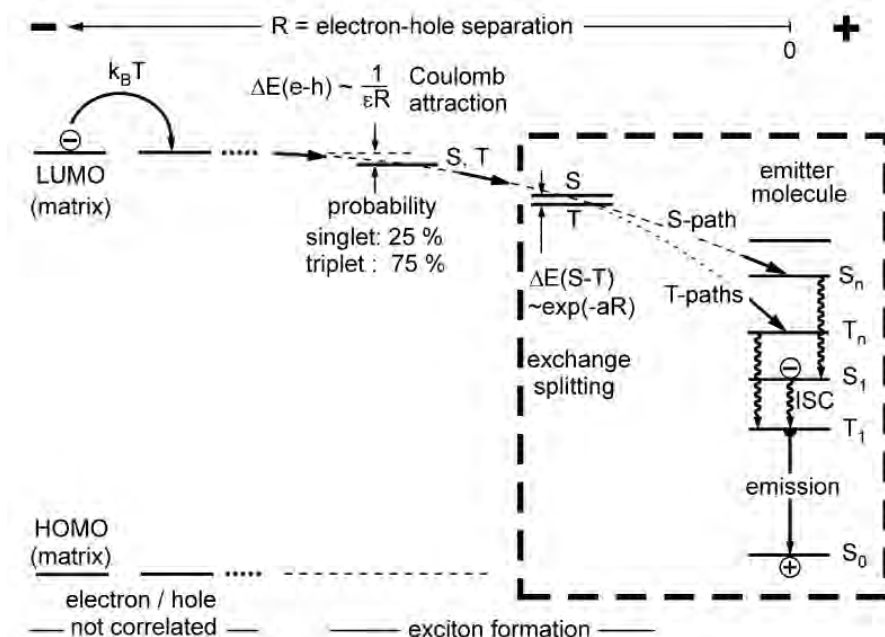
Figure 2.15: *Overview of exciton formation in a matrix-emitter, i.e. an host-guest system comprising a phosphorescent emitter. The hole (+) is assumed to be trapped first on the emitter molecule on the right while the electron movement is thermally assisted ($k_b T$) and finally the electron is captured via coulomb interaction. The system gains the binding energy $\Delta E(e\text{-}h)$ while the singlet-triplet splitting is $\Delta E(S\text{-}T)$. Determined by spin statistics, singlets form 25% and triplets 75% of the total exciton population. Several mechanisms lead to radiative and non-radiative decay, including intersystem crossing (ISC), taken from [84].*

determined by the recombination profile in the OLED is the driving force behind the diffusion process. The one-dimensional exciton distribution $n_x(x,t)$ can be described by the diffusion equation

$$\frac{\partial n_x}{\partial t} = G(x,t) - \frac{n_x}{\tau_x} - Q(n_x, x, t) + D\frac{\partial^2 n_x}{\partial x^2}, \qquad (2.16)$$

where $G(x,t)$ is the distribution of generated excitons, i.e. the recombination profile. $Q(n_x, x, t)$ accounts for exciton quenching processes and τ_x is the exciton lifetime which includes radiative and non-radiative decay mechanisms. D is the diffusion constant.

If the emission layer (EML) enables a preferential transport of one kind of charge carrier, it is justifiable to assume a recombination profile located at a blocking layer interface. If the recombination zone is thin compared to the EML and if one assumes homogenous and isotropic layer properties, the
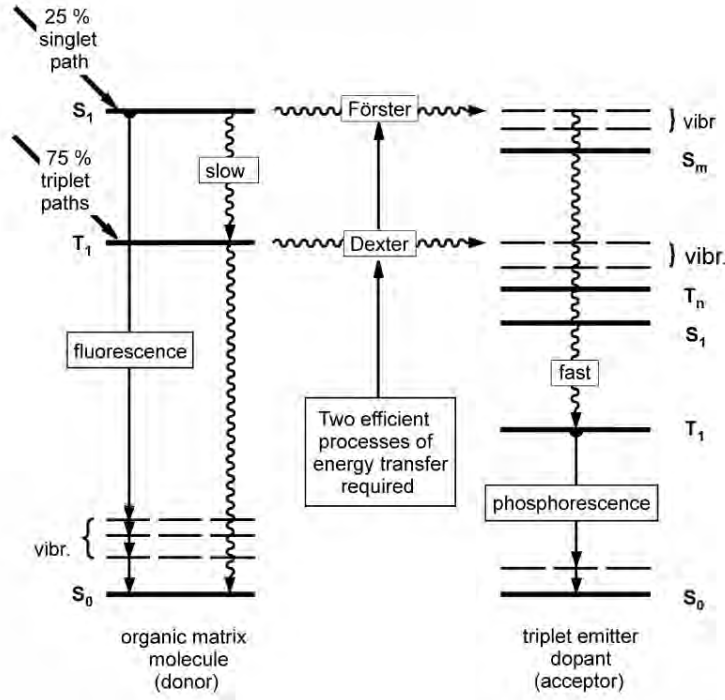
Figure 2.16: Energy transfer mechanisms demonstrated by an host-guest system incorporating a triplet emitter doped into an organic matrix material, taken from [84].

steady-state exciton density can be described by a spatial exponential decay given by

$$n_x(x) = n_0 \cdot \exp(-x/L_D) \quad \text{with} \quad L_D = \sqrt{D\tau}. \tag{2.17}$$

Here, n_0 is the exciton density at the generation interface and L_D is the exciton diffusion length. This quantity can be determined experimentally and can range from about $5\,\text{nm}$ for singlets in PTCDA[1] [116] to almost $15\,\text{nm}$ for triplets in 4P-NPD [117].

At high current densities and therefore high exciton densities, quenching becomes an important loss channel. Two mechanisms should be mentioned here. First, exciton-polaron quenching is the interaction between excitons and localized charge carriers, e.g. at doping sites. The exciton-polaron quenching rate is given by [118, 119]

$$\frac{\partial n_x}{\partial t} = -k_p \frac{\rho_c(j)}{e}, \tag{2.18}$$

with the rate constant k_p and the concentration of charge carriers $\rho_c(j)/e$.

---

[1]3,4,9,10-perylenetetracarboxylic dianhydride

More important for the OLED performance at high current densities is the bi-molecular triplet-triplet-annihilation (TTA). This process leads to non-radiative exciton decay at elevated exciton densities and reduces the triplet diffusion length. Its rate is given by [118]

$$\frac{dn_T}{dt} = -\frac{1}{2}k_{TT} \cdot n_T^2,$$ (2.19)

with the TTA rate constant k_{TT}. In phosphorescent OLEDs, TTA is the dominant process which reduces the device efficiency at high current regimes inducing the so-called efficiency roll-off.

2.2.3 OPTICS IN MULTILAYERED STRUCTURES

In the last section, the path of the charge carriers from injection at the electrodes via transport to the recombination zone has been discussed. Generated excitons diffuse with respect to the spatial recombination profile and in case of radiative decay, photons are emitted. To describe the light propagation, the complete OLED structure has to be considered as a purely optical system. In the following section, the light distribution within a multilayered system, the interactions of radiative molecules with their environment, and finally the light extraction will be discussed in brief.

Excited emitter molecules inside an optical structure can be regarded as emitting electrical dipoles and it is convenient to split the dipole emission into planar and evanescent waves that contribute to the far field and to the near field, respectively. Electromagnetic waves, propagating in an one-dimensional multilayer thin-film structure can be described by a transfer-matrix formalism [120, 121]. The Fresnel coefficients for the field amplitudes

$$r_s = \frac{n_1 \cos\theta_1 - n_2 \cos\theta_2}{n_1 \cos\theta_1 + n_2 \cos\theta_2} \quad \text{and} \quad r_p = \frac{n_1 \cos\theta_2 - n_2 \cos\theta_1}{n_1 \cos\theta_2 + n_2 \cos\theta_1}$$ (2.20)

determine the reflected and

$$t_s = \frac{2n_1 \cos\theta_1}{n_1 \cos\theta_1 + n_2 \cos\theta_2} \quad \text{and} \quad t_p = \frac{2n_1 \cos\theta_1}{n_1 \cos\theta_2 + n_2 \cos\theta_1}$$ (2.21)

the transmitted fractions of light that travel across a planar interface between two adjacent layers of the refractive indices n_1 (incident medium) and n_2. They depend on the polarization (s, p) and the angle of incidence θ_1.

The reflected and transmitted light of a multilayer can then be calculated by accounting for every single interface and their distances with respect to the optical medium in between. There are several formalisms [122–125] which

describe the incorporation of emitting dipoles in such a thin-film system. A detailed description of the model which is used for the optical simulations in this work can be found in the Appendix B.
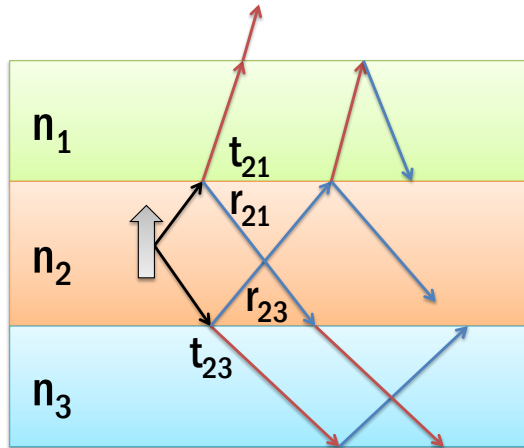

Figure 2.17: *The Fresnel coefficients r_{ij} and t_{ij} characterize the amplitudes of reflected and transmitted propagating light waves across the interfaces in a thin-film structure comprising a radiating dipole (thick arrow). The optical properties of the layers are determined by their thickness and refractive indices n_i.*

Light extraction in OLEDs

The coupling strength of the dipole emission to certain modes is directly connected to the optical environment. This effect is known as cavity effect and can be described classically [122]. Furthermore, the total emitted power of embedded emitter molecules depends on the surrounding media. This is called the Purcell effect [126] which accounts for the modification of the spontaneous emission rate from excited states in the presence of a certain optical environment, e.g. an optical cavity [127]. It is of quantum mechanical nature. Both effects can play a significant role when considering the outcoupling efficiency η_{out} of an OLED defined as

$$\eta_{out} = \frac{\text{generated photons}}{\text{extracted photons}} \qquad (2.22)$$

because they influence the number of both generated and extracted photons. In free-space, the radiative efficiency of an emitter molecule is given by

$$q = \frac{\Gamma_{rad}}{\Gamma_{rad} + \Gamma_{nonrad}} \qquad (2.23)$$

38

with the rates Γ_{rad} for radiative and Γ_{nonrad} for non-radiative decay. Inside an OLED structure, this efficiency has to be modified due to the optical environment which results in the effective radiative quantum yield [128]

$$\eta_{rad}^{eff} = \frac{F(\lambda)q}{1 - q + F(\lambda)q} \qquad (2.24)$$

that includes the total emitted power or Purcell Factor $F(\lambda)$ at a given wavelength λ.

Combining Equations 2.15, 2.22 and 2.24 and with respect to the singlet triplet ratio, the external quantum efficiency is given by

$$\eta_{EQE} = \gamma \cdot \eta_{out} \cdot \eta_{rad}^{eff} \cdot \chi, \qquad (2.25)$$

with the statistical maximum of radiative exciton decays $\chi = 0.25$ for fluorescent emitters and $\chi = 1$ for phosphorescent emitters.

Early approximations of the light extraction in top-emitting OLEDs yield about 20% outcoupling efficiency [129]. In the last years, intense work in this field led to a very good understanding of the light propagation in bottom- and top-emitting OLED devices. Mode analysis studies, carried out for bottom-emitting OLEDs [130, 131] revealed the strong influence of transport layer thickness and more importantly of the intrinsic quantum yield on the outcoupling efficiency. Assuming an electrically ideal charge carrier balance, low ohmic losses and highly efficient emitter molecules, the only limiting factor in OLED efficiency is the outcoupling [132, 133]. Therefore, the investigation of the optical device properties is necessary to identify the loss channels which have to be avoided to retrieve as much light as possible from the OLED layers.

In the case of top-emitting OLED structures, the interplay between device geometry and optical properties is rather complex. Due to the use of metal layers as electrodes that have a fairly high reflectance even at low layer thicknesses, the top-emitting OLED geometry leads to an optical structure which can be regarded as a micro resonator. While a significant part of light is reflected at the semitransparent top electrode, pronounced interference effects emerge. The superposition of all reflected and transmitted light waves inside the thin-film stack creates a steady state of the optical electric and magnetic field components, leading to a spatial field distribution that is localized across all OLED layers. Primarily, this mode distribution depends on the optical geometry of the OLED architecture, meaning sequence and thicknesses of the layers and their refractive indices, respectively. Secondly, the amount of radiative power that is fed into a certain mode depends strongly on the spatial
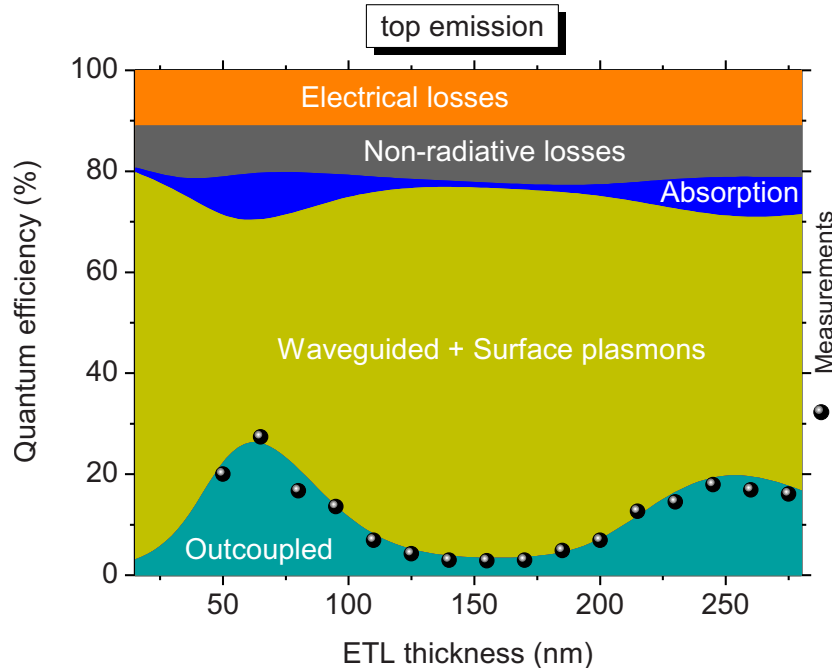
Figure 2.18: *Distribution of loss channels and measured external quantum efficiency (EQE) for a top-emitting OLED depending on the electron transport layer (ETL) thickness. The major loss is found to originate from light coupling to waveguide and surface plasmon polariton modes. The maximum EQE of 27% is measured for a $\lambda/2$ cavity. Taken from [134].*

distribution of emitting molecules inside the OLED [135, 136] and on their preferential orientation [137, 138]. Recently, Schmidt et al. found an evidence of non-isotropic emitter orientation in phosphorescent OLEDs using $Ir(MDQ)_2(acac)$ as emitter and α-NPD as matrix [139].

Experimentally, the mode structure can be observed by means of measuring reflectance and transmittance of such layer architectures. Becker et al. [140] showed that the cavity mode splits into TE (s-polarized)) and TM (p-polarized) polarization with different magnitude due to different phase changes upon reflection at the silver mirrors. Meerheim et al. [134] did a complete mode analysis of top-emitting OLED devices and found coincidence between experimental data and calculations of the outcoupled fraction. Figure 2.18 shows the resulting mode distribution where it becomes apparent that 40 - 60% are lost due to waveguide and surface plasmon polariton modes. The outcoupling maximum is almost 30% while the remaining 20 - 30% are electrical and non-radiative losses as well as absorption. The authors could also determine the quantum yield $q = 0.89$ of the used emitter system NPB doped with 10% of $Ir(MDQ)_2(acac)$, assuming an isotropic orientation of the emitting molecules.

For bottom-emitting OLEDs, several outcoupling techniques have been proposed [141]. For example, using highly refractive glass substrates in combination with substrate surface modifications, highly efficient OLEDs have successfully been demonstrated [14, 142]. The introduction of thin metal layers, deposited on ITO [105] or instead of ITO [143] as well as the use of dielectric mirrors [94, 144] has been shown to influence the micro optics in bottom-emitting OLEDs.

In top-emitting OLED architectures, a substrate modification is much more complicated as the subsequently deposited OLED might be influenced electrically. In 2002, Hobson et al. reported on outcoupling enhancement via surface plasmon coupling using periodic microstructures [145]. The difficulties also hold for modifications of the OLED after the deposition. One possible solution is an additional dielectric capping layer on top of the semitransparent metal contact. Such a layer does not have an electrical influence and can be included in the OLED fabrication process easily [146]. This approach has been applied to improve the efficiency of monochrome top-emitting OLED devices [147–149] and was used to realize white top-emitting OLEDs with metal electrodes [150, 151]. This concept will be further discussed and investigated in detail in Chapter 4.

2.2.4 State of the art inverted OLEDs

In applications like active matrix displays where the cathode is located on the substrate, it is mandatory to invert the complete layer sequence [152]. Thus, the anode layer has to be made of semitransparent metal or conductive oxides like ITO [12] for light outcoupling. The use of such inverted OLEDs for display applications is preferred when n-type thin-film transistors (TFT) from amorphous silicon (a-Si) are used for the backplane driver circuitry [8, 153]. There are other possibilities to avoid inverted OLED structures on Si but they demand complex TFT structures incorporating the OLED pixel [154]. In Figure 2.12 on page 30, the geometry of an inverted top emitting p-i-n OLED is compared to standard bottom- and top-emitting devices. Inverted structures have been investigated simultaneously with common OLEDs but gained not that much interest because of their inferior device performance. This is especially true if injection layers like LiF are used whose functionality require a certain deposition sequence of the OLED. In case of OLEDs based on doped transport layers, the situation is equivalent [10]. In Figure 2.19, the deviations between n-i-p and p-i-n phosphorescent OLEDs regarding driving voltage and luminous power become apparent. Having almost an identical device structure, the p-i-n devices exhibits a much steeper current-voltage characteristic than the corresponding n-i-p device [11].
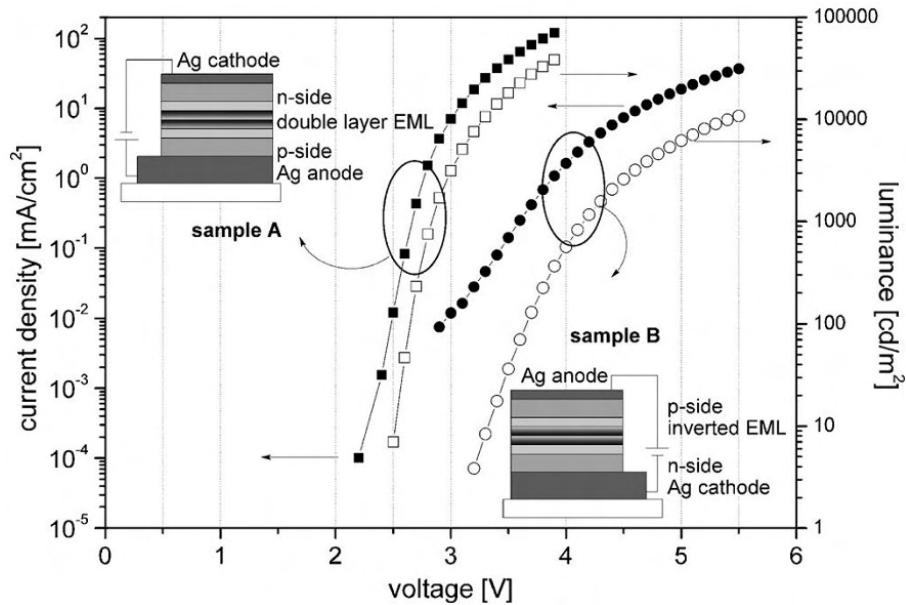
Figure 2.19: *Current density-voltage (j-V) and luminance-voltage characteristics of equivalent p-i-n (A) and n-i-p (B) structured OLED devices. Comparing the j-V curves (filled symbols) a clear discrepancy of up to 2 V is observed, taken from [11].*

In most reports about inverted OLED devices, the high driving voltage is attributed to a poor electron injection from the bottom cathode [155, 156]. In the non-inverted case, the lower voltages are thought to be connected to the effect of metal penetration into organics when depositing the cathode onto the organic layers. This leads to different energy level alignments comparing metal-organic and organic-metal interfaces [11]. In contrary, Shen et al. could demonstrate symmetric three-layer Al-Alq$_3$[2]-Al devices with symmetric current-voltage characteristics [157].

The majority of publications about inverted OLEDs shows device improvements by adding electron injection layers between the bottom cathode and the electron transport layer. Various approaches like ZnS nanoparticles [158], a pentacene interlayer [159] or an Alq$_3$ + LiF + Al tri-layer [13] have been proposed to enhance electron injection in inverted OLEDs. Alkali metal and alkali metal oxide doped injection or transport layers [73, 74, 160], as well as MgO, PbO and WO$_3$ buffer layers [161–163] or oxygen doping [164] are techniques that have also been shown to improve the device performance. A transfer of a non-inverted OLED to another substrate via lamination to form an inverted OLED has been demonstrated as well [165].

---

[2]Tris(8-hydroxyquinolinato)aluminium

In the case of doped charge transport layers, the energetic differences between metal-organic and organic-metal interfaces can be neglected. It can be shown that the injection is not the dominating factor in this case [10]. Therefore, as the voltage drops only across the intrinsic layers, the transport across the organic layers and their interfaces with the corresponding energetic barriers have to be considered as one major reason for the increased voltages as depicted in Figure 2.19.

Recently, thermal annealing has been found to improve the driving voltages [166] of inverted OLEDs. Before, it could be shown several times that thermal annealing improves conventional devices due to enhanced carrier injection and reduced energy barriers by diffusion of dopants like e.g. lithium [167, 168].

Thus, material diffusion processes, activated chemical reactions as well as morphological changes are most probably responsible for the different performances of inverted and non-inverted OLED devices. One aim of this work is to get a deeper understanding of the underlying mechanisms, especially regarding the use of doped charge transport layers. The corresponding investigations are summarized in Chapter 5.

2.2.5 MORPHOLOGY OF THIN FILMS IN ORGANIC DEVICES

ORGANIC FILMS

In organic solids, the molecular orientation and disorder has a significant influence on the distribution of electronic states. Thus, the morphology as well as the molecular structure determine the orbital overlap of adjacent molecules and consequently the hopping probability for charge carriers. The charge transport as well as interface effects are therefore directly connected to the morphology of the organic films and the electrodes.

The layer properties may also change with the position inside a certain film, i.e. there might be differences of transport properties at the interfaces compared to the bulk region of an organic thin film. Consequently, inverting an OLED can have significant changes in injecting and transporting charges from one layer to another.

It can also be shown that the substrate [169], its temperature [170], and the deposition rate have a strong influence on the film growth and the grain size [171].

Due to the fact that organic solar cells benefit from a certain layer morphology, the research in this field is very active. There, phase separation, crystallization, and annealing [172] are very important for the device performance [173]. In OLED devices, layers are assumed to be amorphous with a high degree of disorder. In the last years, more research has been done to understand the layer formation during the film deposition or when being exposed to heat

afterwards. It could be shown that the deposition rate of Alq_3 influences the current-luminance characteristics of underlying OLED devices [174] as it alters the morphology of the Alq_3 film. Alq_3 layers have also been studied with X-ray methods to determine their behavior when being thermally annealed (150-170 °C). They show thermally induced crystallization and an increase of the film density and the surface roughness [175].

Even emitter layers can be strongly influenced by exposure to heat. Neutron reflectometry revealed that the morphological stability of an annealed $Ir(ppy)_3$ doped CBP film is increasing with the $Ir(ppy)_3$ doping concentration. Additionally, BCP molecules tend to diffuse into this emitter layer when being located adjacent to it [176]. Furthermore, an induced crystallization of NPB[3] by an underlying CuPc[4] film could be demonstrated [177].

From the photo-physical point of view, it is interesting that the photoluminescent (PL) intensity and PL excitation spectra of α-NPD films were found to change drastically at annealing temperatures above 70 °C. This effect is shown in Figure 2.20 and correlates to the glass transition temperature of about 95 °C [178] for this material. The authors conclude that α-NPD can change its molecular packaging and orientation of the molecules even below the glass transition temperature. Further, the change in molecular orientation does not have to be homogeneous across a thin-film. It can be shown, that a multilayer system can be made out of one material by changing the substrate temperature during layer deposition. This means that exposure to heat during OLED deposition or annealing afterwards might influence the energetic levels of adjacent organic layers which alters the charge transport.

As common oligomers have glass transition temperatures in the range of 100 °C, it is not surprising that the deposition process has a significant effect on the layer morphology. For example, D'Andrade et al. [180] found an altered OLED device stability by tuning the glass transition temperature T_g of the electron transport layer. It consisted of a BPhen - $BAlq_2$ (T_g = 62 °C and 92 °C) mixture where the glass transition is adjustable by the mixing ratio. Nevertheless, one has to keep in mind that the glass transition temperature of a material is a good indicator when trying to locate possible morphological changes in a multilayered device.

Silver films

Typically, Ag films grow in islands as depicted in Figure 2.21. The coalescence strongly depends on the deposition rate and on the substrate temperature [181]. In addition, the underlying material influences the growth and

---

[3]N,N'-bis(naphthalen-1-yl)-N,N'-bis(phenyl)-benzidine
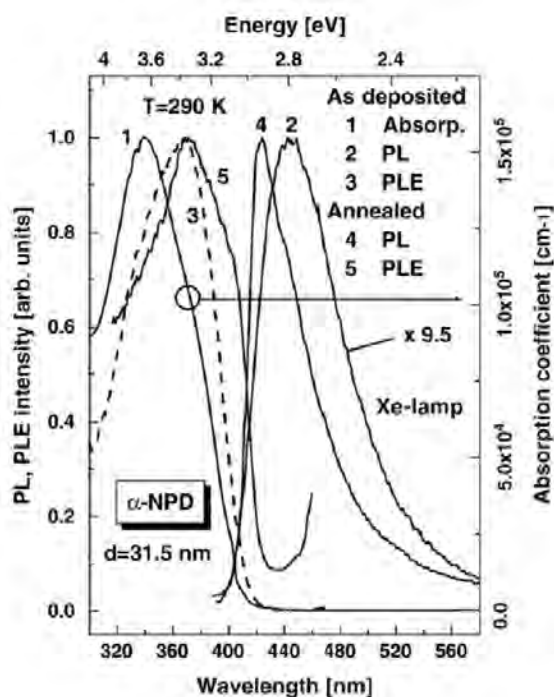[4]copper phthalocyanine

Figure 2.20: Absorption, photoluminescence (PL) and PL excitation spectra of α-NPD films before and after annealing at 80 °C for 120 min, taken from [179].

the optical constants of these thin metallic films. This can be explained by Maxwell-Garnett theory [182]. Since the 1930s it is known that the refractive index n and the absorption coefficient k of Ag films depend on the film thickness as well [183, 184]. Pure evaporated Ag films tend to have a lower surface roughness with increasing deposition rate. Thin layers of Ag show a polycrystalline morphology with a grain size of 20-30 nm [185]. Recently, the effect of an underlying layer on the growth could be shown for thin Ag contacts (15 nm) [186]. Different roughness and film morphology could be observed when Ag was evaporated onto thin organic BPhen films, depending on a 1 nm thick Al surfactant interlayer. Figure 2.22 illustrates the smoother and more closed nature of an 14 nm Ag film with 1 nm Al compared to a pure Ag film which shows holes and larger features with less coalescence. Here, the surfactant layer turns a Volmer-Weber [187] growth into a Frank-van-der-Merwe-like [188] smooth formation of the Ag film.

The dependence on the underlying material can further be investigated by optical spectroscopy. In Figure 2.23, R and T of evaporated Ag films with and without a 30 nm organic BPhen film between the substrate and the Ag film are depicted. The experimental data from the films on glass agree very well
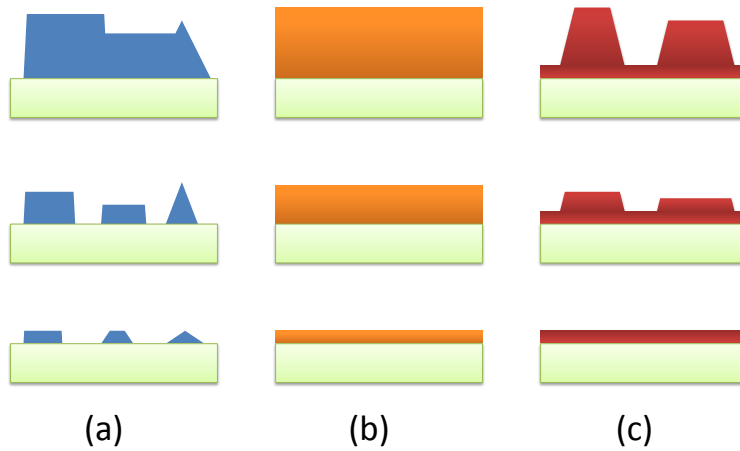
(a)   (b)   (c)

Figure 2.21: The different mechanisms of film growth, evolving from the bottom to the top: a) Volmer-Weber-, b) Frank-van-der-Merwe-, and c) Stranski-Krastanov-mechanism, adopted from [189].

with published data from Sennett and Smith [181] and show the deviation of optical behavior of very thin silver films. Again, this is a confirmation that the aggregation and film formation of Ag depends strongly on the underlying material. Further, when depositing silver onto organics, it seems valid to use a fixed set of optical constants even for silver layers down to 10 nm thickness.

The fit of the experimental data in Figure 2.23 is completely consistent in presence of a BPhen interlayer. In the simple case of Ag films on glass, a fit is not possible anymore. The thickness dependence of the optical constants becomes directly observable.
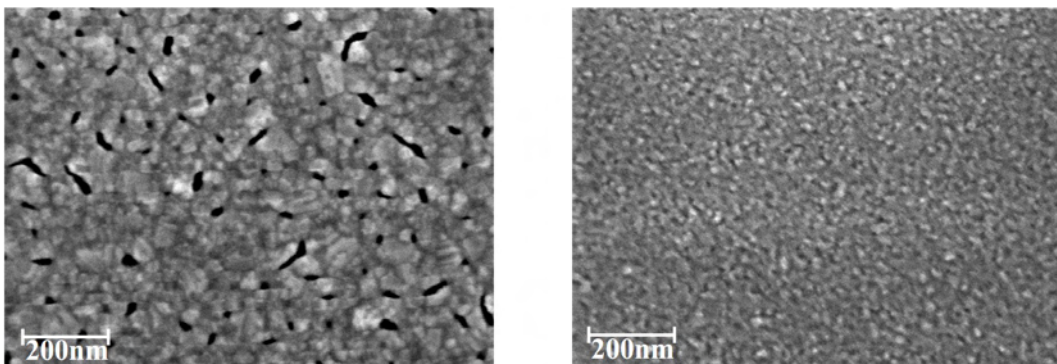

Figure 2.22: Scanning electron microscope (SEM) images of 15 nm thick evaporated Ag films on a 7 nm BPhen layer on glass without (left) and with 1 nm Al as surfactant layer (right), taken from [186].
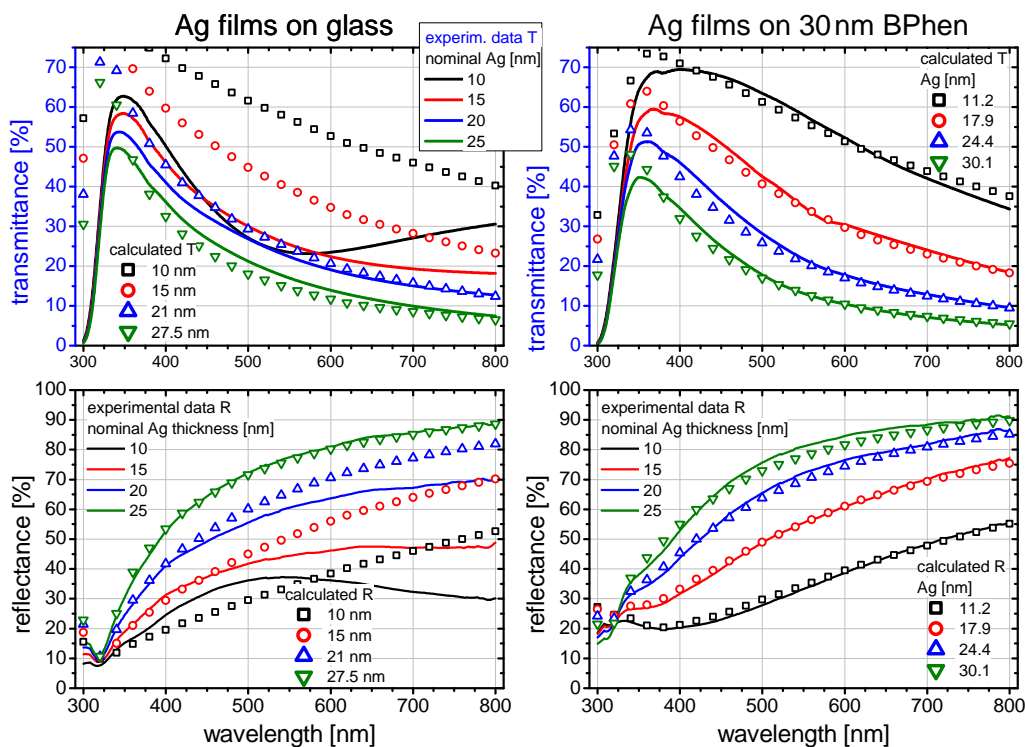
Figure 2.23: Transmittance and reflectance data of nominally 10, 15, 20, and 25 nm thick evaporated Ag films on glass substrate without (left) and with 30 nm BPhen layer (right) as surfactant layer. The quantity and the shape of the calculated R and T show that the additional BPhen film should have almost no influence because these behave very similar when comparing the graphs on the left with the ones on the right (symbols).

Finally, annealing of Ag films in atmosphere leads to a colored, brownish appearance. Electron diffraction reveals the occurrence of silver sulphide and silver oxide when the Ag film is exposed to air for several days [181].

All issues discussed in this section have an influence on the electronic properties at the corresponding layer interfaces. There is no doubt in literature that the different growth during depositing of a certain material leads to different interface formation with respect to the layer sequence. This is especially an issue when comparing metal on organic with organic on metal interfaces. Several scenarios of metal layer formation, including material penetration and film growth according to Figure 2.21 have been proposed and can be validated in the experiment [48].

3 EXPERIMENTAL TECHNIQUES AND MATERIALS

In this chapter, the preparation and the characterization of single thin films and organic devices are described. Further, the experimental techniques that provided the measurement data in this work are briefly discussed.

3.1 PREPARATION OF ORGANIC DEVICES

The experimental part of this work is based on the evaluation of organic thin-film devices. To fabricate these multilayers, every material is deposited by thermal evaporation under ultra-high vacuum conditions between 10^{-7} and 10^{-9} mbar. A multi-chamber deposition tool from Bestec GmbH is used to fabricate small series of samples. This cluster tool contains 4 chambers for evaporation of organic layers, each containing 6 - 8 evaporation sources. For large scale experiments, a single chamber deposition tool from Kurt J. Lesker company is available. It includes 12 sources for organic materials. The layer thickness is monitored by a quartz crystal, operating at 6 MHz. The lateral structuring of the thin-films for the definition of the active device area (e.g. OLED pixel) is realized with a shadow mask. The active area of a single OLED pixel is 6.76 mm^2. Flat glass panels are used as substrates while cavity glass lids act as encapsulation against moisture and oxygen. The encapsulation process is done in nitrogen (N_2) atmosphere. As the transmittance of the encapsulation glass is depending on the polarization, these effects have to be considered to determine the spatial emission of top-emitting OLEDs. This is discussed in Appendix B.

The organic materials are purified by a gradient sublimation technique which is repeated several times to reach an appropriate degree of purity. The fabrication of doped organic layers is done via co-evaporation of the desired materials by adjusting the molar ratio or molecular weight ratio. Uncertainties in layer thickness can occur due to uncertainties of the material density or the spatial dependent evaporation cone of a source which depends on the filling level of the source, the material itself, and the geometry of the chamber. These influences are partially compensated by a rotating substrate during film deposition.

3.2 DEVICE CHARACTERIZATION

CURRENT-VOLTAGE-LUMINANCE

The electro-optical characterization of OLEDs is done with the help of a measurement robot. It automatically contacts the electrodes of a sample and drives the device electrically. The current source is a SMU (source measure unit), model 2400 from Keithley Instruments. While an OLED is driven, the electroluminescence signal is detected by a Si-photodiode. The calibration of this photodiode and the emission spectrum measurement is done with a calibrated spectrometer CAS 140CT from Instrument Systems that is coupled to the measuring head via an optical fiber. The measured quantity is the spectral radiant intensity per unit area I_0^λ [$\mathrm{W/m^2\, sr\, nm}$] of the OLED surface in forward direction (0°) which directly yields the forward luminance L_0 [$\mathrm{cd/m^2}$]. Both quantities are connected by

$$L_0 = K_m \int_{380\,\mathrm{nm}}^{780\,\mathrm{nm}} I_0^\lambda(\lambda)V(\lambda)d\lambda \qquad \left[\frac{\mathrm{lm}}{\mathrm{m^2\, sr}} = \frac{\mathrm{cd}}{\mathrm{m^2}}\right] \qquad (3.1)$$

with the conversion coefficient $K_m = 683\,\mathrm{lm/W}$ and the photopic spectral luminous efficiency function $V(\lambda)$ which accounts for the spectral response of a human observer. For determining the external efficiency of a light source, the total light flux has to be known. As an OLED is a planar light-emitting device, it has a rotational symmetry with respect to the axis of the polar angle φ, i.e. an axis perpendicular to the surface. This means that the total amount of emitted light can be determined by measuring the spectral emission as a function of the azimuthal angle θ. It is known that the spatial emission strongly depends on the OLED architecture [190] and that the angular dependence in most cases deviates from that of a Lambertian emitter whose spatial distribution of the emitted radiant intensity is given by

$$I(\theta) = I_0 \cos(\theta), \qquad (3.2)$$

with respect to the radiant intensity in forward direction I_0. For a driven OLED pixel (voltage V, current I, current density j, luminance L_0) having an active device area A, the current efficiency is determined by

$$\eta_c(j) = \frac{L_0}{I}A = \frac{L_0}{j} \qquad \left[\frac{\mathrm{cd}}{\mathrm{A}}\right]. \qquad (3.3)$$

GONIO-PHOTOMETRY

Since most top-emitting OLEDs do not have a Lambertian emission characteristic it is necessary to measure the spatial emission of each OLED pixel.

This is mandatory for a proper investigation of the optical cavity and to determine the correct value for the totally emitted light per supplied electrical power. A gonio-photometer setup is used to obtain emission spectra from 0° to 90° azimuthal angle with a discretization of 5°. Therefore, the OLED pixel is mounted onto a rotary stage while the emitted light is coupled into an optical fiber and directed to an Ocean Optics USB4000 spectrometer.

From the azimuthal dependent spectral radiant intensity $I(\theta, \lambda)$, every efficiency quantity can be derived. The emitted luminous flux Φ_ν, given by

$$
\begin{aligned}
\Phi_\nu &= K_m \iint\limits_{\Omega \ \lambda} I(\Omega, \lambda) V(\lambda) \, d\Omega \, d\lambda \\
&= K_m \iiint\limits_{\varphi \ \theta \ \lambda} I(\theta, \lambda) V(\lambda) \sin\theta \, d\varphi \, d\theta \, d\lambda \\
&= 2\pi K_m \iint\limits_{\theta \ \lambda} I(\theta, \lambda) V(\lambda) \, d\Omega \, d\lambda
\end{aligned}
\tag{3.4}
$$

can be related to the dissipated electrical power $P = U \cdot I$. This leads to the luminous efficacy η_ν. It accounts for the totally radiated luminous flux by integrating over the whole forward hemisphere ($\theta = 0..\pi$ and $\varphi = 0..2\pi$) and with equation 3.4 it is

$$
\eta_\nu = \frac{\Phi_\nu}{P} = \frac{2\pi K_m}{UI} \iint\limits_{\theta \ \lambda} I(\theta, \lambda) \sin\theta \, d\theta \, d\lambda.
\tag{3.5}
$$

The luminous efficacy η_ν and the current efficiency $\eta_c(j)$ are photometric quantities and important figures of merit when comparing light sources. From the physical point of view, the ratio of extracted photons n_γ to the number of injected electrons n_e within a certain time period is very important, too. This ratio is called external quantum efficiency (EQE) η_q and is calculated by

$$
\eta_q = \frac{n_\gamma}{n_q} = \frac{2\pi e}{Ihc} \iint\limits_{\theta \ \lambda} \lambda I(\theta, \lambda) \sin\theta \, d\theta \, d\lambda,
\tag{3.6}
$$

with the speed of light c and the Planck constant h.

IMPEDANCE SPECTROSCOPY

For detailed studies of charge transport processes inside the OLED, it is not sufficient to measure the current-voltage characteristic of a device. The spectroscopic investigation of the complex electrical impedance of a sample can

provide further information about the physics inside.

The impedance measurements in this work were done using a Hewlett Packard 4284A precision LCR meter in combination with current-voltage measurements with a Keithley 236 Source Measure Unit.

In principle, this technique employs an alternating electrical field of the frequency $\omega = 2\pi f$ at the electrodes while measuring the response of the sample in form of amplitude and phase of the resulting current. From the measured current $I(t)$ and the applied voltage $U(t)$, the complex impedance $\hat{Z} = R + iX$ can be obtained.

One important requirement for a correct impedance measurement is a linear response of the investigated system to the voltage stimulus. This means that the impedance is independent from the magnitude of the periodic perturbation or in other words: the real part R and the imaginary part X fulfill the Kramers-Kronig-relations [191]:

$$X(\omega) = \frac{-2\omega}{\pi} \int_0^\infty \frac{R(\omega') - R(\omega)}{\omega'^2 - \omega^2} d\omega', \tag{3.7}$$

$$R(\omega) = R(\infty) + \frac{2}{\pi} \int_0^\infty \frac{\omega' X(\omega') - \omega X(\omega)}{\omega'^2 - \omega^2} d\omega'. \tag{3.8}$$

The interpretation of the measured impedance differentiates between two approaches where the second one is solely used within this work.

(1) correlation to a mathematical model, based on physical theory which provides an impedance function

(2) correlation to an equivalent electrical circuit

The modulus $|\hat{Z}|$ and the phase φ of the impedance $\hat{Z}$ in the complex plane are given by

$$|\hat{Z}| = \sqrt{R^2 + X^2} \quad \text{and} \quad \varphi = \arctan\left(\frac{X}{R}\right). \tag{3.9}$$

As the thin-film system OLED is very complex and depending on a variety of parameters, an adequate mathematical model for the impedance is not applicable and the only method to interpret impedance data from these devices is the equivalent circuit analysis.

The low charge carrier concentration and the low mobility in intrinsic amorphous organic semiconductors lead to a delayed return of the system to its equilibrium. Measuring the electrical response of an organic semiconductor, one characteristic quantity is the dielectric relaxation time given by [191]

$$\tau_\sigma = \frac{\varepsilon}{\sigma} \quad \text{with } \sigma = q\mu n, \tag{3.10}$$

with the dielectric constant ε, the conductivity σ, the elementary charge q, the mobility μ and the charge carrier density n. From Equation 3.10 it is visible that a high conductivity leads to low relaxation times (fast processes) and vice versa. Consequently, the high frequency regime should monitor the doped region of the devices as the conductivity there is the highest. On the other hand, trapped charges provide a delayed response and should preferentially influence the low frequency signal of the measurement.

When an external electric field is applied and injection of charge carriers does not take place, the system will only be polarized. As the field increases and charge carriers are injected, the relaxation time τ_σ will decrease as a consequence of the increasing charge carrier density n.

EQUIVALENT CIRCUITS

The measured impedance data of most devices within this work is modeled by equivalent electrical circuits. The basic circuit elements are:

- Ohmic resistor R with $\hat{Z}_R = R$

- Capacitor C with $\hat{Z}_C = \frac{1}{i\omega C}$

- Constant phase element $\hat{Z}_{CPE} = \frac{1}{A(i\omega)^\alpha}$

The constant phase element (CPE) is introduced to describe impedance data of real (imperfect) capacitors. If the ideality factor $\alpha = 1$, the CPE acts as ideal capacitor while $\alpha = 0$ describes an ideal resistor. A CPE can also be interpreted as a non-ideal capacitor that possesses a time constant distribution [192]. It is introduced to describe the experimental data more accurately.

The most simple and common equivalent circuit used to describe organic systems is an RC-circuit where a resistor R and a capacitance C are connected in parallel.

At a frequency f, the complex impedance of such an RC element is given by

$$\hat{Z}_{RC} = \frac{1}{\frac{1}{\hat{Z}_R} + \frac{1}{\hat{Z}_C}} = \frac{1}{\frac{1}{R} + i\omega C} \quad \text{where} \quad \omega = 2\pi f. \tag{3.11}$$

Most importantly, for a quantitative analysis the capacitance can be calculated from the measured impedance by

$$C = \frac{1}{2\pi f} \cdot \frac{-X}{R^2 + X^2}. \tag{3.12}$$

In the following, two common basic equivalent circuits which are used to describe organic devices are introduced and the influence of their elements is

shown. A parallel RC-circuit connected to a series resistance R_s as shown in Figure 3.1(a) is the simplest method to describe impedance measurement data obtained from organic thin-film devices.

Figure 3.2 shows the calculated phase $\varphi(f)$ in a Bode-plot, the modulus $|\hat{Z}|$ of the impedance and the capacitance C from Equation 3.12 when varying every single parameter while keeping the others fixed. In the standard circuit, the parameters are fixed as follows: $R_s = 20\,\Omega$, $C_1 = 4\,\text{nF}$ and $R_1 = 1\,\text{M}\Omega$. These values represent typical parameters of organic devices as discussed in Chapter 5. Additionally, for such standard circuit, C_1 is exchanged by a constant phase element having the same capacitance value $A = C_1$ but a variable ideality factor α.
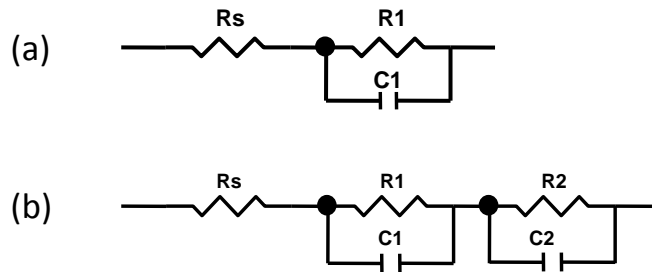

Figure 3.1: *Commonly used equivalent circuits to describe multilayered organic thin-film devices. For this work, the combination of either one (a) or two (b) RC circuits are important. Each of the capacitors can alternatively be replaced by a CPE accounting for non-ideal capacitive behavior or capture and release processes. R_s represents an additional series resistance.*
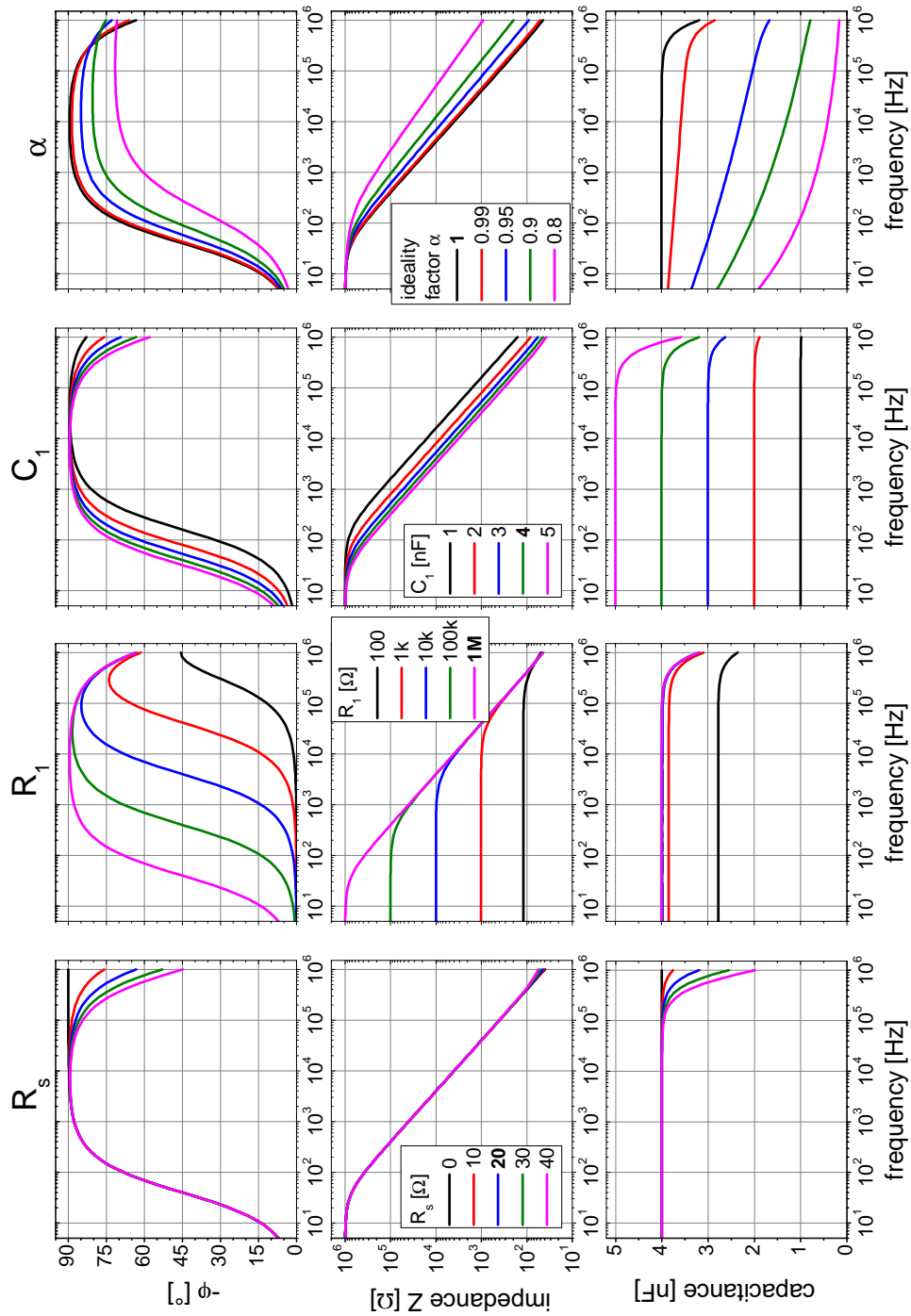
Figure 3.2: *Calculated influence of the elements R_s, C_1 and R_1 on the frequency dependent impedance of the circuit, shown in Figure 3.1(a). The impedance is represented by the negative phase φ (Bode-plot), the modulus of $\hat{Z}$ and the capacitance after Equation 3.12. If C_1 is replaced by a constant phase element, the influence of α is depicted in the last column. The standard values (bold) are $R_s = 20\,\Omega$, $C_1 = 4\,nF$, $R_1 = 1\,M\Omega$ and $\alpha = 1$.*

This calculation is repeated with an additional RC-circuit as shown in Figure 3.1(b). R_s, R_1, and C_1 are fixed at the standard values mentioned above. The influence of the second RC-circuit, characterized by R_2 and C_2 is depicted in Figure 3.3. The impedance is still dominated by the first RC-circuit but shows the frequency dependent disturbance from C_2 and R_2 according to their values.
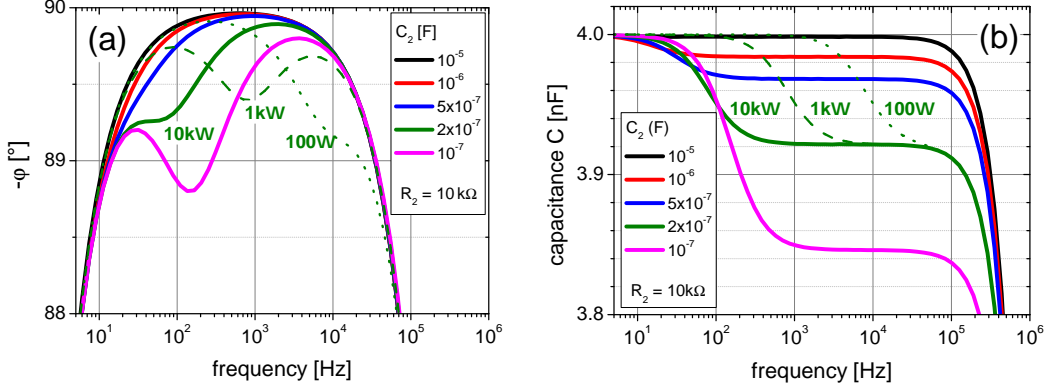

Figure 3.3: Bode plot (a) and capacitive behavior (b) of the circuit depicted in Figure 3.1(b) depending on C_2 calculated by Equation 3.12. The resistor R_2 is fixed at $10\,k\Omega$ and only varied for $C_2 = 200\,nF$ (green line). There, R_2 takes values of 0.1, 1 and $10\,k\Omega$.

Some features in the measured impedance spectra are more intuitive when we think of the geometrical capacitance C_{geo} of a plate-type capacitor. It depends on the device area A, the electrode distance d and the dielectric function ε_r of the material between the electrodes and reads

$$C_{geo} = \varepsilon_0 \varepsilon_r \frac{A}{d}. \tag{3.13}$$

It is important to know the dielectric function ε_r of the used organic materials. In literature, the values vary from 2.8 [193] to 4 [194]. Nevertheless, an assumption of $\varepsilon_r = 3$ seems reasonable for the materials used in the presented experiments [195].

Finally, the expected RC-time for the measured OLED devices can be calculated by $\tau_{RC} = RC$. The geometric capacitance of an OLED structure is mainly determined by the total thickness of the intrinsic blocker and emission layers. Being located between the doped transport layers and the two electrodes, an intrinsic thickness range of 40 - 100 nm results in $C_{geo} = 2 \cdot 10^{-8} - 2 \cdot 10^{-9}\,F$. If the resistance R is assumed to be in the range of 1 - 10 MΩ, the RC-time τ_{RC} is in the range of 0.002 - 0.2 s which equals a frequency range of 5 - 500 Hz. This is equivalent to the transition frequency obtainable from Figure 3.2 where the phase φ changes from 0° (resistive) to -90° (capacitive).

3.3 MATERIALS

Every organic material used in this study can be subdivided regarding its functionality inside an OLED structure. These are in general charge transport materials for holes and electrons, molecular dopants and fluorescent or phosphorescent emitter materials. Figure 3.4 summarizes the electronic levels for the HOMO and the LUMO of the used organic semiconductors determined by ultraviolet photoelectron spectroscopy, cyclic voltametry and measurement of the optical gap. Table 3.1 summarizes the work function values for most common electrode materials used in OLED devices. Finally, in Figures 3.5 and 3.6, the chemical structures of the used organic molecules are illustrated.
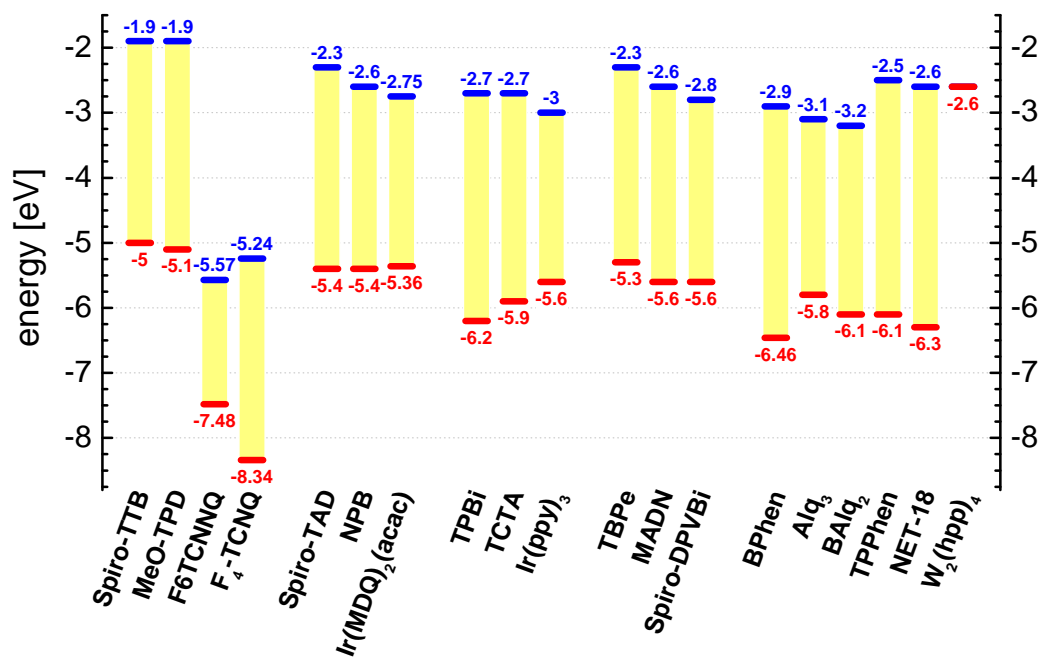

Figure 3.4: *Energetic positions of the HOMO and LUMO levels of the organic materials that were used to fabricate top-emitting OLEDs within this work. The materials are arranged according to their functionality. Starting from the left, hole transporting materials, p-type dopants, host materials, emitter molecules and electron transporting materials are shown.*
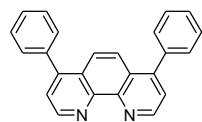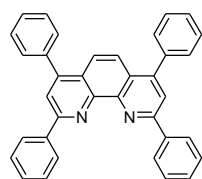
Table 3.1: *Work functions of metallic [196] and other electrode materials commonly used in OLED devices.*

material	work function (eV)
Mg	3.66
Ag	4.26
Al	4.28
Au	5.1
ITO	3.7 - 4.7 [48, 92, 93]
PEDOT:PSS	4.75 - 5.2 [197]

Electron transport

Hole transport

BPhen

MeO-TPD

TPPhen

Spiro-TTB

BAlq$_2$

NPB
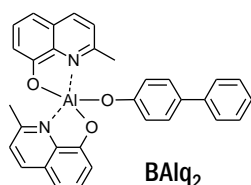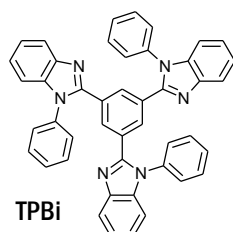
TPBi
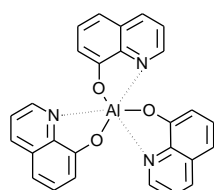
TCTA

Alq$_3$
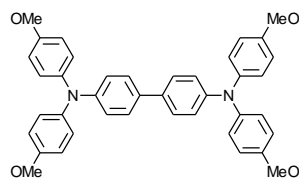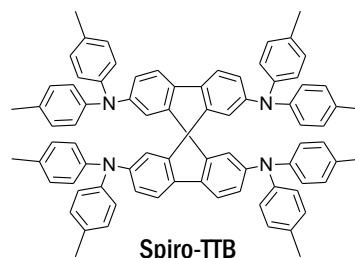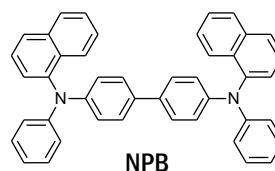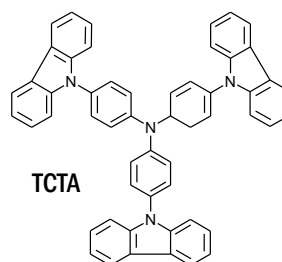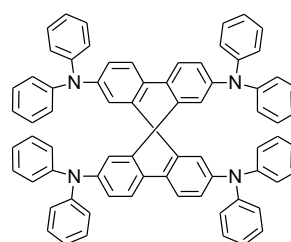
Spiro-TAD

Figure 3.5: Chemical structures of the organic compounds used as charge transport and blocking layers in the experiments within this work. The materials are arranged by their preferentially transported charge carrier type. The complete chemical names are listed on page 196.

Molecular dopants

W$_2$(hpp)$_4$ F6TCNNQ   F$_4$-TCNQ

Emitter molecules

Ir(MDQ)$_2$(acac)   Ir(ppy)$_3$ TBPe

Spiro-DPVBi   MADN
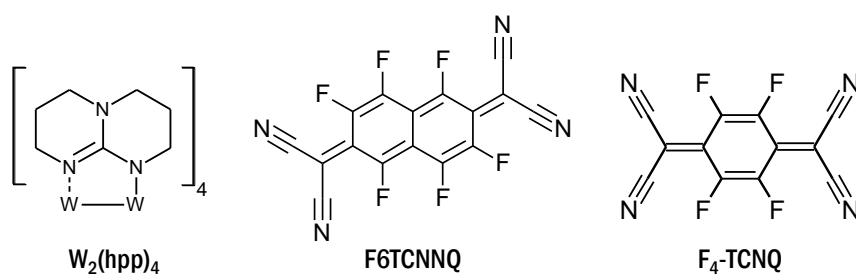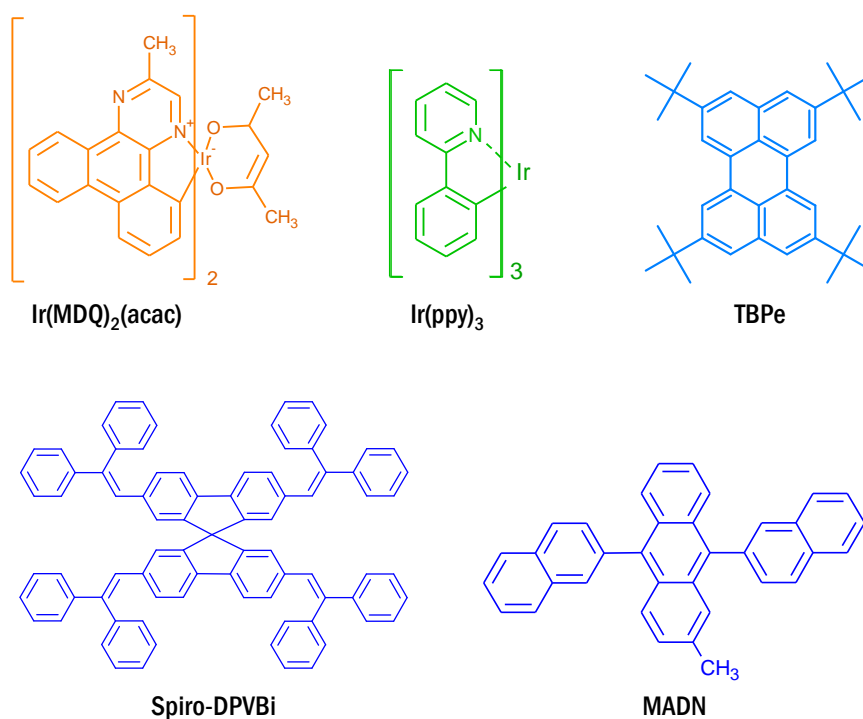
Figure 3.6: Chemical structures of the organic compounds used as acceptor, donor and emitter molecules, respectively. The colors of the emitter structures represent the emission color of each compound. The complete chemical names are listed on page 196.

4 Optical device properties

Within this chapter, the main parameters and their influences on the optical behavior of top-emitting p-i-n OLEDs are discussed. At first, the focus is put on monochrome devices with applied outcoupling enhancement layer (capping layer). A rigorous optimization process is performed by varying the free parameters simultaneously to obtain the global maximum for the outcoupling efficiency. In the second part, the capping layer concept and microlens films are utilized to emit white light from a microcavity top-emitting OLED comprising metal electrodes.

4.1 The bottom metal contact

As a top-emitting OLED is a thin film device having an optical character of a microresonator, it should be designed to have minimized optical losses due to absorptance. One important factor is the presence of metal layers as electrodes. For an inverted OLED, the bottom cathode has to be investigated with the aim of establishing a smooth and highly reflecting contact that is able to inject electrons most efficiently. From previous investigations [181] it is known that silver films can grow very aggregated, leading to pronounced spikes which cause short cuts or a local field enhancement. Such defects enable hot spots across the OLED area. An important indicator for such a rough bottom mirror is the leakage current or backward current in the n-i-p structured OLED device. A rough bottom electrode enables more pathways for the charge carriers to flow in parallel to the intrinsic emission layer. The experience showed that bottom contacts from pure Al do not exhibit that much problems regarding device stability but have a lower reflectance than pure silver contacts. Further, Al films get oxidized at their surface very fast when brought to air as well as in vacuum at lower reaction rate. The native oxide reaches a film thickness up to 30 Å but the change in reflectance is less than 0.3% in the visible (550 nm) [198].

To avoid thick and rough electrode layers, a bilayer combination of aluminum and silver is investigated. This layer combination enables a very high reflectance across the whole visible spectrum that is controllable by the thickness of Ag in the range of 0 - 40 nm.

Figure 4.1 shows the calculated reflectance (R) from an Al/Ag bilayer film on sodalime glass comparing air and an organic film as incident medium at 600 nm wavelength. The main conclusions from this calculation are:

1. An Al thickness $d_{Al} > 40$ nm does not lead to significant change in R.

2. In this case ($d_{Al} > 40$ nm), the absolute R can be adjusted by the Ag thickness, with respect to the electrical stability of the OLED stack that is going to be deposited.

3. For an Ag thickness $d_{Ag} > 30$ nm, R saturates at 97 - 98% if the underlying Al film is $d_{Al} \geq 40$ nm.
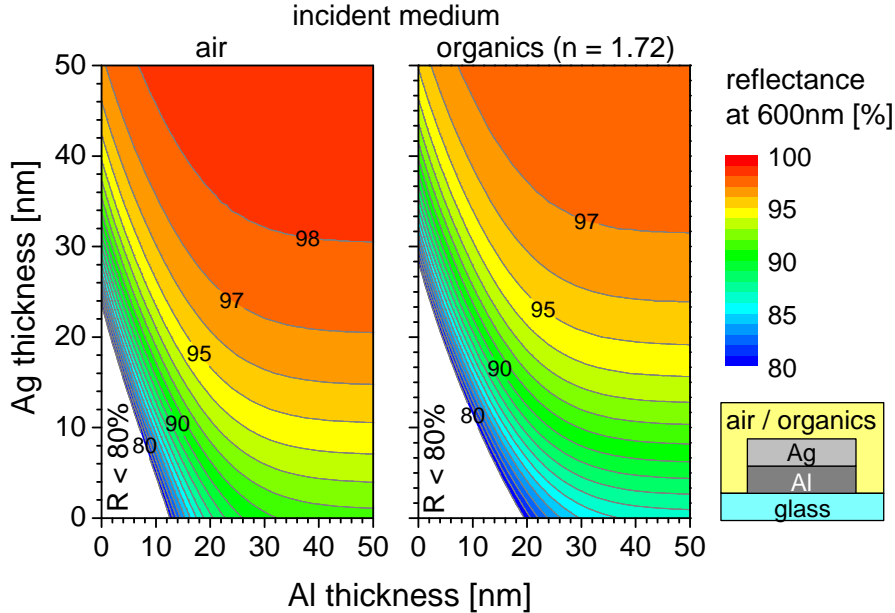
Figure 4.1: *Calculated reflectance at normal incidence of an Al/Ag bilayer cathode on glass depending on the layer thickness and on the optical medium of light incidence (left: from air; right: from organics).*

To verify the results of the calculations, the measured reflectance from pure electrode layers is correlated to the performance of inverted OLEDs. The OLED device structure, starting from the bottom is (thickness in nm):

Al(100) / Ag(0, 10, 20, 40) / BPhen:Cs(50) / BAlq$_2$(10) / NPB:Ir(MDQ)$_2$(acac) (10wt%)(20) / Spiro-TAD(10) / Spiro-TTB:F6TCNNQ(4wt%)(30) / Ag(15)
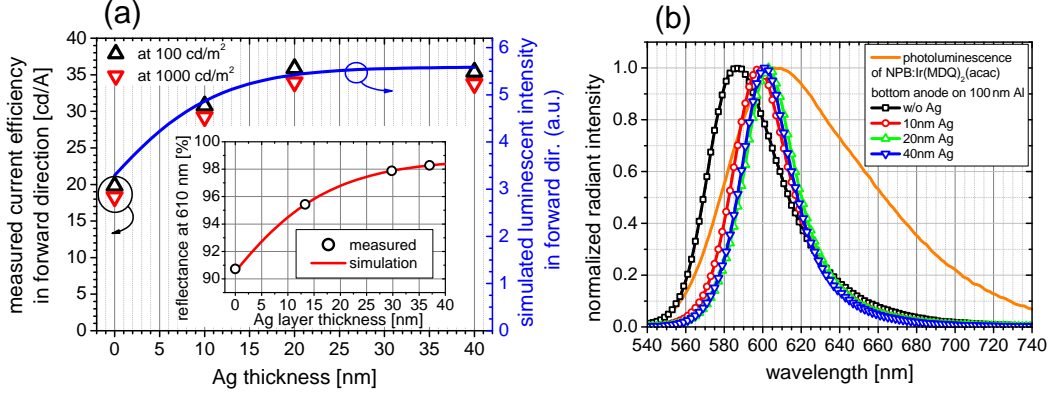
Figure 4.2: Current efficiency of inverted OLEDs at 100 and 1000 cd/m² (triangles) with different Ag layers on a 100 nm Al bottom cathode (a). Inset: Reflectance measurements (black circles) of pure Ag layers on 100 nm Al. All measured quantities are compared to optical simulation results. The corresponding EL spectra of the inverted OLED devices exhibit a red shift while getting narrow with increasing Ag layer thickness when compared to a pure Al anode (b).

In Figure 4.2, the current efficiency in forward direction, the reflectance of the pure electrodes in air and the EL spectra of the OLEDs are shown as a function of the Ag thickness of the Al/Ag contacts. First, the forward light output can be directly correlated to the absolute reflectance R of the bottom contact. The current efficiency as well as R increase with the Ag thickness, concluding that the Ag layer co-determines the outcoupling efficiency. Further, the current efficiency is compared to calculated luminous intensity data from optical simulations. Both experimental quantities depicted in Figure 4.2(a) increase as predicted by the simulations and the gradients fit very well to the experimental results. At around 30 nm of deposited Ag, the reflectance of the electrode saturates which leads to a stagnating current efficiency at approx. 35 cd/A. In the emission spectra of the devices in Figure 4.2(b), a second effect becomes apparent. With increasing Ag thickness and thus increased cathode reflectance, the cavity mode that couples to the far field gets narrowed and red-shifted. These observations can be understood of we introduce the (absorptance-free) finesse

$$F = \frac{\pi \sqrt{R_t R_b}}{1 - R_t R_b} \tag{4.1}$$

of a resonator. This quantity only depends on the reflectance R_t and R_b of the top and bottom contact (mirror), respectively. It is a figure of merit for an optical resonator and inversely proportional to its spectral mode bandwidth. Thus, the additional Ag layer leads to an increased value for the finesse, accompanied with the narrowing of the extracted light mode as it can be observed

from the EL spectra in Figure 4.2(b). The spectral narrowing goes hand in hand with the increasing reflectance and saturates at an Ag thickness of about 20 nm where the spectral bandwidth is dominated by the opposite contact, the semitransparent anode. The shift of the emission peak can be explained by the subsequent change of the phase shift ϕ upon the light reflection at the bottom contact depending on the Ag thickness. At normal incidence, ϕ at a metal (n_1, k_1) - dielectric (n_0) interface is given by [199]

$$\phi = \tan^{-1} \frac{2n_0 k_1}{1 - n_1^2 - k_1^2}. \tag{4.2}$$

It depends on the refractive index of the dielectric n_0 and the complex refractive index $\tilde{n}_1 = n_1 + i k_1$ of the metal that is quite different for Al compared to Ag [200]. As consequence, the optics of the OLED cavity become increasingly dominated by the Ag/organic interface with an increasing Ag thickness as less and less light reaches the Al layer. In conclusion, the application of a thin Ag layer onto an Al contact has a strong optical effect on the light outcoupling not simply by the increased reflectance, but further by an altering of the microcavity response.

4.2 Outcoupling enhancement in monochromic OLEDs

Several possibilities to enhance the light outcoupling in top-emitting OLEDs have been mentioned in Section 2.2.3. In the following, we concentrate on the application of a dielectric capping layer, trying to figure out its working principle. It will be shown that adding such a layer can change the microcavity response completely which has to be taken into account in the optimization process. Therefore, the influence of several parameters of the OLED multilayer system is discussed because they can counteract in influencing the emission properties.

4.2.1 Optimization of the OLED cavity

The quantification of light outcoupling is mainly done using spectrally resolved and spatially integrated quantities. The spectral response or spectral emission affinity of an OLED can be described by the cavity emission intensity that is emitted from such a micro-resonator. It reads [201]

$$C(\lambda, \theta) = \frac{T_t \left[1 + R_b + 2\sqrt{R_b} \cos\left(-\phi_b + \frac{4\pi n_{org} z_0 \cos(\theta_{EML})}{\lambda} \right) \right]}{\left(1 - \sqrt{R_b R_t} \right)^2 + 4\sqrt{R_b R_t} \sin\left(\frac{\Delta\phi}{2} \right)} \tag{4.3}$$

where T_t is the total transmittance of the top layers and z_0 the distance of the radiating molecules to the highly reflecting bottom mirror. The reflectance and the incorporated phase shifts upon reflection for the top and the bottom fraction of a multilayer seen from the position z_0 are denoted by R_t, R_b, ϕ_t and ϕ_b, respectively.

Equation 4.3 describes the coupling of a dipole emitter to a certain optical mode, depending on the location z_0 of the dipole and the mode density determined by R_t, R_b, ϕ_t, and ϕ_b. $C(\lambda, \theta)$ can also be interpreted as cavity enhancement factor which accounts for the cavity effect introduced in Section 2.2.3.

The wave propagation direction θ_{EML} inside the EML is connected to the emission angle θ in air by Snells law:

$$n_{EML} \sin(\theta_{EML}) = n_{air} \sin(\theta). \tag{4.4}$$

Further, the phase shift of the light wave after one cycle in the cavity is given by

$$\Delta\phi = -\phi_b - \phi_t + \sum_i \frac{4\pi n_i d_i \cos(\theta_{org,i})}{\lambda} \tag{4.5}$$

with the resonance condition $\Delta\phi = 2\pi m (m = 0, 1, 2...)$. Any of the organic layers within the cavity is characterized by its thickness d_i and its refractive index n_i.

The spectral radiant intensity $I(\lambda, \theta)$ of the electroluminescence (EL) spectrum of a complete OLED can then be calculated by the convolution

$$I(\lambda, \theta) = I_0(\lambda) \times C(\lambda, \theta) \tag{4.6}$$

of $C(\lambda, \theta)$ and the spectral intensity $I_0(\lambda)$ of the radiating molecules in the absence of the cavity.

The amount of photons that is coupled into a solid angle of a certain direction with respect to the device normal is quantified be the radiant intensity

$$I(\theta) = \int_0^\infty I(\lambda, \theta)\, d\lambda \tag{4.7}$$

whereas the total photon flux n_p (per unit area) that is emitted into the forward hemisphere is calculated by

$$
\begin{aligned}
n_p &= \frac{1}{hc} \iint_{\Omega\ \lambda} \lambda\, I(\theta,\lambda)\, d\lambda\, d\Omega \\
&= \frac{2\pi}{hc} \int_0^{\pi/2} \int_0^{\infty} \lambda\, I(\theta,\lambda) \sin\theta\, d\lambda\, d\theta.
\end{aligned}
\tag{4.8}
$$

Deriving the photon flux from the calculated $C(\lambda,\theta)$ which is a relative quantity describing the emission characteristic of a modeled OLED, we make one important assumption. As explained in Chapter 2, Section 2.2, the radiative decay of excitons inside the cavity is depending on the optical environment. Hence, when comparing the photon flux of different OLED structures, we assume a constant radiative rate for every device geometry which is not true [127]. Nevertheless, this drawback is less pronounced when comparing device structures having an outcoupling efficiency close to the global maximum.

The basic layer structure of the discussed top-emitting OLED system to be optimized is shown in Figure 4.3. The organic layers are located between the semitransparent anode and the highly reflecting cathode. OLEDs comprising a p-i-n or a n-i-p structure have the advantage not being electrically sensitive against changes in the transport layer thickness. The transport layers determine the cavity length L and the location of the emitting molecules z_0 and can easily be adjusted without altering the device electronics. The metal contacts define the cavity finesse by their material and their thickness. The capping layer is deposited on top of the semitransparent anode.

The main influences of the cavity length L, the emitter location z_0 and the semitransparent top anode (d_{anode}) on the cavity emission are illustrated in Figure 4.4. The calculations are done, taking a single layer model OLED where all emitters are lying in one plane. The capping layer is neglected here as its influence will be discussed later in detail. The model structure is (from the bottom to the top):

Ag (100 nm) / organic layer (n=1.8, L=100 nm, z_0=54 nm) / Ag (d_{anode}=20 nm)
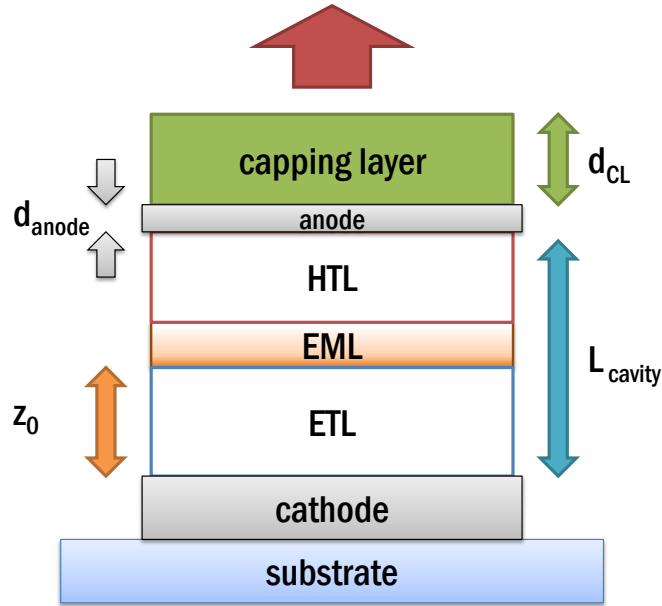
Figure 4.3: *General layer structure of a top-emitting inverted OLED, indicating the four free parameters that determine the optical response of such a multilayer system. During the optimization, z_0 and L are determined by the thickness of ETL and HTL, respectively. For simplicity, the blocking layers for electrons and holes are neglected in this picture because they can be regarded as 10 nm spacers between transport layers and EML.*

The variations of L, z_0 and d_{anode} are done separately, changing one parameter and keeping two fixed at the values given above. From Figure 4.4(a) and (b), it becomes clear that the resonance wavelength of the OLED cavity is dominated by L but also influenced by d_{anode}. With increasing anode thickness, the reflectance R_t also increases. The peak intensity of the cavity mode raises while the full width half maximum (FWHM) of the peaks decreases (see Figure 4.4(a)). This is the analog to the discussed increasing reflectance of the bottom electrode in section 4.1.

As the coupling to the far field is connected to the field strength at the emitter position within the OLED, the cavity emission and the total amount of extracted photons is strongly depending on z_0, shown in Figure 4.4(c). There is also a very weak influence on the resonance wavelength, shifting from 544 nm at $z_0 = 0$ nm to 552 nm at $z_0 = 100$ nm.

As a consequence it is important that a certain emitter is located at a specific position to enable the optimal coupling to the far field with respect to all propagation directions and its intrinsic emitter spectrum. From Figure 4.4(c) we can also conclude that a shift of the emitter position by $\pm$ 20 nm leads to
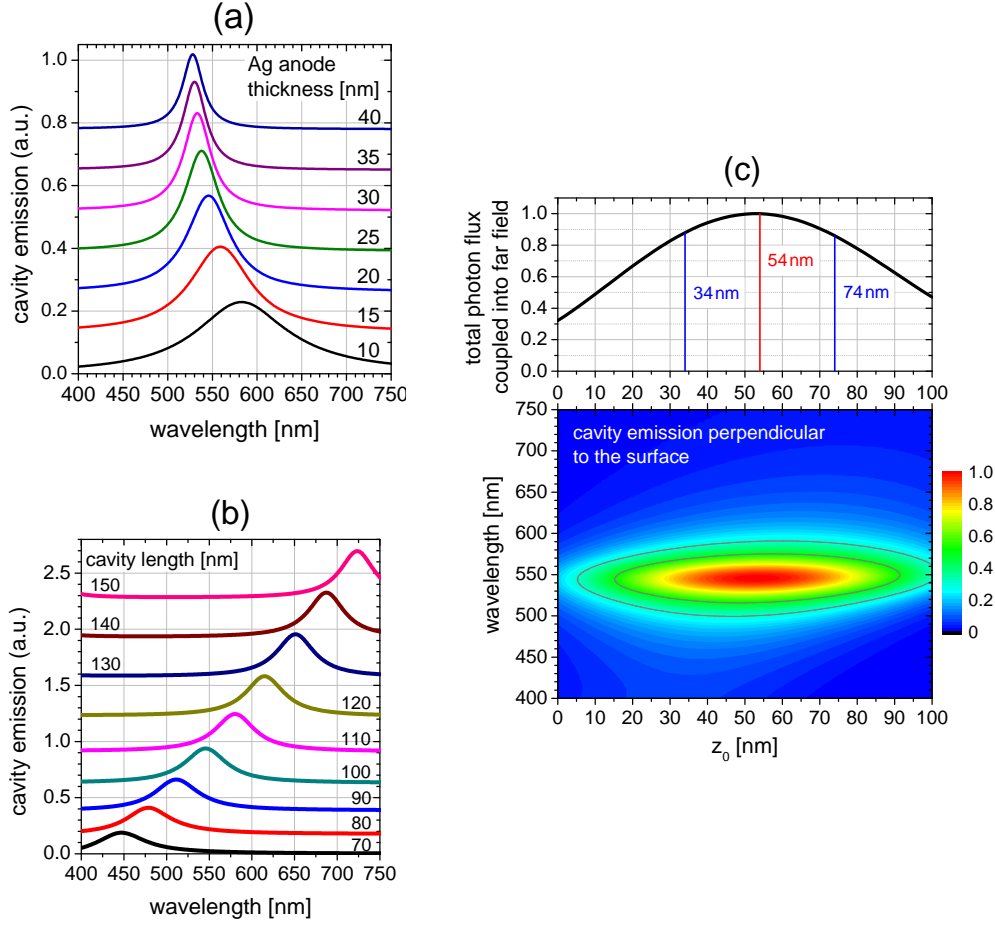
Figure 4.4: Optical simulation results for a simplified but representative top-emitting OLED layer structure. They illustrate the influences of the semitransparent top Ag anode d_{anode} (a), the cavity length L (b) and the emitter location z_0 (c) on the cavity emission and the photon flux n_p.

a decreased overall outcoupling of about 12%. This can be important when we assume that one charge carrier type is preferentially transported across the emitting layer and the emission zone is located next to an interface to a blocker layer.

With the basic understanding of the key parameters, reasonable variation ranges can be determined to find the OLED structure that has the maximum outcoupling efficiency. Therefore we carry out optical simulations with simultaneous variations of the thickness of the ETL, the HTL, the semitransparent Ag anode and the dielectric capping layer. We obtain a layer structure which, in terms of outcoupling, represents the global maximum within the boundary conditions. As bottom cathode, the previously investigated combination of Al

and Ag is used. The thickness of the Al layer was decreased to 50 nm, since such Al layer is almost opaque.

The initial device structure and the optimization results are listed in Table 4.1. The position of the emitting molecules z_0 is determined by the thickness of the ETL. Assuming a lower electron than hole injection into the OLED device, an emitter distribution located directly at the interface to the BAlq$_2$ blocking layer seems reasonable. We approximate the emissive part of the EML by a 2 nm wide active region located at the bottom of the EML with a constant emitter distribution.

Table 4.1: *List of the layer material and thickness parameters for the optical optimization of a complete inverted top-emitting OLED structure. The emissive region of the EML is assumed to be located at the interface to the BAlq$_2$ layer.*

Layer	initial/range (nm)	optimization result (nm)
NPB	0..200	90
Ag	15..25	20
MeO-TPD:F$_4$-TCNQ	20..60	40
NPB	10	10
NPB:Ir(MDQ)$_2$(acac)	20	20
BAlq$_2$	10	10
BPhen:Cs	35..80	65
Ag	40	40
Al	50	50

This assumption is a compromise because triplet excitons are known to diffuse as far as 10 nm until they radiate [117]. The reason to use such a thin emission region is that the model cannot handle the EML as emissive and absorptive at the same time. The tradeoff here is keeping as much as possible of the layer absorptive while having a reasonable thick emissive region. From Figure 4.4 it becomes also appropriate to do this because changing the EML to a width of 10 nm would alter the overall amount of light in the range of 1%. The calculated outcoupling efficiency values are depicted in Figure 4.5.
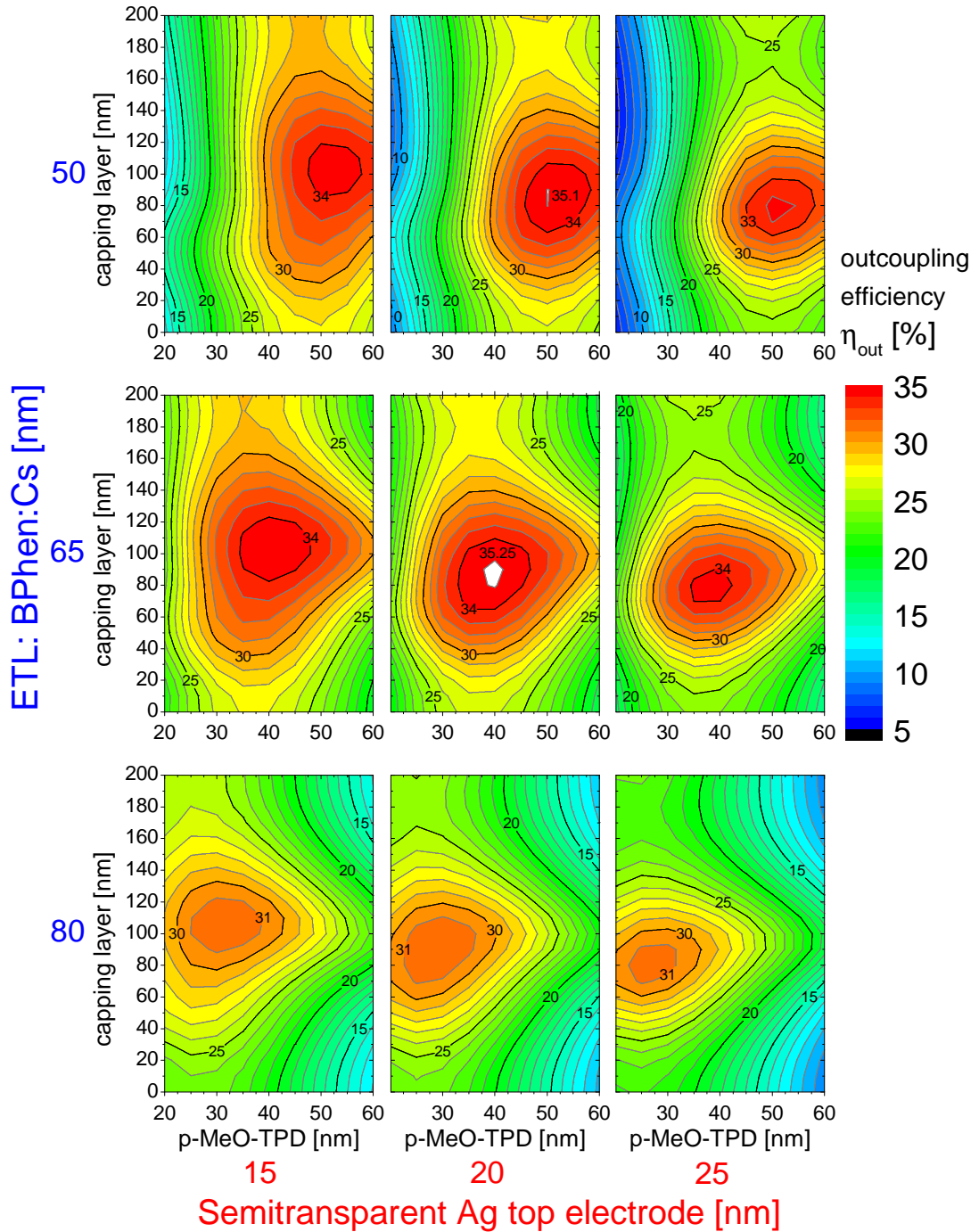
Figure 4.5: *Calculated absolute outcoupling efficiency depending on ETL, HTL, semitransparent top contact and capping layer thickness. From the local maxima, the global one can be found at 65 nm ETL, 40 nm HTL, 20 nm Ag top contact and 90 nm capping layer. The uncertainty for these values are ±5 nm for the capping layer thickness and ±2.5 nm for the other layers. The outcoupling efficiency of the optimized configuration is found to be 35.25%.*

In the following, the main observations from the optimization chart in Figure 4.5 are discussed briefly. Afterwards, the angular light distribution and the effect of the capping layer will be investigated in more detail to substantiate why the parameters of the optimized OLED have the calculated values.

On the one hand, the ETL and HTL thickness mainly determine the resonance condition of the OLED stack, i.e. the spectral range at which the microcavity is tuned to emit light into the far field. As expected, the local outcoupling maximum shifts to a lower HTL thickness (55, 40, 30 nm) with increasing ETL thickness (50, 65, 80 nm) while keeping the cavity length almost unchanged. This is reasonable, because the intrinsic emitter spectrum has a fixed peak at around 610 nm. On the other hand, the absolute outcoupling efficiency changes, as the position of the emitters shifts across the optimum when examining the three graphs in each column of the chart. The shift of the emission zone via the ETL thickness by $\pm$ 15 nm results only in weak changes of 4 - 5% less efficiency, while keeping L constant and adjusting the HTL thickness.

Secondly, the semitransparent Ag top anode has a strong influence on the OLED spectral bandwidth. This is visible when we compare all three graphs in every single row of the chart in Figure 4.5. With increasing Ag thickness, the local maxima get increasingly sensitive to variations of the other layer thicknesses. The reason is the narrowing of the cavity mode, as the reflectance from the top contact is increased. Surprisingly, the absolute outcoupling efficiency is almost invariant toward thickness variations of 15 to 25 nm for the top Ag anode which usually has a strong influence on the device optics. This can be advantageous for an industrial device fabrication process to ensure constant device efficiency with respect to process-related thickness deviations. The influence of the Ag thickness can be compensated by slightly adjusting the capping layer thickness.

As the capping layer has a pure optical function, it can be varied almost independently. In the range of 0 to 200 nm this layer exhibits a strong influence on the outcoupling, while the sensitivity depends on the other cavity parameters. For example we can look at the configuration: ETL = 50 nm and HTL = 30 nm in Figure 4.5, where we find no remarkable capping layer effect. It turned out that for our kind of device, an organic capping layer made from NPB of 80 - 110 nm thickness enables the highest outcoupling efficiencies. The absorptance of the top contact system plays an important role in this case which is discussed in the following section.

Before having a closer look at the optimized OLED structure and its optical properties, we try to validate the absolute values for the efficiency by an experiment and investigate the influence of the cavity tuning on the light outcoupling. This is done by fabricating OLEDs where the ETL thickness is varied around the optimum.
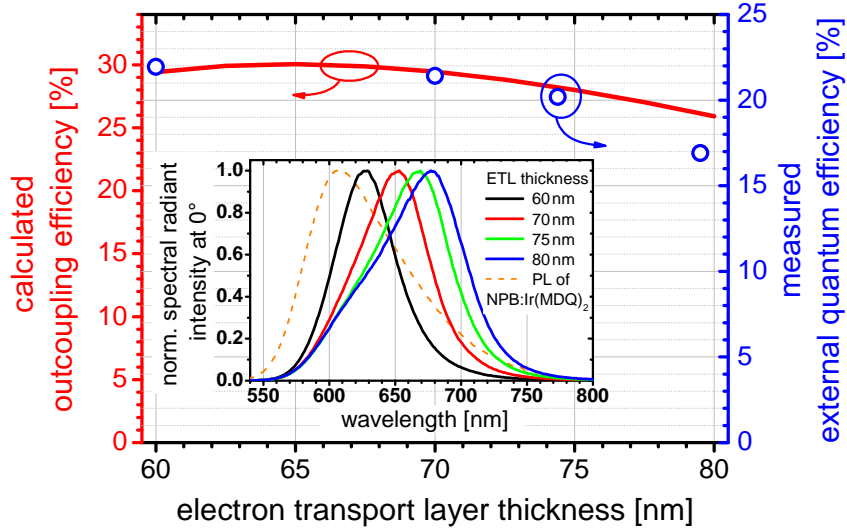
Figure 4.6: *Measured external quantum efficiencies at $14.8\,mA/cm^2$ compared to calculated outcoupling efficiencies of optimized inverted top-emitting OLEDs at four different ETL thicknesses around the optimum at 65 nm. Inset: The peak change of the EL spectrum validates the shift of the cavity resonance, realizing different overlaps with the emitter spectrum.*

The device structures, starting from the bottom are (thickness in nm):

Al(50) / Ag(40) / TPPhen:W$_2$(hpp)$_4$ (8wt%) (60, 70, 75, 80) / BAlq$_2$(10) / NPB:Ir(MDQ)$_2$ (acac) (10wt%)(20) / NPB(10) / MeO-TPD:F6TCNNQ (4wt%) (35) / Ag(20) / NPB(80)

In Figure 4.6, the measured external quantum efficiency (EQE) values for the four different device structures are compared to the calculated outcoupling efficiency. The EQE varies from 22% for 60 nm, 21.5% for 70 nm, 20% for 75 nm to 17% for 80 nm ETL thickness. These values mark the highest efficiencies for inverted top-emitting OLEDs comprising this certain emitter to our knowledge. Nevertheless, the EQE is only 2/3 of the predicted outcoupling efficiency which must be attributed to electrical and excitonic losses but is anyway lower compared to the 27% EQE reported for the non-inverted device [134]. Additionally, the associated emission spectra are plotted in the inset of Figure 4.6. They nicely show a peak shift to larger wavelength with increasing ETL thickness as one would expect. In accordance to Figure 4.5, the calculated outcoupling efficiency shows a flat but decreasing characteristic at constant capping layer thickness with changing ETL thickness from 60 to 80 nm. In contrast to the predicted maximum of outcoupling at around 65 nm ETL, the experiment exhibits the most efficient device at lower ETL thick-

72

ness and a stronger decrease in EQE at larger ETLs. However, this may be attributed to experimental deviations in layer thicknesses.

Finally, the discussed optimization process could be applied to monochrome non-inverted top-emitting OLEDs comprising the phosphorescent emitter Ir(MDQ)$_2$(acac). The results have been published in Hofmann et al. [202] where the cavity order and their influence in the outcoupling are investigated. Surprisingly, the optimized cavity properties seem to represent the optimum configuration when considering cavities of higher orders, meaning HTL thicknesses of 36, 200 and 385 nm, respectively. On the other hand, in OLEDs with increasing cavity length the semitransparent Ag top mirror has to be very thin to achieve a comparable spectral width of the extractable mode. The angular light distribution shows an equivalent overlap with the spectrum of Ir(MDQ)$_2$(acac) independently from the cavity thickness. The optimized layer structure of a $\lambda/2$ cavity exhibits 29% external quantum efficiency demonstrating the potential of this material and layer combination to achieve internal efficiencies as high as 83% [202].

4.2.2 Spatial light distribution

To answer the question about the uniqueness of the optimized parameter set for the used emitter system NPB:Ir(MDQ)$_2$(acac) in this type of top-emitting OLED, we have to have a closer look on the spatial distribution of light emission. First of all it becomes obvious from Equation 4.3 that the cavity emission resonance depends on the light propagation direction inside the OLED. Connected via Snells law to the emission angle θ in air, a blue shift of the EL spectrum with increasing viewing angle is expected. Hereby, the range from 0 to 90° in air is correlated to 0 - 34.6° in organic material (n=1.76). In Equation 4.8, one has to integrate the spectral radiant intensity $I(\theta, \lambda)$ over 2π solid angle which leads to the prefactor $\sin(\theta)$ to obtain the integrated photon flux. This changes the situation towards light emission under large angles and gives rise to a compromise when tuning the cavity to obtain a maximum light outcoupling. In conclusion two important things have to be fulfilled:

- The spectral overlap of the (shifting) cavity mode with the (fixed) intrinsic emitter spectrum has to be maximized for all emission angles.

- The factor $\sin(\theta)$ has to be taken into account for the optimal angular distribution regarding the spectral overlap.
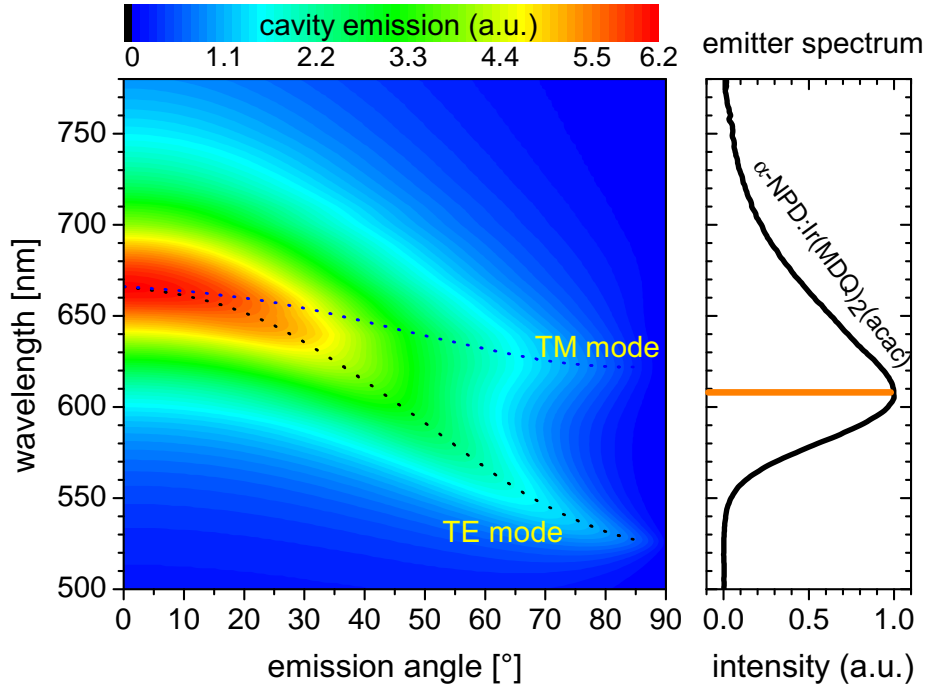
Figure 4.7: *Calculated angular distribution of spectral cavity emission (left) which is a superposition of TE and TM polarized modes, depicted for the optimized OLED structure from Table 4.1. The dotted lines represent the resonance wavelength of the certain TE/TM modes. The outcoupled spectral radiant intensity is assumed to be the convolution of the cavity emission and the intrinsic emitter spectrum (right).*

The first issue is accomplished by adjusting the spectral width of the cavity mode and its angular dependent spectral shift which is further polarization dependent. There, the most impact can attributed to the semitransparent contact in combination with the capping layer. The second point can be addressed by setting the cavity length to a value where the cavity resonance coincides with the peak of the emitter spectrum at large emission angles. In Figure 4.7, the angular distribution of the cavity emission and the intrinsic spectrum of NPB:Ir(MDQ)$_2$(acac) are compared for the optimized OLED configuration from Table 4.1.

The optimized OLED exhibits a cavity mode which is as broad as the emitter spectrum. The peak of the cavity mode resonance at 50° is coinciding with the 610 nm peak of the emitter spectrum. Further, the splitting of the TE- and TM-polarized part of the cavity emission seems to be important as it is beneficial to broaden the extracted modes at emission angles >30° to gain
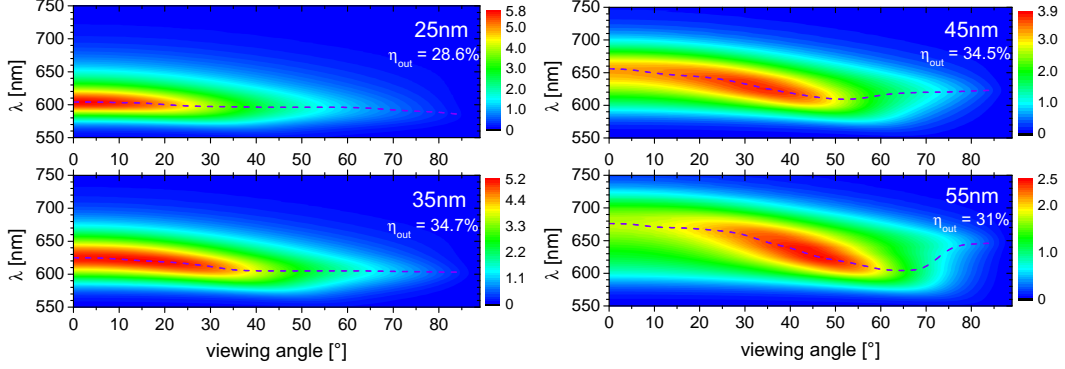
Figure 4.8: *The dependence of the cavity length L_{cavity} (HTL = 25, 35, 45 or 55 nm) on the simulated EL spectrum (spectral radiant intensity) and its angular distribution. The emission peak is traced by a dotted line. The closer the 0° cavity resonance shifts to the peak emission of the emitter system at 610 nm, the less pronounced the angular dependence becomes. With increasing cavity length L, the emission maximum shifts towards larger viewing angles while the width of the EL spectrum is strongly increased.*

an optimized overlap with the intrinsic emitter spectrum. The capping layer plays an important role here and its influence on the angular characteristic is discussed in the next section.

Considering the convolution of the cavity mode with the emitter spectrum both depicted in Figure 4.7, one can analyze the expected angular dependence of the optimized OLED structure. In Figure 4.8 the angular distributions of the spectral radiant intensity for four different cavity lengths are compared, keeping all other parameters as shown in Table 4.1. The cavity length is varied by changing the thickness of the HTL from 25 nm to 55 nm in steps of 10 nm.

With increasing emission angle, the spectral shift is directly connected to the center wavelength at 0° emission direction. If the cavity resonance in normal direction is lower or equal to the intrinsic peak of the emitter spectrum, the angular dependence is weak and most light is coupled into the forward direction. Thus, for 25 nm HTL thickness, only 28.6% outcoupling efficiency is obtained. Surprisingly, if the 0° resonance is set between 620 nm and 670 nm (35-55 nm HTL), the amount of outcoupled photons is not changing that much. The outcoupling efficiency only ranges from 34.7% for 35 nm over 34.5% for 45 nm to 31% for 55 nm HTL thickness. Despite having a strong influence of the cavity length on the spatial distribution of the emission spectra, the total amount of extracted photons is nearly constant. This behavior is verified by the flat trend of EQE values depending on the ETL thickness in the experiment, presented in Figure 4.6.

75

4.2.3 THE CAPPING LAYER CONCEPT

The results from the optimization process indicate that a NPB capping layer of about 80 to 110 nm thickness is always connected with the highest amount of extracted photons. Interestingly, this holds for almost every ETL/HTL configuration (compare Figure 4.5). The absorptive losses in the top contact should provide more information about this fact.
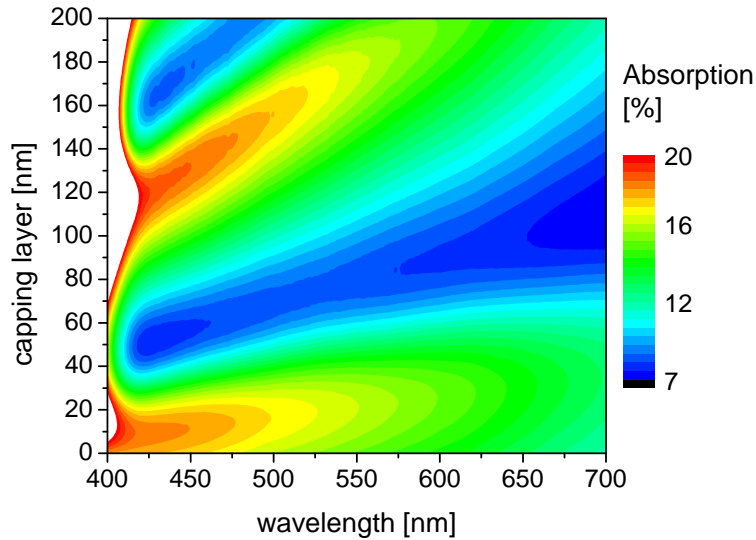
Figure 4.9: *Calculated absorptance of a 20 nm Ag / 0 - 200 nm NPB bi-layer system at normal light incidence, depending on the wavelength λ and the NPB thickness. The semi-infinite medium of incident light is Meo-TPD:F_4TCNQ.*

When the reflectance R and the transmittance T of the following layer system is calculated

MeO-TPD:F_4TCNQ (semi-infinite medium of light incidence) / Ag(20 nm) / NPB (0-200 nm) / air (second semi-infinite medium)

one aspect of the enhanced outcoupling by a capping layer becomes obvious. The resulting absorptance $A = 1 - R - T$ is depicted in Figure 4.9 and confirms that in the spectral range from 550 to 700 nm, a 80 to 110 nm thick NPB layer on top of the semitransparent anode leads to a reduced absorptance. This reduction can be up to a factor of about 0.5 compared to the absence of the capping layer and is valid for the relevant incident directions 0 - 35° against the normal direction in organic material which belongs to the complete hemisphere in air.

Figure 4.10: Calculated spectral cavity emission $C(\lambda, \theta)$ for TE and TM polarization, depending on the viewing angle. The grey artificial lines at 0.45 and 0.5 denote the FWHM of the spectrum at 0°. Both graphs are scaled by one general factor to illustrate the differences in peak intensity between the case without CL on the left (peak intensity = 0.9) and with CL on the right (peak intensity = 1.0).
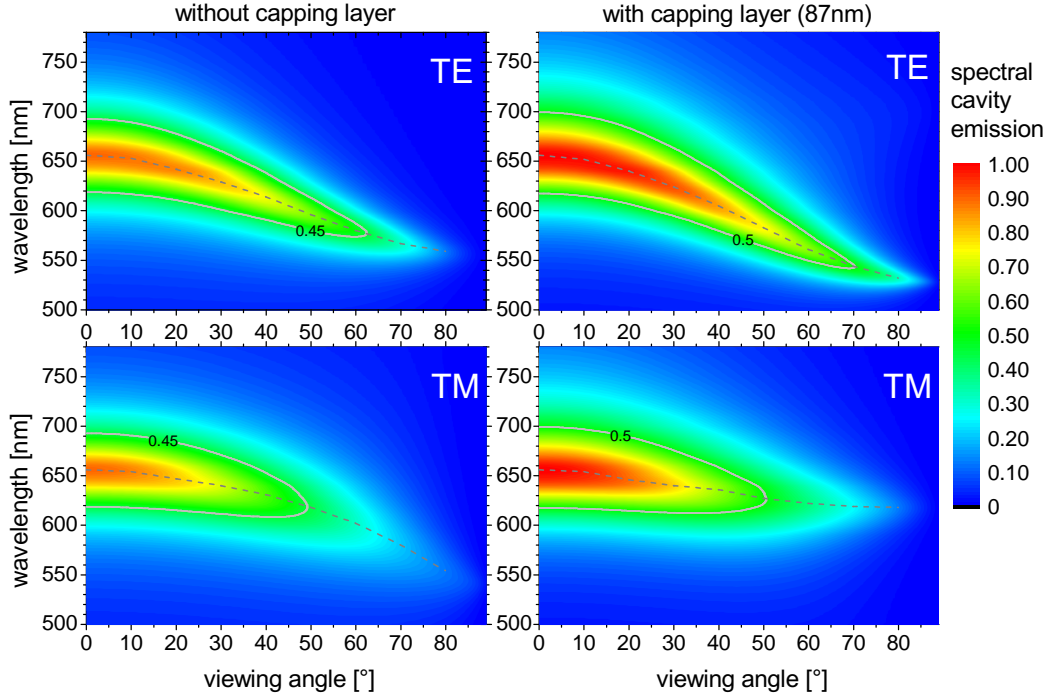
The second important issue is the modification of the cavity resonance of the complete OLED stack. First, we perform optical simulations, comparing two layer structures - one with 87 nm, the other one without a capping layer. Taking the optimized structure as base, the layers of the OLED without capping layer are slightly modified to achieve nearly the same cavity emission in forward direction (same peak position and peak width).

The two OLED structures are as follows (from the bottom, thickness in nm):

Al(40) / Ag(20) / BPhen:Cs(64) / BAlq$_2$(10) / NPB:Ir(MDQ)$_2$ (acac) (10wt%) (20) / NPB(10) / MeO-TPD:F$_4$-TCNQ (4wt%)(33, 43) / Ag(15, 19) / NPB(0, 87)

To reach the same spectral width of the cavity modes without capping layer, we have to decrease the anode Ag thickness from 19 nm to 15 nm. Further the HTL has to be adjusted to equalize the resonance wavelength for both OLED structures. Here it becomes obvious that the capping layer (CL) changes the spectral width of the far field mode and the effective cavity length. The arti-

ficial lines in Figure 4.10 show that the cavity modes have equal center wavelength at 656 nm in normal direction and almost the same spectral width from 619 nm to 691 nm (w/o CL) or 700 nm (87 nm CL), respectively. When analyzing the angular distribution of the modes, significant differences besides the increased intensity with an applied CL become apparent. In the case without a CL, the modes of both polarizations show a blue shift of the resonance up to 550 nm above 80°. Thus, the phase shift that is received by the reflected light at the Ag anode has the same angular trend for TE and TM modes[1]. In contrast to that, when applying a CL of 87 nm, the phase shifts of TE and TM modes proceed completely different. While the TE mode shows the expected blue shift - even with increased magnitude to 530 nm, the TM mode shifts only by 30 nm to 620 nm. This large splitting of the cavity modes should enable an increased coupling to the emitter at larger propagation directions, especially for TM polarized waves.

A mode distribution analysis, performed at the emitter peak wavelength at 610 nm is utilized to further underline these observations. The corresponding power dissipation spectra of the emitting dipoles are plotted in Figure 4.11. They show the totally emitted power at 610 nm, depending on the normalized in-plane wavevector u inside the EML.

From the normalization $u = k_{\parallel}/k_{EML}$, we can divide the spectrum into 3 different coupling regimes:

$0 \leq u \leq 0.5676$	Propagating waves, extracted light to air
$0.5675 < u \leq 1$	Propagating waves that can couple to waveguide modes or surface plasmon polariton (SPP) modes at metal-dielectric interfaces when the dielectric layer has a refractive index lower than the EML
$u > 1$	Evanescent waves that couple only to SPP modes

As the wavevectors k_{EML} in the EML and k_{air} in air are correlated via Snells law, the critical in-plane vector $u_{critical}$ that belongs to a viewing angle of 90° in air is[2] $1/n_{EML} = 0.5676$. Looking carefully at the total amount of emitted power between $u = 0.4$ and $u_{critical}$ in Figure 4.11, the observations and conclusions from Figure 4.10 are confirmed. At large viewing angles, the OLED device with 87 nm CL couples more light into air than the structure without a CL. From 4.11 it becomes directly accessible that this is due to an increased coupling of the emitter molecules to the TM mode. Further, the propagating waves with $0.5675 < u \leq 1$ inside the cavity are heavily modified.

---

[1] Note: The influence of the additionally changed Ag anode thickness (15/19 nm) does not change the angular dependent phase change upon reflection significantly.

[2] The refractive index of NPB:Ir(MDQ)$_2$(acac) $n_{EML} = 1.76$ at 610 nm.
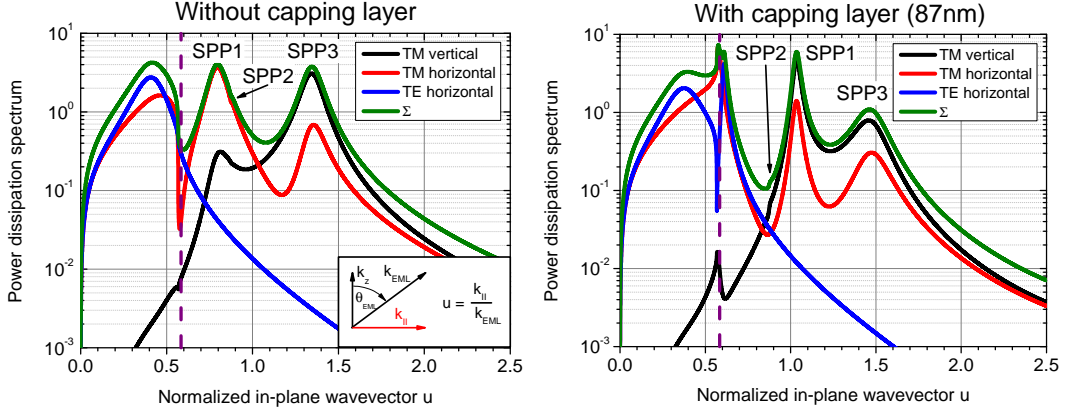
Figure 4.11: Power dissipation spectra at 610 nm for the device structures discussed in Figure 4.10. The total dissipated power Σ per unit in-plane wavevector u is the sum of the three different components $TE_{horizontal}$, $TM_{horizontal}$ and $TM_{vertical}$ The three surface plasmon polariton modes SPP1, SPP2 and SPP3 are marked.

For the discussion of the observed redistribution of the dissipated power inside the OLED, all appearing modes have to be identified.

SPP1:   SPP mode at air/Ag anode or CL/Ag anode interface
SPP2:   SPP mode at glass/Al interface (negligible)
SPP3:   SPP mode at the transport layer/Ag interfaces on both sides of the cavity

Additionally, in case of the structure having a 87 nm CL, a TM0 waveguide mode at $u = 0.576$ and a TE0 waveguide mode at $u = 0.6085$ occur which represent loss channels. The most radiative losses inside the device are due to coupling directly to surface plasmon polariton modes. The SPP1 mode on the left in Figure 4.11 is consequently shifted from $u = 0.797$ to $u = 1.035$ on the right, caused by the change of the refractive index at the outer Ag interface from air (n=1) to NPB (n=1.76) by adding the capping layer. The SPP2 mode is in both cases completely negligible as the amount of light, with is transmitted trough the whole bottom Ag/Al cathode is almost zero. Finally, the SPP3 mode is reduced by a factor of approximately 3.5 and slightly shifted to large in-plane wavevectors u. The total generated power F from the emitting dipoles is defined by [203]

$$F = (1 - \gamma) + \gamma \int_0^\infty K(u)\,du. \tag{4.9}$$

Here, K(u) is the power spectrum denoted by Σ in Figure 4.11 and γ the internal quantum efficiency of the emitting molecules. Assuming $\gamma = 1$, $F =$
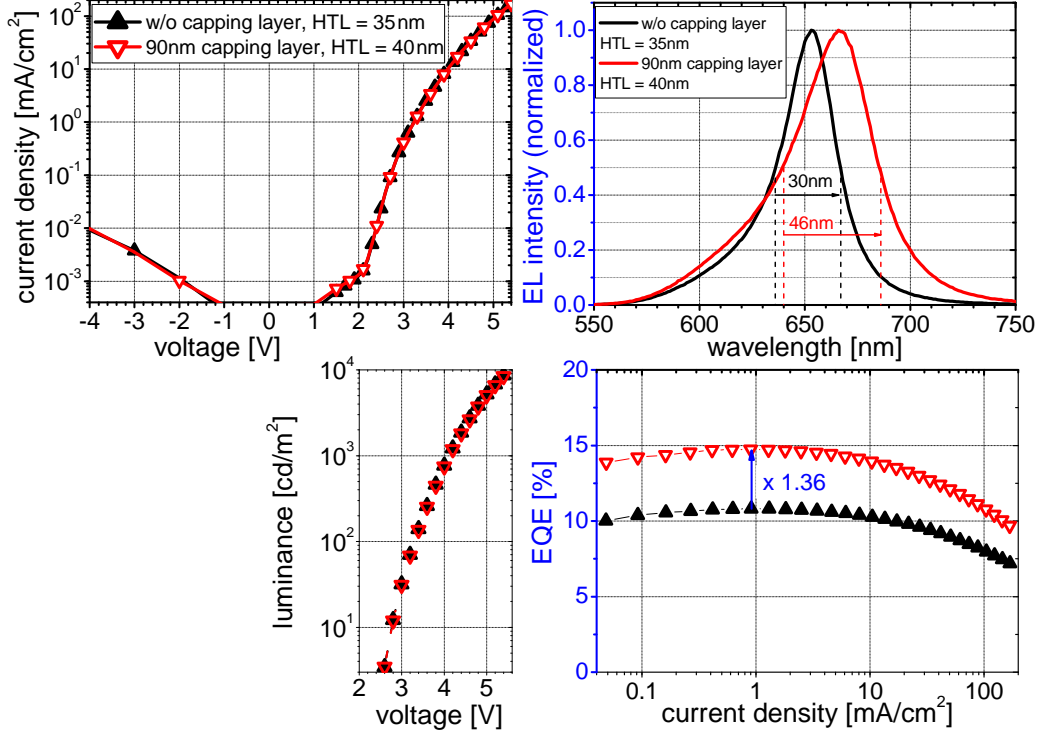
Figure 4.12: *Characteristics of two inverted OLED pixels, one with 90 nm and one without any capping layer having the same structure except 5 nm difference in HTL thickness to compensate the shift of the effective cavity length by the CL.*

2.32 for the OLED structure without the CL and which is lowered to $F = 2.07$ when having the CL applied. This is interesting as the extracted amount of light is comparable in both devices. As consequence, the total outcoupling efficiency increases from 23.2% without the CL to 31.1% with 87 nm CL (factor 1.34). The capping layer effect is finally validated by comparing the following two OLED devices in the experiment.

Al(50) / Ag(20) / BPhen:Cs(60) / BPhen(10) / NPB:Ir(MDQ)$_2$ (acac) (10wt%) (20) / NPB(10) / MeO-TPD:F6TCNNQ (4wt%)(35, 40) / Ag(18) / NPB(0, 90)

As depicted in Figure 4.12, the electrical behavior (current-voltage) of both OLED pixels is completely identical, even the luminance-voltage curves coincide. Unfortunately, there is an unintentional spectral shift between both measured EL spectra, partially induced by the 18 nm top electrode used in both samples. Nevertheless, as we know from the investigations above, the outcoupling efficiency should not be affected much by such a shift. The expected broadening of the EL spectrum is clearly visible as the left branches

80

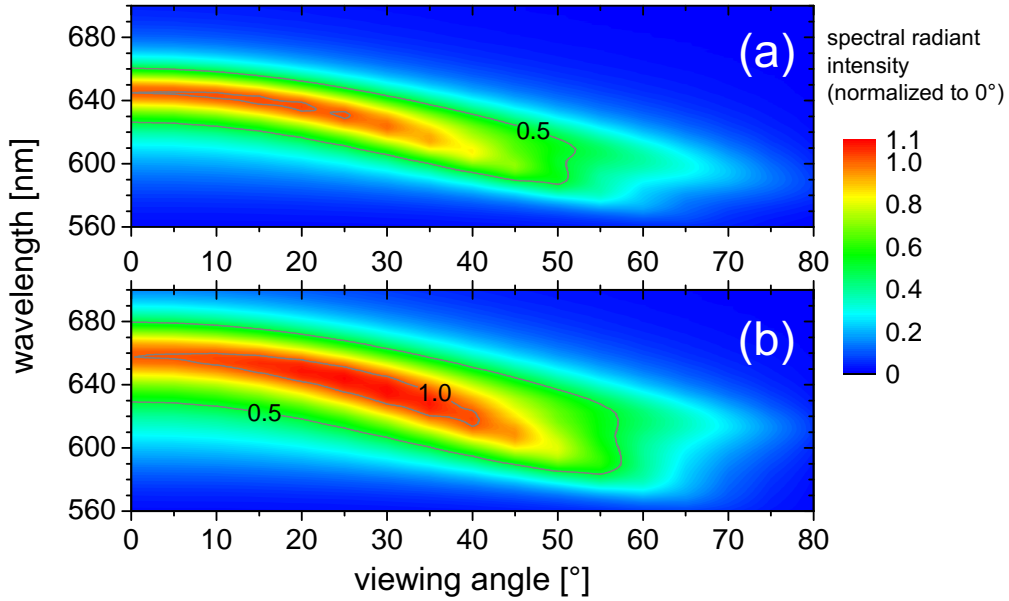*Figure 4.13: The measured angular distribution of the EL spectra emitted by the two inverted OLED pixel (a) HTL=35 nm, without a CL and (b) HTL=40 nm with 90 nm CL. The effect of spectral broadening in case (b) is confirmed and the peak intensity increases with viewing angle, reaching the maximum at 25-30°. Both plots have the same z-scale normalized to the forward intensity of the OLED without CL.*

of both EL peaks in Figure 4.12 nearly coincide up to $\lambda = 640$ nm while the right branches deviate by 20 nm. The increased outcoupling is confirmed by the measured EQE, increasing from 10.8% to 14.7% by a factor of 1.36 which is perfectly predicted by the optical simulation.

The spatial distribution of the EL spectrum of both devices is compared in Figure 4.13. As both OLED structures have a 18 nm Ag anode, we find the predicted spectral broadening of the extracted mode in case of an applied CL. The intensity increases with the viewing angle up to 30° which is in contrast to a saturated and only decreasing EL signal when having no CL on top of the semitransparent Ag anode.

In conclusion, the modification of the optical properties (reflectance, phase shift upon reflection) at the semitransparent top anode by a capping layer can reduce absorptive losses and changes the cavity tuning as well as the angular dependence of the EL spectrum. Further, the internal light distribution is strongly altered by a capping layer, primarily caused by the change of the Ag anode interface to air, where SPP modes couple to. The overall amount of emitted power is assumed to be decreased by a CL but the outcoupling efficiency increases.

81

4.3 OUTCOUPLING OF WHITE LIGHT

4.3.1 ADOPTION OF THE CAPPING LAYER CONCEPT

In the first part of this chapter, the concept of an additional capping layer (CL) was used to rigorously enhance the device outcoupling efficiency for a monochrome emitter system. In the following section, white light emission from top-emitting OLEDs is discussed. Again, an organic capping layer is applied and its influence on the optical properties of such devices with silver as top electrode material are investigated using optical simulations. The results of the theoretical findings are experimentally verified realizing inverted white top-emitting devices on opaque metal-coated glass substrates.

The key challenge regarding top-emitting white OLEDs, compared to their bottom emitting counterparts, is the optimization of the optical properties of these systems. As discussed in the previous sections, the cavity emission properties are preferentially determined by the reflectance of the mirrors, the cavity length and the losses due to internal absorption.

Thus, the optical design of white top-emitting OLEDs is more challenging than for conventional bottom-emitting devices. While bottom-emitting OLEDs on pre-coated glass substrates possess highly transparent electrodes (ITO) that exhibit less multiple interferences within the organic layers [204], the existence of a semitransparent metal top contact in top-emissive devices strongly enhances interference effects - leading to spectrally narrow cavity modes that are not suitable for white light emission. Nevertheless, semi-transparent metal contacts still prove to be the best choice to simultaneously realize high lateral conductivity and reasonable transmittance [6] as well as easy producibility.

From Figures 4.7 and 4.10, a FWHM of the cavity emission as broad as 100 nm can be expected. Therefore, the design of white top-emitting OLEDs with a broad spectrum and high CRI is challenging. This fact represents the optical bottleneck for white light-emitting OLEDs, having a top emissive structure. From equation 4.3 on page 64, we know that the extracted power further depends on the viewing angle θ, which is directly connected to the propagation directions θ_{org} of light within the organic layers and especially to the angle θ_{EML} in the emitting layer via Snells law (Equation 4.4).

Using a common refractive index $n_{org} = 1.8$ for organic material and dispersive optical constants of silver, we can take the model OLED structure from section 4.2.1 and add a CL:

Ag (100 nm) / organic layer (n=1.8, L=100 nm, z_0=54 nm) / Ag (d_{anode}=20 nm) / organic capping layer (n=1.8, d=0 - 400 nm).
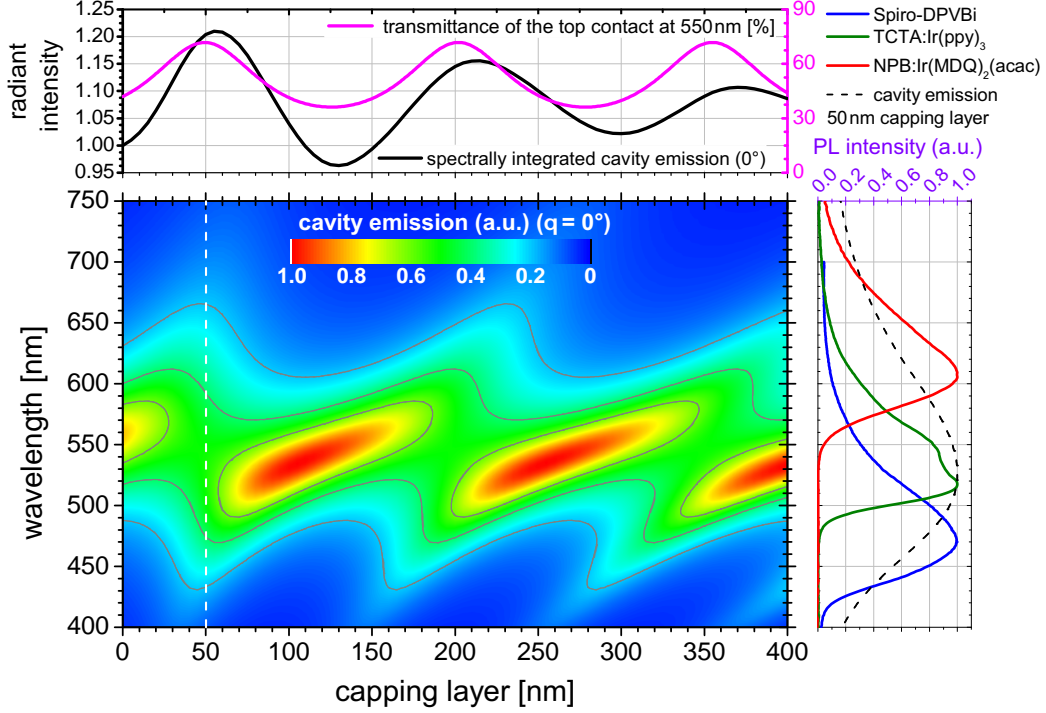
Figure 4.14: Calculated spectral cavity emission into the far-field at $\theta = 0°$, depending on the dielectric capping layer thickness (refractive index n=1.8). The modification of the top contact transmittance alters the finesse of the cavity and consequently influences the FWHM of the cavity mode periodically via thin film interference effects. Thus, the wavelength-integrated cavity emission, depicted in terms of normalized radiant intensity in the upper graph follows this oscillation. On the right, the PL spectra of the typical emitter systems [205] are plotted over the wavelength to compare with the spectral width of the cavity mode.

It is necessary to keep the semitransparent metal top contact as thin as possible for white light emission, while on the other hand the minimum thickness is limited by the layer conductivity. Having the influences of all parameters in mind, we only vary the thickness of the capping layer of this model device and look for a configuration, which enables white light emission. The criteria for optimization are: maximum of extracted power while having a spectral broad and angular independent cavity emission $C(\lambda, \theta)$. As it is depicted in Figure 4.14, by increasing the CL thickness, the transmittance of the top contact oscillates between 40 and 70% with maxima at 50, 200 and 350 nm CL thickness. This results in a pronounced spectral broadening of the extractable cavity mode in these cases. In contrast, the CL thickness range around 100 nm and 250 nm exhibits spectrally very narrow emission bands and the extracted mode without a CL has a FWHM of only 83 nm at 0° (Figure 4.14).
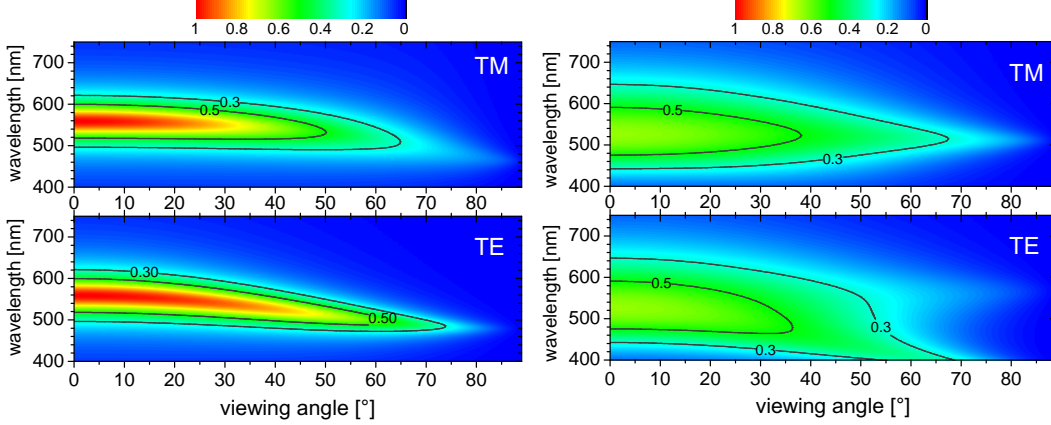
Figure 4.15: Angular dependence of TM and TE modes of the cavity emission that are coupled to the far-field. Without a capping layer (left), both modes show a blue shift, while with a 50 nm organic capping layer (right) the angular dependence of the TM mode is almost compensated. The TE mode splits into a weak angular stable and a deep blue shifted fraction of light at 60°.

The periodically occurring red-shifts of the resonance wavelength with increasing CL thickness demonstrate the thin film interferences, induced by the CL. This change in effective cavity length can be attributed to the continuously increasing phase change ϕ_t at the top contact. With respect to the three chosen emitter systems for red, green and blue emission of a hybrid white OLED approach [205], we concentrate on the capping layer thickness in the range of 50 nm. The correlated cavity mode at this CL thickness covers almost the entire visible range and should exhibit a good overall outcoupling (compare Figure 4.14).

Having found a CL thickness with possibly sufficient spectral mode width, the angular distribution of the corresponding cavity emission has to be investigated. In Figure 4.15, the distribution of extractable modes of two model devices (0 nm and 50 nm CL) is compared.

As expected for a device without any capping layer, the phase lengths belonging to different propagation directions within the cavity create a blue shift of the resonance wavelength and thereby of extracted modes with increasing observation angle. This holds for TE and TM modes. Further on, due to the high reflectance of the contacts, the major intensity is forced to the forward direction. In contrast, these cavity effects are suppressed by the 50 nm capping layer that partially acts as antireflection coating.

Surprisingly, there is almost no blue shift of the outcoupled mode when adding 50 nm organic capping layer. This behavior comes from the reflectance R_t and the phase changes ϕ_t upon reflection at the top silver contact, depending on the polarization. While R_t decreases for TE modes with rising

84

propagation angle θ_{org}, it increases for TM modes. Hence, the TM polarized mode dominates the spectrum at angles >60° and contains a phase shift ϕ_t that compensates the change of phase length between the silver mirrors (see equation 4.3). As a consequence, a weak angular dependence of the complete extracted light is expected. For TE polarized light, there is still a blue shift which leads to the second peak at around 400 nm at 60°. The comparison of both device structures in Figure 4.15 illustrates the strongly minimized micro-cavity effect if a CL of 50 nm thickness is applied.

To compare the simulated results with experimental data, two different types of inverted top-emitting OLEDs are fabricated. The inverted OLED has the advantage to enable an optimal coupling between the cavity mode and the certain emitter molecules as their positions are given by the electrical optimized layer sequence. Nevertheless, the discussed results for the effect of an additional dielectric layer apply for non-inverted devices too. The common device structure for both fabricated samples is based on a hybrid white approach [205], combining a fluorescent blue with highly efficient phosphorescent red and green emitters.

On a glass substrate, pre-coated with a 70 nm opaque molybdenum-tantalum alloy layer, a 30 nm silver layer is evaporated, establishing a highly reflecting bottom contact. The complete OLED structure is (thickness in nm):

Ag(30) / BPhen:Cs(20) / BPhen(10) / Spiro-DPVBi(20) / TCTA:TPBi(4:1)(2) / TCTA:Ir(ppy)$_3$ (8wt%)(3)/ NPB:Ir(MDQ)$_2$ (acac) (5wt%)(20) / Spiro-TAD(10) / MeO-TPD:F4TCNQ (4mol%)(15) / Ag(15) / MeO-TPD(0, 55)

In contrast to the proposed 50 nm capping layer thickness, we use 55 nm which results from the optimization of the experimental OLED stack using the exact optical constants and film thicknesses. The measured EL spectra in Figure 4.16 show the optical behavior of the two OLEDs. Device (a) without any capping layer shows a strong change in color with varying observation angle and low spectral bandwidth of emission, resulting in the absence of light contribution from the blue emitter. The device (b) exhibits all colors of the emitter layers and has quite stable color coordinates near the standard illuminant A (0.44; 0.40). Comparing the performance of both devices at 5.4 mA/cm^2, device (a) shows 10 lm/W in power efficiency, 5.4% external quantum efficiency (EQE) and 17.9 cd/A, whereas device (b) achieves 13.3 lm/W, 7.8% EQE and 26.7 cd/A (current efficiency in forward direction). This enhancement can only be attributed to the difference in the optical properties of the structures. One has to point out that the performance is comparable to that of non-inverted bottom emitting structures based on the same stack [205]. Additionally, it is shown in Figure 4.16 that the optical model coincides very well with the
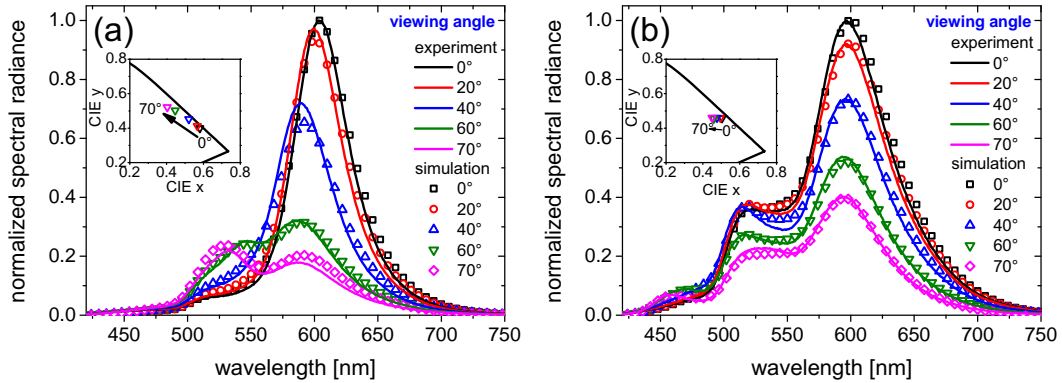
Figure 4.16: Electroluminescence spectra of two inverted top-emitting OLEDs comprising a hybrid white OLED structure. Both devices feature a 30 nm Ag bottom cathode on an opaque substrate and a 15 nm semitransparent Ag anode. Device (a), having no capping layer exhibits pronounced microcavity effects, while device (b) shows a broad and color stable EL spectrum comprising an additional CL of 55 nm thickness. The optical simulations (symbols) agree very well with the experimental data (lines).

measured spectral radiance by fitting the data with the intrinsic emitter intensities as parameters. To yield a reasonable fit, the layer thicknesses had to be adjusted. However, these adjustments are only on the order of a few % which is well within the experimental uncertainties. In conclusion, the concept of an additional organic capping layer in combination with the semitransparent Ag top contact is verified by realizing inverted top-emitting white OLEDs. Both spectral bandwidth and angular stability of color coordinates are significantly improved. Furthermore, the outcoupling efficiency is increased for white light. The predictions of our simulations agree very well with the experimental results.

4.3.2 REDISTRIBUTION OF LIGHT VIA LAMINATED MICROLENS

The capping layer concept discussed formerly is a pure thin film approach to alter the properties of the OLED´s optical cavity. In the following, an alternative solution is presented which explicitly makes use of the strong cavity effects that narrow the spectral emission and increase the viewing angle dependence. Hereby, the approach is applied to inverted as well as to non-inverted OLED structures.

THE WORKING PRINCIPLE

As shown previously, the cavity emission of top-emitting OLEDs can be broadened by introducing a dielectric capping layer deposited on top of the semi-transparent metal contact, leading to reasonable color rendering indices (CRI ≈ 75) and good efficiencies ($13 \, \text{lm/W}$) [206]. Generally, because the interference conditions for different wavelengths diverge with increasing distance between both metal electrodes, the best white top-emitting OLEDs reported so far have cavity length of approximately $100 \, \text{nm}$ [150, 206]. In addition, top-emitting OLEDs suffer the general problem that commonly used external outcoupling techniques, e.g. modification of the glass/air interface of the substrates [14, 207] cannot be applied, because these techniques would damage the soft and sensitive organic layers underneath. However, Yang et al. reported on single emitter top-emitting OLEDs with applied microlenses [208]. Their foil was made of PDMS[3] having a refractive index $n_{PDMS} = 1.43$, which is lower than $n_{glass} = 1.51$ of standard glass, so that the coupling into the lens medium is suppressed. Furthermore, they deposited $1 \, \text{µm}$ thick parylene layers for passivation between the devices and the lenses.

Taking this archetype, we extended the concept to realize white top-emitting OLEDs. Instead of a thin cavity OLED that tries to squeeze all emission bands into the extractable mode, we choose a two-unit stacked white OLED design based on fluorescent blue and phosphorescent red/yellow emitting units leading to overall cavity lengths $> 300 \, \text{nm}$. This system is capable of broadband emission by combining a dual mode cavity with an index-matched microlens foil that is laminated on the device. In our concept, we use the microlens foil as an integrating element to mix the photons emitted under various propagation directions to establish a color stable and white emission spectrum.

---

[3]polydimethylsiloxane
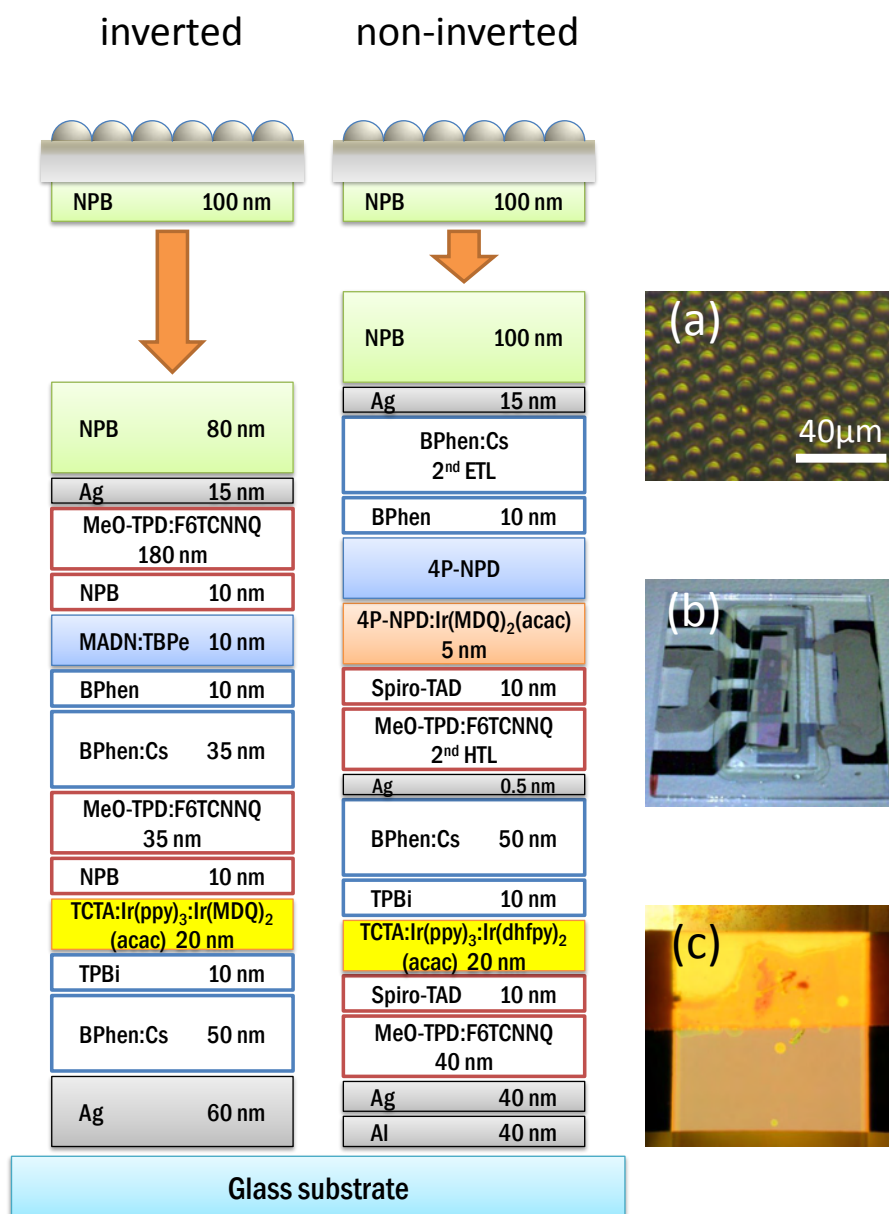
Figure 4.17: *Device layer structures of inverted and non-inverted stacked top-emitting OLED indicating the principle of the microlens foil lamination process. In the inverted OLED, the doping concentration of TBPe and Ir(MDQ)$_2$(acac) is 1wt%. In the non-inverted OLED, Ir(dhfpy)$_2$(acac) is doped with 1wt% and Ir(MDQ)$_2$(acac) has a doping concentration of 5wt%. Ir(ppy)$_3$ has a concentration of 8wt% in both devices. On the right, a microscope image of the foil (a), two laminated OLED pixel on a square inch substrate (b) and a partially laminated operating OLED pixel (c) are shown.*

Typically, organic materials used in OLEDs feature refractive indices in the range of $n_{organic} = 1.7$ - 1.8 [142]. Therefore, a microlens array with a refractive index of $n_\mu = 1.71$ is chosen. Light, created in the organic layers can enter the microlens film without passing an optical interface. The microlens film (C-imide series S10-2, Optmate Corp.) comprises $9\,\mu m$ wide (pitch $10\,\mu m$), $5\,\mu m$ high lenses, arranged in a hexagonal array.

For the lamination process, both the top-emitting OLED and the microlens film are coated with NPB and transferred to a glovebox with nitrogen atmosphere. The microlens film is cut and heated about 15 min at 55°C which enables changes of the NPB film morphology [209]. Without cooling down, it is transferred on the top-emitting OLED so that the NPB layers get in contact to guarantee optimal optical contact between OLED and microlens film as shown in Figure 4.17. Immediately, a soft hemispherical rubber stamp (8 mm in diameter) is used to press the microlens foil to the device with a pressure of (3.0 ± 0.5)MPa with a duration of 8 s. For best comparability, more than one pixel is prepared on each individual substrate so that one pixel can be used as reference device and another one with identical layer layout and thickness for the lamination process.

APPLICATION TO INVERTED OLED

The first experiments are done using an inverted OLED architecture shown in Figure 4.17. The device is composed of a fluorescent blue EML unit based on MADN:TPBe and a phosphorescent yellow unit based on a mixture of $Ir(ppy)_3$ and $IrMDQ_2(acac)$. The mixed EML is located next to the opaque bottom contact coupling to the first field antinode while the blue EML is located in a way to couple to the second field antinode.

As demonstrated in Figure 4.18, the I-V characteristic is not affected by the lamination process. At the same currents we observe an increased luminance. The EQE is shifted upwards from 11.4 to 13.5% by a factor of 1.2 and the angular characteristic of the luminance is completely changed. Interestingly, the OLED without microlens foil attached shows a dip in the angular dependent luminance curve. This can be attributed to the used dual mode cavity, exhibiting only blue and red light in forward direction while the strong shift of the resonance with increasing emission angle leads to a more yellowish spectrum at large angles (see Figure 4.19(b)). Hence, the overlap with the luminosity function leads to a distinct peak in the angular dependent luminance at 75°.

The inferior performance of these stacked inverted devices (e.g. due to charge conversion p-n junction) manifests in very high driving voltages up to 15 V at $1000\,cd/m^2$ which lead to a comparably low luminous efficacy. Nevertheless, a
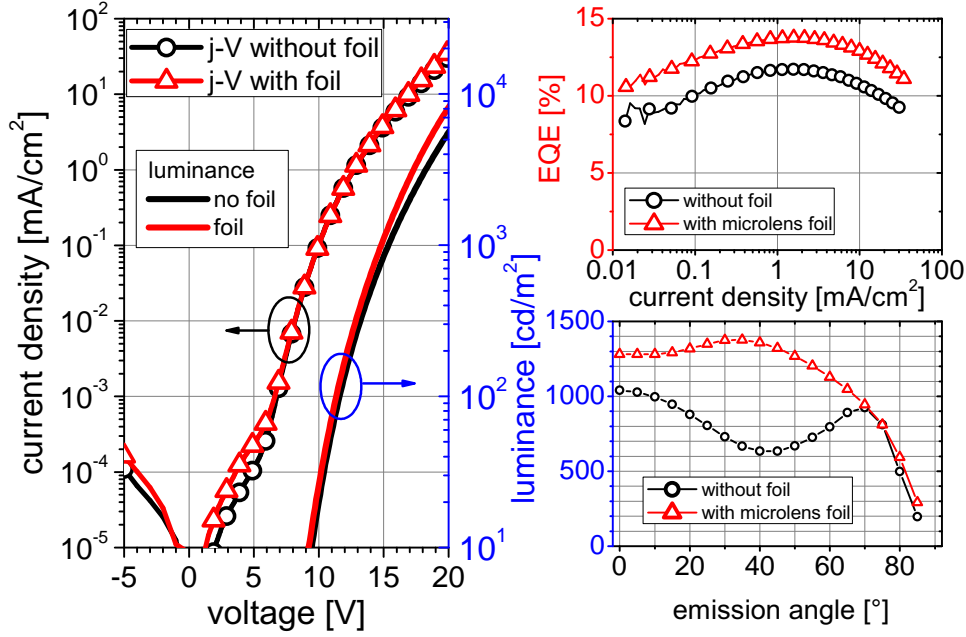
Figure 4.18: *Performance data of white stacked inverted top-emitting OLED with and without microlens. Current density-voltage-luminance characteristics (left) and external quantum efficiency as well as angular dependent luminance (right) exhibit strong optical but no electrical changes during the lamination process.*

gain in EQE of about 20% by attaching the microlens is observed, successfully demonstrating the working principle. The broad white spectrum, shown in Figure 4.19(a), exhibits an angular stable spectrum with a moderate CRI of 70 with room for improvements. Independently from the emission angle, the EL spectrum shows a dip at 550 nm which further contributes to the low luminous efficacy and is because none of the incorporated emitters has a significant intensity in this spectral range.

Table 4.2: *Comparison of the key parameters for the inverted stacked white OLED with and without laminated microlens foil, respectively.*

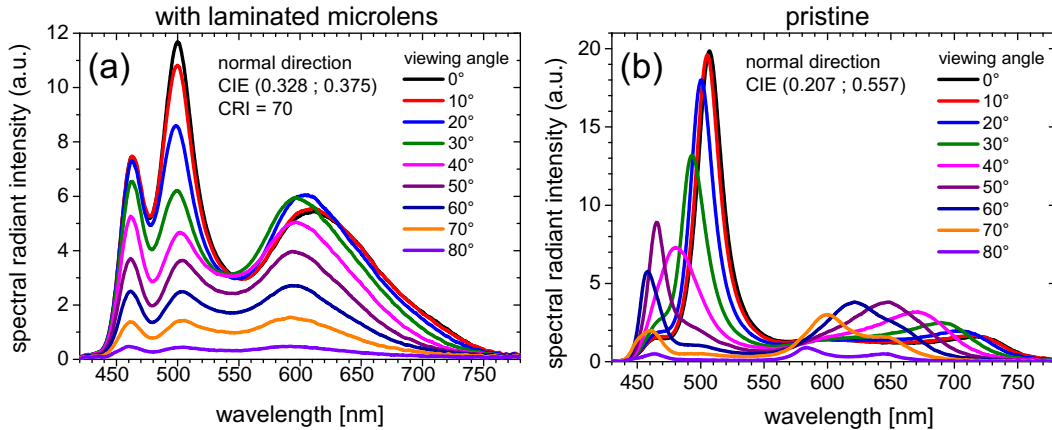| sample	voltage[1] (V)	EQE (%)	LE (lm/W)	L (cd/m^2)	CIE 1931 (x, y)	CRI
w/o foil	15.7	11.4	3.4	1041	(0.207, 0.557)	-
with foil	15.6	13.5	5.7	1415	(0.328, 0.375)	70

[1] at 4.4 mA/cm^2

Figure 4.19: Angular dependent spectral radiant intensity of a laminated (a) and a pristine (b) inverted OLED in the range of 0-80°. Both pixel show the contributions from all three emitters.

HIGHLY EFFICIENT NON-INVERTED OLED

To further investigate the potential of our concept, a second OLED structure is used. It incorporates an additional phosphorescent yellow emitting dye to close the spectral gap at 550 nm described above. Due to the complexity and the inferior device performance of the inverted structures, we switched to a more reliable and proven device concept. The OLED is a two-unit stacked device based on a layout published by Rosenow et al. in 2010 [210]. The color tuning in this device design is achieved through two different variations:

1. The first variation is the thickness of the 4P-NPD layer in the triplet harvesting blue/red unit. Triplet harvesting is based on the lateral spacing of a fluorophor and a phosphor that the singlet excitons remain in the fluorophor and the triplet excitons diffuse to the phosphor. An internal efficiency of 100% can be realized theoretically. However, this is only possible for one specific spectral distribution, i.e. if 25% of the singlets are on the fluorophor and 75% of the triplets are on the phosphor. Increasing the 4P-NPD layer thickness will suppress red phosphorescence, thus giving in turn relatively more blue emission accepting reduced overall efficiency.

2. The use of doped transport layers enables the change of the layer thicknesses without changing the electrical performance of the device. Thus, by changing the ETL and HTL thickness, it is possible to change the cavity length and the position of the emitters with respect to the electric field distribution within the cavity. Accordingly, the dipoles have an

altered probability to couple to a certain optical mode, which alters the emitted spectrum of the device.

We have employed both methods to change the emitted color of our devices. The variations can be found in Table 4.3 while they are illustrated in Figure 4.17. The blue and red emitters are located next to each other inside the cavity, coupling to the optical field of a $3/2\lambda$ and λ mode, respectively. The position of the yellow unit is optimized to also meet the field antinode of a λ mode. From the devices that were fabricated, four different ones are discussed under the following aspects.

Device 1 is designed to have the highest contribution from the blue emitter, which is best suitable to discuss the dual mode character of these devices. Devices 2 - 4, with small variations in their layer structure (compare Table 4.3), are optimized for highest efficiency and best color quality. All reference devices, i.e. without applied microlens film, already make use of the capping layer concept (100 nm NPB capping layer). The current-voltage-luminance characteristics for devices 1 - 3 are shown in Figure 4.20. There, an increase in leakage currents of approximately one order of magnitude and a strong increase of luminance after lamination can be observed.
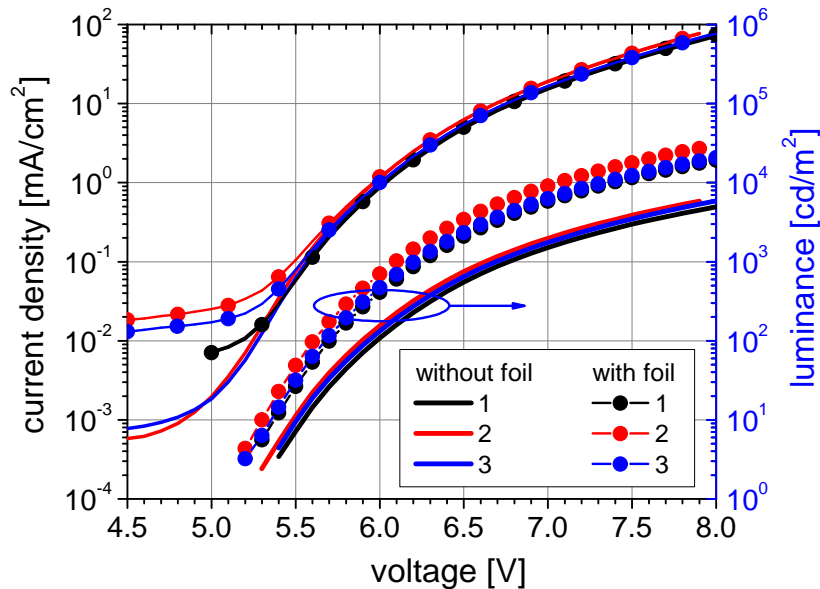

Figure 4.20: Current density-voltage-luminance characteristics of non-inverted top-emitting OLEDs with and without laminated microlens. The increase in leakage current can be seen below 5 V driving voltage.
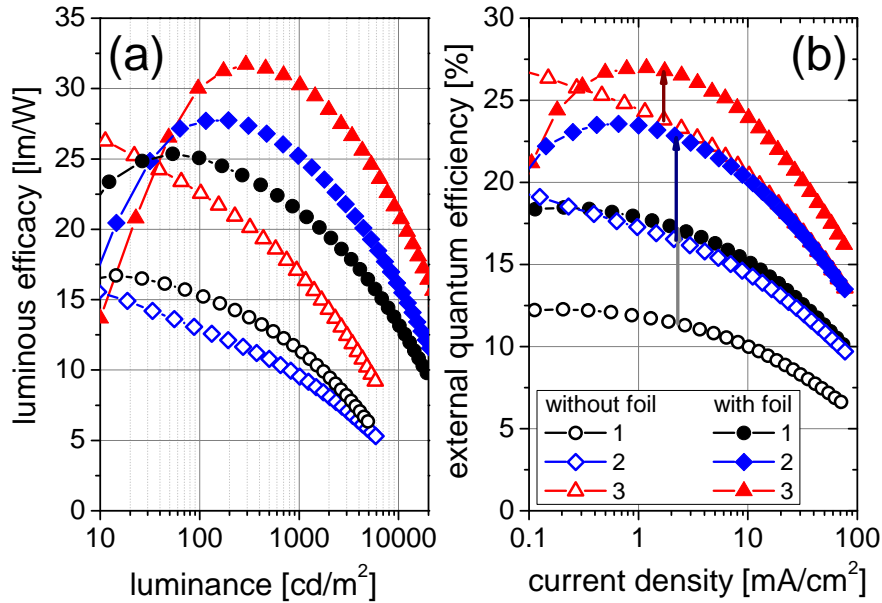
Figure 4.21: Luminous efficacy (a) and external quantum efficiency (b) of non-inverted stacked top-emitting OLED devices 1, 2, and 3 with and without microlens foils, measured in a calibrated integrating sphere. The drop of the curves at low luminance and current densities is due to increased leakage current which becomes apparent in the I-V characteristics shown in Figure 4.20 in the range from 5 V to 5.7 V driving voltage. The vertical arrows in graph (b) illustrate the efficiency enhancement at $1000\,cd/m^2$, which are summarized in Table 4.3.

The external quantum efficiencies (EQE) and luminous efficacies are shown in Figure 4.21. At current densities corresponding to $1000\,\mathrm{cd/m^2}$ (j_{1k}) and $10000\,\mathrm{cd/m^2}$ (j_{10k}) of the laminated devices, efficiencies are measured in a calibrated integrating sphere. Unfortunately, the lamination of device 4 only led to partial optical contact so that the efficiency of device 4 could not be determined. The highest efficiency is obtained for device 2, reaching 26.8% EQE and $30.1\,\mathrm{lm/W}$ at $1,000\,\mathrm{cd/m^2}$. In Figure 4.21, the vertical lines indicate the enhancement of the laminated device at $1,000\,\mathrm{cd/m^2}$. The improvement in EQE varies from a factor of 1.13 to 1.51, depending on the actual device layout. The enhancement induced by the foil is reduced for OLEDs whose corresponding reference device already shows high quantum efficiency. Nevertheless, it has to be kept in mind that the reference devices do not emit white light. Table 4.3 summarizes the key figures of the non-inverted white OLEDs with microlens. The CRIs of these devices are very high. Device 4 reaches a CRI of 93 which is much higher than the values obtained for the bottom-emitting white OLEDs based on the same device design [210] and is to our knowledge the highest

Table 4.3: *Summary of the structural and performance parameters of non-inverted stacked white OLED at a current density of $4.4\,mA/cm^2$. The EL spectrum of device 4 is shown in Figure B.2 on page 168 in Appendix B.*

no.	cavity	2nd HTL [nm]	2nd ETL [nm]	4P-NPD layer [nm]
1	312	30	130	7
2	320	100	70	5
3	330	100	80	5
4	342	100	90	7

no.	CIE (x,y)	CRI	EQE[1][%]	LE [lm/W]
1	(0.442, 0.418)	72	21.3 (1.51)	21.3
2	(0.542, 0.416)	75	26.8 (1.13)	30.1
3	(0.516, 0.420)	86	22.8 (1.38)	25.2
4	(0.472, 0.430)	93	n.a.	n.a.

[1] brackets contain the enhancement factor (with/without foil) at $1000\,cd/m^2$

value reported for top-emitting white OLEDs.

The far-field emission of the devices completely changes with application of the index-matched microlens film. In particular for the λ mode, the device shows highest radiance at a viewing angle of 50 - 60°. Our optical device design allows superior integrated efficiencies for this kind of OLEDs, however it is detrimental for obtaining white emission at all viewing angles. Actually, all reference devices 1 - 4 (without foil) do not emit a high quality white spectrum at any viewing angle.

Figure 4.17 shows an OLED pixel with the foil covering half of the active area. Optical contact is only made in the bright areas. Without contact, the foil still works as a diffuser or integrating element, however with much lower efficiency. Figure 4.22(a) shows the angular emission of device 1 with attached foil. In contrast to Figure 4.22(b), the spectrum improves drastically. The emission is only slightly dependent on viewing angle and, more importantly, is changed to a broadband, high quality white light. The angular pattern changes to a sub-Lambertian angular distribution.

The spectral enhancement $[S_\mu/S_{ref}]_{exp}$, shown in Figure 4.23(a) can be calculated by dividing the integrated spectrum of both, reference (S_{ref}) and laminated (S_μ) pixel as obtained at the same current density j_{10k}. Interestingly, all devices show large spectral enhancements up to a four-fold increase in between both cavity modes (Figure 4.23(a)). Thus, the microlens foil does not only mix/integrate the emission from the underlying OLED device but also couples out modes that cannot escape to air from a flat layer. The peak enhancement shifts to the red with increasing cavity length.
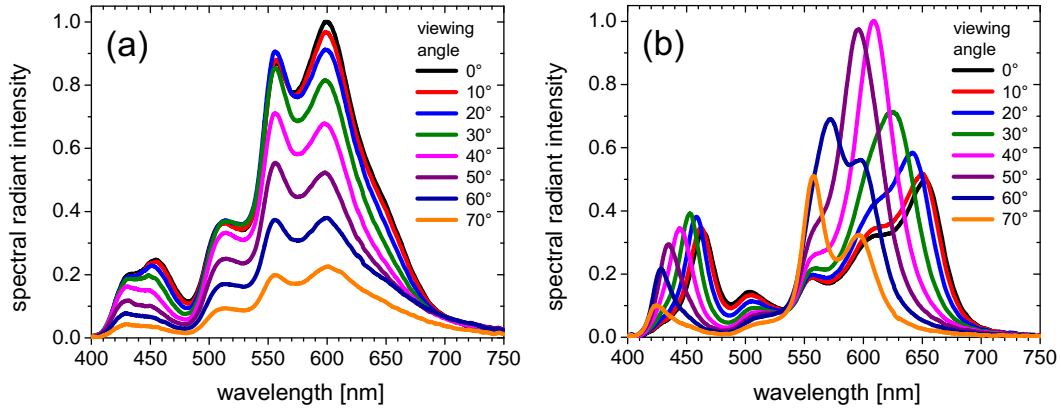
Figure 4.22: Electroluminescence spectra of OLED device 1, depending on the viewing angle of a laminated (a) and a pristine OLED pixel (b).

Comparing samples of identical layer structure, we found that $[S_\mu/S_{ref}]_{exp}$ is very reproducible across all studied devices. The strong outcoupling enhancement in the green spectral region is observed in the microscope image (Figure 4.23(b)) with photograph of edge emission. At the edge, where bottom and top metal contacts stop overlapping, green emission is observed that fades away with increasing distance. This is the light that is originally trapped in the organic layers and now outcoupled by the microlenses.

Additionally, optical modeling is used to validate the spectral enhancement $[S_\mu/S_{ref}]_{calc}$, which is plotted in Figure 4.23. First, the angular dependent EL spectra for the OLED devices without the foil and the spectral light distribution inside the foil are calculated. Slight adjustments of layer thickness have to be applied that account for experimental deviations during deposition. Both spectral light distributions are weighted with the sine of the propagation angle of each spectrum to account for the fraction of photons that is coupled into a certain solid angle. After integration over the total forward hemisphere (propagation angle 0-90°), both electroluminescence spectra S_μ and S_{ref} can be correlated to obtain the ratio $[S_\mu/S_{ref}]$. One important assumption made here is that every propagating mode in the foil is contributing to the integrated far-field electroluminescence spectrum in air. This assumption is equal to the use of a perfectly hemispherical, index-matched outcoupling structure that is large compared to the active area of the OLED. The microlens film on the other hand differs from such perfect system having noticeable gaps between adjacent microlenses as their width is 9 µm while their distance is 10 µm. This geometrical factor can lead to a suppression of certain modes with their corresponding propagation directions which ends up in spectral deviations between calculation and experiment.
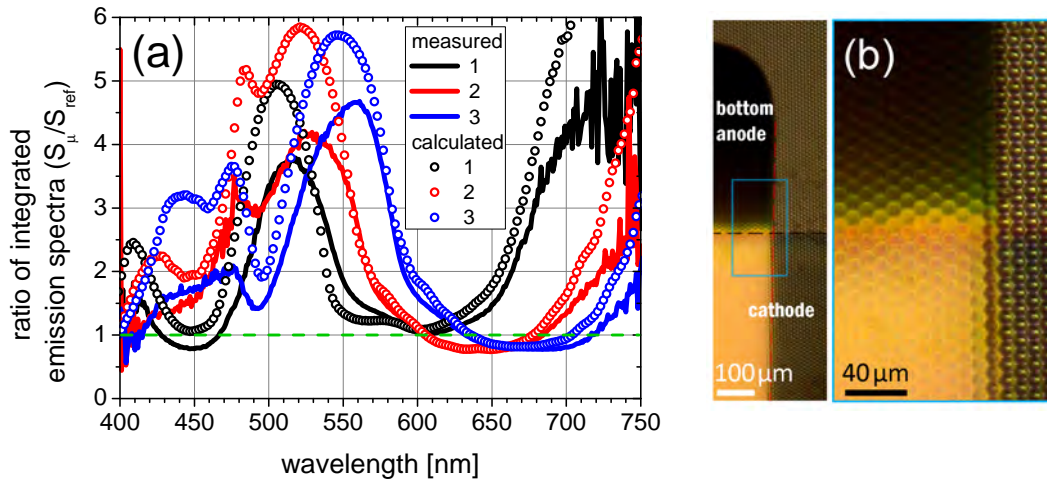
Figure 4.23: Spectral enhancement ratio of integrated EL spectra of devices with attached microlens foil (S_μ) and without foil (S_{ref}) (a). The photograph of the laminated OLED shows the outcoupling enhancement effect at the pixel edge (b). Formerly wave-guided light is coupled into the microlens film and redirected into the forward direction which can still be detected in absence of the OLED but with a present bottom mirror underneath (zoom on the right).

Nevertheless, the calculation shows qualitatively good agreement with the experiment, being able to mirror the spectral shape of $[S_\mu/S_{ref}]_{exp}$ as well as its dependence on the cavity length. The overestimation of the calculation, especially in the region of high enhancement factors can be attributed to the imperfection of the microlenses mentioned above having slightly different properties compared to a large hemispherical optical system.

In order to understand the effects observed, we employed additional thin-film optical simulations. Figure 4.24(a) shows the cavity emission of the reference device 1 that couples to the far-field, i.e. the modes reaching the observer in air. The two cavity modes (TE2, TM2: $3/2\lambda$ and TE1,TM1: λ) are clearly visible which show splitting into TE- and TM-polarization [211]. Splitting originates from the fact that the phase change, the reflection and the transmission at interfaces are depending on the polarization of the propagating wave. Taking the photoluminescence of the incorporated emitters into account, it is possible to calculate the emitted spectrum as a function of the viewing angle. Figure 4.24 shows the excellent agreement between the experimentally measured emission pattern of the reference device (c) and the optical simulation result (b).
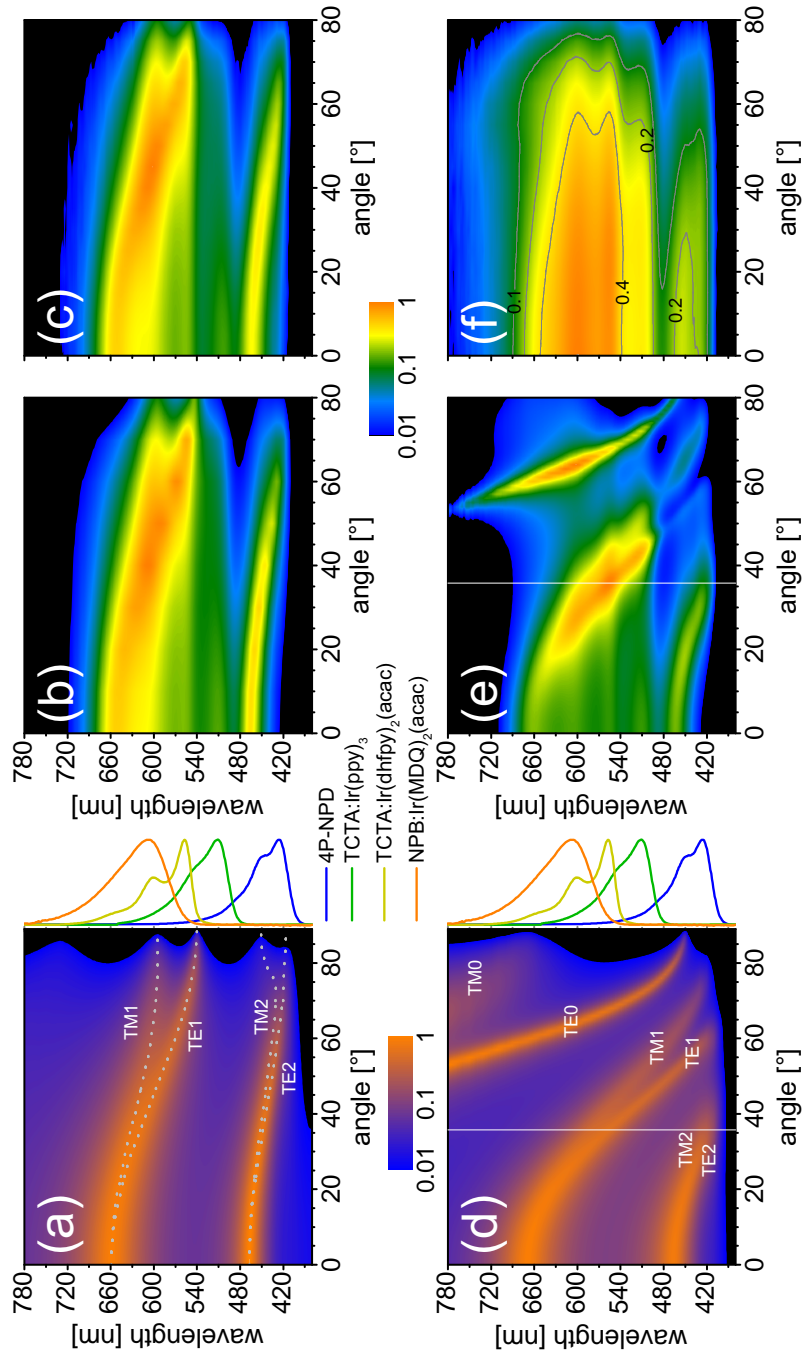
Figure 4.24: *Optical simulation of the cavity response of device 1 without (a) and with microlens (d) attached. In case (a) the observer is located in air, in case (d) inside the high refractive index microlens film. The vertical white line (d) accounts for the critical angle for total internal reflection in a flat device of the same refractive index n_μ=1.71. On the right of (a) and (d) the photoluminescence of the four emitters is depicted. The calculated EL intensity without microlens foil (b) fits well to the experimental data (c). The simulated EL intensity distribution inside the foil (e) shows the light modes that finally lead to a broad and angular stable white OLED emission by light redirection through the microlenses (f).*

The same calculation is performed for the laminated device 1 placing the observer in the high refractive index medium of the foil ($n_\mu = 1.71$). The results are shown in Figure 4.24(d). The white vertical line indicates the critical angle of total internal reflection (35.8°) for light, escaping the high-index material to air in case of a flat interface to air. At large angles, additional modes (TM0 and TE0) appear and sweep across the complete visible spectrum from low to high energy. Figure 4.24(e) shows the calculated light distribution inside the microlens foil, again with the white line indicating the fraction of light that could escape to air when facing a flat interface (n_μ/n_{air}). We expect two effects from the integrated spectral enhancement by applying a microlens foil to the OLED:

1. Light which is emitted at angles larger than the critical angle for a flat device can escape to air, increasing the number of outcoupled photons. This is due to the matched refractive indices of NPB and the laminated film.

2. The microlens integrate the spectral emission over a wide region of propagating directions and turn the emitted spectrum to an almost viewing-angle independent one.

These effects lead to the measured angular distribution of device 1 with applied microlens foil as shown in Figure 4.24(f). The comparison of both plots (e) and (f) reveals the capability of the microlens array to function as efficient integrating element, turning a highly complex mode structure into a broadband emission that is almost constant as a function of the viewing angle.

Following the light which is coupled from the OLED into the foil, the emission angle for an incoming propagation direction α_0 at a lateral coordinate x is calculated analytically. According to Figure 4.25(b), the intersection coordinate x has to be determined by solving the equation

$$\tan(\alpha_0) = \frac{|x_0 - x|}{r^2 - (x - r)^2},\tag{4.10}$$

which depends on the input parameters α_0 and x_0. The angle of incidence α at the boundary can be calculated from

$$\Gamma(x) = \arctan\left[\frac{(r - x)}{\sqrt{2xr - x^2}}\right]\tag{4.11}$$

using the angular relations $\alpha_0 = \Gamma + \alpha$ and $\theta = \Gamma + \beta$ with α and β connected by Snells law. The result is shown in Figure 4.25(a).
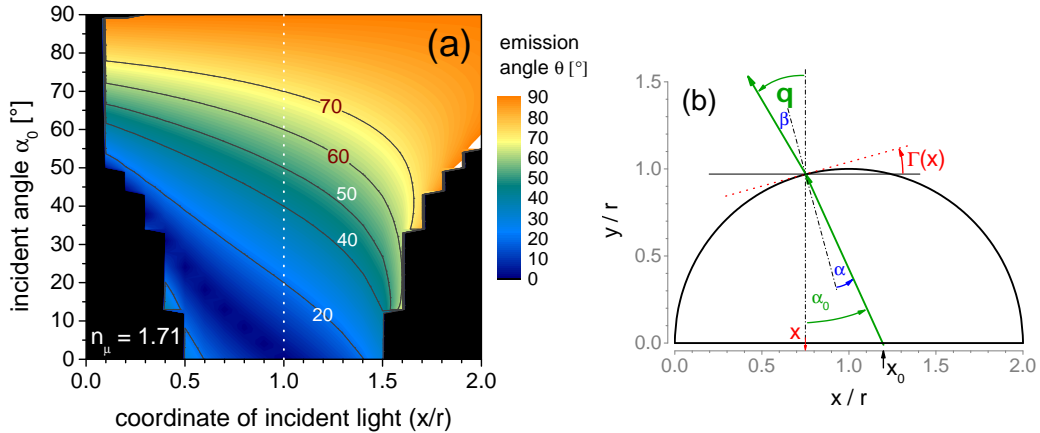
Figure 4.25: Analytical calculation of the emission angle for incident light rays at an incoming angle of α_0 at a position x_0 with respect to an ideal half lens having a refractive index $n_\mu = 1.71$ (a). The scheme of the raytracing model is depicted on the right (b) and considers incident angles from 0 - 90°. Of course, the range $\alpha_0 = 0°$ to $-90°$ is valid too, which means that graph (a) has to be mirrored at the straight line with $x/r = 1$ where $\theta = \alpha_0$.

At first, it becomes obvious that only light in the region 0° - 40° can be coupled into the forward direction. On the other hand, the 20° cone can include internal modes traveling up to 55° with respect to the normal direction. With increasing angle of incidence, the redirection of light decreases as incoming and emitted light feature nearly identical directions being independent from the position of incidence. Hereby, the outer regions of the lenses contribute to nearly every emission direction but can only be fed by light under large incoming angles. These findings validate why the spectral green fraction of light at the pixel edges in Figure 4.23(b) can only be observed at the circumference of the microlenses. Nevertheless, this calculation allows to reconstruct the redistribution of light modes by the attached microlens film.

In conclusion, we have presented an alternative to existing routes to realize highly efficient white-light emission with superior color quality from top-emitting OLEDs. Using a microlens array enables to exploit emission from a highly complex optical system. We expect the lamination process to be cost-effective and roll-to-roll compatible. Furthermore, water and oxygen barrier functionality can be added to the film turning it into an encapsulation film at the same time. Reaching very high color rendering indices (CRI) of up to 93, our approach makes it possible to surpass the color quality of the corresponding bottom-emitting device while the foil enables an improvement of the outcoupling efficiency (up to 50%) which is beyond the enhancement possible by a capping layer [148, 212]. Losses like waveguide modes or absorption by the semitransparent anode are reduced by optical tuning, but plasmonic losses

(e.g. losses that are connected to the emitter orientation) are not regarded here. For example, it could be shown that there might be non isotropic emitter orientation in the emitter systems investigated here [139] and that if one could control the orientation of molecules, the transport and the outcoupling could be further improved [213].

5 CHARGE INJECTION AND CHARGE BALANCE

The following chapter focusses on the investigation of the injection, the transport and the confinement of charge carriers in monochrome inverted top-emitting OLED devices comprising the orange phosphorescent emitter Ir(MDQ)$_2$(acac). Stepwise, from the outer to the inner layers, the electronic mechanisms which are responsible for a well charge balanced n-i-p OLED are investigated. Thermal annealing of the complete layer stack is found to drastically change the device electronics which can increase the device efficiency and helps to explain the differences in device performance compared to the p-i-n layered counterpart.

After figuring out the key parameters for an optimized light outcoupling in top-emitting OLED devices comprising Ag/Al electrodes one can try to elaborate the electronic mechanisms that are important to handle when designing a n-i-p inverted OLED device. The question we like to suggest answers to is:

What has to be considered when inverting an OLED structure?

It is already clear that it is not simply fabricating the reverse sequence of deposited layers. Apparent differences between n-i-p and its p-i-n OLED equivalent which are shown e.g. in Figure 2.19 on page 42 represent one motivation to do a comprehensive investigation of inverted OLED devices. At this point, it has to be mentioned that there is a lack of consequently comparing p-i-n to n-i-p devices in this work because it is not possible to have an equivalent p-i-n for every n-i-p that was investigated in this study. On the other hand, if the key parameters which limit electrical performance are found, the reason for the divergence must be connected to them.

From literature and theory, electrical and optical loss mechanisms are well described. If we can identify them in the experiment, a way to circumvent them can be developed.

The base OLED structure, a monochrome orange emitting device, has been studied intensively as p-i-n sequenced bottom-emitting OLED configuration [110, 214]. Ultraviolet photoelectron spectroscopy (UPS) measurements of

the electronic structure of this system revealed the built-in potential and the energetic positions of the transport levels which can be correlated to the I-V characteristic. They are depicted in Figure 2.13 on page 32.

5.1 Role of the electrodes and the transport layers

5.1.1 Injection and transport of electrons

The optical behavior of the bottom electrode has been discussed in Section 4.1. In the following, the injection properties of the cathode, employing thin Ag films on an Al sublayer to act as bottom contact are investigated. In Figure 5.1, the current-voltage-luminance and spectral characteristics of n-i-p structured OLEDs as a function of the Ag layer thickness are depicted. All devices exhibit comparable electrical characteristics except from an increase of 0.1 - 0.2 V driving voltage if the Ag layer is omitted. Notwithstanding the presence of ultra-high-vacuum (UHV) conditions, the Al contact forms a thin oxide film at the cathode surface [215] which influences the electron injection, observable at current densities $>10\,\mathrm{mA/cm^2}$. Due to the usage of a doped electron transport layer (ETL) this effect is rather weak. Further, the exchange of BPhen:Cs as ETL by TPPHen:W_2(hpp)$_4$ leads to lowered voltages in the driving regime above $10\,\mathrm{mA/cm^2}$ (by 0.5 V at $100\,\mathrm{mA/cm^2}$).
The investigated structure, starting from the bottom electrode, is (thickness in nm):

Al(100) / Ag(0, 10, 20, 40) / BPhen:Cs or TPPhen:W_2(hpp)$_4$(50) / BAlq$_2$(10) / NPB:Ir(MDQ)$_2$(acac)(10wt%)(20) / Spiro-TAD(10) / Spiro-TTB:F6TCNNQ (4wt%)(30) / Ag(15)

The corresponding external quantum efficiencies are depicted in Figure 5.2 which show a flat curve and a continuous decrease with increasing current density. At a luminance of about $1000\,\mathrm{cd/m^2}$, the devices with a single-layer Al cathode and BPhen:Cs as ETL exhibit an EQE of about 3.8% ($5\,\mathrm{mA/cm^2}$), compared to 6.2% ($3\,\mathrm{mA/cm^2}$) with a 40 nm Ag cathode, respectively. Besides the rather low absolute efficiencies of all OLEDs, two important issues are illustrated. First, devices incorporating BPhen:Cs as ETL show a higher efficiency than samples containing TPPhen as ETL. The sample with an additional Ag interlayer is expected to be more efficient due to optical reasons which are discussed in Section 4.1. On the other hand, the roll-off depends on the ETL material. When the quantum efficiency curves are scaled and su-
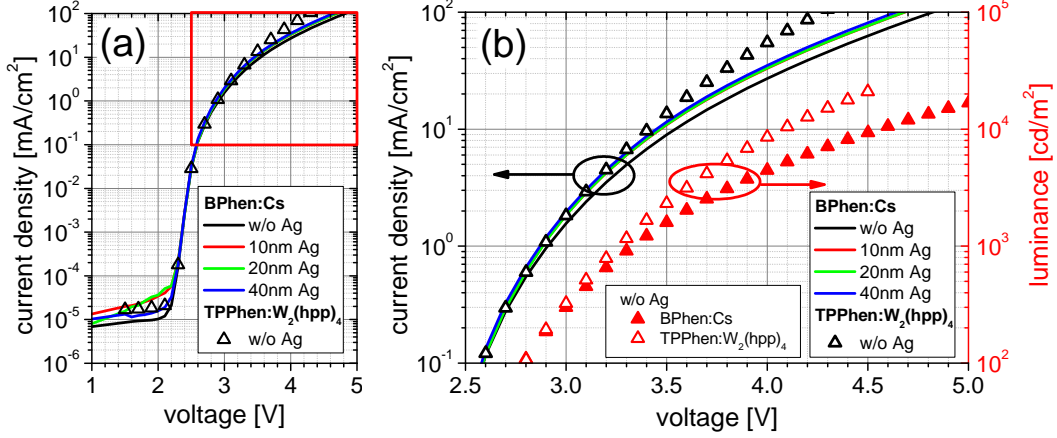
Figure 5.1: Current-voltage characteristics (a) and zoom of luminance characteristics (b) depending on the bottom contact and the ETL material. BPhen:Cs has been deposited onto an Al cathode without and with Ag interlayers of 10-40 nm thickness, respectively. The characteristics for the ETL system TPPhen:W_2(hpp)$_4$ are shown for the bare Al cathode only.

perimposed, both characteristics for BPhen:Cs coincide while the roll-off for the TPPhen based OLED is less pronounced. This fact suggests an electron transport or injection limitation for BPhen:Cs. An increased roll-off accounts for elevated losses at high currents and hence higher triplet densities which result in enhanced triplet-triplet-annihilation (TTA) processes [119]. Hence, a more localized recombination zone, originated by the different charge carrier management is most probably.

As there is no influence from the cathode, the ETL material determines the amount of electrons in the emitting layer (EML) in this case. Thus, the hole injection and transport into the EML must be very efficient which is not surprising if we assume comparable energy levels as reported in the non-inverted OLED [110].

The electroluminescence spectra from these OLEDs can validate this assumption. In Figure 5.3, the angular resolved emission spectra for devices without Ag and with a 40 nm Ag bottom cathode are depicted in logarithmic scale. Surprisingly, in devices without an Ag layer, a second emission peak appears at 510 nm under 60° viewing angle, shifting to smaller wavelengths with increasing angle. This peak can be directly attributed to a parasitic fluorescent emission from the $BAlq_2$ blocking layer whose photoluminescence peak is expected at 493 nm [214]. Optical simulation results confirm this fact if an electroluminescence from the $BAlq_2$ hole blocking layer (HBL) is assumed to
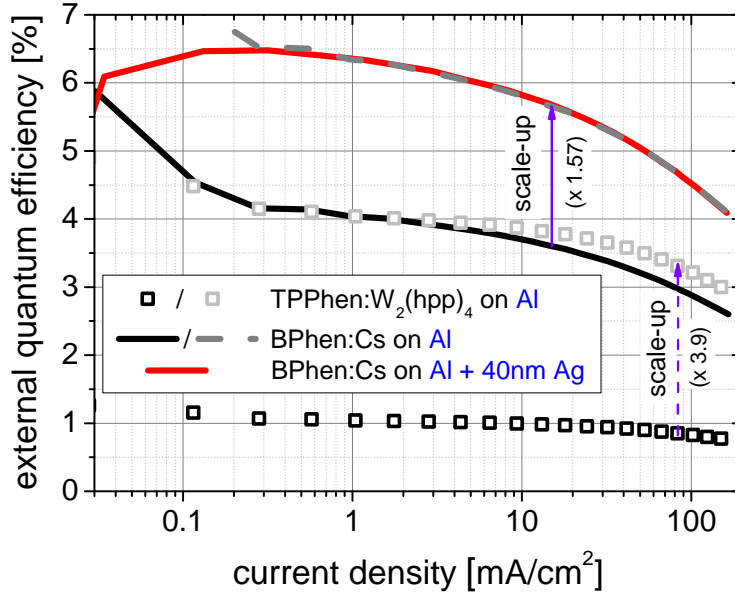
Figure 5.2: *External quantum efficiency data of inverted OLED devices, represented by the current-voltage-luminance characteristics in Figure 5.1. The grey dashed line/symbols are scaled to compare the roll-off depending on the electron transport layer material (ETL) and the bottom cathode, respectively.*

contribute with an intensity as high as 5% of the intensity of the main emitter system $NPB:Ir(MDQ)_2(acac)$. This effect validates the described high resistance for electrons at the Al-BPhen:Cs interface. The amount of electrons reaching the EML at elevated voltages is too less to avoid a hole-accumulation at the EML-HBL interface. Thus, a small part of holes can enter the $BAlq_2$ hole blocking layer, leading to a shift of the recombination zone towards it. Such pronounced charge accumulation can introduce exciton quenching processes that decrease the overall device efficiency [216]. In contrast, the recombination of holes and electrons in devices with 40 nm Ag layer is completely located inside the EML because these devices do not show any emission from $BAlq_2$. From the spectral characteristics, the reasons for the low external quantum efficiencies can be derived. One the one hand, an internal loss mechanism due to the poor electron injection into the EML is found. On the other hand, the optical cavity is de-tuned to smaller wavelengths with respect to the photoluminescence peak of the emitter system at around 610 nm. No outcoupling enhancement techniques like capping layers have been applied. One can conclude that TPPhen seems to be more efficient in terms of charge injection and transport and that a pure Al bottom contact indeed introduces an additional resistance. This is only observable at large driving currents as the intrinsic layers become highly conductive in this case.
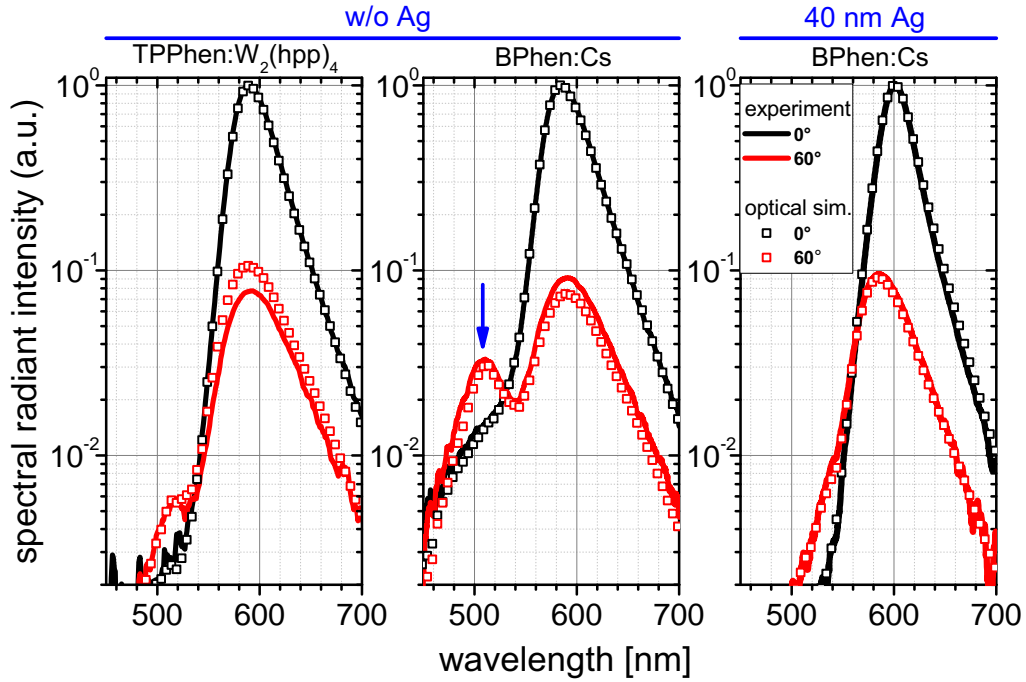
Figure 5.3: Angular resolved emission spectra of inverted OLED devices comprising TPPhen (left) and BPhen:Cs (middle) as ETL without Ag and with 40 nm Ag (right) on 100 nm Al bottom cathode. The measured spectra can be modeled accurately, validating a fluorescent light contribution from the hole blocking material BAlq$_2$ (blue arrow).

In an additional experiment, the influence of the cathode combination Al/Ag is investigated using TPPhen and NET-18[1] as ETL materials, doped with W$_2$(hpp)$_4$. The device structure is (thickness in nm):

Al(50) / Ag(0, 10, 20, 40) / NET18:W$_2$(hpp)$_4$, TPPhen:W$_2$(hpp)$_4$(60) / BAlq$_2$ (10) / NPB:Ir(MDQ)$_2$(acac)(10wt%)(20) / NPB(10) / MeO-TPD:F6TCNNQ (4wt%)(35) / Ag(20) / NPB(80)

The current-voltage-luminance characteristics for a variation of the Ag thickness on a 50 nm Al cathode are shown in Figure 5.4. The absolute voltages are about 1 V higher than in the previous experiments (compared to Figure 5.1) but the HTL and electron blocking layer (EBL) materials have changed, too. Interestingly, there is no influence from the Ag layer which means that no injection limitation for electrons is observed. On the other hand, the efficiency characteristics in Figure 5.5(a) exhibit a defined peak in the current efficiency.

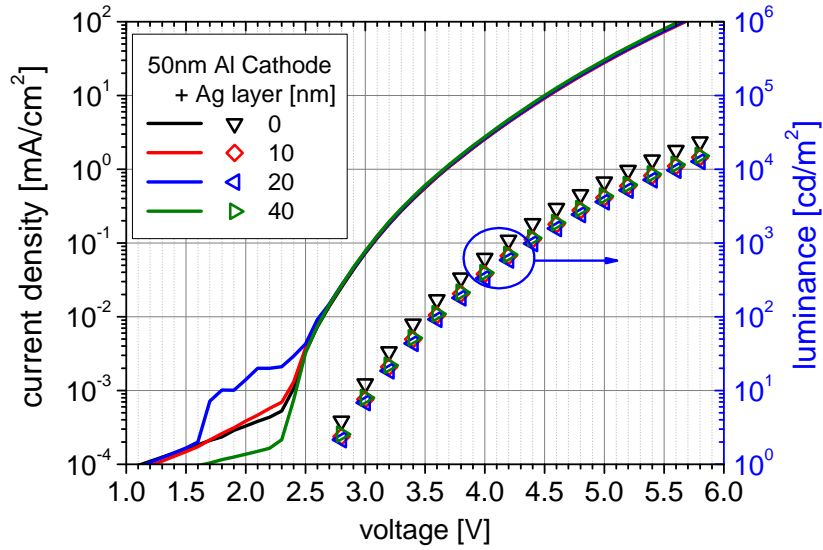[1]proprietary electron transport material by NOVALED AG

Figure 5.4: *Current-voltage-luminance characteristics depending on thin Ag interlayers, deposited onto an Al cathode for inverted OLED comprising NET-18 as ETL. The data demonstrates that there is no electrical influence coming from the cathode except a cavity resonance shift by the different optical properties of Al and Ag, respectively.*

This means there is an imbalance of the charge carrier ratio in the EML at low voltages (and currents) or that the leakage currents diminish the number of photons per charge carriers or both issues contribute.

Further, the OLEDs on the pure Al cathode exhibit the highest current efficiency which is caused by the optical tuning of the cavity and its resulting spectral overlap with the luminous efficiency function $V(\lambda)$. At this point, the absolute numbers of efficiency do not matter, but one has to keep in mind that the shape of the current efficiency characteristic has changed with the HTL material. The emission spectra in Figure 5.5(b) validate the optical effect of the changed cathode surface as it has been discussed in Section 4.1. The shift of the emission peak is much more pronounced as it is expected from optical simulation which are directly compared in the plot. The thickness of the organic layers influence the cavity length and one has to keep in mind that these samples are made on a $15 \times 15 \, \text{cm}^2$ substrate. Thus, they include a thickness gradient from the outer to the inner region of the large substrate due to deposition inhomogeneity. This effect contributes to the spectral position of the cavity resonance and has to be superimposed with the intentional linear thickness gradient of the bottom Ag layer. Anyway, the optical simulation validates the experimental data qualitatively.
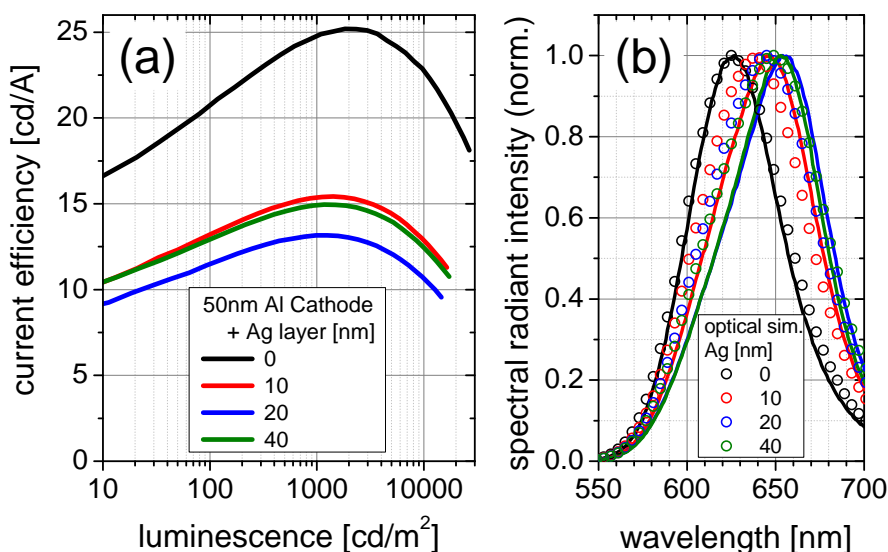
Figure 5.5: *Current efficiency (a) and electroluminescence spectra (b) depending on the cathode surface for inverted OLEDs comprising NET-18 as ETL. The optical influence of the Ag interlayer can be observed in both experimental data (lines) which is analog to results shown in Figure 4.2 on page 63. It is qualitatively in accordance to optical simulations (symbols).*

In a last comparison, NET-18 and TPPhen, both doped with 8 weight % of $W_2(hpp)_4$, are used as ETL on an $Al(50\,nm)+Ag(40\,nm)$ cathode. The resulting OLED characteristics in Figure 5.6(a) show minimal differences in the current-voltage characteristics of about $0.2\,V$. This is not surprising as the electronic levels of both materials are nearly the same (Table 5.1). In contrast to that, the voltage difference at $10^4\,cd/m^2$ is $0.5\,V$. This fact is correlated to a strongly different efficiency as validated in Figure 5.6(b). As there are slight changes in the related EL spectra, one might argue that the differences are of optical nature. If optical simulation is used to fit[2] the angular dependent spectral emission, one finds a clear discrepancy.

At about $2.3\,mA/cm^2$, the EQE for NET-18 based device is 13.1% while the OLED comprising TPPhen as ETL matrix material shows 18.2%. The ratio of these EQE values is $0.131/0.182 = 0.72$ while the optical simulation yields a ratio of 1.2 when comparing the total number of outcoupled photons if the internal efficiency is assumed to be equal for both ETL materials. The simulated EL spectra are depicted in the inset of Figure 5.6(b) as circles.

---

[2]Slight changes in the layer thickness of the Ag anode or the transport layers lead to optical deviations of the cavity resonance and have to be considered in the optical simulation.
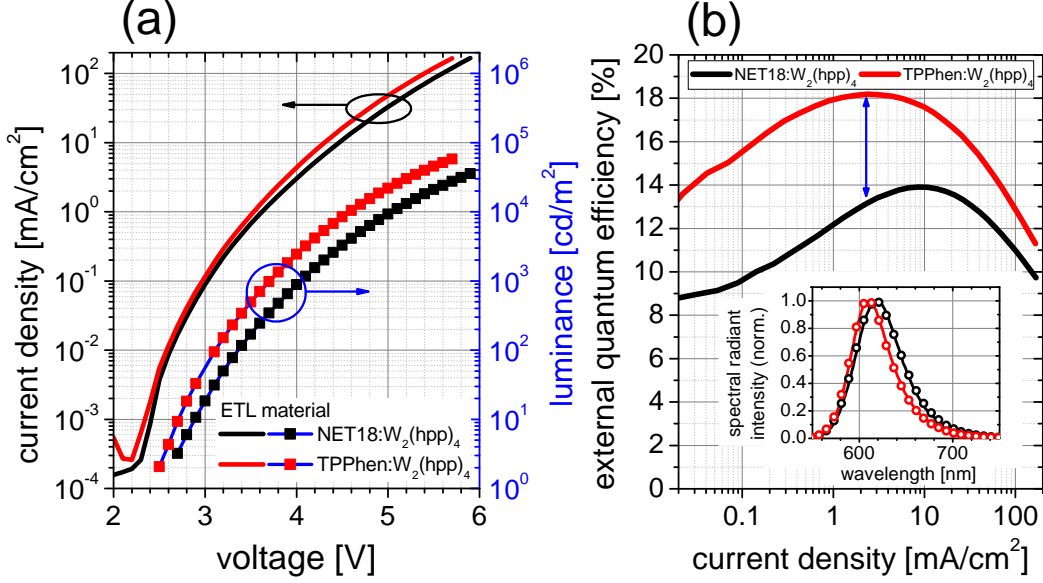
Figure 5.6: *Current-voltage-luminance characteristics (a) of inverted OLEDs with either NET18:W$_2$(hpp)$_4$ or TPPhen:W$_2$(hpp)$_4$ as ETL on a 40 nm Ag cathode on 50 nm Al. The emission spectra (lines: experimental data, circles: fit by optical simulation) are comparable (inset (b)) while the external quantum efficiencies diverge in graph (b). The blue arrow denotes the EQE at 2.3 mA/cm^2.*

Further, if the forward current efficiency of both devices is compared, the NET-18 based OLED exhibits 28.6 cd/A while the TPPhen based OLED shows 56 cd/A at 2.3 mA/cm^2 (ratio 0.51). Again, the optical simulation can be used to calculate the luminous intensity in forward direction for a fixed internal efficiency and current density. This assumption is equivalent to a constant source term in the model. The effect of the slightly different optics in both OLEDs lead to a factor of 0.84 between the luminous intensities in forward direction. The discrepancy between experiment and simulation is consistent for the spatial emission (EQE) and the forward current efficiency. It is nearly $exp./sim. = 0.72/1.2 \approx 0.51/0.84 \approx 0.6$ which represents the differing factor of internal efficiency between NET-18 and TPPhen based OLEDs.

Table 5.1: *Comparison of the material parameters of the used electron transporters.*

material	IP (eV)	EA (eV)	T$_g$ (°C)
TPPhen	-6.1	-2.5	105
NET-18[1]	-6.3	-2.6	131
BPhen	-6.46	-2.9	62

5.1.2 METAL-ORGANIC CO-EVAPORATION

In literature, the effect of metal penetration into organic layers when electrodes are deposited onto them is used as argument for the inferior performance of inverted OLEDs. This might be true for devices without using doped transport layers but has to be investigated in our case. For this purpose, some of the inverted OLED devices make use of metal-organic interlayers, deposited on the cathode to demonstrate the influence of penetrated electrode metal atoms inside the ETL at the cathode interface. The principle of organic-metal co-evaporation has been studied the first time by Aziz et al. in 2003 [217, 218]. Their work focused on low reflectance Alq_3:Ag back-cathodes for high contrast OLED pixels. Later in 2006, Chiu et al. investigated the optical but also the electrical behavior of Ag-doped MPPDI[3] [219]. They observed increasing conductivity of 75 nm thick mixed films with increasing Ag concentration up to ohmic conduction. At a MPPDI/Ag volume ratio of 5:1, no injection barrier is found as limitation for the charge transport.

In this work, an equivalent approach is applied to investigate the effects of charge injection at metal bottom contacts. This is done by inserting a 5 nm layer of BPhen:Cs:Ag between the bottom cathode and the ETL BPhen:Cs. The Ag concentrations are 0, 12, 24, 36 and 48wt% with respect to the molar mass of 332.13 g/mol of BPhen (Ag: 107.9 g/mol). The OLED layer structures are as follows (thickness in nm):

Al(50) / Ag(30) / BPhen:Cs:Ag(0, 12, 24, 36, 48wt%)(5) / BPhen:Cs(60) / BAlq$_2$(10) / NPB:Ir(MDQ)$_2$(acac)(10wt%)(20) / NPB(10) / MeO-TPD:F6TCNNQ(4wt%)(42) / Al(1) / Ag(19) / NPB(85)

The results are depicted in Figure 5.7. The current-voltage characteristics are not affected by a 5 nm Ag-doped interlayer. Only the leakage current is altered slightly. The efficiency curves on the other hand follow the doping fraction systematically. An increase of Ag in BPhen:Cs lowers the EQE and seems to saturate above 36wt%. Hence, such a behavior should be connected to the device optics again. In Figure 5.8, the normalized EL spectra are compared, showing no difference except a slight shift of the peak toward larger wavelengths. This shift can also be attributed to each sample position on the $15 \times 15\,cm^2$ substrate glass wafer during deposition. The devices with 0 and 48wt% Ag fraction were located at the edges of the wafer and exhibit the peak at the smallest wavelength. The only possible explanation for the trend in the efficiency could be a systematic decrease of cathode reflectivity with increasing Ag concentration which is similar to the findings of Chiu et al. [219].

---

[3]N,N'-bis(2,6-di-isopropylphenyl)-1,7-bis(4-methoxy-phenyl)perylene-3,4,9,10-tetracarboxy- diimide
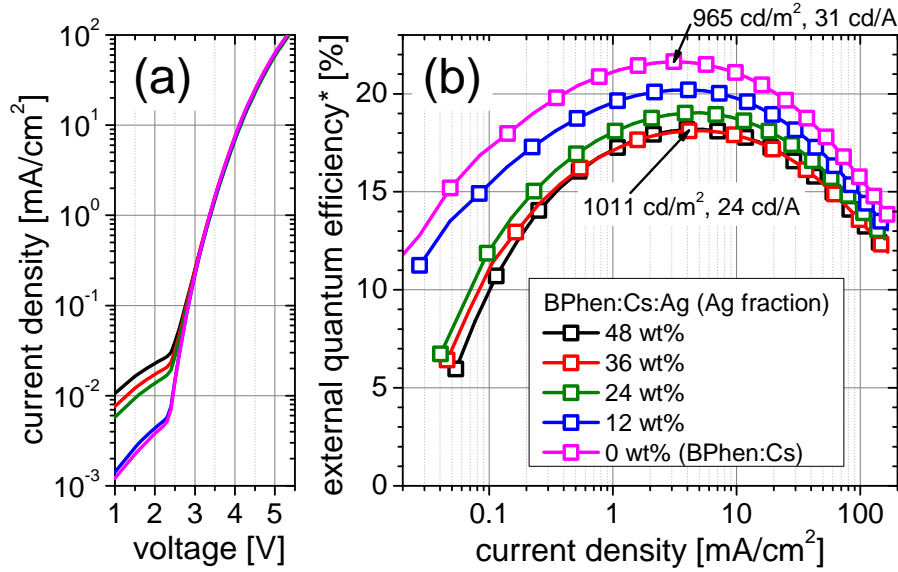
Figure 5.7: The current-voltage (a) and external quantum efficiency (EQE) (b) demonstrates the influence of a 5 nm BPhen:Cs:Ag interlayer at the cathode-ETL bottom interface on the OLED performance. The leakage current increases with raising Ag fraction which could be due to increased roughness or enhanced lateral conductivity. A Lambertian emission characteristic is assumed for the determination of the EQE (*).

Figure 5.8: Influence of 5 nm BPhen:Cs:Ag interlayer on the EL spectrum. The experimental variations of layer thickness across the substrate is dominant as demonstrated by the peak shift and the slight spectral broadening.

In conclusion, the use of doped electron transport layers enables efficient injection of electrons from a metal bottom contact and the effect of a metal-organic interlayer is most probably only of optical nature.
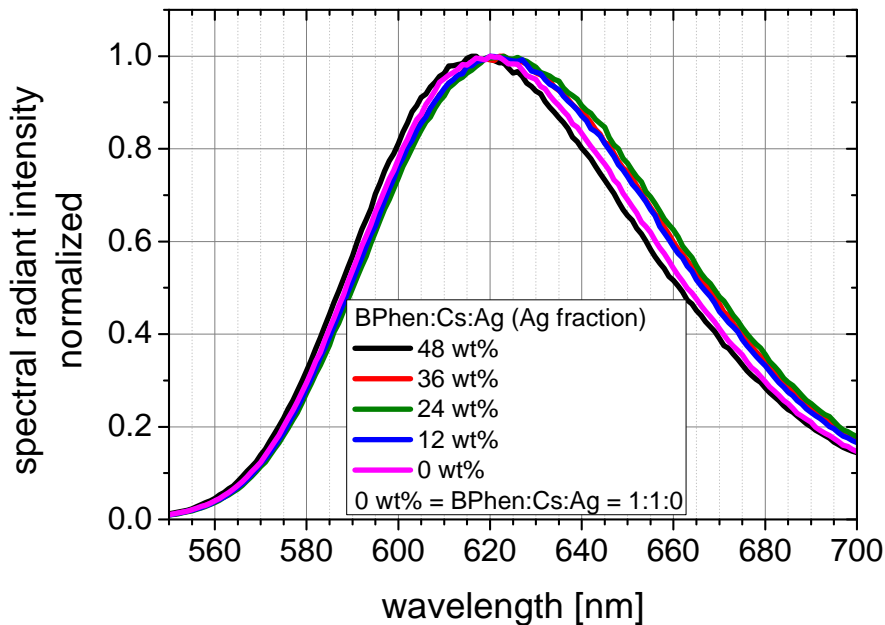
5.1.3 INJECTION AND TRANSPORT OF HOLES

The previous section described the injection and transport of electrons in complete inverted OLED devices. In the following, the hole injection is discussed in brief.

At first, the effect of an anode modification by a thin 1 nm Al surfactant layer is demonstrated. From literature, it is known that such layer can increase the stability of top-emitting OLED devices [220] and enhance the efficiency of organic solar cells [221]. The influence of this Al interlayer on the hole transport is studied by single-carrier p-i-p layered samples. The device structure is (thickness in nm):

Al(40) / Ag(30) / MeO-TPD:F6TCNNQ (2wt%)(30) / Spiro-TAD (50, 100) or NPB (50, 100) / MeO-TPD:F6TCNNQ (2wt%)(30) / Al (0, 1) / Ag(20)
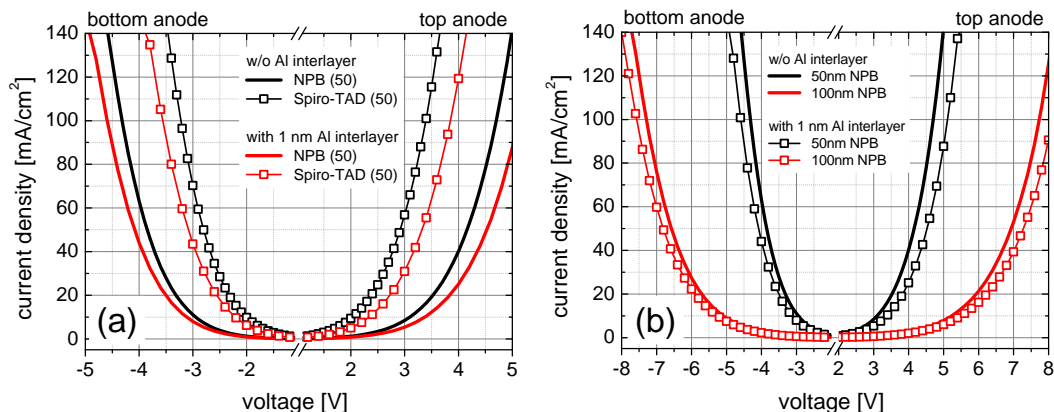
Figure 5.9: *Current-voltage characteristics of single-carrier devices (p-i-p) with either NPB (lines) or Spiro-TAD (squares) as intrinsic material (a). The influence of an Al interlayer of 1 nm thickness on the I-V characteristics can be as large as 0.5 V, while it is independent from the layer thickness, shown for NPB (b).*

In Figure 5.9, the corresponding voltage dependent current densities are depicted for positive and negative bias. For a given current, the 1 nm Al interlayer leads to an increased resistance which is clearly visible in a voltage increase of up to 0.5 V. This observation does not depend on the intrinsic material between the doped hole transporting layers. A combination of two effects may explain this strong impact. On the one hand, the thin Al acts as surfactant

layer for the Ag anode deposition which than grows in a different morphology with changed energetics at the interface to the organic layer beneath [186]. On the other hand, 1 nm Al may oxidize or react with the underlying materials and create an additional barrier even though it is not a closed layer. This strong effect of 1 nm Al should be considered when discussing complete OLED devices which make use of a 1 nm Al surfactant layer. In previous studies, such an effect has been observed in p-i-p devices as well and a 2 nm interlayer of NDP-2[4] followed by an Au top contact has been proposed as solution [43]. For example, it is claimed that there is a formation of an insulating layer during the deposition of a top metal on the hole transporting material NHT-5[5]. The presence of a barrier for holes is further validated by the fact that the influence is only slightly depending on the bias polarity as it occurs for in- as well as for ejection of holes at the top contact. An injection limitation is not observed because the dependence of intrinsic layer thickness is visible for all measured voltages. Hence, the contact resistance slightly lowers the electric field that drops across the organic layers.

Further, the results of p-i-p layered devices in Figure 5.9(a) show the influence of the intrinsic material which is discussed in detail in the next section. However, intrinsic Spiro-TAD exhibits much higher currents at a given voltage compared to NPB and an asymmetry of the I-V curves is observed. Holes seem to be transported more efficiently when coming from the bottom contact compared to the case in inverted OLEDs when they are injected from the top contact. As this effect is independent from the bulk thickness, it has to be related to the p-doped layers and/or to the energetics at the organic-organic interface which seem to be asymmetric. Detailed explanations are given in Section 5.3.2.

After discussing the effects at the anode interface, the influence of the hole transport layer (HTL) is investigated. The results should give a further hint why inverted OLEDs show inferior driving voltages when compared to non-inverted ones.

In the following experiment, two inverted OLEDs with different HTL materials are compared. It has to be pointed out that they additionally differ in some other parameters e.g. layer thicknesses. Hence, they are not comparable regarding absolute efficiency as they feature different light outcoupling. Nevertheless, electrically they are comparable. The differing parameters that belong to a certain device feature the same color in the layer list (thickness in nm):

---

[4]proprietary p-type dopant by NOVALED AG
[5]proprietary hole transport material by NOVALED AG

Al(100, 50) / Ag(0, 40) / TPPhen:W$_2$(hpp)$_4$(50, 55) / BAlq$_2$(10) / NPB:Ir(MDQ)$_2$ (acac)(10wt%)(20) / Spiro-TAD(10) / Spiro-TTB:F6TCNNQ(30)(4wt%) or MeO-TPD:F6TCNNQ(4wt%) (35) / Ag(15, 20) / NPB(0, 80)
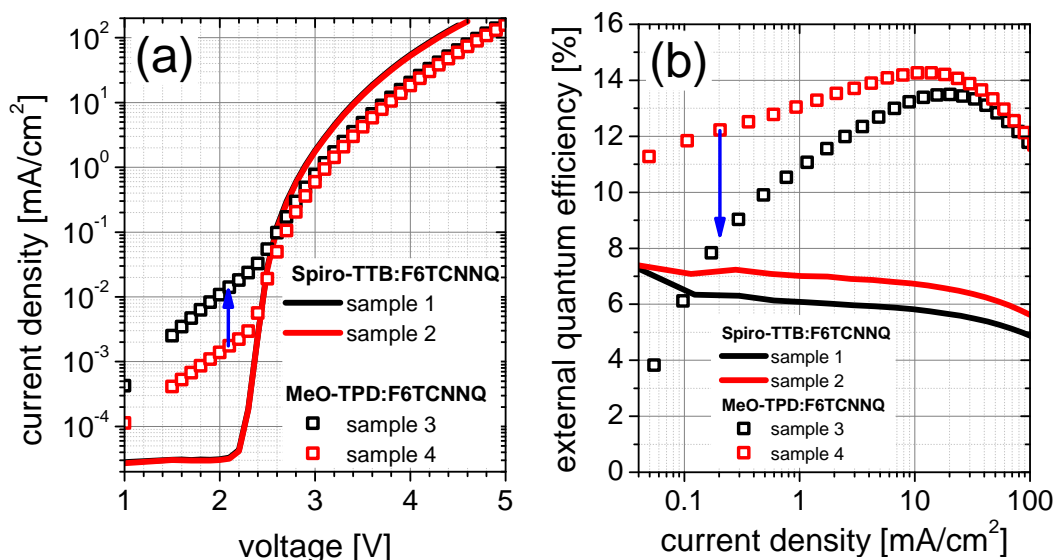

Figure 5.10: *Current-voltage characteristics of inverted OLED devices depending on the HTL material (a), each represented by two equal samples to demonstrate the variations within one experiment. The deviations in the leakage currents directly influence the external quantum efficiency at low currents (blue arrows) (b). The absolute difference between the efficiency of different HTL-based OLEDs is not only due to the different optics of both structures. Nevertheless, the shape of the curves is completely different.*

The comparison between MeO-TPD and Spiro-TTB as HTL in Figure 5.10 yields the following important information. First, inverted top-emitting OLEDs having a n-i-p structure seem to be very sensible against small changes of the hole injection and hole transport materials. If we compare the material properties summarized in Table 5.2, we find very equivalent transport levels but completely different glass transition temperatures. Secondly, the leakage currents differ by two orders of magnitude which might be due to the different cathode structures. This leads to decreased OLED device efficiency at low current densities and induces an EQE curve with a distinct peak. On the other hand, the choice of the HTL material can alter the charge balance and therefore lead to an unbalanced charge carrier ratio at low current densities. In case of MeO-TPD the devices need higher voltages to reach the maximum of efficiency whereas Spiro-TTB shows an almost flat current dependent EQE with a slight decrease of efficiency. Although both samples were not fabricated in

the same run, the comparison shows first hints that the hole-transporting side is more critical regarding the driving voltage of the device than the electron-transporting side.

Table 5.2: Comparison of the material parameters of the used hole transporters.

material	IP (eV)	EA (eV)	T_g (℃)	References
Spiro-TTB	-5.0	-1.9	145	[220]
MeO-TPD	-5.1	-1.9	55	[48]

5.2 Control of the charge confinement: the intrinsic layers

In the last sections, the influence of the cathode and anode interface to its adjacent organic charge transport layers has been discussed. Using donor-doped ETL material systems we neither found pronounced influence on the current-voltage characteristics from typical cathode surfaces (Ag or Al) nor from the ETL itself. On the other side of the device, the anode is more sensitive to changes of the interface components. In contrast, the device efficiency is found to be strongly influenced by both sides (ETL and HTL) of the n-i-p structure. To go one step further, the intrinsic blocking layers are studied in this section. First, the electron blocker which is located between EML and HTL is varied. The device structure is (thickness in nm):

Al(50) / Ag(40) / TPPhen:W_2(hpp)$_4$ (60, 70, 75, 80) / BAlq$_2$(10) / NPB:Ir(MDQ)$_2$ (acac) (10wt%)(20) / Spiro-TAD or NPB (10) / MeO-TPD:F6TCNNQ (4wt%)(35) / Ag(20) / NPB(80)

Comparing the I-V characteristics of OLEDs comprising either NPB or Spiro-TAD (EBL), shown in Figure 5.11, a behavior analogous to the previous discussed variation of the HTL material can be found. This is reasonable as the energetic barrier between HTL and EBL that holes have to overcome is changed. In accordance to reports from Freitag et al. [206], Spiro-TAD facilitates a more efficient hole injection from doped MeO-TPD as the energy barrier is supposed to be 0.31 eV compared to 0.38 eV for NPB.

Further, from this study one can conclude that the external applied voltage only drops across the intrinsic layers as an additional EML (comparison p-i-p and p-i-i-i-p with equally layer thickness in total) does not show any influence on the I-V characteristic as shown in Figure 5.12.
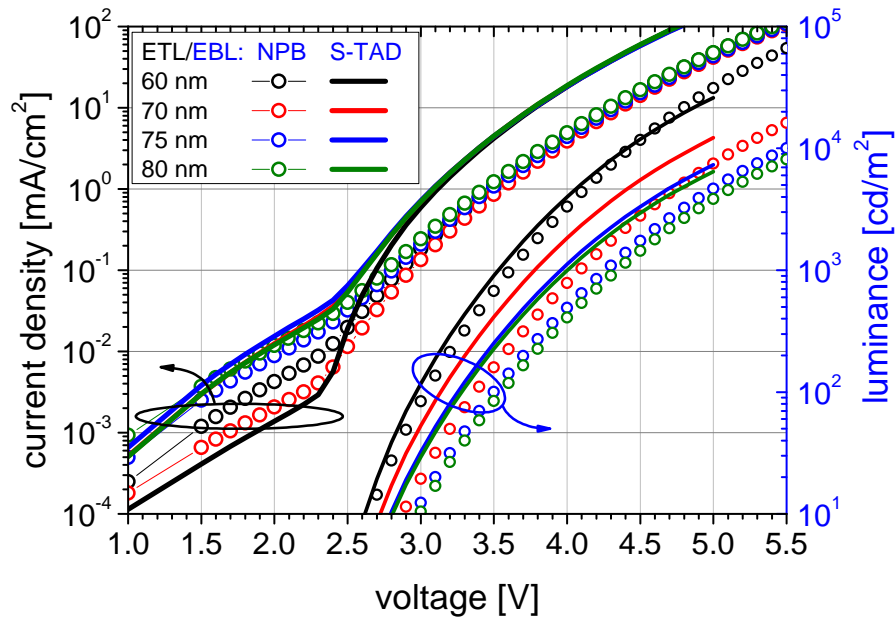
Figure 5.11: Current-voltage-luminance characteristics of inverted OLEDs depending on the ETL thickness and the use of either Spiro-TAD or NPB as electron blocking layer (EBL).

Interestingly, the p-i-i-i-p device comprising Spiro-TAD shows higher currents in the positive voltage regime below 3 V compared to negative bias. This behavior is due to the asymmetric layer thicknesses which vanishes for higher voltages like 5 V as the bulk layer properties do not play a role anymore. In this high voltage regime, only the energy barriers at the interfaces which are assumed to be symmetric define the I-V characteristic. This behavior could also be validated in single carrier devices where I-V measurements are successfully correlated to electrical simulations [222, 223]. The energetic width of the density of states (DOS) is important for the transport across the interfaces as well as the carrier mobility for the overall efficiency [224]. The fact, that the devices cited from literature are made on ITO and are finalized with an opaque Al electrode should be mentioned, as it might explain differences between these results and the ones observed in this work.

Nevertheless, the results from the electron blocker variation inside an inverted OLED coincide with the observations from p-i-p single carrier devices, depicted in Figure 5.9 on page 111. The corresponding external quantum efficiencies and electroluminescence spectra are depicted in Figure 5.13. Featuring the same leakage currents, the steeper I-V curves in the devices which contain Spiro-TAD lead to flat EQE curves compared to the NPB based samples that exhibit a distinct peak. The difference in the absolute efficiency of both kinds
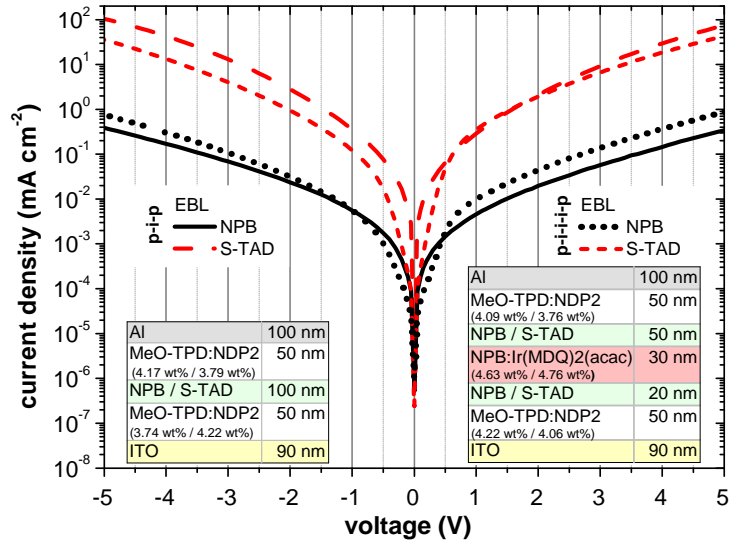
Figure 5.12: *Current-voltage-characteristics of p-i-p and p-i-i-p single carrier devices comprising the layer structures shown below. The influence of the intrinsic material (NPB or Spiro-TAD) is clearly visible. Image taken from [206].*

of devices is very interesting. Optically they are equal which is validated by the EL spectra in Figure 5.13(b) but the higher current at a given voltage does not lead to a significant increase of luminance as it can be seen in Figure 5.11.
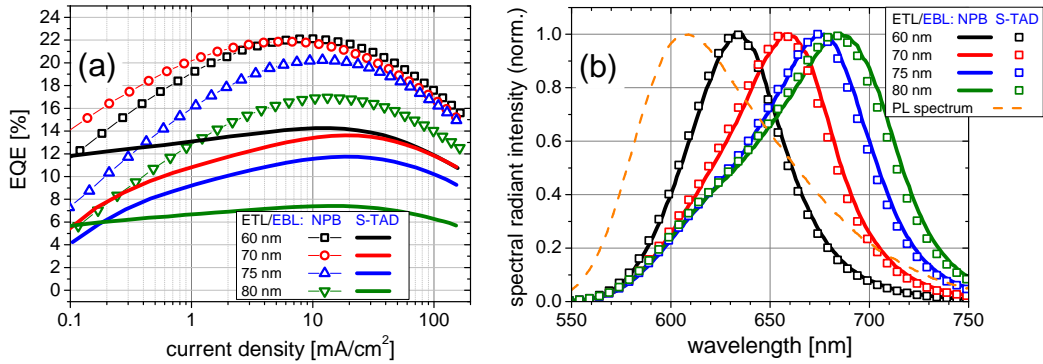
Figure 5.13: *External quantum efficiency (a) and emission spectrum (b) of inverted OLEDs with either NPB or Spiro-TAD as EBL for different ETL thicknesses. The data is partially equivalent to the data in Figure 4.6.*

The role of the hole blocking layer (HBL) material in the inverted OLED has to be discussed as well. The two materials BPhen and $BAlq_2$ are compared as they have proven to enable efficient and stable OLED devices [106, 202]. Additionally, the comparison to equivalent non-inverted devices is drawn. Ta-

ble 5.3 summarizes both experimental layer sequences and Figure 5.14 shows the experimental results.
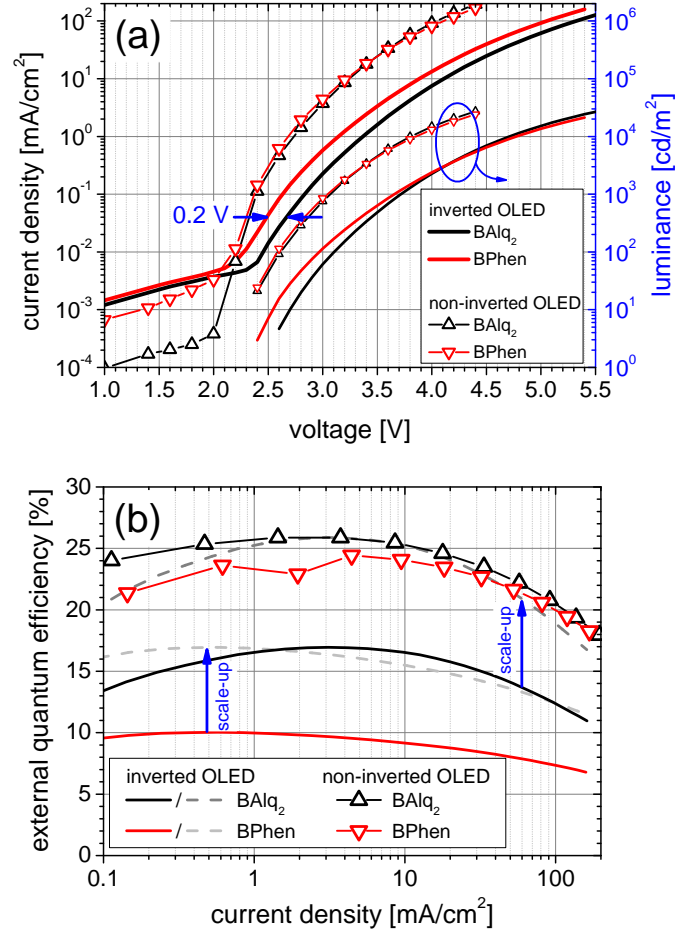
Figure 5.14: Current-voltage-luminance characteristics (a) and external quantum efficiency (b) of inverted (n-i-p) and non-inverted (p-i-n) top-emitting OLEDs comprising either BAlq2 or BPhen as hole blocking layer material.

In contrast to the influence of the electron blocking layer (EBL) discussed previously, one can see a completely different influence on the I-V characteristics as well as different shapes of the EQE curve (see Figure 5.14(b)). The difference between BAlq$_2$ and BPhen in the inverted case dominates the low voltage regime and leads to reduced turn-on voltage of about 0.2 V for BPhen as HBL material. Here, both materials seem to exhibit different currents in the trap-charge limited regime. It is known that transport in BAlq$_2$ can be described assuming an exponential trap distribution [225].

Table 5.3: *Layer sequence for the comparison of inverted and non-inverted OLED comprising BPhen and BAlq$_2$ as HBL, respectively. The corresponding performance data is depicted in Figure 5.14.*

inverted OLED (nm)	non-inverted OLED (nm)
NPB (85)	NPB (82)
Ag (19)	Ag (20)
Al (1)	-
MeO-TPD:F6TCNNQ (4wt%) (42)	BPhen:Cs (64)
NPB (10)	BPhen or BAlq$_2$ (10)
NPB:Ir(MDQ)$_2$(acac)(10 wt%) (20)	NPB:Ir(MDQ)$_2$(acac)(10 wt%) (20)
BPhen or BAlq$_2$ (10)	NPB (10)
BPhen:Cs (60)	MeO-TPD:F6TCNNQ (4wt%) (37)
Ag (30)	Ag (40)
Al (50)	Al (40)

This fact could explain that in the BPhen based device, recombination starts at lower voltages because in case of BAlq$_2$, the trapped electrons influence the I-V characteristic and alter the radiative recombination process [44].

In contrast, the non-inverted OLED does not exhibit an influence induced by exchanging the HBL material. The difference in driving voltage of non-inverted compared to inverted OLEDs is up to $1\,V$ at $100\,mA/cm^2$. If the EQE curves for the BAlq$_2$ based devices are scaled, a clear difference in the onset (influenced by leakage) as well as in the roll-off can be seen. This leads to the conclusion that deviations in the spatial recombination profile, in the exciton dynamics, and as consequence an absolute difference in EQE of about a factor of 1.5 - 2.5 are likely. As shown in literature, the modification of the recombination zone inside the EML and accumulated or leaked charges can strongly alter the roll-off characteristics [226].

Table 5.4: *Comparison of the material parameters of the used intrinsic blocker materials. The properties of BPhen are listed in Table 5.1.*

material	IP (eV)	EA (eV)	T$_g$ (°C)	μ_0 (cm^2 V^{-1} s^2)	References
Spiro-TAD	-5.4	-2.6	133	$2.5 \cdot 10^{-4}$	[227]
NPB	-5.4	-2.52	96	$8.8 \cdot 10^{-4}$	[48, 227]
BAlq2	-6.08	-3.0	92	$3.08 \cdot 10^{-7}$	[43, 48, 180]

At this point, we have evidence that the intrinsic blocker layers in n-i-p OLED devices might have a dramatic influence on the overall charge balance

in the emitting layer - unlike to equivalent p-i-n OLEDs. This fact emphasizes the assumption that charge imbalance leads to lowered device efficiency, an increased driving voltage at a given brightness and an altered roll-off. If there is a lack in one kind of charge carrier, the slope of the I-V characteristic flattens, especially if the hole transport is inferior. This is reasonable because the other sort of charge carrier has to accumulate as insufficient recombination paths are present until an elevated voltage is reached. Further, in the inverted OLEDs the leakage current has significant influence on the EQE at low bias, leading to decreased efficiency in the low voltage regime. As the voltage increases, the ratio of recombination current compared to leakage current increases, resulting in raising efficiency up to the case where processes like triplet-triplet-annihilation or triplet-polaron quenching herald the typical roll-off.

The difference of carrier transport is found to depend on the deposition sequence of the adjacent layers and secondly on the materials themselves. Thereby, the glass transition temperature of the materials has to be considered as well. In the next section, the OLED performance is investigated in more detail and possibilities for device improvement are developed.

5.3 Thermal annealing of inverted OLED devices

The choice of materials, in combination with the evaporation sequence of organic materials that form functional interfaces in OLEDs can play an important role for the overall device performance. Injection efficiency and thus charge carrier balance is strongly influenced and can lead to decreased efficiencies.

Inverting an OLED structure leads to complete changes in the charge carrier balance via changed charge injection into the EML. Reasons can be the different growth and morphology of organic layers induced by different heat exposure and deposition sequence. Therefore, the glass transition temperature T_g of the materials is of importance. Previously, n-i-p layered OLEDs were found to show reduced device performances after fabrication, compared to p-i-n OLEDs. In this section, the change of the electrical behavior of the inverted OLED during thermal annealing is investigated and the results are correlated to the performance deviations between inverted and non-inverted devices. The influence of the cathode-ETL interface has been found to be less relevant in case of using a doped ETL. So far, the device samples discussed in Section 5.1.2 are investigated regarding the influence of a thermal treatment on the overall performance like voltage, EQE, and luminous efficacy.
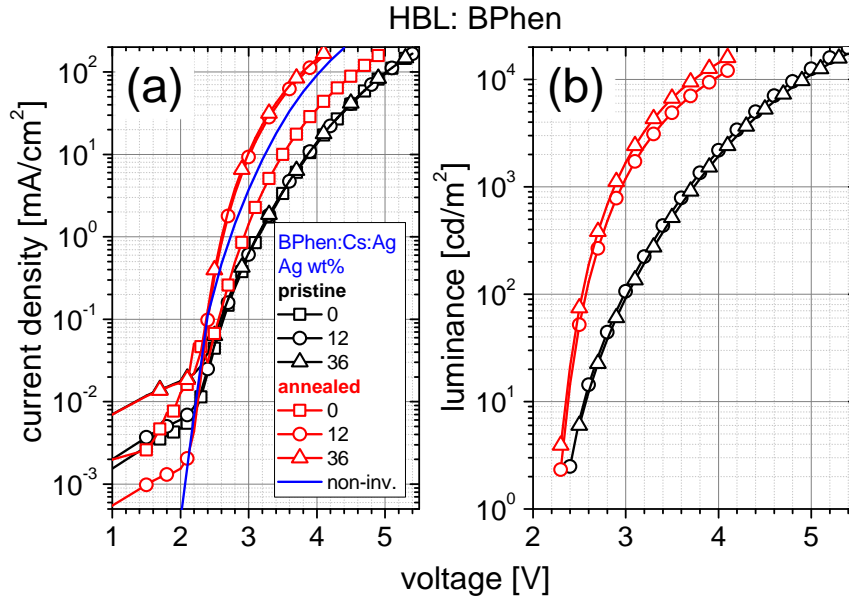
Figure 5.15: *Current-voltage (a) and luminance-voltage (b) characteristics of pristine and thermally annealed inverted OLEDs. BPhen has been used as HBL. The sample without an interlayer has been annealed 20 min at 70 ℃ while the devices with 12wt% and 36wt were annealed 30 min at 75 ℃.*

The device structures are (thickness in nm):

Al(50) / Ag(30) / BPhen:Cs:Ag (0, 12, 24, 36, 48 wt% Ag)(5) / BPhen:Cs(60) / BPhen or BAlq$_2$(10) / NPB:Ir(MDQ)$_2$ (acac) (10wt%)(20) / NPB(10) / MeO-TPD:F6TCNNQ (4wt%)(42) / Al(1) / Ag(19) / NPB(85)

The current-voltage-luminance characteristics for devices containing BPhen or BAlq$_2$ as HBL are shown in Figure 5.15 and 5.16, respectively. As discussed before, there is no difference in the I-V when comparing n-i-p devices with and without an organo-metallic BPhen:Cs:Ag interlayer (IL) at the cathode interface. Nevertheless, comparing pristine and annealed OLEDs, we find large differences in their electrical performances. On the one hand, the I-V curve exhibits a much steeper slope, leading to largely reduced driving voltages, for example by 1.2 V at 100 mA/cm^2 in case of BPhen. The driving voltages are even lower than for a pristine non-inverted equivalent p-i-n OLED (see Figure 5.15). This effect is observed for 12% and 36% Ag concentration in the BPhen:Cs:Ag layer. The sample without an Ag-doped BPhen:Cs interlayer was annealed at 70 ℃ for 20 min, compared to 75 ℃ for 30 min annealing conditions for the other samples. This difference leads to less pronounced changes for the sample without an organo-metallic IL. Following this observation, the influence of annealing time and temperature is investigated in the next section.
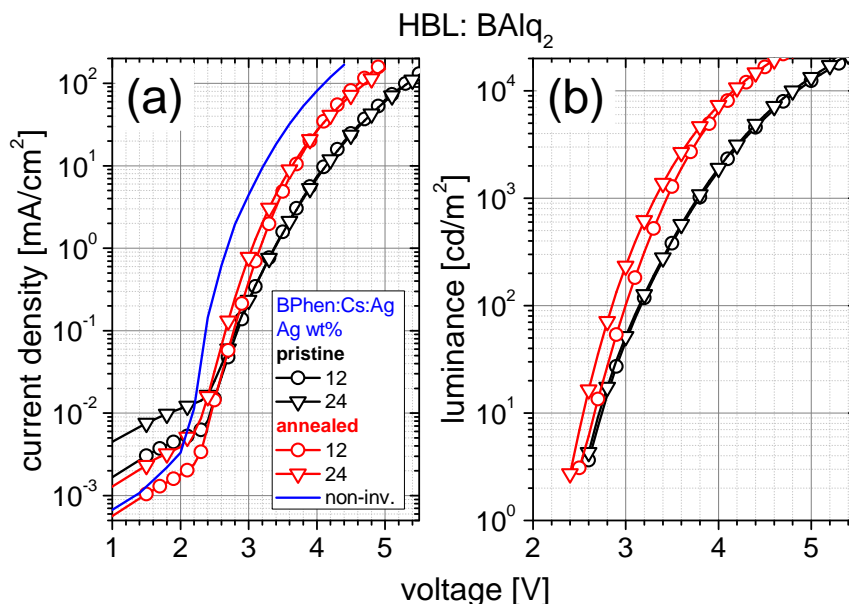
Figure 5.16: *Current-voltage (a) and luminance-voltage (b) characteristics of pristine and thermally annealed inverted OLEDs. BAlq$_2$ has been used as HBL. The device with 12wt% Ag was annealed for 20 min, the sample with 24wt% Ag for 30 min, both at 75 °C. The blue line indicates the current-voltage characteristic of an equivalent non-inverted OLED device.*

Further, the observed leakage currents show an invariance or a decrease during the annealing process. Thinking of rearranged molecules in the films leading to increased charge transport perpendicular to the interfaces, the lateral conductivity might accordingly be decreased.

According to the improved I-V in annealed n-i-p OLEDs and because the luminance scales in a wide range linearly with the current, the luminance at a given voltage similarly increases as validated in Figure 5.15(b). The voltage at 10^4 cd/m^2 drops from 5 V to 3.8 V after the thermal annealing process. The luminance onset slightly shifts to lower voltages but if one assumes that recombination and light emission starts when reaching the built-in voltage, Figure 5.15(b) gives rise to the fact that the built-in voltage is unchanged during annealing. Further, the difference in the luminance above 3 V between the samples comprising 12wt% and 36wt% Ag is an interesting feature in Figure 5.15(b). As the I-V curves of both samples are almost identical, the difference in luminance motivates a deviation in the efficiency.

In comparison, OLEDs with BAlq$_2$ acting as HBL do not show these strong changes in I-V when being annealed at 75 °C. This is important if one considers the glass transition temperatures T$_g$ of BPhen (62 °C) and BAlq$_2$ (92 °C), where the used annealing temperature of 75 °C lies in between.
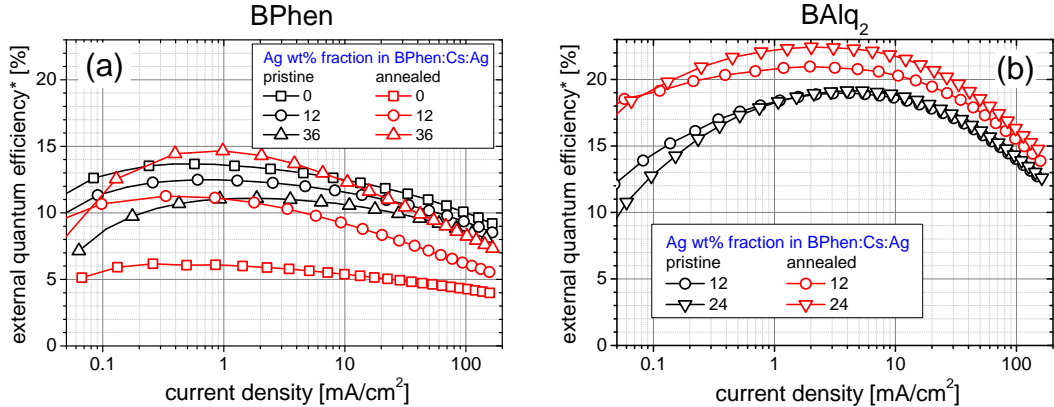
Figure 5.17: External quantum efficiency of inverted top-emitting OLEDs comprising either BPhen (a) or BAlq$_2$ (b) as hole blocking layer material. (*) The EQE is calculated assuming a Lambertian emission characteristic.

Looking more closely to the I-V and the luminance characteristics in Figure 5.16 and considering the different annealing durations for both samples, one finds an opposite trend to the devices with BPhen as HBL. In the BAlq$_2$ based OLED, the I-V characteristic above 4 V is almost independent from the sample and therefore from the annealing time. Below 4 V, there is a distinct difference between 20 min and 30 min annealing which is also reflected in the luminance curves in Figure 5.16(b). Thus, a multi-step mechanism can be assumed when annealing these OLED devices. One process is dominating the upper current regime which is faster and finished within 20 min at 75 °C. This first mechanism realizes the improvement in samples comprising both HBL materials. The other one seems to be dominant at the low voltage part of the I-V and needs at least 20-30 min to show an effect. If both processes take place, an altering in device performance can be expected. In Section 5.3.2 a separation of these effects is tried to be carried out.

The external quantum efficiencies of the n-i-p OLEDs comparing BAlq$_2$ and BPhen are plotted in Figure 5.17. They show improved performance in case of BAlq$_2$ as well as for one sample in case of BPhen after annealing. However, as the EQE increases from 11% to almost 15% (BPhen) and from 19% to over 22% (BAlq$_2$), the charge balance must have improved. This change in charge carrier ratio is underlined by the slight shift of the maximum of the EQE curve to lower currents while the device optics remain unchanged. Furthermore, the combination of improved EQE and decreased driving voltages lead to a general increase of luminous efficacy. This is demonstrated in Figure 5.18 where only one OLED comprising BPhen as HBL shows a lower luminous efficacy after annealing.
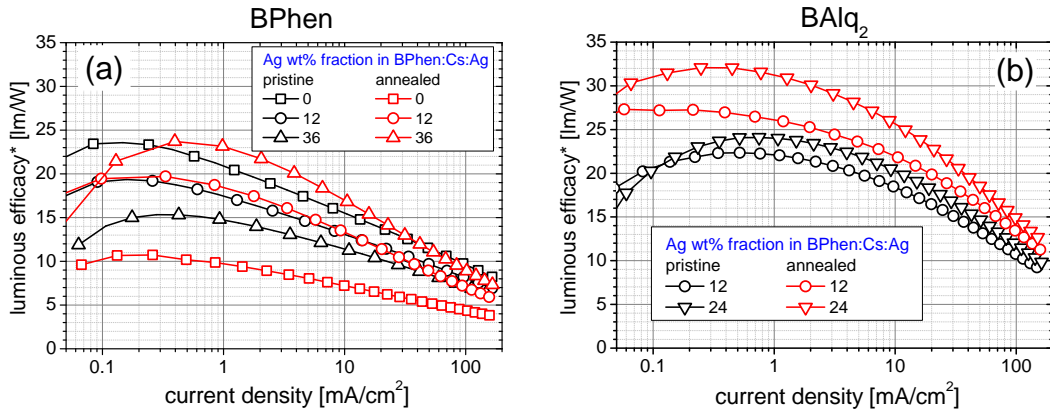
Figure 5.18: Luminous efficacy of inverted top-emitting OLEDs comprising either BPhen (a) or BAlq$_2$ (b) as hole blocking layer material. (*) The luminous efficacy is calculated assuming a Lambertian emission characteristic.

Unfortunately, a more pronounced roll-off is observed after annealing. This indicates increased exciton quenching and exciton annihilation processes at higher charge- and therefore exciton densities. This is valid if hole injection into the EBL and the EML is assumed to be improved and therefore the recombination zone is more concentrated at the EML-HBL interface. Additionally, annealing above the T_g of BPhen might lead to a diffusion of Cs dopants into the HBL and thus triplet-polaron-quenching can occur. In the case of BAlq$_2$, the roll-off does not suffer from the annealing process.

Finally, it is important to mention that Figure 5.17 contains EQE data with the assumption of Lambertian emission characteristics. Unfortunately, the real EQE is not available for these samples but does not give any further information here as it scales the absolute numbers by a constant factor. From optical considerations, a decrease by a factor of approximately 0.73 for BPhen and 0.8 for BAlq$_2$ should be considered.

In conclusion, the annealing effect does not depend on the cathode interface but it is rather sensitive to time and annealing temperature while experimental deviations cause different results as seen in the EQE curves for the samples containing BPhen as HBL. These deviations might originate from a different heat transport, temperature uncertainty etc. Nevertheless, the differences between p-i-n and n-i-p OLEDs can be eliminated by subsequent thermal annealing of the whole n-i-p OLED. Here we do not consider annealing effects in p-i-n devices but it is known that the I-V characteristics can improve there as well [228]. At this point, the HBL (BPhen or BAlq$_2$) and the ETL material system BPhen:Cs have been found to be responsible for one part of the performance deviations of the n-i-p OLED as they exhibit changes during annealing. Anyway, a second process which enhances hole injection and transport has to

be considered as well. An alternative experiment, using TPPhen:W$_2$(hpp)$_4$ as ETL incorporating an organo-metallic IL has been done as well. The results are summarized in Appendix B.
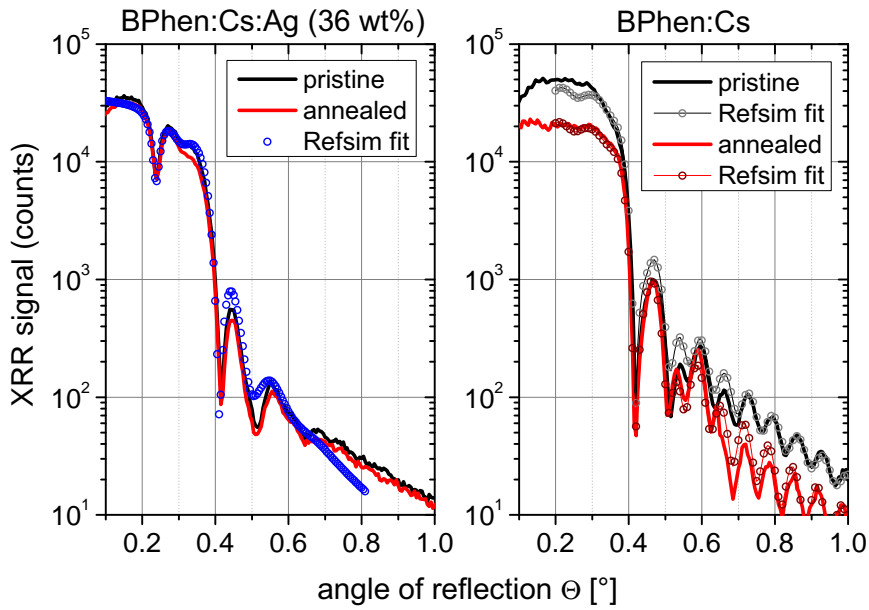
The BPhen:Cs:Ag interlayer

Figure 5.19: *X-ray reflectometry data of 30 nm BPhen:Cs:Ag or BPhen:Cs films that are deposited on 20 nm Ag covered glass substrate. The obtained parameters from a fitting procedure are summarized in Table 5.5.*

Again, there is no experimental proof that the cathode material Ag, doped into BPhen:Cs has an influence on the electrical properties of inverted OLED devices. The injection is efficient enough so that metal penetration is a minor effect when comparing inverted to non-inverted structures. When annealing these OLEDs, the effect on the BPhen:Cs:Ag mixed film could be interesting. Therefore, 30 nm films of BPhen:Cs and BPhen:Cs:Ag (24wt%) have been investigated using X-ray reflectometry (XRR). The recorded spectra are shown in Figure 5.19, comparing the influence of thermal annealing for 30 min at 75 °C on the morphology of the films. Interestingly, only BPhen:Cs films show distinct changes after thermal treatment, while the heavily Ag-doped sample is not affected by the annealing process.
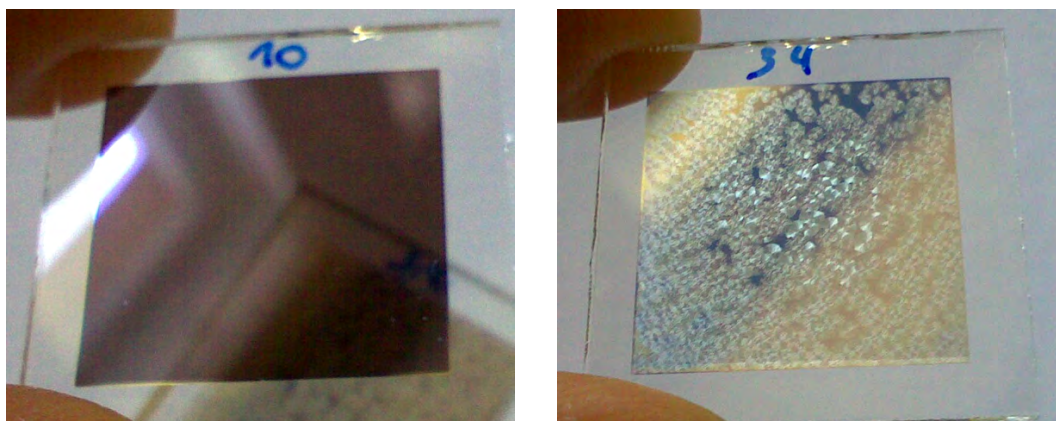
124

Figure 5.20: *Appearance of 30 nm films of BPhen:Cs:Ag (24wt%) (left) and BPhen:Cs (right) after annealing at 75 °C for 30 min plus 3 days in atmosphere. The organic films are deposited on 20 nm Ag on a glass substrate.*

Table 5.5: *Material and layer parameters that were obtained from the fit of the XRR data, shown in Figure 5.19. Both samples were annealed at 75 °C for 30 min. Sample 1 did not show any morphological changes.*

Layer	thickness (nm)	roughness (nm)	density (g/cm^3)
sample 1 (no change)			
BPhen:Cs:Ag (36 wt%)	31.1	3.55	2.7
Ag	23.3	3.3	9.5
SiO$_2$ (substrate)		0.75	2.43
sample 2 (pristine)			
BPhen:Cs	34.3	1.0	1.24
Ag	21.4	3.05	9.5
SiO$_2$ (substrate)		0.45	2.35
sample 2 (annealed)			
BPhen:Cs	35.2	0.47	1.17
Ag	21.5	2.79	9.4
SiO$_2$ (substrate)		0.55	2.35

A fit of the data is carried out, using the software Refsim by Bruker AXS. The missing oscillations in the spectra of BPhen:Cs:Ag indicate a pronounced roughness which is validated by the simulation and might be due to Ag cluster formation comparable to the growth of single Ag films (compare Section 2.2.5). The full entity of fitted parameters are listed in Table 5.5. The film thicknesses obtained from the fit reproduce the nominal values, except we find a trend of slightly too thick ETL layers. The key information here is the density

and the roughness of the films. While BPhen:Cs:Ag is stable against thermal treatment, BPhen:Cs shows a smoothed surface, an increased thickness and therefore a slightly decreased density. Thus, a rearrangement of molecules is very likely in this case. Finally, it has to be noted that BPhen:Cs films change their appearance and their morphology even at room temperature within a period of a few days or weeks. Figure 5.20 shows the two kinds of samples after annealing and 3 days in atmosphere. The BPhen:Cs film clearly exhibits a completely polycrystalline surface while BPhen:Cs:Ag looks like in pristine condition as homogeneous and strongly absorbing film.

5.3.1 Time and temperature dependence

In the previous section, a multi-step process during annealing of inverted OLED devices was found to be most likely. In the following, the annealing effect is systematically investigated. First, the temperature dependent time development of the current-voltage characteristic of an inverted OLED is determined. It is measured on four equivalent inverted OLED samples having slight structural changes (only of optical importance) but with identical electrical behavior. These devices are annealed at 50, 60, 70 and 80 °C, respectively for up to 40 min and were measured every 5 - 10 min. The device structures are (thickness in nm):

Al(50) / Ag(40) / BPhen:Cs:Ag (12wt%)(5) / BPhen:Cs(60) / BAlq$_2$(10) / NPB:Ir(MDQ)$_2$(acac)(10wt%)(20) / NPB(10) / MeO-TPD:F6TCNNQ (2wt%)(48-50) / Al(1) / Ag(18-22) / NPB(85)

The time dependent change of current density ($j_{annealed}/j_{pristine}$) at different temperatures is depicted in Figure 5.21. It shows a small enhancement (1.5x) at lower temperatures $\leq$60 °C and a strong increase above 70 °C. Further, at 70 °C the I-V curve saturates after approximately 40 min with a maximum increase in current of 4.5 times. The currents at voltages below 2.3 V (leakage currents) are almost unchanged for every device (ratio $\approx$ 1), except the samples which were annealed at 70 °C. There, an increasing leakage current of up to 8 times is observed. In the working regime above 2.3 V, the ratio of current densities exhibits a fixed maximum at 3.7 V for all temperatures except 80 °C. In this case, the enhancement in the I-V proceeds very fast and shows a completely different dependence from the voltage, indicated by a shift of the maximum to lower voltages. After 15 min annealing at 80 °C, the current decreases below the values of the pristine sample. The enhancement factor increasingly drops below 1 at voltages >3 V.
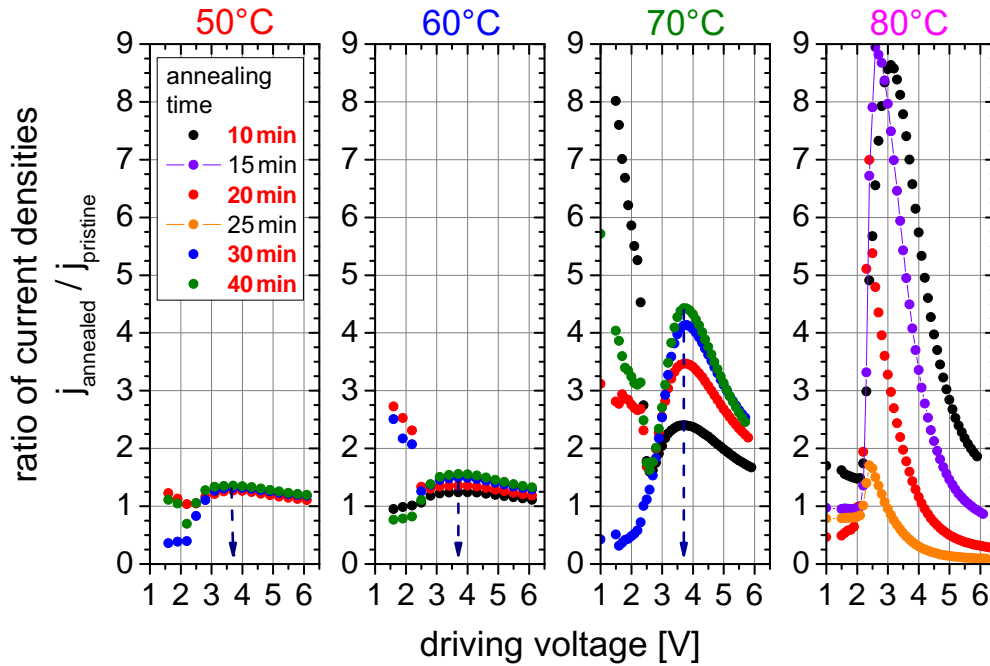
Figure 5.21: Ratio of the current densities $j_{annealed}$ and $j_{pristine}$ depending on the driving voltage after annealing of the complete inverted OLED at 50 °C, 60 °C, 70 °C and 80 °C for the duration of 10 to 40 min. The peaks at 3.7 V are indicated by arrows.

We can draw the following conclusions from these results:

1. Because of the stable peak at 3.7 V (0.925 MV/cm for 40 nm intrinsic layer thickness), we can conclude that the processes within the investigated OLEDs during thermal treatment are comparable and time and temperature are coupled in a reverse manner. The higher the temperature, the faster the process.

2. The used temperature addresses only these materials which have a correspondingly low glass transition temperature. For 50, 60 and 70 °C, the current at a given voltage increases in a comparable way with a temperature dependent quantity. At 80 °C another mechanism is effective which changes the voltage dependent enhancement characteristics. A factor below 1 represents a decreased current density after annealing and therefore less efficient charge transport.

Another important aspect is the conduction of heat in organic material. For example, the thermal conductivity of Alq$_3$ is determined to be 0.1 W/(m·K)
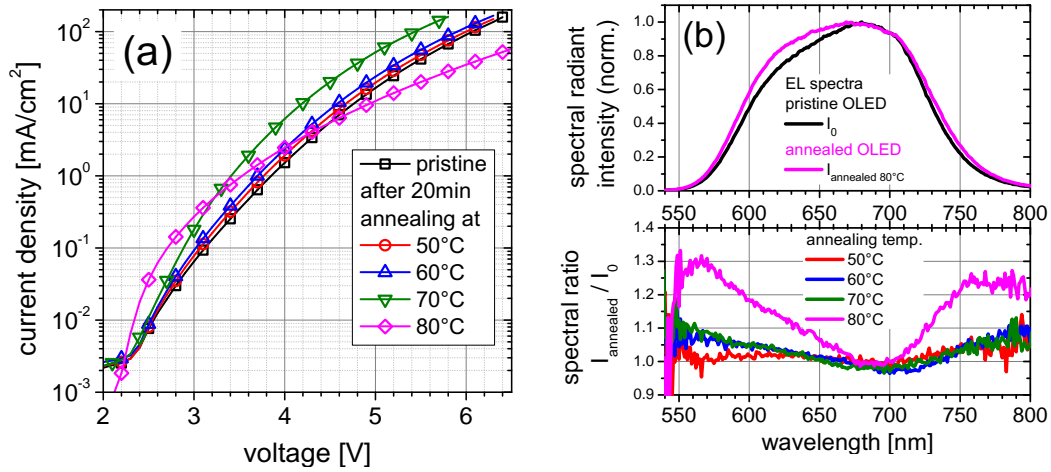
Figure 5.22: Left: Temperature dependent current-voltage characteristic of inverted OLEDs (a) having almost identical layer sequence, annealed at 50 ℃, 60 ℃, 70 ℃ and 80 ℃ for the duration of 20 min. A broadening of the emission spectrum is observed for the sample which has been annealed at 80℃ (b). The spectral change is demonstrated by the ratio $I_{annealed}/I_0$ of pristine and heated OLED samples for all four temperatures.

at room temperature [229]. For comparison, wood and typical plastics like polyethylene have a comparably low thermal conductivity while usual sodalime glass shows up to 1 and metals several hundreds of W/(m·K) [230]. This implies that layers in proximity to the substrate might react first while effects in the outer layers should start later. With respect to the different glass transition temperatures of the incorporated materials, it seems that several processes in certain layers can happen simultaneously.

To have a closer look at these effects, Figure 5.22 shows the I-V characteristics after an annealing period of 20 min. One can clearly distinguish the temperature range below 70 ℃, where almost no changes occur, from that above 70 ℃, where the current for a given voltage starts to increase. In case of 80 ℃, the low voltage regime exhibits the highest currents while the high voltage regime suggests a device degradation, indicated by a decreased current compared to the pristine sample. The EL emission undergoes negligible changes below 80 ℃ but exhibits a broadened and changed spectrum for 80 ℃. Here, the semitransparent top contact is most likely damaged by the underlying layers and structural changes occur which can directly be validated in an altering of the optical response of the cavity.

Further investigations of the annealing process are done by time dependent measurements of one single OLED sample. A fixed temperature of 75 ℃ has
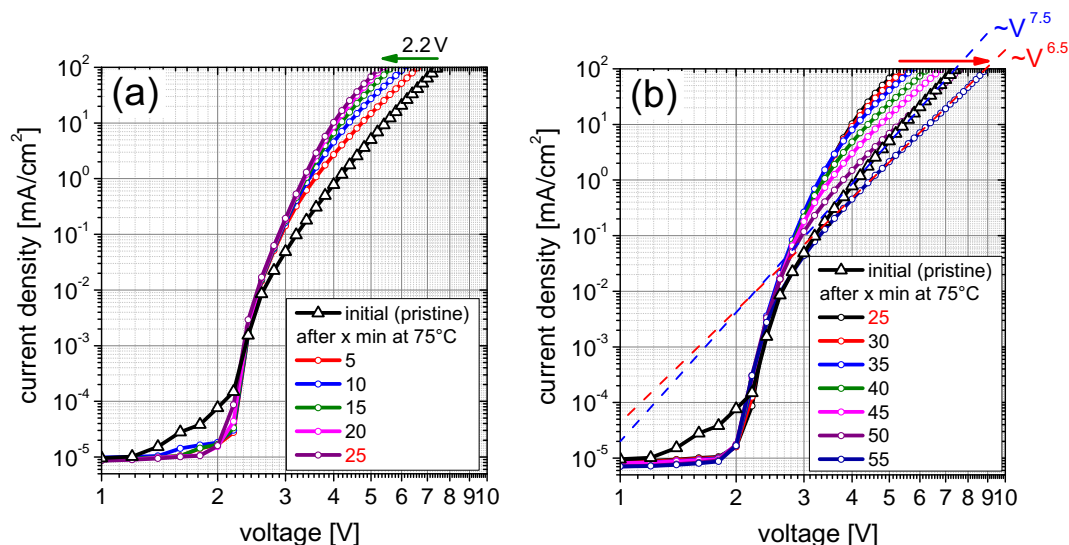
Figure 5.23: *Time dependent current-voltage characteristics of an OLED device until 25 min duration of thermal treatment (a) showing a constant decrease of driving voltage. After 25 min the I-V shows an opposite trend which is due to decomposition of organic material (b). The change of slope after 55 min compared to the pristine condition is indicated.*

been used to induce every possible mechanism in combination with a reasonable low heating time. The changes of the I-V characteristic should be slow enough to be recorded and should undergo every possible effect that is expected. During the experiment, the current-voltage characteristic and impedance spectra are recorded every 5 min. The OLED structure is (thickness in nm):

Al(50) / Ag(40) / BPhen:Cs(65) / BAlq$_2$(10) / NPB:Ir(MDQ)$_2$ (acac) (10wt%) (20) / NPB (10) / MeO-TPD:F6TCNNQ (2wt%)(45) / Al(1) / Ag(20) / NPB(85)

The resulting development of the I-V curve is shown in Figure 5.23 where several competing processes can be observed. First, an increase in current at a given voltage takes place until 25 min of annealing (see Figure 5.23(a)) determined by the temporal evolution of the processes that increase the charge transport, i.e. changes of molecular orientation, morphology, doping profile or doping efficiency that alter the mobility or/and reduce energetic barriers at interfaces. This increase is depending on the voltage and on the annealing time. At $100 \, \text{mA/cm}^2$, a very strong voltage reduction by $2.2 \, \text{V}$ is observed.

In Figure 5.24, the ratio of the current densities (pristine/annealed) is shown after each annealing step. As the increase in current density depends on the voltage, the slope of the I-V changes with time.
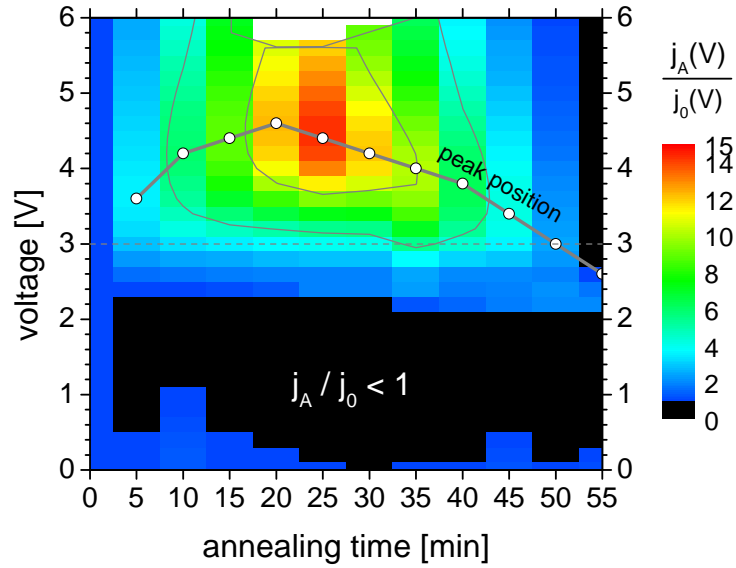
Figure 5.24: *Temporal evolution of the current density, depending on the driving voltage within the first 55 min at constant annealing temperature of 75 °C. The circles indicate the voltages, where the current exhibits the peak enhancement after a certain annealing time.*

The region below 2 V belongs to the leakage current regime where the current drops slightly in the first minutes but stays constant afterwards. Between 2 and 2.5 V, no significant change occurs, but at 3 V one can observe an increase up to 5 times in current density (see dashed line in Figure 5.24 at 3 V). This process reaches its maximum after 35 min, which seems to be caused by a second mechanism in this experiment.

Compared to the data in Figure 5.21, the peak enhancement at 3.7 V is already reached after 5 min. Continuously, the currents increase up to an enhancement factor of 15 at 4.4 V and 25 min. After that, the charge transport degrades, dominating the high voltage regime, which leads to a back-shift of the current enhancement factor towards lower voltages. This leads to I-V curves with a decreased slope after an annealing time of more than 25 min (Figure 5.23(b)). This decrease of the overall enhancement factor can be explained by a material decomposition of a certain or some parts of the layer structure which leads to less efficient charge transport. Such process counteracts the initial enhancement and thus increases with time as more and more molecules are damaged [231].

As the corresponding transport materials have different glass transition temperatures, the effect on each charge carrier type should belong to different temperatures or amounts of heat if the annealing temperature is above both T_g which means the effects belong to different annealing times.
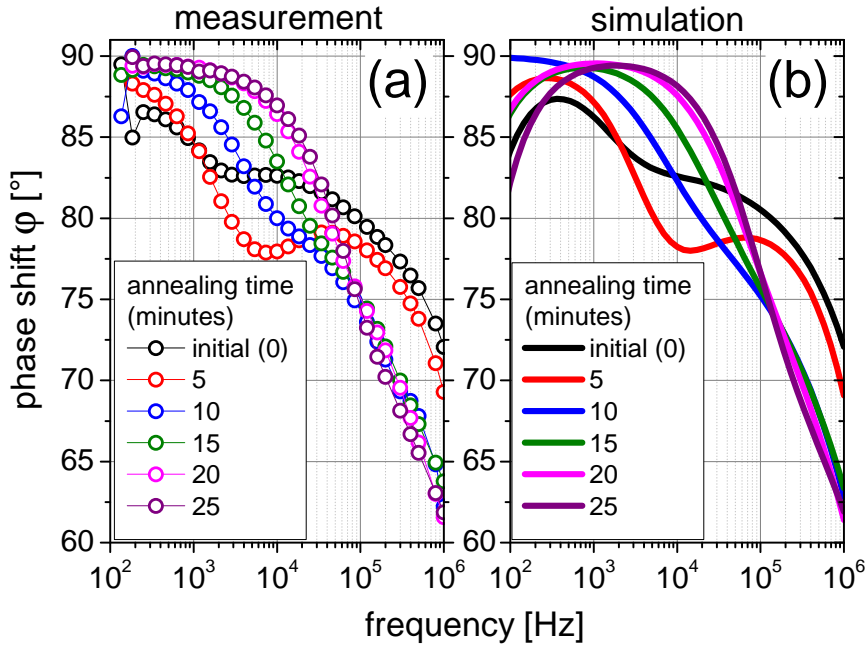
Figure 5.25: Bode-plot, comparing the temporal evolution of the phase φ in the experiment (a) with the simulated one (b) using the equivalent circuit shown in the inset of Figure 5.26.

From the symmetry of the temporal behavior of the annealing effect at 75 °C and with respect to the low T_g of MeO-TPD (55 °C) it is most likely that the described processes are dominated by the HTL. In the first minutes, the layer properties change and enable a more efficient charge transport accompanied with a lowering in driving voltage. Passing the maximum current density at a given voltage after 25 - 35 min, most probably the same layer is changed or damaged, leading to a considerable reduction of the charge transport.

Another interesting issue has to be pointed out here. If one roughly compares the I-V of pristine samples of the last two experiments (Figures 5.22(a) and 5.23(a)), one finds 6 V and over 7 V at $100 \, \text{mA/cm}^2$, respectively. This fact might be explained by the change in doping ratio of the MeO-TPD. Initially 4wt% were used while now only 2wt% have been utilized. In non-inverted OLEDs such difference has no dramatic change to our knowledge but as inverted devices are very sensitive to such changes, this might play an important role. Further, this would be consistent with the assumption that the p-doped MeO-TPD layer is one of the bottle necks in inverted devices.

The evolution of the impedance with time of the sample is used to get a more detailed understanding on the processes discussed above. Figure 5.25 shows the phase shift φ as a function of the frequency in a Bode-plot. A fast initial
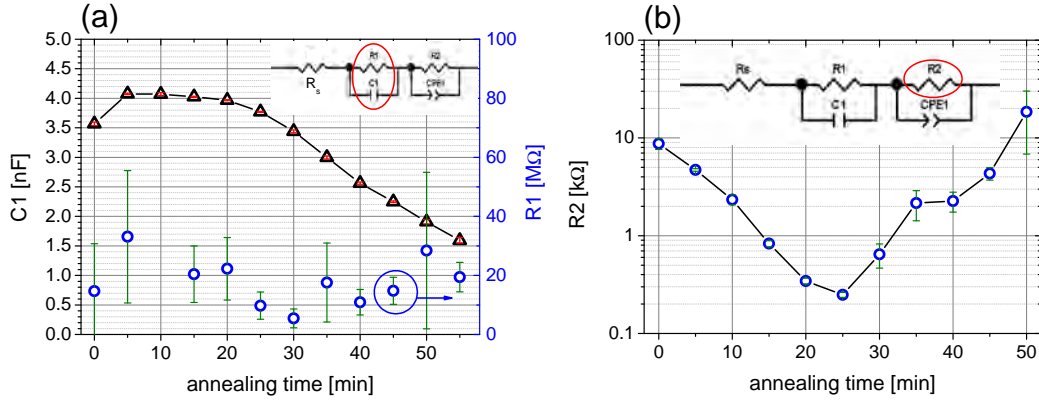
Figure 5.26: *Parameters of the equivalent circuit (inset) that describes the measured impedance data at 0 V during an annealing process. C_1 and R_1 can be assigned to the intrinsic layers while R_2 is assumed to represent a part of the Meo-TPD layer. The series resistance R_s is in the range of 10-20 Ω.*

change of the impedance within the first 10 min is observed. The shift of the dip in the phase towards higher frequencies can be explained by a decreasing resistance [232] inside the layer stack and can be comprehended with the model calculations in Figure 3.3 on page 56.

An appropriate explanation is developed by using an equivalent circuit model to describe the impedance numerically. The circuit and the temporal development during the annealing process are depicted in Figure 5.26. Considering the findings from the investigation of the I-V behavior during thermal annealing, a correlation of parts of the OLED stack to the parts of the equivalent circuit is assumed. In terms of impedance measurements, it is reasonable that the intrinsic layers between the highly conductive transport layers represent a capacitive part at 0 V offset bias. We identify the EML and blocker layers by a single RC circuit. The series resistances from the electrodes and the transport layers are combined in R_s. To fit the experimental data and especially to accommodate the frequency dependent phase shift, another circuit has to be added. A second RC circuit with a constant phase element (CPE) is found to be appropriate which represents a non-ideal capacitor. It accounts for inhomogeneities of the capacitor surfaces, e.g. roughness or slow capture and release processes like charge carrier trapping. If the simulated phase φ is compared to the measured one, we find very good accordance in Figure 5.25. If we now examine the obtained parameters, a fast increase of C_1 within the first 5 minutes is found. Being constant until 20 min annealing time, a linear decrease follows as depicted in Figure 5.26(a). If C_1 is interpreted as geometric capacitance[6] via Equation 3.13, a total intrinsic thickness of 50 nm

---

[6]dielectric constant assumed to equal $\varepsilon = 3$

in the pristine sample is obtained. This thickness decreases to a stable value of 45 nm (25 min) which increases again steadily with time until 113 nm at 55 min. The nominal thickness of the intrinsic layers in total is 40 nm which means that some additional effect is observed as thickness errors above 20% are very unlikely. The uncertainty of the dielectric function ε_r is one possible explanation. An inhomogeneous doping efficiency inside the MeO-TPD bulk or at the MeO-TPD - NPB interface can further be of importance. Annealing leads to diffusion of dopants towards the NPB layer. After that, the dopants and/or the matrix material is damaged and the conductivity of the doped MeO-TPD decreases completely. The resistance of the intrinsics R_1 can be assumed to stay constant at 15 MΩ which is reasonable at a bias of 0 V. The reason is the built-in voltage of about 2.3 V that has to be applied before both kinds of charge carriers can enter the EML. If we assume the second RC circuit to represent a part of the MeO-TPD layer the picture becomes consistent. During the annealing process, its resistance R_2 drops from (8.7 ± 1.1) kΩ to 249 ± 15 Ω (factor 35) within the first 25 min (see Figure 5.26(b)). Afterwards, the reverse process leads to the increase of R_2 above the initial values. This behavior can explain the temporal behavior of the I-V and its shape if we consider the influences that must be related to the hole injection and hole transport.

5.3.2 Annealing effect on hole and electron transport

Electron transport

To distinguish between possible mechanisms of the found processes so far, single carrier devices are investigated in the following. Advantageously, they do not exhibit a built-in voltage, i.e they are in flat band condition at 0 V and charge carriers are injected immediately when applying a voltage. This is only true if there is no injection barrier which is most likely as doped transport layers are used. The injection has then to be realized at the doped layer - intrinsic layer interface.

At first, injection, transport, and the influence of annealing is discussed for electrons. Therefore, n-i-n devices with the layer structure, depicted in Figure 5.27(a), are fabricated.
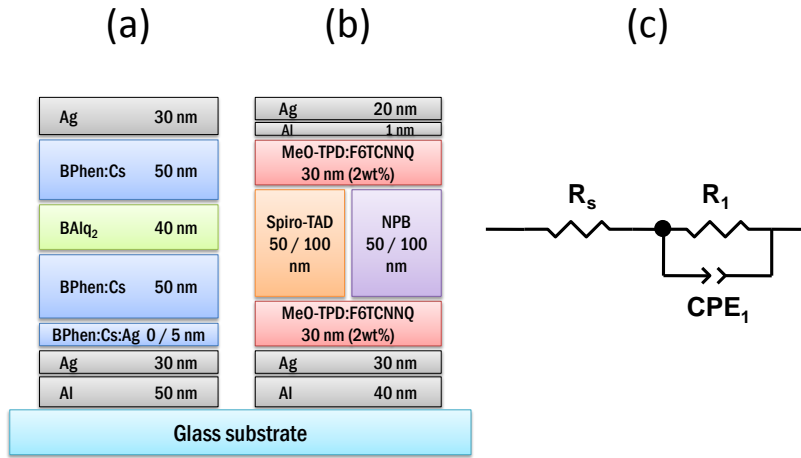
Figure 5.27: *Layer structures of single carrier devices for electrons (a), for holes (b) and the used equivalent circuit (c) to model the impedance data.*
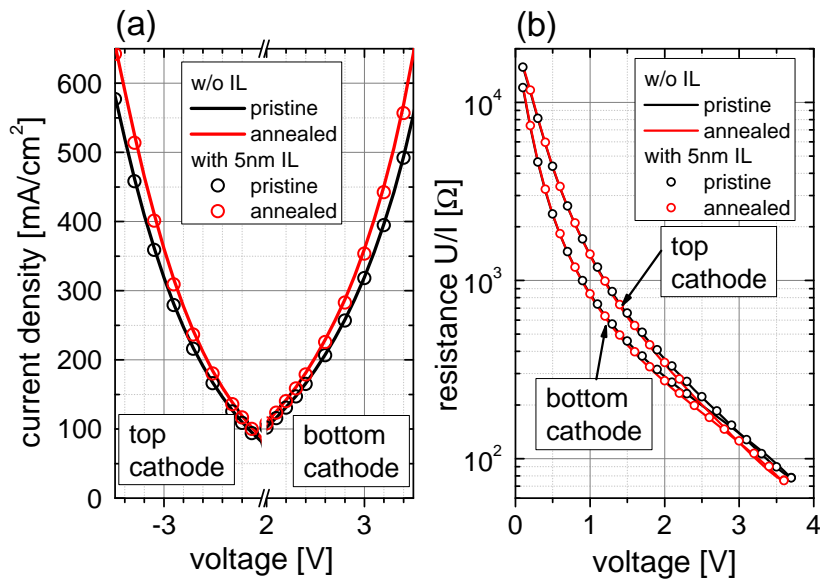
Figure 5.28: *Current-voltage characteristics of n-i-n single carrier devices. Comparison between pristine and annealed (30 min at 75 °C) samples.*

We examine the electrical behavior of n-i-n single carrier devices including a 5 nm BPhen:Cs:Ag interlayer (IL) with an Ag concentration of 24 wt%. None of the previous experiments could show an influence of such IL on the OLED performance, which will finally be validated here. As depicted in Figure 5.28(a), the injection of electrons is not influenced by the IL. The I-V characteristics of

the n-i-n devices show an almost symmetric behavior above 2 V. In contrast, below 2 V forward and reverse currents deviate from each other. Interestingly, if electrons are injected from the bottom contact (as in an inverted OLED), the resistance in the region 0.5 - 1 V is half the resistance than at reverse bias (see Figure 5.28(b)). Thus, we observe a dependence of bias polarity on the current density below 2 V which can be approximated by electric fields below 0.5 MV$/$cm across the intrinsic BAlq$_2$ layer. Such asymmetry can only be related to the sample geometry and the deposition sequence, leading to slightly different charge transport across interfaces or inhomogeneous transport layer properties. At voltages above 2 V, these effects become negligible which results in a very symmetric I-V characteristic.

Further thermal annealing for 30 min at 75 °C leads to an unchanged I-V at low voltages and a slight but noticeable reduction of voltages above 100 mA/cm^2 or 2 V, respectively. This is observed at both device polarities. We observe a splitting in the I-V characteristics, depending on the polarity at low bias which represents inhomogeneous sample properties like interfacial traps or energy barriers resulting from the deposition process in cooperation with the low T$_g$=62 °C of BPhen. At higher voltages, the only splitting can be observed between pristine and annealed sample condition. In this case, the charge carrier concentration is already high, even in the bulk of BAlq$_2$. A very small reduction of the resistance after annealing is observed, coinciding with the findings in complete OLED devices (compare Figure 5.16).

A more detailed analysis is done with the help of impedance spectroscopy. In general, the impedance of n-i-n or p-i-p devices can be described by assuming a simple RC equivalent circuit. Nevertheless, we replace the ideal capacitor by a constant phase element (CPE) as the fit gets more precise. The complete equivalent circuit is shown in Figure 5.27(c) and the frequency and voltage dependent impedance data are fitted with the parameters shown in Figure 5.29. First of all, it is shown that the series resistance R$_s$ represents not only the resistance of the cables or electrodes but comes to a large extend from the organic charge transport layers.

For example, assuming the conductivity of $\sigma = 5 \times 10^{-6}$ S$/$cm, mentioned in Section 2.1.4 on page 23 for doped MeO-TPD which should be equivalent to the one of doped BPhen, we can estimate the resistance of a 30 - 60 nm thick transport layer used in the devices (area A = 0.0676 cm^2). The resulting $R = 1/\sigma \cdot \frac{d}{A} = 9 - 19$ Ω. The fitted values for R$_s$ in Figure 5.29(a) agree quite well with that approximation if we account for a slightly lower conductivity of BPhen:Cs and with respect to some additional resistance from the electrical contacts.
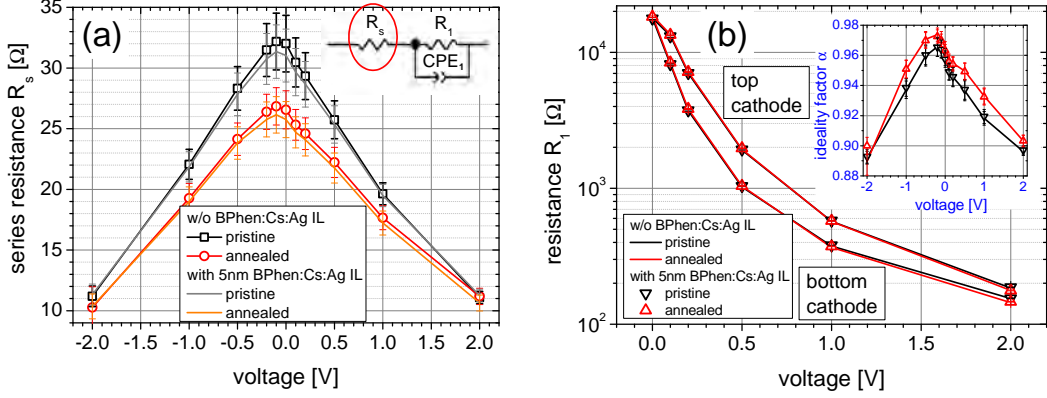
135

Figure 5.29: *Calculated series resistance R_s and its change after thermal annealing (30 min at 75 ℃) of the n-i-n device depending on the driving voltage (a). The measured impedance is fitted with the equivalent circuit depicted in the inset. Error bars mark the uncertainty of the fit results. The resistance R_1 in graph (b), obtained from fitting with the same equivalent circuit is in accordance to the calculated resistance from the current-voltage characteristics in Figure 5.28. The CPE parameter α accounts for the sample asymmetry which must be due to interface properties between the ETL and the intrinsic layer or due to the ETL properties themselves. The bulk resistance of the intrinsic $BAlq_2$ must not depend on the device polarity.*

From Figure 5.29(a), one finds almost symmetric properties of the contacts and the doped layers, represented by R_s. Thermal annealing slightly influences the transport via morphological changes because R_s is slightly decreased. For an elevated charge carrier concentration at higher voltages this effect vanishes (e.g. at 2 V in Figure 5.29(a)). The increasing carrier density is also the reason for the decrease of R_s with raising voltage. For sake of completeness, the data for samples that include a BPhen:Cs:Ag interlayer is shown in Figure 5.29(a) as well. If there is an effect from this BPhen:Cs:Ag layer, then it is very small and below the measurement accuracy or less than the fitting errors.

The parameters of the R-CPE circuit are shown in Figure 5.29(b). The obtained R_1 mirrors the asymmetry of the I-V characteristic which means that the transport over the intrinsic layer depends on the bias polarity. Further, R_1 is not changed during the annealing except of small changes in the higher voltage regime as seen in the I-V curves. The exponent α in the CPE (ideality factor) ranges from 0.9 to 0.96 but its asymmetric behavior denotes the inhomogeneity of the organic-organic interfaces or their proximity. This behavior could be explained if we assume non-abrupt interfaces and a region of exponential change in conductivity [233]. As the current increases, α decreases which should be an effect of increased carrier density and a less capacitive
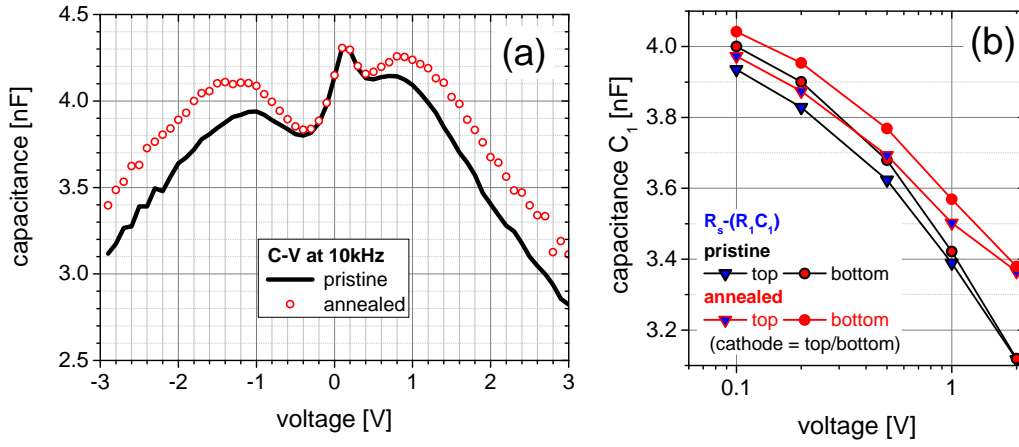
Figure 5.30: Capacitance-voltage data of n-i-n device (a). A geometrical capacitance of 4.2 nF corresponds to 42.8 nm electrode distance which fits quite well to the BAlq$_2$ thickness. An additional fit of the measured impedance using a capacitor instead of a CPE leads to the capacitance C_1 as a function of driving voltage (b).

behavior ($\alpha = 0$ for ideal resistor, $\alpha = 1$ for ideal capacitor). Unfortunately, no information about the annealing process can be deduced here because its influence dominates the I-V above 2 V.

These observations can be underlined directly by capacitance-voltage (C-V) measurement data, shown in Figure 5.30(a). The capacitance C at 0 V equals the geometrical capacitance of the intrinsic BAlq$_2$ layer. The low change of the capacity around the initial 4 nF in the range of -2 to +2 V indicates that the charge carrier transport is still dominated by the highly resistive (compared to the ETL) intrinsic layer and the organic-organic interfaces. Interestingly, the C-V curve shows an asymmetric behavior with a slight increase of C within ± 1 V in forward as well as in reverse polarity. This is an indication for asymmetric charge accumulation at the BAlq$_2$ - BPhen:Cs interfaces and is in accordance with the slightly asymmetric ideality factor, depicted in Figure 5.29(b).

Comparing the C-V spectra of annealed and pristine sample condition, an increase of C above ± 1 V is observable and the annealing effect is not depending on the polarity. This is a validation of the assumption that only BPhen:Cs with its low glass transition is assumed to show changes during the thermal treatment.

A second fit of the impedance data, assuming $\alpha = 1$ (ideal capacitor), yields reasonable fit results with slightly higher errors. These results for an ideal capacitor C_1 (instead of a CPE) are shown in Figure 5.30(b). The geometrical

capacitance of about $4\,\mathrm{nF}$ at $0\,\mathrm{V}$ can directly be validated. At low bias, only marginal changes between the pristine and the annealed state are visible. According to Figure 5.30(a), the differences get pronounced above $\pm 1\,\mathrm{V}$ where an increase of $\mathrm{C_1}$ is observed.

In conclusion, the electron transport in n-i-n structured single-carrier devices comprising $\mathrm{BAlq_2}$ is only polarity dependent at low voltages and originates from asymmetric interfacial energetics between $\mathrm{BAlq_2}$ and BPhen:Cs. Accumulated charge carriers at the interface or the presence of interfacial trap states in $\mathrm{BAlq_2}$ [225] are most likely. Thermal annealing is found to slightly influence the transport in these n-i-n devices. The reason is the low glass transition temperature of BPhen:Cs ($62\,°\mathrm{C}$) because after annealing, the device characteristics only change for elevated voltages when the $\mathrm{BAlq_2}$ layer has a similar low resistance compared to the BPhen:Cs layers. Nevertheless, the electron injection and transport is found to be relatively stable against elevated temperatures ($75\,°\mathrm{C}$) in n-i-n devices comprising $\mathrm{BAlq_2}$ as intrinsic material.

HOLE TRANSPORT

In a comparable way, the hole injection in n-i-p layered OLEDs can be studied by p-i-p single carrier devices. As intrinsics, the blocker materials NPB and Spiro-TPD are used, respectively. The device structure is depicted in Figure 5.27(b). The results of current-voltage measurements are shown in Figure 5.31(a). From there, an asymmetric I-V characteristic is observable after preparation. A thermal annealing process, lasting 20 minutes at $75\,°\mathrm{C}$ leads to a strong reduction of the resistance in the p-i-p devices whereas the effect of this process is also depending on the polarity. If holes are injected from the bottom contact like in p-i-n OLEDs, the effect of annealing is less pronounced than in the reverse. The reduction in voltage at $100\,\mathrm{mA/cm^2}$ is 0.7 - 0.8 V for bottom and 1.4 - 1.6 V for top injection and depends on the intrinsic material. This is observed for $100\,\mathrm{nm}$ of intrinsic NPB and Spiro-TAD, respectively. Further, comparing the absolute currents of Spiro-TAD and NPB based devices the trend is consistent with the findings in Section 5.2, where a more efficient injection with Spiro-TAD is observed compared to NPB acting as EBL.

When calculating the ratio of current density before and after the annealing process as depicted in Figure 5.31(b), we find similar relationships for Spiro-TAD and NPB with pronounced maxima at symmetric electric fields (Spiro-TAD $\approx 0.3\,\mathrm{MV/cm}$ and NPB $\approx 0.5\,\mathrm{MV/cm}$) but different enhancement factors. For $100\,\mathrm{nm}$ intrinsic layer thickness, the resistance decreases by a factor of 3 - 5 in forward direction and is not exceeding a factor of 2.5 in reverse direction. Just like in n-i-n devices, an asymmetric formation of interfaces or different transport layer properties is very likely. The injection from
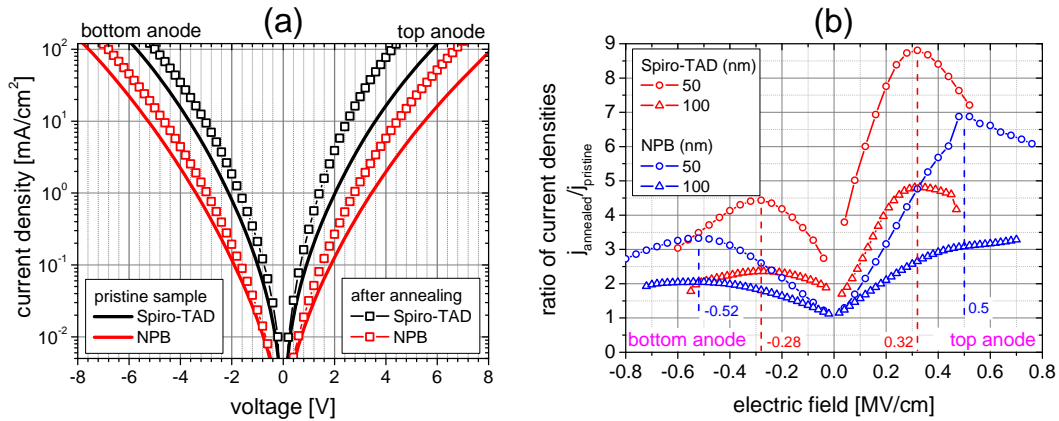
Figure 5.31: *Current-voltage characteristics of p-i-p layered single carrier devices with 100 nm intrinsic NPB and Spiro-TAD, respectively (a). The effect of thermal annealing for 21 min at 75 °C shows a strong increase in current density at a given external field (b). Due to the high conductivity of doped MeO-TPD, the field is assumed to drop completely across the intrinsic layer.*

the anode into the doped MeO-TPD might play a role as well but its impact is assumed to be much weaker as shown in Figure 5.9 on page 111.

Consequently, these results can explain the increased driving voltages of a fabricated n-i-p OLED compared to a p-i-n OLED. The asymmetry of the I-V and the polarity dependent improvement of the hole transport in p-i-p devices indicate different energy barriers at the interface of p-doped MeO-TPD and NPB/Spiro-TAD or in other words at the hole transport layer - electron blocking layer interface in the n-i-p OLED. The annealing process seems to equalize the p-i and i-p interfaces in terms of charge transport.

Impedance measurements again can give important insights to the responsible mechanisms. The frequency dependent capacitance (C-f) at 0 V is shown in Figure 5.32(a) for the NPB based p-i-p devices. An almost stable plateau in capacitance until $2 \cdot 10^4$ Hz is observable which denotes the geometrical capacitance of the intrinsic layer. In the pristine samples, the capacitance is lower than in annealed samples. This can be interpreted as a shrink of the capacitive region. It is observed for 50 and 100 nm intrinsic layer thickness (see Figure 5.32(a)), respectively.

At 10 kHz, C-V measurements are performed and the results are shown in Figure 5.32(b). In pristine condition, the samples show an increase of capacitance starting at 0.3 V in forward and -0.5 V at reverse bias for NPB. Here, the 1 nm Al interlayer at the anode interface might be the reason for this slight asymmetry.
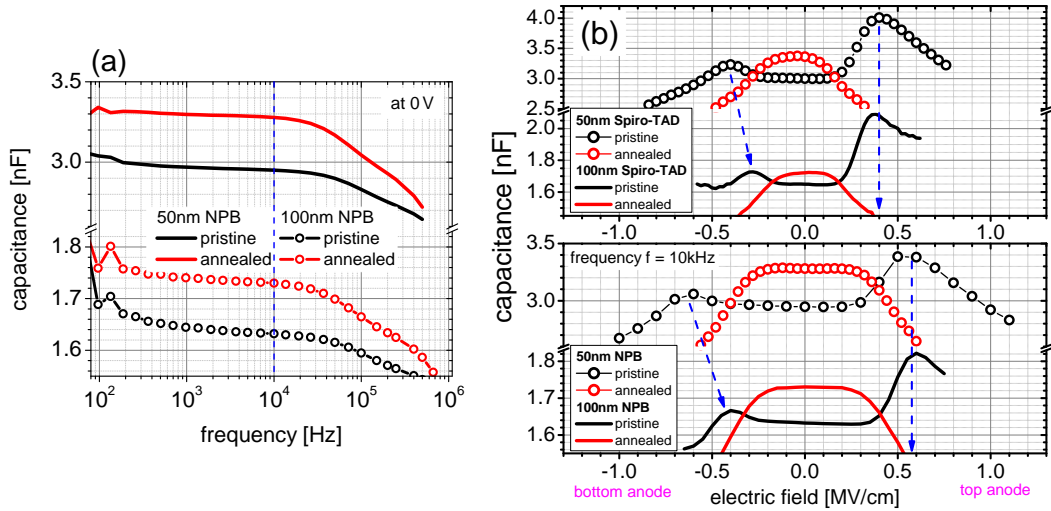
139

Figure 5.32: *Capacitance-frequency data of p-i-p devices with 50 and 100 nm NPB as intrinsic layer (a). The voltage dependent capacitance data at 10 kHz shows an increase at ±0.5 MV/ cm which confirms the presence of asymmetric transport for holes (b). This completely vanishes after a thermal annealing process at 75 ℃ for 21 min. The electric field is assumed to completely drop across the intrinsic layer.*

Nevertheless, with respect to the applied electric field we expect a relatively symmetric capacitive behavior which implies a charge accumulation at the energy barrier at the MeO-TPD - NPB interface. Interestingly, the capacitance maximum is higher at forward than at reverse bias which is in accordance to the I-V characteristics. This difference is independent from the intrinsic material as well as from its thickness. In reverse direction, a slight difference in the capacitance peak between 50 and 100 nm in observed (Figure 5.32)(b). At approximately 0.5 MV/ cm the capacitance decreases again in case of NPB, which accounts for an adequate number of charge carriers that pass the barrier and enter the intrinsic layer as the external field is high enough. The capacitive behavior turns into a conductive one as the amount of charge carriers increases inside the NPB layer. When the devices are annealed, we observe a completely vanishing of the capacitance peak. There seems to be no charge accumulation at 10 kHz anymore and charges can directly enter the NPB layer. Every observation described for NPB as intrinsic material is also valid for Spiro-TAD, except the fact that the capacitance reaches its maximum at ±0.4 V. Here, it seems that the electrical field strength of maximum charge carrier accumulation correlates to the electric field of the highest current enhancement during the thermal annealing process (compare Figure 5.31(b)).

Table 5.6: *Fit parameters of the impedance data, shown in Figure 5.32. The intrinsic layer thickness is 100 nm for all devices. In general, the fitting errors are below 5% except the cases where the errors are given explicitly. Positive voltage denotes the case where the top contact acts as anode which is equivalent to the polarity of an inverted OLED. The parameters with a * are that of annealed sample condition (75 °C, 21 min).*

intrinsic	voltage	R_s (Ω)	R_1 ($k\Omega$)	A_{CPE} (F)	α_{CPE}
STAD	-3 V	16.8 ± 1.3	2.705	$2.10 \cdot 10^{-9}$	0.980
STAD	0 V	19.9	405	$1.83 \cdot 10^{-9}$	0.990
STAD	+3 V	9.9 ± 4.5	2.357	$3.1 \pm 0.4 \cdot 10^{-9}$	**0.953**
STAD*	-3 V	24.2	1.249	$1.82 \cdot 10^{-9}$	0.990
STAD*	0 V	26.5	443	$1.93 \cdot 10^{-9}$	0.988
STAD*	+3 V	23.4	0.531	$1.82 \cdot 10^{-9}$	**0.990**
NPB	-7 V	17.3	0.388	$2.08 \cdot 10^{-9}$	0.981
NPB	-4 V	17.4	5.446	$1.95 \cdot 10^{-9}$	0.985
NPB	0 V	19.7	1710	$1.77 \cdot 10^{-9}$	0.992
NPB	+4 V	14.9 ± 2.0	6.364	$2.20 \cdot 10^{-9}$	0.976
NPB	+7 V	11.7 ± 1.5	0.533	$3.12 \cdot 10^{-9}$	0.950
NPB*	0 V	25.0 ± 1.5	1610	$1.90 \cdot 10^{-9}$	0.990

Additional C-f measurements are evaluated with the assumption of a R-CPE equivalent circuit as shown in Figure 5.27(c). The slightly decreasing capacitance with increasing frequency between 0.1 and 10 kHz in Figure 5.32(a) indicates for slight inhomogeneities in layer conductivity which is considered by using a constant phase element again. The fit parameters are summarized in Table 5.6.

The series resistance values R_s in Table 5.6 again fit very well to the approximated resistance of 10 - 20 Ω for a transport layer in the range of 30-60 nm thickness. The increase of R_s after thermal treatment is observed for both samples and represents a change in layer conductivity or less efficient doping effect in the bulk of the doped MeO-TPD. The resistance R_1 represents the intrinsic layer and shows a resistance of 0.4 - 1.7 MΩ at 0 V which drops below 1 kΩ as the charge carrier concentration is much higher for an elevated electrical field. The parameter A_{CPE} can be interpreted as effective capacitance and changes slightly by the annealing. However, the most interesting fact is the behavior of the ideality factor α_{CPE} which is, similar to n-i-n devices, almost 1. In contrast to n-i-n devices, we observe a change of α_{CPE} when the p-i-p samples that contain Spiro-TAD are annealed. The change is very weak in reverse direction (non-inverted case or bottom anode) but very pronounced at forward bias. This fact is another indication that we have an asymmetric bar-

rier formation at the HTL-intrinsic interface. The asymmetry of the ideality factor is obtained for Spiro-TAD and NPB while its change during annealing has unfortunately only been measured for Spiro-TAD. It is most likely that the effect applies for both materials in the same way and is related to the MeO-TPD:F6TCNNQ hole transport layer. A possible explanation could be a formation of a non or weakly doped region in the first few nm of the HTL which can be "repaired" by an annealing process above the glass transition temperature (55 °C for MeO-TPD) of the host material. A rearrangement of host molecules forming new matrix-dopant pairs or simply diffusion of dopants can lead to an increase of ionized dopant states yielding more free charge carriers.

Table 5.7: *Fit parameters of the impedance data, shown in Figure 5.32, assuming an ideality factor $\alpha = 1$. In this case, the CPE parameter A_{CPE} corresponds to the real capacitance C_1. If C_1 is interpreted as geometrical capacitance, Equation 3.13 on page 56 yields the corresponding thickness d_{geo} of the capacitive region. The errors of C_1 are below 2% and the * indicates the fit parameters of the annealed devices.*

thickness	material	C_1 (nF)	C^*_1 (nF)	d_{geo} (nm)	d^*_{geo} (nm)
50 nm	STAD	2.96	3.25	60.7	55.1
100 nm	STAD	1.64	1.69	109.5	106.3
50 nm	NPB	2.91	3.16	61.7	56.8
100 nm	NPB	1.62	1.71	110.8	105.0

As suggested in Table 5.6, the CPE shows nearly an ideal capacitive character and could be replaced be a capacitance C_1. Then, the fitted parameters for C_1 can be obtained from the same C-f data and are listed in Table 5.7. Coinciding with the findings above, it shows an increase of capacity for all samples. If C_1 is interpreted as geometrical capacitance, the determined distance d_{geo} reduces by approximately 5 nm, independently from the intrinsic material and its layer thickness.

To exclude any other effects due to the annealing step, n-i-p OLED samples, simplified n-i-p diodes and n-i-m diodes are fabricated. The sample structures are shown in Figure 5.33, labeled with the capital letters A, B and C on whose the text will refer to.

In Figure 5.34(a), I-V characteristics before and after thermal annealing are depicted. An increase in current for a given voltage is visible in the OLED A and the n-i-p device B, whereas the n-i-m structure C does not show any reaction on the thermal treatment. This proves MeO-TPD as the main reason for the annealing effect. Figure 5.34(b) shows the corresponding C-V data.
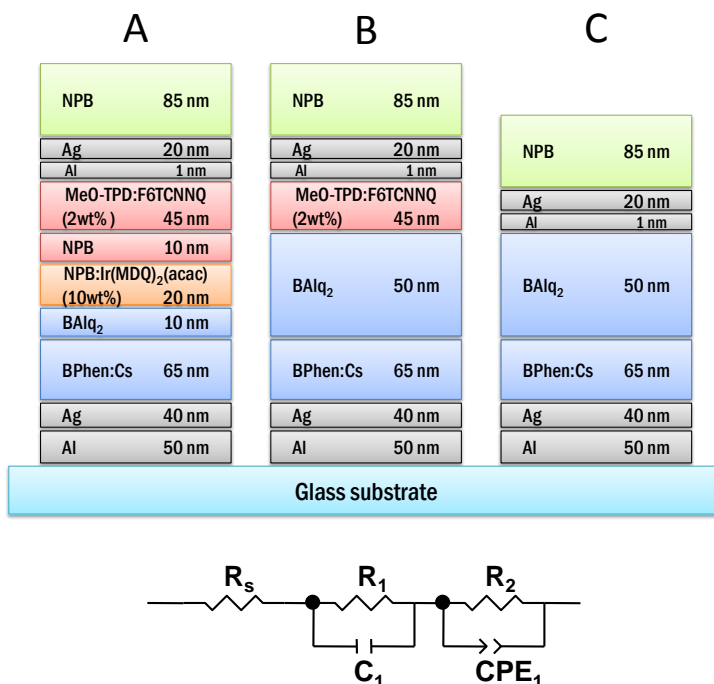
Figure 5.33: Layer structures of the investigated n-i-p OLED (A), n-i-p (B) and n-i-m diode (C) and the equivalent circuit which was used to model the impedance data.

The pristine samples A and B exhibit two distinct peaks corresponding to different charge accumulation processes. According to the results shown in Figure 5.30, we correlate the first one to electron injection via $BAlq_2$ as this peak appears at lower voltages (2.5 V). Further it also appears in the C-V spectrum of device C and therefore must be related to $BAlq_2$ which is stable against annealing. The second increase in capacitance at 4 - 5 V must be related to hole injection via the doped MeO-TPD. This feature is only visible in samples A and B and vanishes completely during annealing. The data of C-f measurements are fitted to the equivalent circuit shown in Figure 5.33. The voltage dependent results for R_1 and R_2 are shown in Figure 5.35. From these, a simple understanding of the working principle and transport mechanisms in the devices can be derived.

R_1 represents the resistance of the pure intrinsic layers in the devices. It stays constant until the built-in voltage is reached (flat-band condition) and injection of charge carriers starts. In the n-i-m structured device C, this condition is reached earlier and injection proceeds at much lower voltages which lets R_1 drop very rapidly. Further, the influence of an annealing step is visible as an increase of R_1 below 2.5 V where lateral conduction over the doped layers and almost no current through the device is assumed. Thus, R_1 accounts for leakage
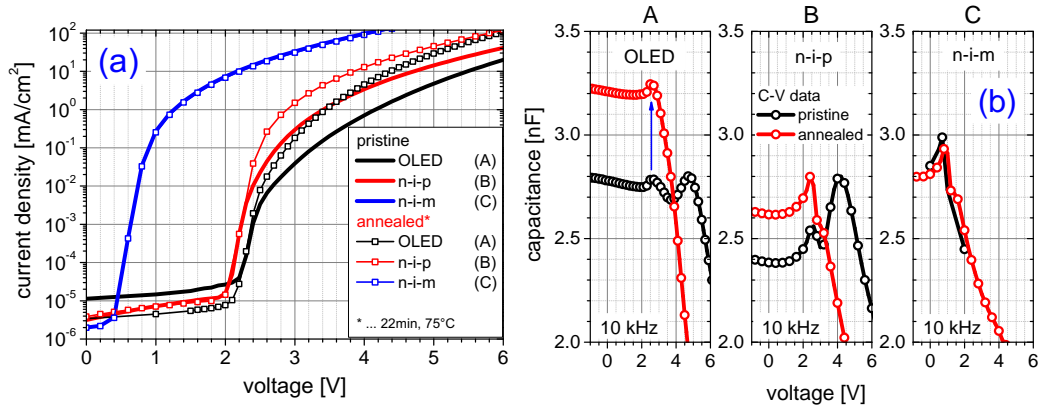
Figure 5.34: *Current-voltage characteristics of the OLED device A and the n-i-p diode B show an reduced driving voltage after thermal annealing, while the n-i-m diode C does not (a). Capacitance-voltage measurements at 10 kHz of the same samples (b) exhibit two peaks in devices A and B, while after annealing one vanishes.*

currents in that case. Above $2.5\,\mathrm{V}$, R_1 decreases after thermal annealing in the devices A and B which contributes to the lowered driving voltages.

On the other hand, R_2 is assumed to be related to traps and interface barriers. It is also constant until the built-in voltage and when trap states are occupied, this leads to an increase of resistance which agrees very well with the measured increase of capacitance in the C-V data in Figure 5.34.
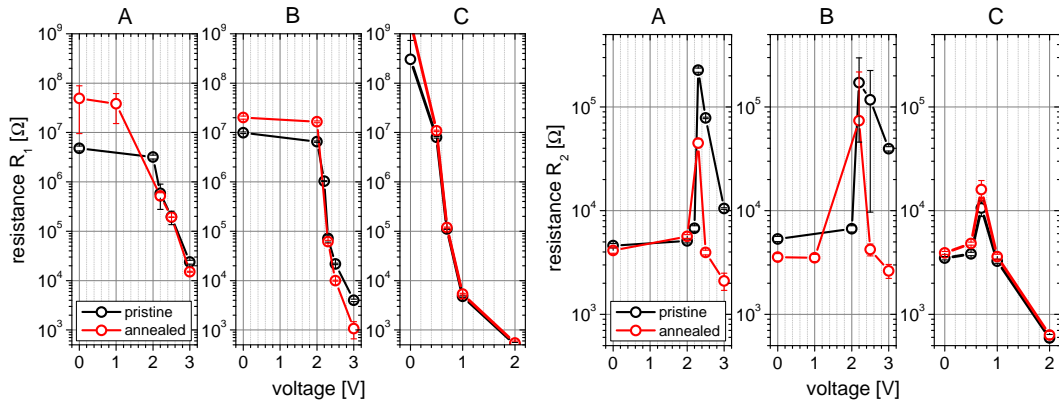

Figure 5.35: *Simulated resistances R_1 and R_2 of samples A, B and C that were obtained from fitting C-f data to the equivalent circuit model shown in Figure 5.33.*
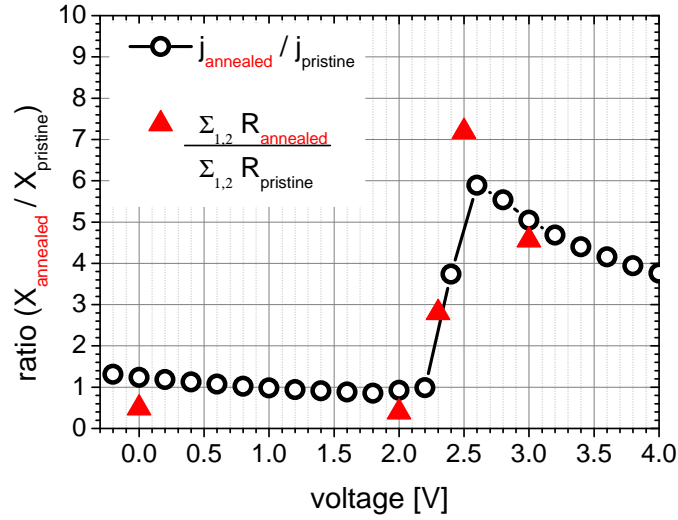
Figure 5.36: *The ratio of current density for n-i-p device (B) before ($j_{pristine}$) and after ($j_{annealed}$) thermal annealing shows a six-fold enhancement which fits very well to the ratio of added resistances R_1 and R_2, obtained from impedance spectroscopy (Figure 5.35).*

At voltages above 2 V, R_2 drops for devices A and B, as charge carriers are injected into the emission layer and recombination starts. In this region, large differences up to one order of magnitude in R_2 are observed when comparing pristine and annealed devices A and B. In device C, R_2 does not change during thermal treatment. Thus, R_2 seems to additionally describe a resistance related to the MeO-TPD.

If the sum of R_1 and R_2 before and after the annealing process is calculated for device B, a good agreement to the changes of the I-V curve is obtained comparing the pristine and annealed state of the sample (see Figure 5.36).

In the last experiment, the influence of the electron and hole blocking layers on the charge balance and the efficiency of inverted OLEDs is investigated. Again, monochrome phosphorescent OLEDs are fabricated with a variable blocking layer thickness. The general device structure is (thickness in nm):

Al(50) / Ag(40) / BPhen:Cs (65) / BAlq$_2$(0, 3, 6, 10) / NPB:Ir(MDQ)$_2$(acac) (10wt%)(20) / NPB(5, 10, 15) / MeO-TPD:F6TCNNQ (2wt%)(45) / Al(1) / Ag(20) / NPB(85)
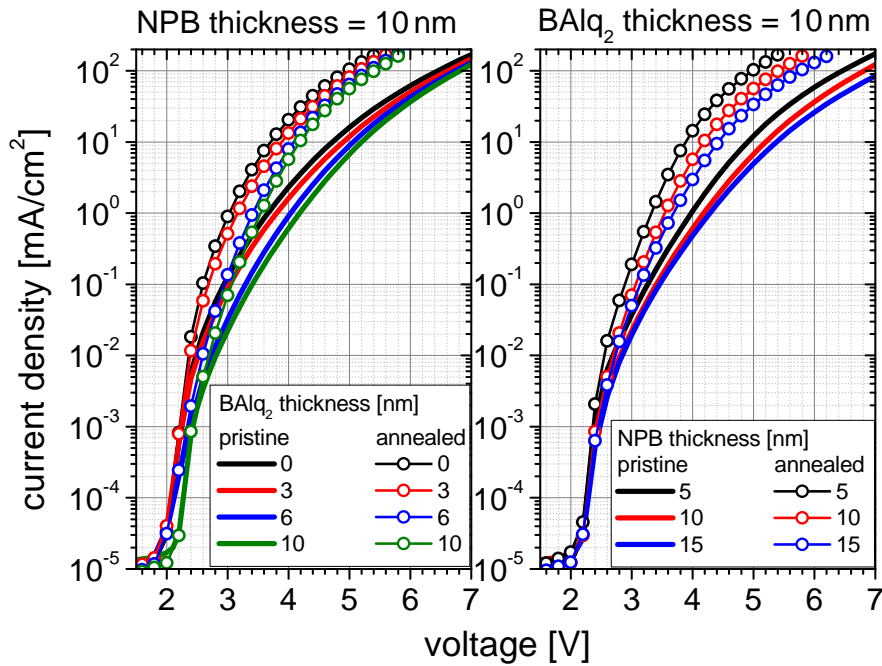
Figure 5.37: *Current-voltage characteristics of inverted OLED devices with variation of the blocking layers $BAlq_2$ and NPB. The graphs superimpose measured data for pristine and annealed (21 min at 75 °C) sample condition.*

The current-voltage characteristics are shown in Figure 5.37, either keeping the $BAlq_2$ layer or the NPB layer thickness constant at 10 nm. Nicely, one can see the influence on the I-V curves when altering the electron side or the hole side. If the $BAlq_2$ thickness is changed, only the currents between 3 and 5 V are influenced remarkably. This is in accordance to the observations in Figure 5.14 on page 117 where $BAlq_2$ is exchanged by BPhen. This behavior is stable against thermal annealing as the influence of the varied $BAlq_2$ thickness is still observable after the treatment. On the other hand, changing the hole transport by altering the NPB thickness, pronounced deviations in the I-V above 4 V are obtained.

When the ratio of current densities of the annealed samples and the pristine ones are calculated, the recent findings are confirmed as shown in Figure 5.38. The increase in current is neither depending on the presence of $BAlq_2$ nor its thickness while NPB exhibits a decreased annealing effect with increasing thickness. As expected, the peak in enhancement shifts to higher voltages as the intrinsic layer thickness increases. The external voltage has to raise to accomplish the same electric field inside the OLED.

Examining the external quantum efficiency of these OLED devices, shown in Figure 5.39, the influence of the $BAlq_2$ (HBL) layer becomes very clear. If the
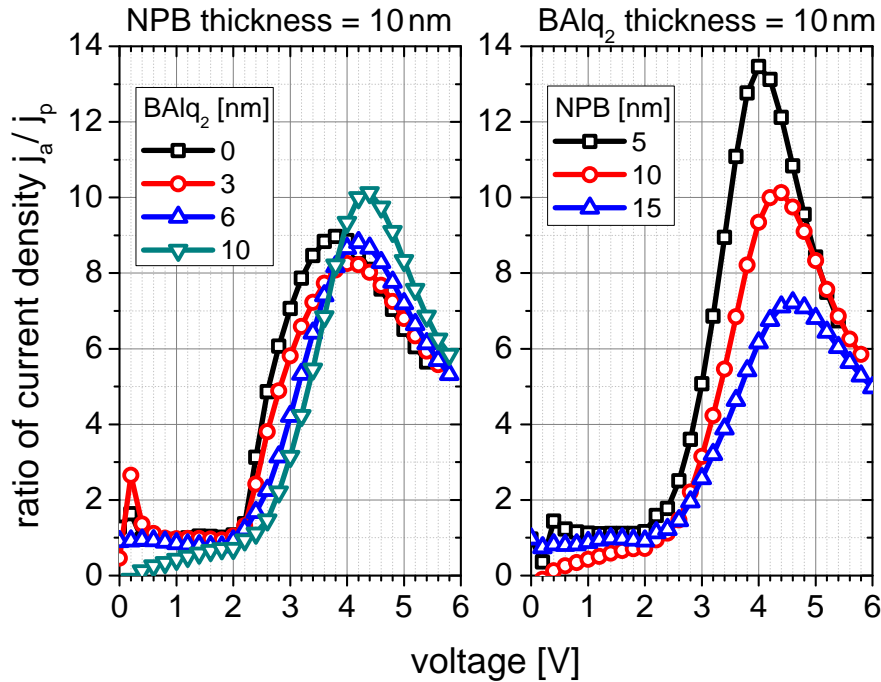
Figure 5.38: *Ratio of the current densities j_a after annealing and of the pristine sample j_p depending on the driving voltage of the complete inverted OLED. The annealing temperature was 75 °C for a duration of 21 min.*

HBL is omitted, we observe considerably good efficiencies at low currents and a strong and constant decrease with increasing current density in the EQE. On the other extreme, if a BAlq$_2$ thickness of 10 nm is used, the efficiency curves show a distinct peak around 2 - 4 mA/cm^2. A charge imbalance at low currents (voltages), coinciding with the influence on the I-V characteristic is most likely. The intermediate thickness range of 3 - 6 nm seems to be an optimum, showing the sensitivity of the inverted OLED against changes of the blocking layer. In OLEDs with 3 - 6 nm BAlq$_2$, the EQE curves show a flat behavior over the current density showing maximum absolute values of 20%. In contrast, the NPB layer thickness does not have a significant influence on the EQE unless the NPB thickness is raised to 15 nm where we observe the lowest efficiency values.
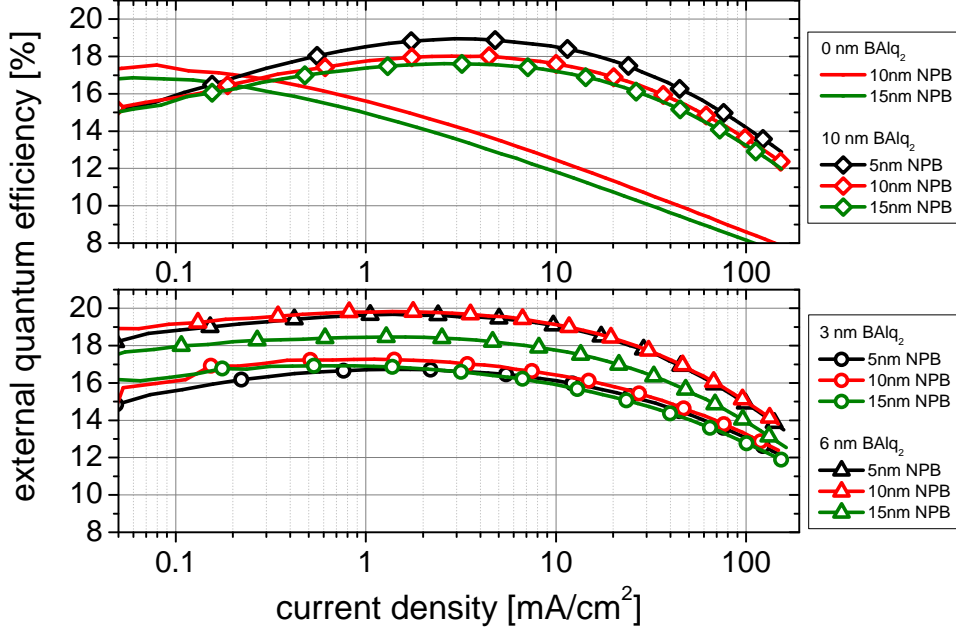
Figure 5.39: External quantum efficiency as a function of the current density for pristine inverted OLED devices depending on the HBL (BAlq₂) and EBL (NPB) thickness.

A more detailed understanding of the processes inside the EML can be gained if the roll-off is discussed quantitatively. Therefore, we apply the rate equation for the triplet density to fit the EQE curves for 0 and 6 nm BAlq$_2$. According to Reineke et al. [119], the rate equation for the exciton density $[n_{ex}]$ which includes triplet-polaron quenching (k_p) and triplet-triplet annihilation (k_{TT}) reads:

$$\frac{d[n_{ex}]}{dt} = -\frac{[n_{ex}]}{\tau} - \frac{1}{2}k_{TT}[n_{ex}]^2 - k_p\left[\frac{\rho_c(j)}{e}\right][n_{ex}] + \frac{j}{ew}. \qquad (5.1)$$

Here, τ is the phosphorescent lifetime, j the current density, ρ_c the charge carrier density and e the elementary charge. The generation term j/ew accounts for the exciton formation induced by the current density j where the parameter w is the thickness of the generation zone. In the steady-state where $d[n_{ex}]/dt = 0$, the current dependent quantum efficiency can be approximated by

$$\frac{\eta(j)}{\eta_0} = \Theta\left[\sqrt{\frac{\Delta^2 + \Gamma k_{TT}}{k_{TT}^2}} - \frac{\Delta}{k_{TT}}\right], \qquad (5.2)$$

with

$$\Theta = \frac{ew}{\tau j}, \qquad \Delta = \left(\frac{1}{\tau} + k_p C j^{1/(l+1)} \right) \tag{5.3}$$

and

$$\Gamma = \frac{2j}{ew}. \tag{5.4}$$

The parameter C describes material properties, e.g the carrier mobility. Knowing τ, we can fit the rate constants k_p and k_{TT} as well as the generation zone w to the external quantum efficiency. Hence, the results can help to identify pronounced exciton quenching processes due to an unbalanced charge carrier ratio [118, 234]. In Figure 5.40, the experimental data (symbols) is compared with the results from the fit with different approximations.
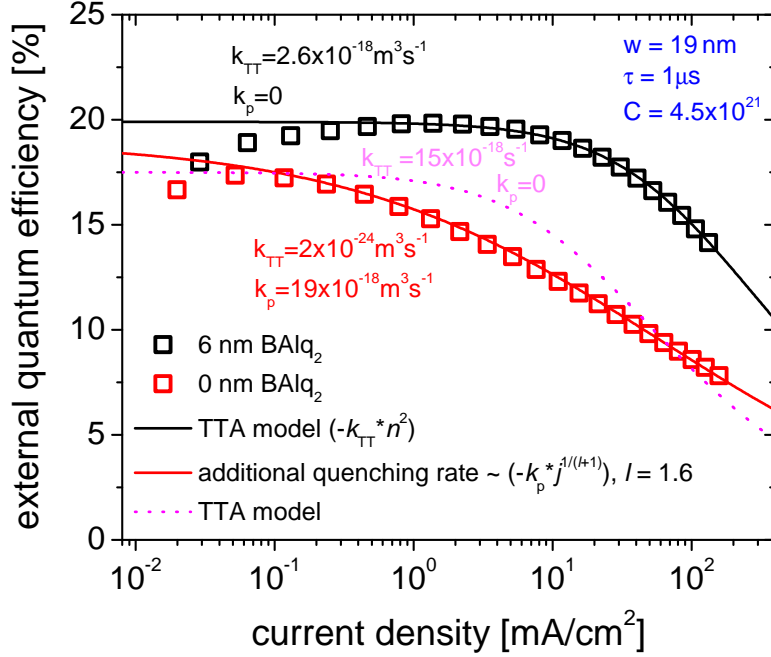

Figure 5.40: *External quantum efficiency depending on the current density of inverted OLED devices comprising 10 nm NPB acting as EBL. The roll-off strongly depends on the BAlq$_2$ (HBL) thickness and can be fitted with Equation 5.2. If no HBL is used, an additional quenching rate k_p has to be introduced to describe the roll-off. The complete parameter set is depicted as well.*

For the used emitter system NPB:Ir(MDQ)$_2$(acac) the triplet lifetime is assumed to be 1 µs [235]. Considering the device having 6 nm HBL first, the measured EQE curve can be fitted by only applying a rate for triplet-triplet annihilation ($k_{TT} = 2.6 \times 10^{-18}\,\mathrm{m^3\,s^{-1}}$). If the same procedure is applied

to the EQE characteristic of the sample without a $BAlq_2$ layer, a reasonable fit is not possible until an additional rate for triplet-polaron quenching ($k_{TT} = 2 \times 10^{-24}\,\mathrm{m^3\,s^{-1}}$; $k_p = 19 \times 10^{-18}\,\mathrm{m^3\,s^{-1}}$) is added. This means that one can validate the presence of triplet excitons at the hole blocking layer - emission layer interface although a pronounced hole limitation in the devices is most likely. Nevertheless, the Cs atoms in the BPhen:Cs ETL act as efficient quenchers and give rise to the observed strong roll-off.

On the other hand, it is very interesting that even $3\,\mathrm{nm}$ $BAlq_2$ can completely avoid triplet quenching at Cs dopant atoms. This means either we have a low triplet concentration at this interface which seems not convincing, because of the huge drop in EQE when a $BAlq_2$ blocker is missing. The second possibility is that $3\,\mathrm{nm}$ can cover the BPhen:Cs ETL efficiently to avoid interactions with the triplets in the EML. Furthermore, if the device is thermally annealed, no additional quenching in samples with $BAlq_2$ is observed. Both effects assign $BAlq_2$ as efficient blocker against triplet quenching and diffusion of Cs dopants toward the EML. Thereby, the high glass transition temperature of $BAlq_2$ ($92\,^\circ\mathrm{C}$) is important. If we make a comparison to the devices using BPhen as HBL, an enhanced efficiency roll-off after annealing is observed (see Figure 5.17 on page 122).
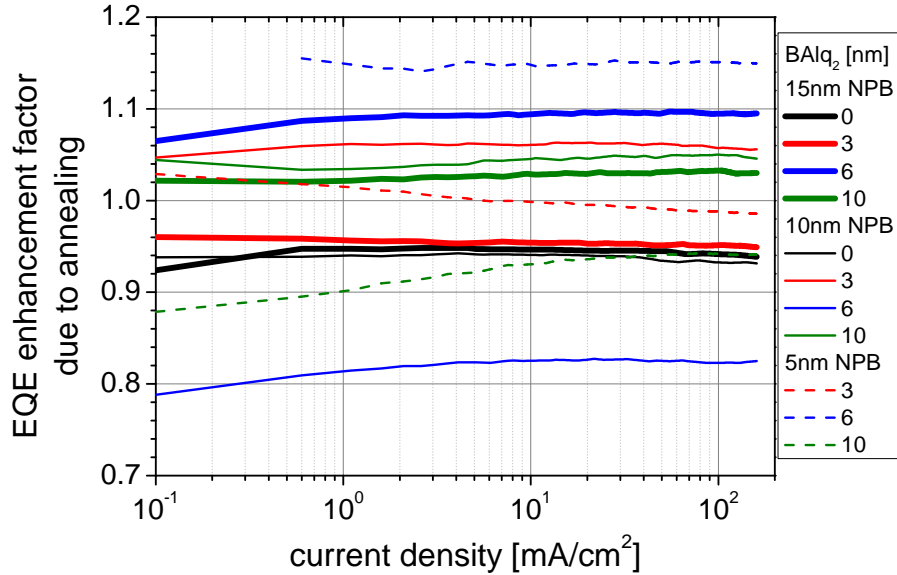

Figure 5.41: Enhancement factor $EQE_{annealed}/EQE_{pristine}$ depending on the current at different HBL and EBL layer thickness. Neither a correlation to a thickness variation nor to a current regime can be observed.
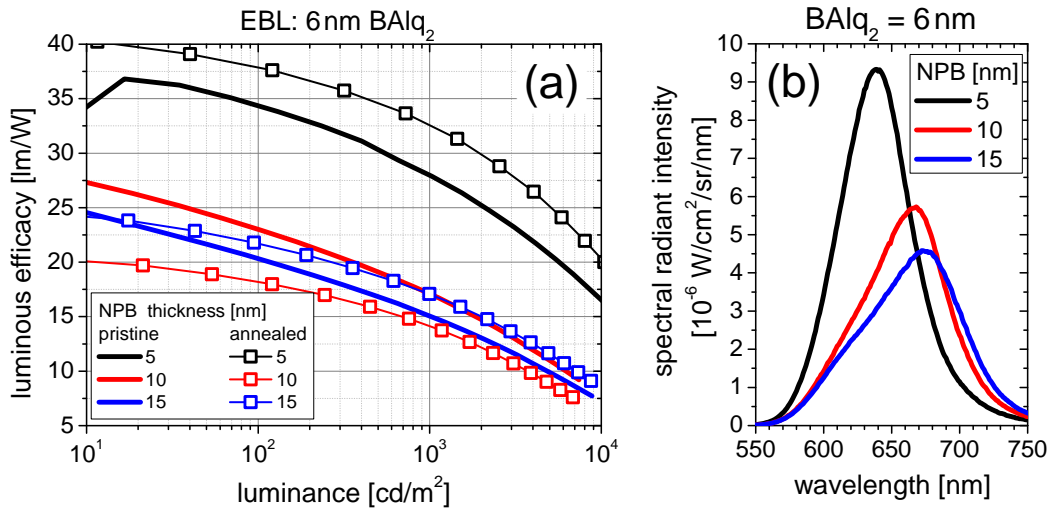
Figure 5.42: *Luminous efficacy as a function of luminance depending on the EBL thickness for $BAlq_2 = 6\,nm$ (a). The annealed samples (dotted line) show an improved efficacy for 5 an 15 nm NPB compared to the pristine ones (lines). The large difference of the absolute values is mainly determined by the emission peak of the electroluminescence (shown at $4.4\,mA/cm^2$), shifting with the thickness of NPB (b).*

The external quantum efficiency of the pristine samples is compared to the efficiency after the thermal annealing step in Figure 5.41. After 21 min at $75\,°C$, no pronounced effect is found. On the one hand, the flat behavior of the enhancement factor exhibits no current dependence, i.e. neither an influence on the charge balance nor an altered roll-off can be observed. On the other hand, no reproducible enhancement can be concluded as the factors range from 0.8 to 1.15 which can partially be due to measurement uncertainties.

On the other hand, the luminous efficacy (LE) should exhibit an improvement after the annealing process as the driving voltage has reduced for the entirety of OLED devices. Figure 5.42 shows the LE for OLEDs comprising $6\,nm\ BAlq_2$ (HBL) as a representative example. As expected, the thickness of the NPB has a strong influence on the LE because the peak of the EL spectrum and the voltage drop across the intrinsic layers depends on the NPB layer. Interestingly, the improvements are nearly identical to the EQE relations which means that the reduced voltage has only marginal effects.

Finally, impedance measurements are performed on these devices to correlate the results to the I-V as well as to the EQE curves. The capacitance-voltage results are depicted in Figure 5.43(a)-(d) arranged according to the $BAlq_2$ thickness and normalized to the geometrical capacitance of the intrinsic layers
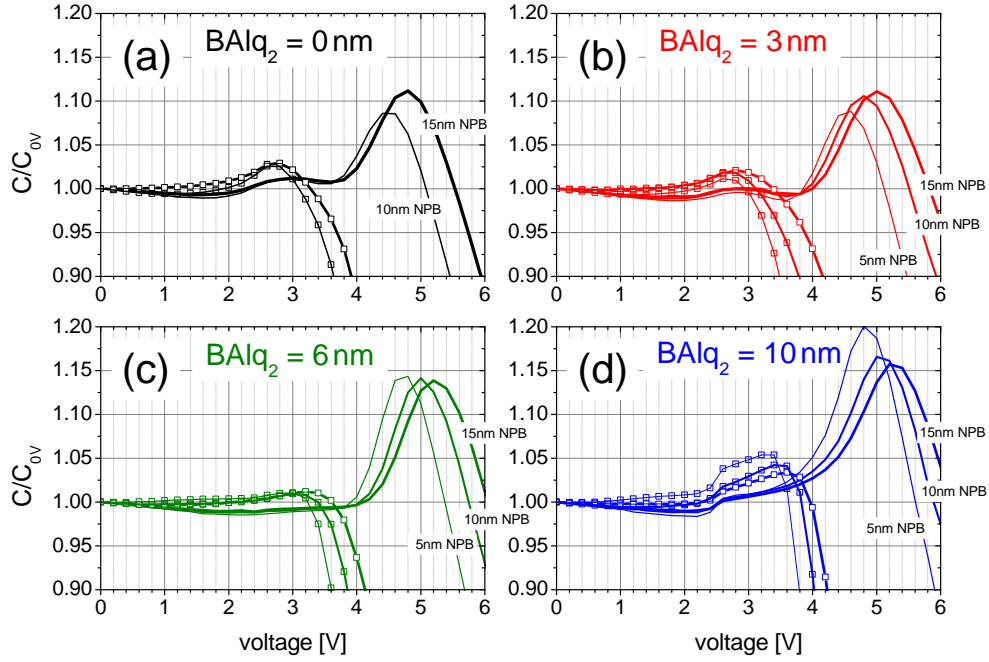
Figure 5.43: *Capacitance-voltage data for pristine (lines) and annealed (lines with symbols) sample condition depending on the HBL (BAlq$_2$) and the EBL (NPB) layer thickness. The line width denotes for the NPB layer thickness.*

observed at 0 V. Again, we can see the two peaks in the C-V data of pristine samples, shifting with respect to the intrinsic layer thickness. The thicker the intrinsic layers get, the lower is the field drop at a fixed external voltage. The NPB layer thickness influences the second peak, located at 4.5 - 5 V that previously has been identified as accumulation of holes in the MeO-TPD:F6TCNNQ or/and at the MeO-TPD:F6TCNNQ - NPB interface. Anyway, the NPB layer does not show an influence on the first peak, located at 2.5 - 3 V which can be related to trapped electrons in the BAlq$_2$ layer or accumulated electrons at the BPhen:Cs - NPB:Ir(MDQ)$_2$(acac) interface, respectively. Very interestingly, the amount of accumulated electrons seems to reach a minimum at a BAlq$_2$ thickness of 6 nm. Therefore, we expect a barrier between BPhen:Cs and NPB:Ir(MDQ)$_2$(acac) (see Figure 5.43(a)). If a 3 nm BAlq$_2$ layer is inserted (b), the first peak in the C-V data slightly decreases, vanishes at 6 nm (c) and re-appears in form of a step at 2.5 V in the C-V curve (d) again. A possible explanation could be that a thin BAlq$_2$ layer enhances the electron injection into the EML through transport over trap/gap states. If the layer becomes thicker (10 nm), the trapping of charges leads to an increased barrier again.
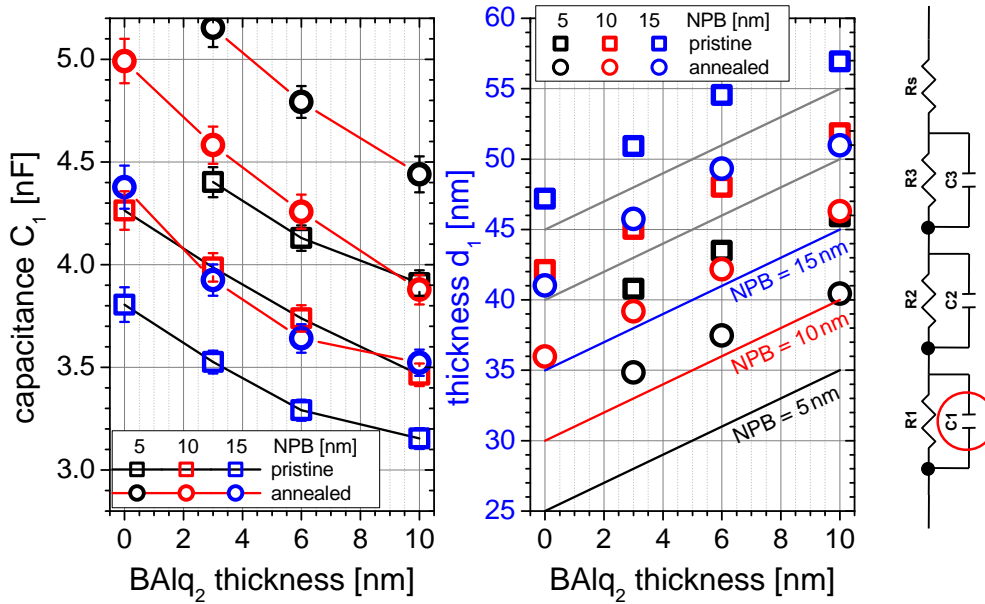
Figure 5.44: *The geometrical capacitance C_1, obtained by fitting the equivalent circuit on the right to impedance data at 0 V shows the influence of the intrinsic layer thickness variation and a reduction of the capacitive region during thermal treatment by constantly 5 nm. The colored lines denote the nominal total thickness of the intrinsic layers. The dielectric function is assumed to be $\varepsilon_r = 3$.*

As seen before, after thermal annealing the second peak in the C-V data disappears completely. The peak in the current ratio, depicted in Figure 5.38 is located at 4 - 4.5 V which corresponds to the region where the capacitance exhibits the ascending branch of the vanishing peak. There, the disappearing injection barrier has the most influence on the I-V. However, the first peak which comes from the electron accumulation slightly increases during the annealing of the samples.

The change of the geometrical capacitance C_1, obtained from fitting impedance data to an equivalent circuit is shown in Figure 5.44. Consequently, we find the influence of HBL (BAlq$_2$) and EBL (NPB) thickness variation, respectively. Thermal annealing at 75 °C for 21 min again shows a constant decrease of the capacitive region independent from the absolute intrinsic layer thickness. Further, the determined thicknesses are thicker than expected which can be explained by the assumption of the dielectric function $\varepsilon_r = 3$ and can further be related to less conductive regions of the MeO-TPD:F6TCNNQ layer in proximity to the NPB blocking layer.

Coming back to the question from the beginning of this chapter about the issues we have to pay attention to when designing an inverted OLED, the following can be summarized.

The inverted OLED shows a very sensitive interplay between hole and electron injection which depends on the driving voltage. At a given operating point, if one kind of charge carrier (without loss of generality holes) has to overcome a higher barrier, charges will accumulate at this barrier and hinder the transport of the following charges by repulsive Coulomb interaction or in other words by reduction of the external electric field. Thus, the number of holes cannot compete with the number of electrons at that given voltage and recombination only depends on the amount of the charge carrier minority. From the other point of view, electrons can travel into the EML but do not find enough recombination paths and if they have considerably high lifetime they accumulate in the EML which also hinders the following electrons. As consequence, if the device is not balanced energetically, the overall driving voltage is drastically increased. These considerations are not necessarily connected to a maximum in efficiency and a minimal voltage in case of a perfect charge balance. For example, OLED devices can have high efficiencies if the recombination zone is well distributed but operate at high voltages. This means that the charge balance from the outer side is only an important condition for high efficiency OLEDs. The usage of doped transport layers can assist to reduce the overall driving voltages to a minimum.

The charge transport of electrons and holes inside the EML is important as well as the exciton lifetime which is further connected to their diffusion length. If excitons are generated efficiently but are highly concentrated (due to selective transport of either holes or electrons) in a small region of the EML, elevated triplet-triplet annihilation and triplet-polaron-quenching occur and decrease the internal efficiency.

In the investigated organic devices, the glass transition of the used materials turned out to be important. These effects become observable when the devices experience thermal annealing after device preparation. Diffusion of dopants, leading to migration or phase separation of the corresponding materials are possible results. This is equivalent when we think of the deposition sequence where every step is connected with a heat transfer to the underlying layers. For example in non-inverted OLEDs, it seems beneficial for the electron transport to deposit a doped ETL like BPhen:Cs onto intrinsic blocker materials like $BAlq_2$ or BPhen and for the hole transport to deposit intrinsic blocker materials onto the doped HTL like MeO-TPD:F6TCNNQ. Anyway, the deposition sequence in combination with the material properties or material doping concentrations define the energetics at the corresponding interfaces and the layer morphology which altogether determines the resulting device performance.

6 SUMMARY AND OUTLOOK

6.1 SUMMARY

In this work, optical and electrical aspects of top-emitting OLEDs with inverted layer structure are investigated. The use of electrically doped transport layers facilitates the fabrication of p-i-n and n-i-p structured devices which offers the separation of optical and electrical optimization.

Thus, the optical cavity is easily tunable by the transport layer thicknesses as well as the position of the emission layer within the OLED structure. Further, an additional outcoupling layer in combination with a semi-transparent metal top-contact determines the properties of such micro-resonator OLED. With the help of optical simulation, an optimized layer sequence for n-i-p OLEDs is obtained including a highly reflective bottom contact. Showing 35% outcoupling efficiency in theory, an overall external quantum efficiency of almost 23% is reached for inverted top-emitting OLEDs. The spatial emission of the OLED devices is analyzed which shows a beneficial polarization splitting of the resonant cavity modes. Further, the outcoupling layer is found to reduce the absorption at the semitransparent top-mirror while it additionally alters the mode distribution inside the cavity. These findings are validated in the experiment.

The challenge of white light emission from top-emitting OLED devices is addressed by two approaches. First, the concept of an outcoupling layer is adapted which exhibits angular color stable spectral broad emission from a thin $\lambda/2$ cavity. Secondly, a two-unit stacked OLED is used to realize a multi-mode cavity which couples the light into an externally laminated microlens foil. This foil can mix the different modes and further enables trapped light to contribute to an outstanding broad spectral bandwidth. Showing outcoupling enhancement factors up to 1.5, a luminous efficacy of $30\,\mathrm{lm/W}$ is demonstrated. A second device exhibits a record color rendering index of 93 [236].

Comparing the performance of inverted and non-inverted OLED devices, there is a clear deviation between p-i-n and n-i-p layered devices. The second part of this work tries to disclose the main reasons for this fact. It is found that the injection from the bottom cathode is not a limiting factor if the opposite side of the OLED is well designed. In contrast, oxygen-contaminated Al contacts can introduce a series resistance that shifts the recombination

zone towards the blocking layer where parasitic fluorescence diminishes the efficiency of phosphorescent inverted OLEDs. Generally, the charge balance is a critical issue in the investigated OLED devices because every functional layer shows a strong impact on the current-voltage characteristic. Thereby, the layers that facilitate the hole transport into the emission layer have a key role. This is validated by single carrier devices that show strong influences on current and device impedance depending on the material choice of either the organic and the electrodes.

Further, post-fabrication thermally annealing of complete inverted OLED samples is found to drastically increase the current density at a given voltage. This effect is correlated to the glass transition temperature T_g of the used materials. In accordance to the investigations of the charge balance, the hole transport layer as low T_g material is identified to be the origin of the inferior performance regarding the current-voltage characteristic. Nevertheless, in some cases an improved device efficiency as well as an altered roll-off is observed after thermal treatment which can be attributed to dopant diffusion. From the investigation of the material $BAlq_2$ it becomes clear that high T_g materials are preferred. It could be shown that $BAlq_2$ is effective as blocking layer for excitons as well as against dopant diffusion.

6.2 OUTLOOK

Degradation has been observed after thermal annealing of OLED samples above 70 °C for longer than 30 min. The study of degradation mechanisms is a topic beyond the scope of this work. Nowy et al. [130] showed that impedance spectroscopy is a very powerful tool to study degradation processes as observed within this work. This is one aspect where future work can continue. Here, mainly the improvement of charge injection and transport and the influence of heat on these processes are of interest. Especially, a more detailed analysis of the sequence dependent film formation during the deposition process in combination with the usage of low T_g materials could be interesting. This would finally offer a complete understanding of the differences between inverted and non-inverted OLED structures.

Finally, there is still a deviation in the device efficiency between the p-i-n and the n-i-p OLED architecture. A deeper understanding of the fundamental processes inside the layer structure under operation like the recombination profile or the charge distribution in the steady state could resolve these unknown issue.

Appendices

Appendix A: Inverted OLEDs on metal substrates

Appendix A contains a brief summary of the results of inverted top-emitting OLEDs fabricated on industry aluminum foil substrates. The feasibility of OLED deposition and the performance data is discussed.

In parallel to the investigations presented in Chapters 4 and 5, inverted top-emitting monochrome OLED pixels have been fabricated on industry metal foil substrates. Comparably to former studies [237, 238] the substrates are supplied by the company Alanod[1].

Substrate properties

The metal substrates are cut into pieces from a 0.5 mm thick Al foil which is pre-coated with a nanocomposite varnish to smoothen the very rough Al surface. The surface was investigated by atomic force microscopy (AFM) where a root mean square value of 1.86 nm and a maximum hight of 13.3 nm has been measured [238]. Thus, the substrate surface quality is comparable to that of glass. Figure A.1 shows a picture of a clean substrate as used to prepare the OLED devices. Further, the reflectivity under 5° and 45° light incidence against the normal direction validates that there is a transparent layer on the metal surface. Incoming light is reflected at the metal surface beneath the varnish and at the substrate surface. The occurring interference oscillations depend on the thickness of the varnish and the optical path of the light. Interestingly, the amplitude of the oscillations decreases with wavelength and below 400 nm the oscillations vanish. There, the coherence limit is reached and no interference occurs as the thickness of the varnish is higher than the coherence length of the incident light.

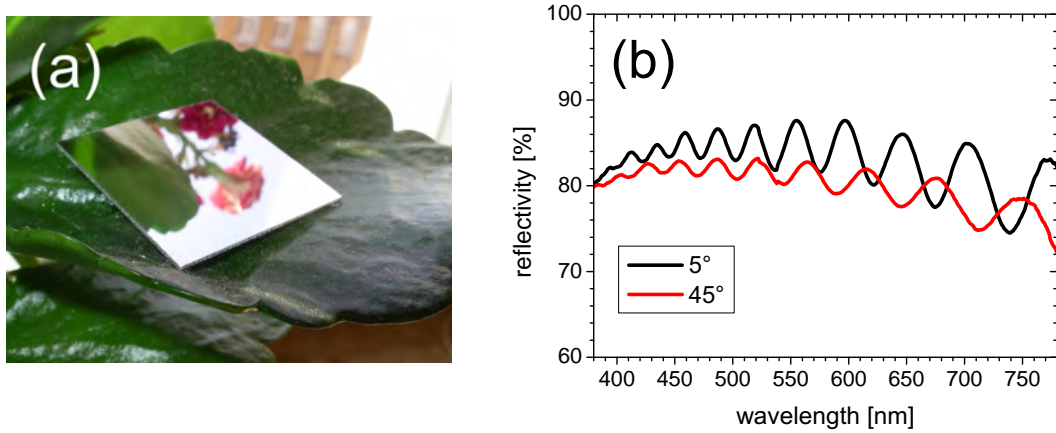[1]ALANOD Aluminium-Veredlung GmbH & Co. KG, Ennepetal, Germany

Figure A.1: Picture of a $25 \times 25\,mm^2$ Alanod substrate (a) used for device preparation and the measured spectral reflectivity (b) of a clean substrate for 5° and 45° light incidence. The oscillations originate from interference effects due to the transparent dielectric varnish which is coated onto the rough Al surface acting as smoothing layer.

INVERTED RGB OLED PIXEL

To demonstrate the feasibility of stable working OLED pixels on metal substrates first experiments are done. These are connected with the investigation of an appropriate cathode structure. The main objective is a low leakage current in the OLED characteristics which correlates to a smooth cathode surface. Thick transport layers ($> 200\,$nm) could further be used to compensate substrate and cathode roughness. Numerous fails due to electrical short cuts of the OLED devices have been observed and one of the first results of successful experiments is depicted in Figure A.2.

The device structures are (thickness in nm):

glass / Al(10) / Ag(50) / BPhen:Cs(210) / BAlq$_2$(10) / NPB:Ir(MDQ)$_2$ (acac) (10wt%)(20) / Spiro-TAD (10) / MeO-TPD:F$_4$TCNQ (2wt%)(30) / Ag(15)

Alanod substrate / Al(40) / Ag(15) / BPhen:Cs(50, 220) / BPhen(10) / NPB:Ir(MDQ)$_2$ (acac) (10wt%)(20) / Spiro-TAD (10) / MeO-TPD:F$_4$TCNQ (2wt%)(30) / Ag(15)

The test revealed that a highly reflecting and electrically feasible contact can not be made only of a thick silver layer because of its poor surface quality. As shown in Figure A.2, a 50 nm Ag cathode in combination with 10 nm Al acting as seed layer leads to leakage currents of about $1\,mA/cm^2$ on glass substrates
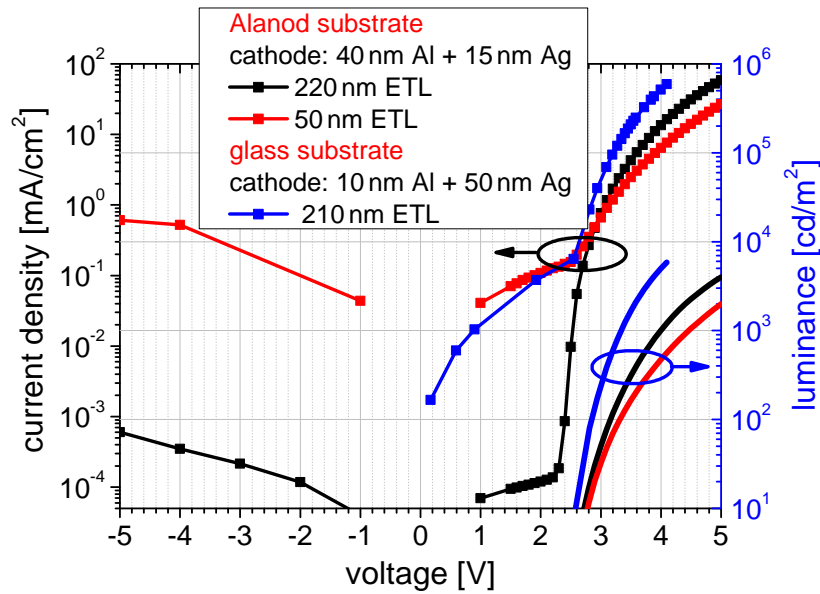
Figure A.2: Current-voltage-luminance characteristics of inverted OLED devices on Alanod and glass substrates depending on the cathode system and the ETL thickness. These first results show the influence of the leakage current on the Ag layer thickness. The roughness of the bottom cathode can be minimized by decreasing the Ag thickness and high leakage can be avoided with thick transport layers. In case of the Alanod substrate, even $\lambda/2$ cavity OLEDs can be realized.

even with 210 nm ETL. OLEDs with an ETL thickness below 100 nm failed in almost every case during the first measurement cycles. Almost the same OLED structure comprising a 40 nm opaque Al layer in combination with a 15 nm Ag film as cathode shows three orders of magnitude lower leakage currents. As already shown in Section 4.1, this cathode system is still highly reflective and able to realize top-emitting inverted OLEDs with a $\lambda/2$ cavity (ETL = 50 nm) as demonstrated in A.2, too.

Based on this cathode structure, OLED devices of the three elementary colors red, green and blue (RGB) are tested to demonstrate the device performance of inverted OLEDs on Alanod metal substrates. The device layer structures are (thickness in nm):

Blue OLED:

Al(100) / Ag(15) / BPhen:Cs(175) / Alq$_3$(10) / MADN:TBPe (1wt%)(10) / NPB (10) / MeO-TPD:F$_4$TCNQ (4wt%)(20) / Ag(15)

Green OLED:

Al(50) / Ag(15) / BPhen:Cs(190) / BPhen(10) / TPBi:Ir(ppy)$_3$ (8wt%)(10) / TCTA::Ir(ppy)$_3$ (8wt%)(5) / Spiro-TAD (10) / MeO-TPD:F$_4$TCNQ (4wt%)(30) / Ag(15) / NPB(80)

Red OLED:

Al(40) / Ag(20) / BPhen:Cs(64) / BAlq$_2$(10) / NPB:Ir(MDQ)$_2$ (acac) (10wt%)(20) / NPB (10) / MeO-TPD:F$_4$TCNQ (2wt%)(43) / Ag(19) / NPB(87)

The current-voltage-luminance characteristics and the efficiencies are summarized in Figure A.3. First of all, the blue and green devices make use of a thick ETL to circumvent short cuts. The red device shows slightly higher leakage but works with a thin ETL. The onset voltage where luminance can be detected is about 3 V for all types of OLEDs. The red OLED (ETL = 64 nm) exhibits driving voltages of 4.2 V at 1000 cd/m^2, 19 lm/W and 17% EQE. As the other devices use a thick ETL they show less efficient OLED performances. Further, the blue OLED device comprises MADN and TBPe as emitters which are fluorescent materials. This results in external quantum efficiencies below 2%. The electroluminescence spectra as well as pictures of the OLED pixels are shown in Figure A.4.
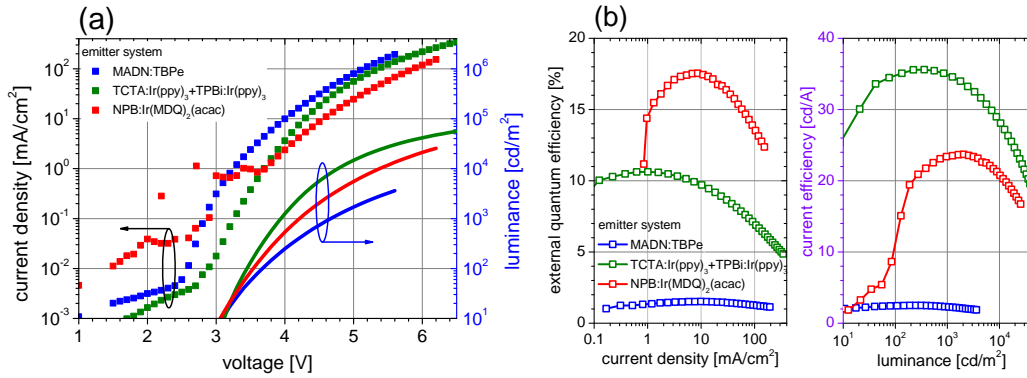

Figure A.3: *Current-voltage-luminance characteristics (a) and external quantum and current efficiency (b) of red, green and blue inverted top-emitting OLED pixels fabricated on Alanod metal substrates. The blue emission is realized by MADN:TBPe, the green by a two layered emission layer doped with Ir(ppy)$_3$ and the red by NPB:Ir(MDQ)$_2$(acac).*
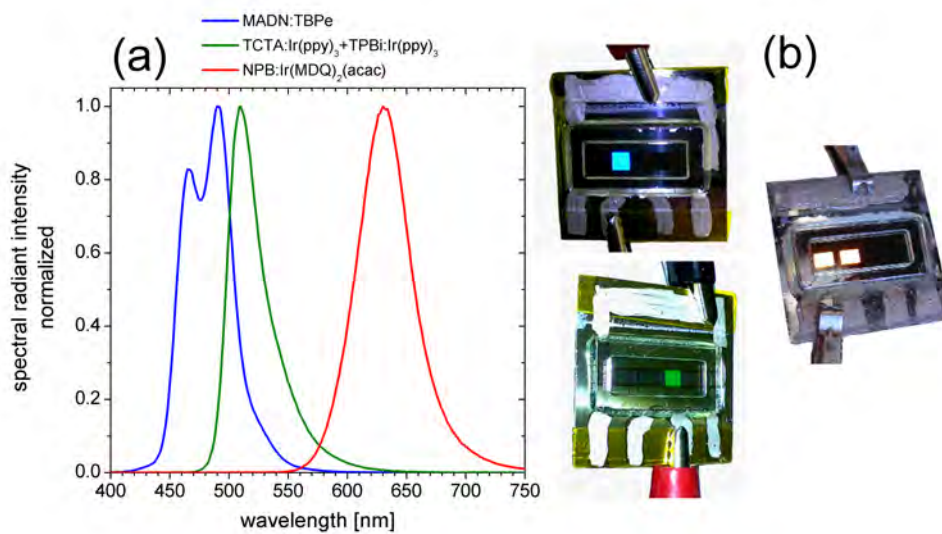
Figure A.4: Emission spectra of red, green and blue inverted top-emitting OLED pixels (a) and pictures of operating devices (b) deposited on metal substrates and encapsulated with glass lids.

The substrate surface (Figure A.4(b)) is manually passivated with adhesive tape to protect the thin smoothing layer. Conductive varnish which contains silver is used to contact the thin metal films that end on the substrate to lead the current on top of the passivation. This procedure is important as measurement pins can penetrate the thin smoothing layer and generate a short cut over the underlying Al substrate.

Appendix B: Optical simulation and supplementary information

Appendix B contains supplementary information about the optical simulation model and its correlation to experimental data. Further, the spectral data a white top-emitting OLED exhibiting a CRI of 93 as well as supplementary data of inverted OLEDs comprising a metal-organic interlayer is shown.

Encapsulation glass

Glass lids made from soda lime glass are used to provide a transparent encapsulation for top-emitting OLEDs within this work. As there is a gap of nitrogen between OLED and encapsulation, the transmission characteristic depends on the polarization and on the propagation direction of the emitted light. When evaluating spatial emission characteristics of OLED devices, these effects have to be taken into account when comparing the experimental data with optical simulation results. Figure B.1 shows the calculated transmission values for TE and TM polarized light. From the findings in Section 4.2, optimized top-emitting OLEDs show a strong polarization splitting under large emission angles. In combination with the transmission characteristic of the encapsulation, this leads to changes in the spectral shape as TE polarized light is coupled more efficiently into air than the TM polarized part of a spectrum.

The optical model

As introduced in Section 2.2.3, every optical simulation of OLED devices in this work is done by using an optical thin-film model which describes the radiative decay of excited emitter molecules as dipole radiation. The model was developed and implemented by Mauro Furno and is validated with numerous experiments [128]. The input parameters of the model are the refractive indices of every material, the intrinsic spectral emission of the emitter, the distribution of emitting molecules within the emission layer, and each layer thickness. The simulation software yields angular resolved electroluminescence spectra,
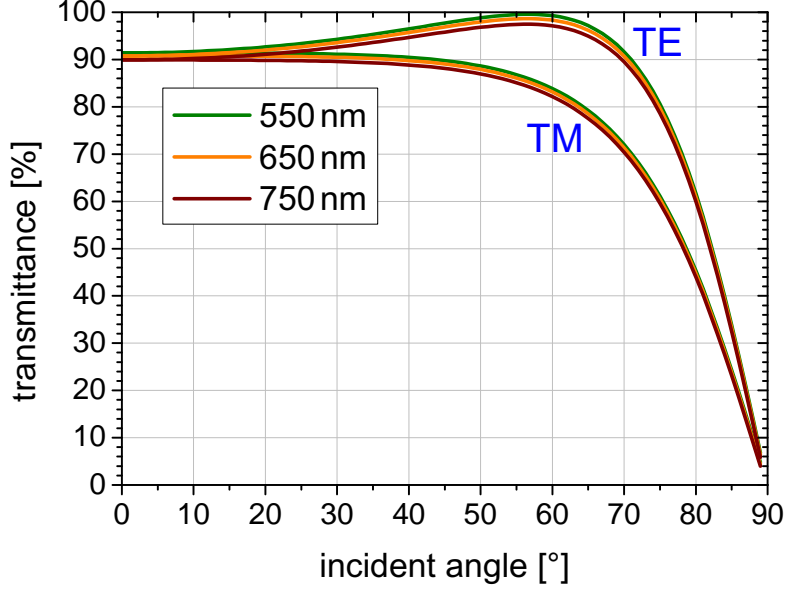
Figure B.1: Calculated transmittance T of a 0.5 mm thick glass lid which is used to encapsulate the top-emitting OLEDs investigated in this study. It shows the dependence of T of the polarization of the incident light and emphasizes the fact that the encapsulation alters the emission spectrum of an OLED operating underneath.

luminous intensities and an integrated number of outcoupled photons which all can be compared directly with experimental data. The model accounts for the Purcell factor F and for the cavity effect. The externally radiated or outcoupled power at a certain wavelength λ is given by

$$U(\lambda) = \int_0^{u_{crit}(\lambda)} K_{out}(\lambda, u) \ du^2, \qquad (B.1)$$

with the externally radiated power density $K_{out}(\lambda, u)$ per unit normalized in-plane wavevector u. This transverse wavevector is given by $u = k_p/k$, where k is the total wavevector at the emitter location and k_p the projected wavevector in the plane of the dipole source. u_{crit} limits the wavevector range in which the optical system allows light propagation into the far-field. K_{out} has to be determined separately for three different orthogonal orientations of the electric dipole because an isotropic dipole emission can be composed of these three orientations. Besides the orientation, the dipole coupling is also depending on the polarization state of light. Horizontal dipoles only couple to p-polarized (TM) modes whereas vertical oriented dipoles couple to both, s-

(TE) and p-polarized modes.

In this work, an isotropic dipole orientation is assume rigorously where the total dissipated power density K is given by [124]

$$K = \frac{1}{3}K_{TMv} + \frac{2}{3}(K_{TMh} + K_{TEh}).$$ (B.2)

The fractions v and h of K denote the power densities of vertically and horizontally oriented dipole sources with respect to the plane of the multilayer.

In most of the simulations performed in this work, only propagating wave components that belong to emission into the far-field are calculated. Evanescent modes are neglected and hence, no correlation between total generated power and outcoupled power is considered. The full integration of K over the whole u-space is only done for the optimization of the outcoupling efficiency, shown in Figure 4.5 on page 70.

To compare optical simulation with electroluminescence data from OLEDs, the internal emission spectrum of the emitting dye molecules has finally to be applied. A calculated EL spectrum is given by the convolution of the relative extracted spectral power with the measured photoluminescence spectrum of the dye. If not given explicitly, a delta-distributed region of emitting dipoles is assumed. In some cases this assumption is changed to a constant distribution having a width of 2 nm. The complete set of formulas, describing the model in detail can be found in Furno et al. [128].

Optical constants

The optical constants of the used metals Ag and Al are obtained from literature [230, 239, 240] or the Sopra data base [241]. The dispersion of all used organic materials is extracted using an iterative algorithm which is used to simultaneously fit measured reflectance and transmittance of single organic films [242].

Laminated microlens foil

As described in Section 4.3.2, OLED device 4 comprising a microlens exhibits a very high CRI of 93. Figure B.2 shows the corresponding EL spectrum covering the whole visible range.
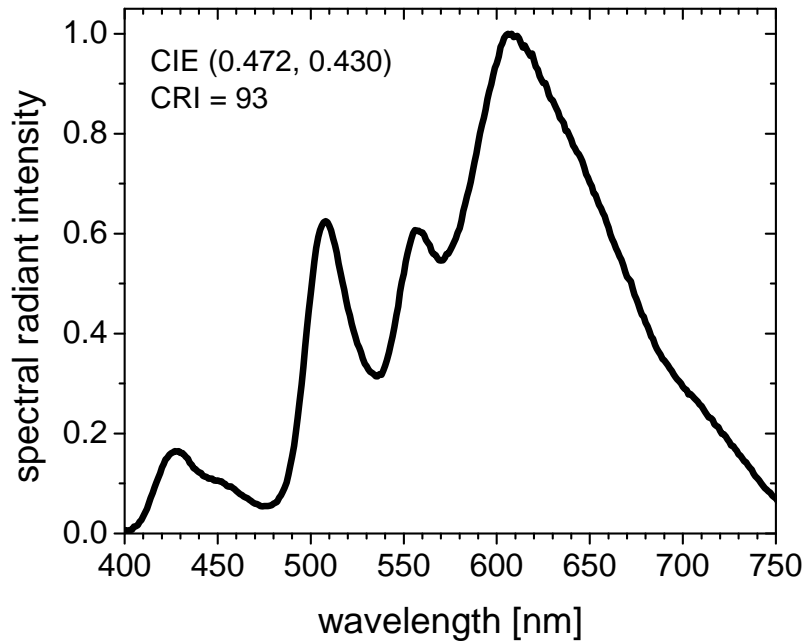
Figure B.2: Electroluminescence spectrum measured at $4.4\,mA/cm^2$ of OLED device 4 (with microlens foil attached) mentioned in section 4.3.2. The OLED exhibits a very high CRI of 93 which originates from the broad spectral width and benefits from the spectral fraction in the deep red where $\lambda > 700\,nm$.

ORGANO-METALLIC INTERLAYER

Alternatively, TPPhen is used as ETL and a TPPhen:W_2(hpp)$_4$:Ag interlayer is applied between cathode and ETL. The OLED structure is (thickness in nm):

Al(50) / Ag(40) / TPPhen:W_2(hpp)$_4$:Ag(0, 20, 40wt% Ag) (5) / TPPhen:W_2(hpp)$_4$(60) / BAlq$_2$(10) / NPB:Ir(MDQ)$_2$ (acac) (10wt%)(20) / NPB (10) / MeO-TPD:F6TCNNQ (2wt%)(40) / Al(1) / Ag(20) / NPB(85)

The OLED characteristics are depicted in Figure B.3, showing the influence of two different Ag concentrations in comparison to the case without an interlayer. OLEDs having an alternative electron transport layer exhibit annealing effects as well. In this case, the material TPPhen features a glass transition temperature $T_g = 105\,°C$ compared to $T_g = 62\,°C$ for BPhen [180].
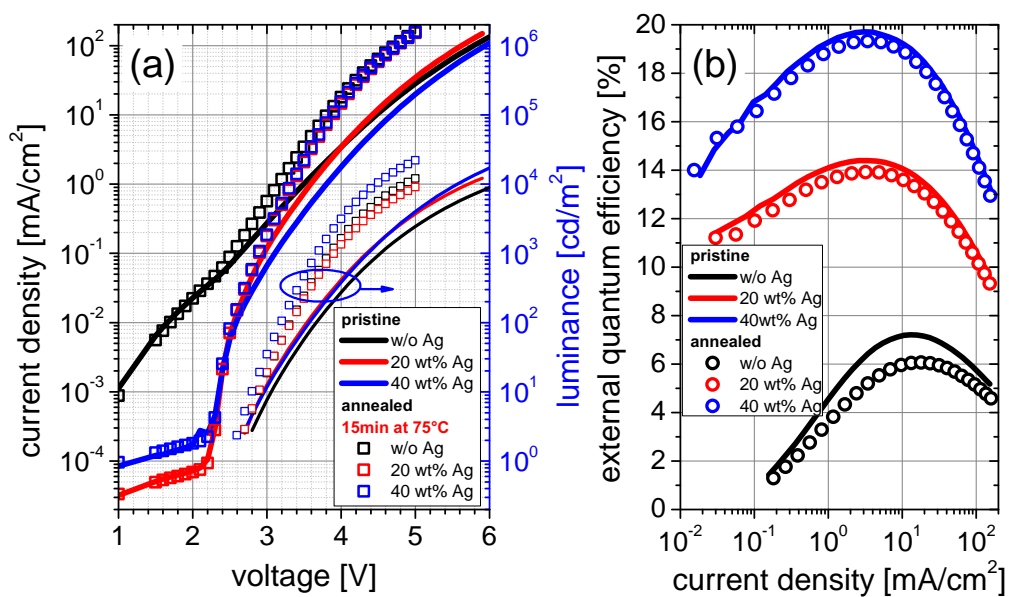
Figure B.3: *Current-voltage-luminance characteristics (a) of inverted top-emitting OLEDs comprising TPPhen as electron transport layer in pristine and annealed condition. The influence of a 5 nm organo-metallic interlayer TPPhen:W_2(hpp)$_4$:Ag (0, 20, 40wt% Ag) between the bottom cathode and the ETL is illustrated and show significant impact on the device efficiency (b).*

BIBLIOGRAPHY

[1] R. P. Feynman, "There´s Plenty of Room at the Bottom", in *Lecture at a meeting of the American Physical Society*, (Caltech) (December 1959).

[2] C. W. Tang and S. A. VanSlyke, "Organic electroluminescent diodes", *Applied Physics Letters* **51**(12), pp. 913–915 (1987).

[3] C. W. Tang, S. A. VanSlyke, and C. H. Chen, "Electroluminescence of doped organic thin films", *Journal of Applied Physics* **65**(9), pp. 3610–3616 (1989).

[4] T. W. Canzler, S. Murano, D. Pavicic, O. Fadhel, C. Rothe, A. Haldi, M. Hofmann, and Q. Huang, "66.2: Efficiency Enhancement in White PIN OLEDs by Simple Internal Outcoupling Methods", *SID Symposium Digest of Technical Papers* **42**(1), pp. 975–978 (2011).

[5] http://www.osram.com, "Efficiency record with flexible oled." press release (November 2011).

[6] S. Chen, L. Deng, J. Xie, L. Peng, L. Xie, Q. Fan, and W. Huang, "Recent Developments in Top-Emitting Organic Light-Emitting Diodes", *Advanced Materials* **22**(46), pp. 5227–5239 (2010).

[7] S. Hofmann, M. Thomschke, B. Lüssem, and K. Leo, "Top-emitting organic light-emitting diodes", *Opt. Express* **19**, pp. A1250–A1264 (2011).

[8] P. Servati, S. Prakash, A. Nathan, and C. Py, "Amorphous silicon driver circuits for organic light-emitting diode displays", *Journal of Vacuum Science & Technology A: Vacuum, Surfaces, and Films* **20**(4), pp. 1374–1378 (2002).

[9] T. Dobbertin, *Invertierte organische Leuchtdioden für Aktiv-Matrix OLED-Anzeigen*, Cuvillier Verlag, Göttingen (2005).

[10] M. Pfeiffer, S. R. Forrest, X. Zhou, and K. Leo, "A low drive voltage, transparent, metal-free n-i-p electrophosphorescent light emitting diode", *Organic Electronics* **4**(1), pp. 21 – 26 (2003).

[11] S. Scholz, Q. Huang, M. Thomschke, S. Olthof, P. Sebastian, K. Walzer, K. Leo, S. Oswald, C. Corten, and D. Kuckling, "Self-doping and partial oxidation of metal-on-organic interfaces for organic semiconductor devices studied by chemical analysis techniques", *Journal of Applied Physics* **104**(10), 104502 (2008).

[12] T. Dobbertin, M. Kroeger, D. Heithecker, D. Schneider, D. Metzdorf, H. Neuner, E. Becker, H.-H. Johannes, and W. Kowalsky, "Inverted top-emitting organic light-emitting diodes using sputter-deposited anodes", *Applied Physics Letters* **82**(2), pp. 284–286 (2003).

[13] C.-W. Chen, C.-L. Lin, and C.-C. Wu, "An effective cathode structure for inverted top-emitting organic light-emitting devices", *Applied Physics Letters* **85**(13), pp. 2469–2471 (2004).

[14] S. Reineke, F. Lindner, G. Schwartz, N. Seidler, K. Walzer, B. Lussem, and K. Leo, "White organic light-emitting diodes with fluorescent tube efficiency", *Nature* **459**(7244), pp. 234–238 (2009).

[15] H. Haken and H. C. Wolf, *Molekülphysik und Quantenchemie*, Springer, Berlin, 5th ed. (2006).

[16] http://www.orgworld.de (2011).

[17] M. Hoffmann, *Vorlesungsskript Organische Halbleiter*, IAPP, TU Dresden (2006).

[18] M. Pfeiffer, *Controlled Doping of Organic Vacuum Deposited Dye Layers: Basics and Applications.* PhD thesis, Technische Universität Dresden (1999).

[19] M. Schwoerer and H. C. Wolf, *Organic Molecular Solids*, WILEY-YCH, Weinheim (2007).

[20] H. Ishii, K. Sugiyama, E. Ito, and K. Seki, "Energy level alignment and interfacial electronic structures at organic metal and organic organic interfaces", *Advanced Materials* **11**, 605 (1999).

[21] Y. Shirota, "Photo- and electroactive amorphous molecular materials-molecular design, syntheses, reactions, properties, and applications", *J. Mater. Chem.* **15**, pp. 75–93 (2005).

[22] J. Berréhar and M. Schott, "Hole Mobilities and Anomalous Current Transients in Crystalline Naphthalene", *Molecular Crystals and Liquid Crystals* **46**(3), pp. 223–228 (1978).

[23] W. Warta and N. Karl, "Hot holes in naphthalene: High, electric-field-dependent mobilities", *Phys. Rev. B* **32**(2), pp. 1172–1182 (1985).

[24] N. Karl, K.-H. Kraft, J. Marktanner, M. Münch, F. Schatz, R. Stehle, and H.-M. Uhde, "Fast electronic transport in organic molecular solids?", in *Papers from the 45th National Symposium of the American Vacuum Society, Papers from the 45th National Symposium of the American Vacuum Society* **17**(4), pp. 2318–2328, AVS (1999).

[25] P. Peumans, *Organic thin-film photodiodes*. PhD thesis, Princeton University (2004).

[26] H. Böttger and V. V. Bryksin, *Hopping conduction in solids*, VCH (1985).

[27] H. Bässler, "Localized States and Electronic Transport in Single Component Organic Solids with Diagonal Disorder", *physica status solidi (b)* **107**(1), pp. 9–54 (1981).

[28] H. Bässler, "Charge Transport in Disordered Organic Photoconductors a Monte Carlo Simulation Study", *physica status solidi (b)* **175**(1), pp. 15–56 (1993).

[29] J. Staudigel, M. S. el, F. Steuber, and J. Simmerer, "A quantitative numerical model of multilayer vapor-deposited organic light emitting diodes", *Journal of Applied Physics* **86**(7), pp. 3895–3910 (1999).

[30] N. Tessler, Y. Preezant, N. Rappaport, and Y. Roichman, "Charge Transport in Disordered Organic Materials and Its Relevance to Thin-Film Devices: A Tutorial Review", *Advanced Materials* **21**(27), pp. 2741–2761 (2009).

[31] V. Ambegaokar, B. I. Halperin, and J. S. Langer, "Hopping Conductivity in Disordered Systems", *Phys. Rev. B* **4**, pp. 2612–2620 (Oct 1971).

[32] M. C. J. M. Vissenberg and M. Matters, "Theory of the field-effect mobility in amorphous organic transistors", *Phys. Rev. B* **57**, pp. 12964–12967 (1998).

[33] R. Zallen, *The physics of amorphous solids*, John Wiley & Sons, Inc. (1983).

[34] H. Scher and E. W. Montroll, "Anomalous transit-time dispersion in amorphous solids", *Phys. Rev. B* **12**, pp. 2455–2477 (1975).

[35] A. Miller and E. Abrahams, "Impurity Conduction at Low Concentrations", *Phys. Rev.* **120**, pp. 745–755 (1960).

[36] M. Pope and C. Swenberg, *Electronic Processes in Organic Crystals and Polymers*, Oxford University Press, New York, 2$^{\text{nd}}$ ed. (1999).

[37] N. Karl, "Charge carrier transport in organic semiconductors", *Synthetic Metals* **133-134**, pp. 649 – 657 (2003). Proceedings of the Yamada Conference LVI. The Fourth International.

[38] R. G. Kepler, "Charge Carrier Production and Mobility in Anthracene Crystals", *Phys. Rev.* **119**(4), pp. 1226–1229 (1960).

[39] R. G. Kepler, P. M. Beeson, S. J. Jacobs, R. A. Anderson, M. B. Sinclair, V. S. Valencia, and P. A. Cahill, "Electron and hole mobility in tris(8-hydroxyquinolinolato-N1,O8) aluminum", *Applied Physics Letters* **66**(26), pp. 3618–3620 (1995).

[40] G. Horowitz, "Organic Field-Effect Transistors", *Advanced Materials* **10**(5), pp. 365–377 (1998).

[41] G. Horowitz, R. Hajlaoui, H. Bouchriha, R. Bourguiga, and M. Hajlaoui, "The concept of "threshold voltage" in organic field-effect transistors", *Advanced Materials* **10**(12), pp. 923–927 (1998).

[42] G. Horowitz, R. Hajlaoui, D. Fichou, and A. El Kassmi, "Gate voltage dependent mobility of oligothiophene field-effect transistors", *Journal of Applied Physics* **85**(6), pp. 3202–3206 (1999).

[43] G. Schwartz, *Novel Concepts for High-Efficiency White Organic Light-Emitting Diodes.* PhD thesis, Technische Universität Dresden (2007).

[44] P. W. M. Blom, M. J. M. de Jong, and J. J. M. Vleggaar, "Electron and hole transport in poly(p-phenylene vinylene) devices", *Applied Physics Letters* **68**(23), pp. 3308–3310 (1996).

[45] P. N. Murgatroyd, "Theory of space charge limited current enhanced by Frenkel effect", *Journal of Physics D* **3**(2), pp. 151–156 (1970).

[46] Y. Gao, "Surface analytical studies of interfaces in organic semiconductor devices", *Materials Science and Engineering: R: Reports* **68**(3), pp. 39 – 87 (2010).

[47] A. Kahn, N. Koch, and W. Gao, "Electronic structure and electrical properties of interfaces between metals and π-conjugated molecular films", *Journal of Polymer Science Part B: Polymer Physics* **41**(21), pp. 2529–2548 (2003).

[48] S. Olthof, *Photoelectron Spectroscopy on Doped Organic Semiconductors and Related Interfaces*. PhD thesis, Technische Universität Dresden (2010).

[49] U. Wolf, V. I. Arkhipov, and H. Bässler, "Current injection from a metal to a disordered hopping system. I. Monte Carlo simulation", *Phys. Rev. B* **59**(11), pp. 7507–7513 (1999).

[50] R. H. Fowler and L. Nordheim, "Electron Emission in Intense Electric Fields", *Proc. R. Soc. Lond. A* **119**, pp. 173–181 (1928).

[51] K. C. Kao and W. Hwang, *Electrical transport in solids*, Pergamon Press, Oxford, New York, Toronto, 1st ed. (1981).

[52] W. Gao and A. Kahn, "Electronic structure and current injection in zinc phthalocyanine doped with tetrafluorotetracyanoquinodimethane: Interface versus bulk effects", *Organic Electronics* **3**, pp. 53 – 63 (2002).

[53] M. Kröger, *Device and Process Technology for Full-Color Active-Matrix OLED Displays*, Cuvillier Verlag, Göttingen (2007).

[54] V. I. Arkhipov, H. von Seggern, and E. V. Emelianova, "Charge injection versus space-charge-limited current in organic light-emitting diodes", *Applied Physics Letters* **83**, pp. 5074–5076 (2003).

[55] V. I. Arkhipov, E. V. Emelianova, Y. H. Tak, and H. Bässler, "Charge injection into light-emitting diodes: Theory and experiment", *Journal of Applied Physics* **84**(2), pp. 848–856 (1998).

[56] E. M. Conwell and M. W. Wu, "Contact injection into polymer light-emitting diodes", *Applied Physics Letters* **70**(14), pp. 1867–1869 (1997).

[57] M. Y. Chan, S. L. Lai, K. M. Lau, C. S. Lee, and S. T. Lee, "Application of metal-doped organic layer both as exciton blocker and optical spacer for organic photovoltaic devices", *Applied Physics Letters* **89**(16), 163515 (2006).

[58] M. Grobosch and M. Knupfer, "Charge-Injection Barriers at Realistic Metal/Organic Interfaces: Metals Become Faceless", *Advanced Materials* **19**(5), pp. 754–756 (2007).

[59] C. K. Chan, W. Zhao, S. Barlow, S. Marder, and A. Kahn, "Decamethylcobaltocene as an efficient n-dopant in organic electronic materials and devices", *Organic Electronics* **9**(5), pp. 575 – 581 (2008).

[60] J. Hwang, A. Wan, and A. Kahn, "Energetics of metal-organic interfaces: New experiments and assessment of the field", *Materials Science and Engineering: R: Reports* **64**(1-2), pp. 1–31 (2009).

[61] M. A. Baldo and S. R. Forrest, "Interface-limited injection in amorphous organic semiconductors", *Phys. Rev. B* **64**(8), 085201 (2001).

[62] B. N. Limketkai and M. A. Baldo, "Charge injection into cathode-doped amorphous organic semiconductors", *Phys. Rev. B* **71**(8), 085207 (2005).

[63] I. Hill, D. Milliron, J. Schwartz, and A. Kahn, "Organic semiconductor interfaces: electronic structure and transport properties", *Applied Surface Science* **166**(1-4), pp. 354 – 362 (2000).

[64] S. Braun, W. R. Salaneck, and M. Fahlman, "Energy-Level Alignment at Organic/Metal and Organic/Organic Interfaces", *Advanced Materials* **21**(14-15), pp. 1450–1472 (2009).

[65] K. Walzer, B. Maennig, M. Pfeiffer, and K. Leo, "Highly Efficient Organic Devices Based on Electrically Doped Transport Layers", *Chemical Reviews* **107**(4), pp. 1233–1271 (2007).

[66] H. Kleemann, C. Schuenemann, A. A. Zakhidov, M. Riede, B. Lüssem, and K. Leo, "Structural phase transition in pentacene caused by molecular doping and its effect on charge carrier mobility", *Organic Electronics* **13**(1), pp. 58 – 65 (2012).

[67] V. I. Arkhipov, P. Heremans, E. V. Emelianova, and H. Bässler, "Effect of doping on the density-of-states distribution and carrier hopping in disordered organic semiconductors", *Phys. Rev. B* **71**(4), 045214 (2005).

[68] J. Blochwitz, M. Pfeiffer, T. Fritz, and K. Leo, "Low voltage organic light emitting diodes featuring doped phthalocyanine as hole transport material", *Applied Physics Letters* **73**(6), pp. 729–731 (1998).

[69] R. Krause, F. Steinbacher, G. Schmid, J. H. Wemken, and A. Hunze, "Cheap p- and n-doping for highly efficient organic devices", *Journal of Photonics for Energy* **1**(1), 011022 (2011).

[70] P. K. Koech, A. B. Padmaperuma, L. Wang, J. S. Swensen, E. Polikarpov, J. T. Darsell, J. E. Rainbolt, and D. J. Gaspar, "Synthesis and Application of 1,3,4,5,7,8-Hexafluorotetracyanonaphthoquinodimethane (F6-TNAP): A Conductivity Dopant for Organic Light-Emitting Devices", *Chemistry of Materials* **22**(13), pp. 3926–3932 (2010).

[71] B. Männig, M. Pfeiffer, A. Nollau, X. Zhou, K. Leo, and P. Simon, "Controlled p-type doping of polycrystalline and amorphous organic layers: Self-consistent description of conductivity and field-effect mobility by a microscopic percolation model", *Phys. Rev. B* **64**(19), 195208 (2001).

[72] K. S. Yook, S. O. Jeon, S.-Y. Min, J. Y. Lee, H.-J. Yang, T. Noh, S.-K. Kang, and T.-W. Lee, "Highly Efficient p-i-n and Tandem Organic Light-Emitting Devices Using an Air-Stable and Low-Temperature-Evaporable Metal Azide as an n-Dopant", *Advanced Functional Materials* **20**(11), pp. 1797–1802 (2010).

[73] S.-Y. Chen, T.-Y. Chu, J.-F. Chen, C.-Y. Su, and C. H. Chen, "Stable inverted bottom-emitting organic electroluminescent devices with molecular doping and morphology improvement", *Applied Physics Letters* **89**(5), 053518 (2006).

[74] T. Xiong, F. Wang, X. Qiao, and D. Ma, "Cesium hydroxide doped tris-(8-hydroxyquinoline) aluminum as an effective electron injection layer in inverted bottom-emission organic light emitting diodes", *Applied Physics Letters* **92**(26), 263305 (2008).

[75] A. Nollau, M. Pfeiffer, T. Fritz, and K. Leo, "Controlled n-type doping of a molecular organic semiconductor: Naphthalenetetracarboxylic dianhydride (NTCDA) doped with bis(ethylenedithio)-tetrathiafulvalene (BEDT-TTF)", *Journal of Applied Physics* **87**(9), pp. 4340–4343 (2000).

[76] F. Li, M. Pfeiffer, A. Werner, K. Harada, K. Leo, N. Hayashi, K. Seki, X. Liu, and X.-D. Dang, "Acridine orange base as a dopant for n doping of C[sub 60] thin films", *Journal of Applied Physics* **100**(2), 023716 (2006).

[77] A. G. Werner, F. Li, K. Harada, M. Pfeiffer, T. Fritz, and K. Leo, "Pyronin B as a donor for n-type doping of organic thin films", *Applied Physics Letters* **82**(25), pp. 4495–4497 (2003).

[78] A. Werner, F. Li, K. Harada, M. Pfeiffer, T. Fritz, K. Leo, and S. Machill, "n-Type Doping of Organic Thin Films Using Cationic Dyes", *Advanced Functional Materials* **14**(3), pp. 255–260 (2004).

[79] C. J. Bloom, C. M. Elliott, P. G. Schroeder, C. B. France, and B. A. Parkinson, "Low Work Function Reduced Metal Complexes as Cathodes in Organic Electroluminescent Devices", *The Journal of Physical Chemistry B* **107**(13), pp. 2933–2938 (2003).

[80] K. Harada, A. G. Werner, M. Pfeiffer, C. J. Bloom, C. M. Elliott, and K. Leo, "Organic Homojunction Diodes with a High Built-in Potential:

Interpretation of the Current-Voltage Characteristics by a Generalized Einstein Relation", *Phys. Rev. Lett.* **94**(3), 036601 (2005).

[81] P. Wei, J. H. Oh, G. Dong, and Z. Bao, "Use of a 1H-Benzoimidazole Derivative as an n-Type Dopant and To Enable Air-Stable Solution-Processed n-Channel Organic Thin-Film Transistors", *Journal of the American Chemical Society* **132**(26), pp. 8852–8853 (2010).

[82] T. Menke, D. Ray, J. Meiss, K. Leo, and M. Riede, "In-situ conductivity and Seebeck measurements of highly efficient n-dopants in fullerene C_{60}", *Applied Physics Letters* **100**(9), 093304 (2012).

[83] G. Parthasarathy, C. Shen, A. Kahn, and S. R. Forrest, "Lithium doping of semiconducting organic charge transport materials", *Journal of Applied Physics* **89**(9), pp. 4986–4992 (2001).

[84] H. Yersin, "Triplet Emitters for OLED Applications. Mechanisms of Exciton Trapping and Control of Emission Properties", in *Transition Metal and Rare Earth Compounds*, H. Yersin, ed., **241**, pp. 1–26, Springer Berlin / Heidelberg (2004).

[85] M. Levichkova, *Influence of the Matrix Environment on the Optical Properties of Incorporated Dye Molecules.* PhD thesis, Technische Universität Dresden (2007).

[86] M. Klessinger and J. Michl, *Excited States and Photochemistry of Organic Molecules*, John Wiley & Sons, 1st ed. (1995).

[87] M. E. Thompson, "The Evolution of Organometallic Complexes in Organic Light-Emitting Devices", *MRS Bulletin* **32**, pp. 694–701 (2007).

[88] V. Bulović, G. Gu, P. E. Burrows, S. Forrest, and M. E. Thompson, "Transparent light-emitting devices", *Nature* **380**(6569), pp. 29–29 (1996).

[89] G. Gu, V. Bulović, P. E. Burrows, S. R. Forrest, and M. E. Thompson, "Transparent organic light emitting devices", *Applied Physics Letters* **68**(19), pp. 2606–2608 (1996).

[90] G. Parthasarathy, P. E. Burrows, V. Khalfin, V. G. Kozlov, and S. R. Forrest, "A metal-free cathode for organic semiconductor devices", *Applied Physics Letters* **72**(17), pp. 2138–2140 (1998).

[91] J. Lee, S. Hofmann, M. Thomschke, M. Furno, Y. H. Kim, B. Lüssem, and K. Leo, "Highly efficient bi-directional organic light-emitting diodes

by strong micro-cavity effects", *Applied Physics Letters* **99**(7), 073303 (2011).

[92] Y. Park, V. Choong, Y. Gao, B. R. Hsieh, and C. W. Tang, "Work function of indium tin oxide transparent conductor measured by photoelectron spectroscopy", *Applied Physics Letters* **68**(19), pp. 2699–2701 (1996).

[93] T. Ishida, H. Kobayashi, and Y. Nakato, "Structures and properties of electron-beam-evaporated indium tin oxide films as studied by x-ray photoelectron spectroscopy and work-function measurements", *Journal of Applied Physics* **73**(9), pp. 4344–4350 (1993).

[94] M. Agrawal, Y. Sun, S. R. Forrest, and P. Peumans, "Enhanced outcoupling from organic light-emitting diodes using aperiodic dielectric mirrors", *Applied Physics Letters* **90**(24), 241112 (2007).

[95] T. Minami, "Transparent conducting oxide semiconductors for transparent electrodes", *Semiconductor Science and Technology* **20**(4), S35 (2005).

[96] L. Wang, J. S. Swensen, E. Polikarpov, D. W. Matson, C. C. Bonham, W. Bennett, D. J. Gaspar, and A. B. Padmaperuma, "Highly efficient blue organic light-emitting devices with indium-free transparent anode on flexible substrates", *Organic Electronics* **11**(9), pp. 1555 – 1560 (2010).

[97] G. Parthasarathy, C. Adachi, P. E. Burrows, and S. R. Forrest, "High-efficiency transparent organic light-emitting devices", *Applied Physics Letters* **76**(15), pp. 2128–2130 (2000).

[98] D. R. Baigent, R. N. Marks, N. C. Greenham, R. H. Friend, S. C. Moratti, and A. B. Holmes, "Conjugated polymer light-emitting diodes on silicon substrates", *Applied Physics Letters* **65**(21), pp. 2636–2638 (1994).

[99] H. Kim, T. Miller, E. Westerwick, Y. Kim, E. Kwock, M. Morris, and M. Cerullo, "Silicon compatible organic light emitting diode", *Journal of Lightwave Technology* **12**, pp. 2107 –2113 (dec 1994).

[100] C.-W. Chen, P.-Y. Hsieh, H.-H. Chiang, C.-L. Lin, H.-M. Wu, and C.-C. Wu, "Top-emitting organic light-emitting devices using surface-modified Ag anode", *Applied Physics Letters* **83**(25), pp. 5127–5129 (2003).

[101] H. Gothe, "Kombination von organischen Leuchtdioden mit Mikroresonatoren", Diploma thesis, TU Dresden (2006).

[102] J. M. Bharathan and Y. Yang, "Polymer/metal interfaces and the performance of polymer light-emitting diodes", *Journal of Applied Physics* **84**(6), pp. 3207–3211 (1998).

[103] J. Huang, M. Pfeiffer, A. Werner, J. Blochwitz, K. Leo, and S. Liu, "Low-voltage organic electroluminescent devices using pin structures", *Applied Physics Letters* **80**(1), pp. 139–141 (2002).

[104] R. Meerheim, K. Walzer, G. He, M. Pfeiffer, and K. Leo, "Highly efficient organic light emitting diodes (OLED) for diplays and lighting", in *Proc. SPIE*, P. L. Heremans, M. Muccini, and E. A. Meulenkamp, eds., *Organic Optoelectronics and Photonics II* **6192**(1), 61920P, SPIE (2006).

[105] R. Meerheim, R. Nitsche, and K. Leo, "High-efficiency monochrome organic light emitting diodes employing enhanced microcavities", *Applied Physics Letters* **93**(4), 043310 (2008).

[106] R. Meerheim, K. Walzer, M. Pfeiffer, and K. Leo, "Ultrastable and efficient red organic light emitting diodes with doped transport layers", *Applied Physics Letters* **89**(6), 061111 (2006).

[107] H. You, Y. Dai, Z. Zhang, and D. Ma, "Improved performances of organic light-emitting diodes with metal oxide as anode buffer", *Journal of Applied Physics* **101**(2), 026105 (2007).

[108] L. S. Hung, C. W. Tang, and M. G. Mason, "Enhanced electron injection in organic electroluminescence devices using an Al/LiF electrode", *Applied Physics Letters* **70**(2), pp. 152–154 (1997).

[109] C. C. Wu, C. I. Wu, J. C. Sturm, and A. Kahn, "Surface modification of indium tin oxide by plasma treatment: An effective method to improve the efficiency, brightness, and reliability of organic light emitting devices", *Applied Physics Letters* **70**(11), pp. 1348–1350 (1997).

[110] S. Olthof, R. Meerheim, M. Schober, and K. Leo, "Energy level alignment at the interfaces in a multilayer organic light-emitting diode structure", *Phys. Rev. B* **79**(24), 245308 (2009).

[111] G. A. H. Wetzelaer, M. Kuik, H. T. Nicolai, and P. W. M. Blom, "Trap-assisted and Langevin-type recombination in organic light-emitting diodes", *Phys. Rev. B* **83**, 165204 (2011).

[112] P. Langevin, "Recombinaison et mobilites des ions dans les gaz", *Annales de chimie et de physique* **28**, 433 (1903).

[113] U. Albrecht and H. Bässler, "Efficiency of charge recombination in organic light emitting diodes", *Chemical Physics* **199**(2-3), pp. 207 – 214 (1995).

[114] T. Förster, "Zwischenmolekulare Energiewanderung und Fluoreszenz", *Annalen der Physik* **437**(1-2), pp. 55–75 (1948).

[115] D. L. Dexter, "A Theory of Sensitized Luminescence in Solids", *Journal of Chemical Physics* **21**(5), pp. 836–850 (1953).

[116] R. R. Lunt, N. C. Giebink, A. A. Belak, J. B. Benziger, and S. R. Forrest, "Exciton diffusion lengths of organic semiconductor thin films measured by spectrally resolved photoluminescence quenching", *Journal of Applied Physics* **105**(5), 053711 (2009).

[117] J. Wünsche, S. Reineke, B. Lüssem, and K. Leo, "Measurement of triplet exciton diffusion in organic light-emitting diodes", *Phys. Rev. B* **81**(24), 245201 (2010).

[118] M. A. Baldo, C. Adachi, and S. R. Forrest, "Transient analysis of organic electrophosphorescence. II. Transient analysis of triplet-triplet annihilation", *Phys. Rev. B* **62**, pp. 10967–10977 (Oct 2000).

[119] S. Reineke, K. Walzer, and K. Leo, "Triplet-exciton quenching in organic phosphorescent light-emitting diodes with Ir-based emitters", *Phys. Rev. B* **75**(12), 125328 (2007).

[120] O. S. Heavens, *Optical Properties of Thin Solid Films*, Dover Publications, 2nd ed. (1991).

[121] P. Yeh, *Optical Waves in Layered Media*, Wiley series in pure and applied optics, WILEY (1988).

[122] K. G. Sullivan and D. G. Hall, "Enhancement and inhibition of electromagnetic radiation in plane-layered media. I.Plane-wave spectrum approach to modeling classical effects", *J. Opt. Soc. Am. B* **14**, pp. 1149–1159 (1997).

[123] H. Benisty, R. Stanley, and M. Mayer, "Method of source terms for dipole emission modification in modes of arbitrary planar structures", *J. Opt. Soc. Am. A* **15**(5), pp. 1192–1201 (1998).

[124] K. A. Neyts, "Simulation of light emission from thin-film microcavities", *J. Opt. Soc. Am. A* **15**(4), pp. 962–971 (1998).

[125] J. A. E. Wasey and W. L. Barnes, "Efficiency of spontaneous emission from planar microcavities", *Journal of Modern Optics* **47**(4), pp. 4495–4497 (2000).

[126] E. M. Purcell, H. C. Torrey, and R. V. Pound, "Resonance Absorption by Nuclear Magnetic Moments in a Solid", *Phys. Rev.* **69**(1-2), pp. 37–38 (1946).

[127] Q. Huang, S. Reineke, K. Walzer, M. Pfeiffer, and K. Leo, "Quantum efficiency enhancement in top-emitting organic light-emitting diodes as a result of enhanced intrinsic quantum yield", *Applied Physics Letters* **89**(26), 263512 (2006).

[128] M. Furno, R. Meerheim, S. Hofmann, B. Lüssem, and K. Leo, "Efficiency and rate of spontaneous emission in organic electroluminescent devices", *Phys. Rev. B* **85**, 115205 (Mar 2012).

[129] L. H. Smith, J. A. E. Wasey, and W. L. Barnes, "Light outcoupling efficiency of top-emitting organic light-emitting diodes", *Applied Physics Letters* **84**(16), pp. 2986–2988 (2004).

[130] S. Nowy, B. C. Krummacher, J. Frischeisen, N. A. Reinke, and W. Brütting, "Light extraction and optical loss mechanisms in organic light-emitting diodes: Influence of the emitter quantum efficiency", *Journal of Applied Physics* **104**(12), 123109 (2008).

[131] D. S. Setz, T. D. Schmidt, M. Flämmich, S. Nowy, J. Frischeisen, B. C. Krummacher, T. Dobbertin, K. Heuser, D. Michaelis, N. Danz, W. Brütting, and A. Winnacker, "Comprehensive efficiency analysis of organic light-emitting devices", *Journal of Photonics for Energy* **1**(1), 011006 (2011).

[132] Y. Kawamura, K. Goushi, J. Brooks, J. J. Brown, H. Sasabe, and C. Adachi, "100semiconductor films", *Applied Physics Letters* **86**(7), 071104 (2005).

[133] D. Tanaka, H. Sasabe, Y.-J. Li, S.-J. Su, T. Takeda, and J. Kido, "Ultra High Efficiency Green Organic Light-Emitting Devices", *Japanese Journal of Applied Physics* **46**(1), pp. L10–L12 (2007).

[134] R. Meerheim, M. Furno, S. Hofmann, B. Lüssem, and K. Leo, "Quantification of energy loss mechanisms in organic light-emitting diodes", *Applied Physics Letters* **97**(25), 253305 (2010).

[135] M. C. Gather, M. Flämmich, N. Danz, D. Michaelis, and K. Meerholz, "Measuring the profile of the emission zone in polymeric organic light-emitting diodes", *Applied Physics Letters* **94**(26), 263301 (2009).

[136] S. L. M. van Mensfoort, M. Carvelli, M. Megens, D. Wehenkel, M. Bartyzel, H. Greiner, R. A. J. Janssen, and R. Coehoorn, "Measuring the light emission profile in organic light-emitting diodes with nanometre spatial resolution", *Nature Photonics* **4**(5), pp. 329–335 (2010).

[137] D. Yokoyama and C. Adachi, "In situ real-time spectroscopic ellipsometry measurement for the investigation of molecular orientation in organic amorphous multilayer structures", *Journal of Applied Physics* **107**(12), 123512 (2010).

[138] J. Frischeisen, D. Yokoyama, C. Adachi, and W. Brütting, "Determination of molecular dipole orientation in doped fluorescent organic thin films by photoluminescence measurements", *Applied Physics Letters* **96**(7), 073302 (2010).

[139] T. D. Schmidt, D. S. Setz, M. Flämmich, J. Frischeisen, D. Michaelis, B. C. Krummacher, N. Danz, and W. Brütting, "Evidence for non-isotropic emitter orientation in a red phosphorescent organic light-emitting diode and its implications for determining the emitter's radiative quantum efficiency", *Applied Physics Letters* **99**, 163302 (2011).

[140] H. Becker, S. E. Burns, N. Tessler, and R. H. Friend, "Role of optical properties of metallic mirrors in microcavity structures", *Journal of Applied Physics* **81**(6), pp. 2825–2829 (1997).

[141] K. Saxena, V. Jain, and D. S. Mehta, "A review on the light extraction techniques in organic electroluminescent devices", *Optical Materials* **32**(1), pp. 221 – 233 (2009).

[142] H. Greiner, "Light Extraction from Organic Light Emitting Diode Substrates: Simulation and Experiment", *Japanese Journal of Applied Physics* **46**(7A), pp. 4125–4137 (2007).

[143] H. Peng, X. Zhu, J. Sun, Z. Xie, S. Xie, M. Wong, and H.-S. Kwok, "Efficient organic light-emitting diode using semitransparent silver as anode", *Applied Physics Letters* **87**(17), 173505 (2005).

[144] D. P. Puzzo, M. G. Helander, P. G. O'Brien, Z. Wang, N. Soheilnia, N. Kherani, Z. Lu, and G. A. Ozin, "Organic Light-Emitting Diode Microcavities from Transparent Conducting Metal Oxide Photonic Crystals", *Nano Letters* **11**(4), pp. 1457–1462 (2011).

[145] P. Hobson, S. Wedge, J. Wasey, I. Sage, and W. Barnes, "Surface Plasmon Mediated Emission from Organic Light-Emitting Diodes", *Adv. Mat.* **14**(19), 1393–1396 (2002).

[146] L. S. Hung, C. W. Tang, M. G. Mason, P. Raychaudhuri, and J. Madathil, "Application of an ultrathin LiF/Al bilayer in organic surface-emitting diodes", *Applied Physics Letters* **78**(4), pp. 544–546 (2001).

[147] H. Riel, S. Karg, T. Beierlein, W. Riess, and K. Neyts, "Tuning the emission characteristics of top-emitting organic light-emitting devices by means of a dielectric capping layer: An experimental and theoretical study", *Journal of Applied Physics* **94**(8), pp. 5290–5296 (2003).

[148] Q. Huang, K. Walzer, M. Pfeiffer, V. Lyssenko, G. He, and K. Leo, "Highly efficient top emitting organic light-emitting diodes with organic outcoupling enhancement layers", *Applied Physics Letters* **88**(11), 113515 (2006).

[149] Q. Huang, K. Walzer, M. Pfeiffer, K. Leo, M. Hofmann, and T. Stubinger, "Performance improvement of top-emitting organic light-emitting diodes by an organic capping layer: An experimental study", *Journal of Applied Physics* **100**(6), 064507 (2006).

[150] S.-F. Hsu, C.-C. Lee, S.-W. Hwang, and C. H. Chen, "Highly efficient top-emitting white organic electroluminescent devices", *Applied Physics Letters* **86**(25), 253508 (2005).

[151] X. Zhu, J. Sun, X. Yu, M. Wong, and H.-S. Kwok, "High-Performance Top-Emitting White Organic Light-Emitting Devices", *Japanese Journal of Applied Physics* **46**(7A), pp. 4054–4058 (2007).

[152] V. Bulović, P. Tian, P. E. Burrows, M. R. Gokhale, S. R. Forrest, and M. E. Thompson, "A surface-emitting vacuum-deposited organic light emitting device", *Applied Physics Letters* **70**(22), pp. 2954–2954 (1997).

[153] H. Lee, Y.-C. Lin, H.-P. Shieh, and J. Kanicki, "Current-Scaling a-Si:H TFT Pixel-Electrode Circuit for AM-OLEDs: Electrical Properties and Stability", *IEEE Transactions on Electron Devices* **54**(9), pp. 2403–2410 (2007).

[154] C.-W. Han, M.-K. Han, M. Kim, W.-J. Nam, S.-J. Bae, K.-Y. Kim, and I.-J. Chung, "Top-emitting OLED pixel employing cathode-contact structure with a-Si:H thin-film transistors", *Electronics Letters* **43**(11), pp. 623–624 (2007).

[155] N. J. Watkins, L. Yan, and Y. Gao, "Electronic structure symmetry of interfaces between pentacene and metals", *Applied Physics Letters* **80**(23), pp. 4384–4386 (2002).

[156] W. Song, S. K. So, J. Moulder, Y. Qiu, Y. Zhu, and L. Cao, "Study on the interaction between Ag and tris(8-hydroxyquinoline) aluminum using x-ray photoelectron spectroscopy", *Surface and Interface Analysis* **32**(1), pp. 70–73 (2001).

[157] C. Shen, A. Kahn, and J. Schwartz, "Chemical and electrical properties of interfaces between magnesium and aluminum and tris-(8-hydroxy quinoline) aluminum", *Journal of Applied Physics* **89**(1), pp. 449–459 (2001).

[158] H. Lee, I. Park, J. Kwak, D. Y. Yoon, and C. Lee, "Improvement of electron injection in inverted bottom-emission blue phosphorescent organic light emitting diodes using zinc oxide nanoparticles", *Applied Physics Letters* **96**(15), 153306 (2010).

[159] C. Yun, H. Cho, H. Kang, Y. M. Lee, Y. Park, and S. Yoo, "Electron injection via pentacene thin films for efficient inverted organic light-emitting diodes", *Applied Physics Letters* **95**(5), 053301 (2009).

[160] X. Zhou, M. Pfeiffer, J. S. Huang, J. Blochwitz-Nimoth, D. S. Qin, A. Werner, J. Drechsel, B. Maennig, and K. Leo, "Low-voltage inverted transparent vacuum deposited organic light-emitting diodes using electrical doping", *Applied Physics Letters* **81**(5), pp. 922–924 (2002).

[161] H. W. Choi, S. Y. Kim, W.-K. Kim, and J.-L. Lee, "Enhancement of electron injection in inverted top-emitting organic light-emitting diodes using an insulating magnesium oxide buffer layer", *Applied Physics Letters* **87**(8), 082102 (2005).

[162] Q. Wang, Z. Deng, and D. Ma, "Highly efficient inverted top-emitting organic light-emitting diodes using a lead monoxide electron injection layer", *Opt. Express* **17**(20), pp. 17269–17278 (2009).

[163] J. Meyer, T. Winkler, S. Hamwi, S. Schmale, H.-H. Johannes, T. Weimann, P. Hinze, W. Kowalsky, and T. Riedl, "Transparent Inverted Organic Light-Emitting Diodes with a Tungsten Oxide Buffer Layer", *Advanced Materials* **20**(20), pp. 3839–3843 (2008).

[164] K. Hong, K. Kim, and J.-L. Lee, "Enhancement of electrical property by oxygen doping to copper phthalocyanine in inverted top emitting organic light emitting diodes", *Applied Physics Letters* **95**(21), 213307 (2009).

[165] K.-H. Kim, S.-Y. Huh, S.-M. Seo, and H. H. Lee, "Inverted top-emitting organic light-emitting diodes by whole device transfer", *Organic Electronics* **9**(6), pp. 1118 – 1121 (2008).

[166] P.-S. Wang, I.-W. Wu, and C.-I. Wu, "Enhancement of current injection in inverted organic light emitting diodes with thermal annealing", *Journal of Applied Physics* **108**(10), 103714 (2010).

[167] J. X. Sun, X. Zhu, M. Yu, H. Peng, M. Wong, and H. Kwok, "Improving the performance of organic light-emitting diodes containing BCP/LiF/Al by thermal annealing", *Journal of Display Technology* **2**(2), pp. 138–142 (2006).

[168] G.-T. Chen, S.-H. Su, C.-C. Hou, and M. Yokoyama, "Effects of Thermal Annealing on Performance of Organic Light-Emitting Diodes", *Journal of The Electrochemical Society* **154**(5), pp. J159–J162 (2007).

[169] L. Li, W. Hu, H. Fuchs, and L. Chi, "Controlling Molecular Packing for Charge Transport in Organic Thin Films", *Advanced Energy Materials* **1**(2), pp. 188–193 (2011).

[170] D. Wynands, M. Levichkova, M. Riede, M. Pfeiffer, P. Baeuerle, R. Rentenberger, P. Denner, and K. Leo, "Correlation between morphology and performance of low bandgap oligothiophene:C60 mixed heterojunctions in organic solar cells", *Journal of Applied Physics* **107**(1), 014517 (2010).

[171] S. Caria, E. D. Como, M. Murgia, R. Zamboni, P. Melpignano, and V. Biondo, "Enhanced light emission efficiency and current stability by morphology control and thermal annealing of organic light emitting diode devices", *Journal of Physics: Condensed Matter* **18**(33), S2139 (2006).

[172] K. B. Krueger, P. E. Schwenn, K. Gui, A. Pivrikas, P. Meredith, and P. L. Burn, "Morphology dependent electron transport in an n-type electron accepting small molecule for solar cell applications", *Applied Physics Letters* **98**(8), 083301 (2011).

[173] S. Pfützner, C. Mickel, J. Jankowski, M. Hein, J. Meiss, C. Schuenemann, C. Elschner, A. A. Levin, B. Rellinghaus, K. Leo, and M. Riede, "The influence of substrate heating on morphology and layer growth in C60:ZnPc bulk heterojunction solar cells", *Organic Electronics* **12**(3), pp. 435 – 441 (2011).

[174] C. Lee, A. Uddin, X. Hu, and T. Andersson, "Study of Alq3 thermal evaporation rate effects on the OLED", *Materials Science and Engineering: B* **112**(1), pp. 14 – 18 (2004).

[175] M.-H. Wang, T. Konya, M. Yahata, Y. Sawada, A. Kishi, T. Uchida, H. Lei, Y. Hoshi, and L.-X. Sun, "Thermal change of organic light-emitting ALQ3 thin films", *Journal of Thermal Analysis and Calorimetry* **99**, pp. 117–122 (2010).

[176] A. R. G. Smith, J. L. Ruggles, H. Cavaye, P. E. Shaw, T. A. Darwish, M. James, I. R. Gentle, and P. L. Burn, "Investigating Morphology and Stability of Fac-tris (2-phenylpyridyl)iridium(III) Films for OLEDs", *Advanced Functional Materials* **21**(12), pp. 2225–2231 (2011).

[177] J. Cui, Q. Huang, J. C. G. Veinot, H. Yan, Q. Wang, G. R. Hutchison, A. G. Richter, G. Evmenenko, P. Dutta, and T. J. Marks, "Anode Interfacial Engineering Approaches to Enhancing Anode/Hole Transport Layer Interfacial Stability and Charge Injection Efficiency in Organic Light-Emitting Diodes", *Langmuir* **18**(25), pp. 9958–9970 (2002).

[178] D. Loy, B. Koene, and M. Thompson, "Thermally Stable Hole-Transporting Materials Based upon a Fluorene Core", *Advanced Functional Materials* **12**(4), pp. 245–249 (2002).

[179] K. Osipov, V. Pavlovskii, E. Lutsenko, A. Gurskii, G. Yablonskii, S. Hartmann, A. Janssen, H.-H. Johannes, R. Caspary, W. Kowalsky, N. Meyer, M. Gersdorff, M. Heuken, P. van Gemmern, C. Zimmermann, F. Jessen, H. Kalisch, and R. Jansen, "Influence of thermal annealing on photoluminescence and structural properties of N,N'-diphenyl-N,N'-bis(1-naphthylphenyl)-1,1'-biphenyl-4,4'-diamine (α-NPD) organic thin films", *Thin Solid Films* **515**(11), pp. 4834 – 4837 (2007).

[180] B. W. D'Andrade, S. R. Forrest, and A. B. Chwang, "Operational stability of electrophosphorescent devices containing p and n doped transport layers", *Applied Physics Letters* **83**(19), pp. 3858–3860 (2003).

[181] R. S. Sennett and G. D. Scott, "The Structure of Evaporated Metal Films and Their Optical Properties", *J. Opt. Soc. Am.* **40**, pp. 203–210 (1950).

[182] P. L. Clegg, "The Optical Constants of Thin Metallic Films Deposited by Evaporation", *Proceedings of the Physical Society. Section B* **65**(10), 774 (1952).

[183] F. Goos, "Durchlässigkeit und Reflexionsvermögen dünner Silber-schichten von Ultrarot bis Ultraviolett", *Zeitschrift für Physik* **100**, pp. 95–112 (1936).

[184] H. Murmann, "Der spektrale Verlauf der anomalen optischen Konstanten dünnen Silbers", *Zeitschrift für Physik* **101**, pp. 643–648 (1936).

[185] J. Seidel, *Propagation, Scattering and Amplification of Surface Plasmons in Thin Silver Films*. PhD thesis, Technische Universität Dresden (2005).

[186] S. Olthof, J. Meiss, B. Lüssem, M. Riede, and K. Leo, "Photoelectron spectroscopy investigation of thin metal films employed as top contacts in transparent organic solar cells", *Thin Solid Films* **519**(6), pp. 1872 – 1875 (2011).

[187] M. Volmer and A. Weber, "Keimbildung in übersättigten Gebilden", *Z. phys. Chem.* **119**, pp. 277–301 (1926).

[188] F. C. Frank and J. H. van der Merwe, "One-Dimensional Dislocations. I. Static Theory", *Proceedings of the Royal Society of London A* **198**(1053), pp. 205–216 (1949).

[189] E. Bauer, "Phänomenologische Theorie der Kristallabscheidung an Ober-flächen. I", *Zeitschrift für Kristallographie* **110**(1-6), pp. 372–394 (1958).

[190] J. Lee, N. Chopra, and F. So, "Cavity effects on light extraction in organic light emitting devices", *Applied Physics Letters* **92**(3), 033303 (2008).

[191] J. R. Macdonald, *Impedance Spectroscopy - Emphasizing Solid Materials and Systems*, John Wiley & Sons Inc. (1987).

[192] B. J. Leever, C. A. Bailey, T. J. Marks, M. C. Hersam, and M. F. Dur-stock, "In Situ Characterization of Lifetime and Morphology in Oper-ating Bulk Heterojunction Organic Photovoltaic Devices by Impedance Spectroscopy", *Advanced Energy Materials* **2**(1), pp. 120–128 (2012).

[193] H. Kleemann, R. Gutierrez, F. Lindner, S. Avdoshenko, P. D. Man-rique, B. Lüssem, G. Cuniberti, and K. Leo, "Organic Zener Diodes: Tunneling across the Gap in Organic Semiconductor Materials", *Nano Letters* **10**(12), pp. 4929–4934 (2010).

[194] J. Lee, D. Hwang, C. Park, S. Kim, and S. Im, "Pentacene-based pho-todiode with Schottky junction", *Thin Solid Films* **451-452**(0), pp. 12 – 15 (2004).

[195] W. Brütting, *Physics of Organic Semiconductors*, Wiley-V C H Verlag GmbH (2005).

[196] H. B. Michaelson, "The work function of the elements and its periodicity", *Journal of Applied Physics* **48**(11), pp. 4729–4733 (1977).

[197] K. Fehse, *Organische Leuchtdioden mit Polymeranoden*. PhD thesis, Technische Universität Dresden (2007).

[198] G. Hass and J. E. Waylonis, "Optical Constants and Reflectance and Transmittance of Evaporated Aluminum in the Visible and Ultraviolet", *J. Opt. Soc. Am.* **51**(7), pp. 719–722 (1961).

[199] F. Ma and X. Liu, "Phase shift and penetration depth of metal mirrors in a microcavity structure", *Appl. Opt.* **46**(25), pp. 6247–6250 (2007).

[200] A. D. Rakic, A. B. Djurišic, J. M. Elazar, and M. L. Majewski, "Optical Properties of Metallic Films for Vertical-Cavity Optoelectronic Devices", *Appl. Opt.* **37**(22), pp. 5271–5283 (1998).

[201] D. Deppe, C. Lei, C. C. Lin, and D. L. Huffaker, "Spontaneous Emission from Planar Microstructures", *Journal of Modern Optics* **41**(2), pp. 325–344 (1994).

[202] S. Hofmann, M. Thomschke, P. Freitag, M. Furno, B. Lüssem, and K. Leo, "Top-emitting organic light-emitting diodes: Influence of cavity design", *Applied Physics Letters* **97**(25), 253308 (2010).

[203] M. Furno, R. Meerheim, M. Thomschke, S. Hofmann, B. Lüssem, and K. Leo, "Outcoupling efficiency in small-molecule OLEDs: from theory to experiment", in *Proc. SPIE*, K. P. Streubel, H. Jeon, L.-W. Tu, and N. Linder, eds., *Light-Emitting Diodes: Materials, Devices, and Applications for Solid State Lighting XIV* **7617**(1), 761716, SPIE (2010).

[204] H. Kanno, Y. Sun, and S. R. Forrest, "High-efficiency top-emissive white-light-emitting organic electrophosphorescent devices", *Applied Physics Letters* **86**(26), 263502 (2005).

[205] G. Schwartz, K. Fehse, M. Pfeiffer, K. Walzer, and K. Leo, "Highly efficient white organic light emitting diodes comprising an interlayer to separate fluorescent and phosphorescent regions", *Applied Physics Letters* **89**(8), 083509 (2006).

[206] P. Freitag, S. Reineke, S. Olthof, M. Furno, B. Lüssem, and K. Leo, "White top-emitting organic light-emitting diodes with forward directed

189

emission and high color quality", *Organic Electronics* **11**(10), pp. 1676 – 1682 (2010).

[207] S. Möller and S. R. Forrest, "Improved light out-coupling in organic light emitting diodes employing ordered microlens arrays", *Journal of Applied Physics* **91**(5), pp. 3324–3327 (2002).

[208] C.-J. Yang, S.-H. Liu, H.-H. Hsieh, C.-C. Liu, T.-Y. Cho, and C.-C. Wu, "Microcavity top-emitting organic light-emitting devices integrated with microlens arrays: Simultaneous enhancement of quantum efficiency, cd/A efficiency, color performances, and image resolution", *Applied Physics Letters* **91**(25), 253508 (2007).

[209] M. Xu, J. Xu, and J. An, "Visualization of thermally activated morphology evolution of N, N'-di(naphthalene-1-yl)- N, N'-diphthalbenzidine films on ITO/copper phthalocyanine underlying layer", *Applied Physics A: Materials Science & Processing* **81**, pp. 1151–1156 (2005).

[210] T. C. Rosenow, M. Furno, S. Reineke, S. Olthof, B. Lüssem, and K. Leo, "Highly efficient white organic light-emitting diodes based on fluorescent blue emitters", *Journal of Applied Physics* **108**(11), 113113 (2010).

[211] N. Tessler, S. Burns, H. Becker, and R. H. Friend, "Suppressed angular color dispersion in planar microcavities", *Applied Physics Letters* **70**(5), pp. 556–558 (1997).

[212] M. Thomschke, R. Nitsche, M. Furno, and K. Leo, "Optimized efficiency and angular emission characteristics of white top-emitting organic electroluminescent diodes", *Applied Physics Letters* **94**(8), 083303 (2009).

[213] D. Yokoyama, "Molecular orientation in small-molecule organic light-emitting diodes", *J. Mater. Chem.* **21**, pp. 19187–19202 (2011).

[214] R. Meerheim, S. Scholz, S. Olthof, G. Schwartz, S. Reineke, K. Walzer, and K. Leo, "Influence of charge balance and exciton distribution on efficiency and lifetime of phosphorescent organic light-emitting devices", *Journal of Applied Physics* **104**(1), 014510 (2008).

[215] C. Shen, I. G. Hill, and A. Kahn, "Role of Electrode Contamination in Electron Injection at Mg:Ag/Alq3 Interfaces", *Advanced Materials* **11**(18), pp. 1523–1527 (1999).

[216] Z. B. Wang, M. G. Helander, Z. W. Liu, M. T. Greiner, J. Qiu, and Z. H. Lu, "Controlling carrier accumulation and exciton formation in organic light emitting diodes", *Applied Physics Letters* **96**(4), 043303 (2010).

[217] H. Aziz, Y.-F. Liew, H. M. Grandin, and Z. D. Popovic, "Reduced reflectance cathode for organic light-emitting devices using metalorganic mixtures", *Applied Physics Letters* **83**(1), pp. 186–188 (2003).

[218] H. Grandin, H. Aziz, S. Gardner, C. Jennings, A. Paine, P. Norton, and Z. Popovic, "Light-Absorption Phenomena in Novel Low-Reflectance Cathodes for Organic Light-Emitting Devices Utilizing Metal-Organic Mixtures", *Advanced Materials* **15**(23), pp. 2021–2024 (2003).

[219] T.-L. Chiu, W.-F. Xu, C.-F. Lin, J.-H. Lee, C.-C. Chao, and M.-K. Leung, "Optical and electrical characteristics of Ag-doped perylene diimide derivative", *Applied Physics Letters* **94**(1), 013307 (2009).

[220] Q. Huang, *High efficiency top-emitting organic light-emitting diodes: Design and fabrication.* PhD thesis, Technische Universität Dresden (2007).

[221] M. R. J. Meiss and K. Leo, "Optimizing the morphology of metal multi-layer films for indium tin oxide (ITO)-free inverted organic solar cells", *Journal of Applied Physics* **105**, 063108 (2009).

[222] M. Schober, S. Olthof, M. Furno, B. Lüssem, and K. Leo, "Single carrier devices with electrical doped layers for the characterization of charge-carrier transport in organic thin-films", *Applied Physics Letters* **97**(1), 013303 (2010).

[223] M. Schober, M. Anderson, M. Thomschke, J. Widmer, M. Furno, R. Scholz, B. Lüssem, and K. Leo, "Quantitative description of charge-carrier transport in a white organic light-emitting diode", *Phys. Rev. B* **84**, 165326 (2011).

[224] N. Seidler, S. Reineke, K. Walzer, B. Lüssem, A. Tomkeviciene, J. V. Grazulevicius, and K. Leo, "Influence of the hole blocking layer on blue phosphorescent organic light-emitting devices using 3,6-di(9-carbazolyl)-9-(2-ethylhexyl)carbazole as host material", *Applied Physics Letters* **96**(9), 093304 (2010).

[225] S. van Mensfoort, R. de Vries, V. Shabro, H. Loebl, R. Janssen, and R. Coehoorn, "Electron transport in the organic small-molecule material BAlq – the role of correlated disorder and traps", *Organic Electronics* **11**(8), pp. 1408 – 1413 (2010).

[226] Z. B. Wang, M. G. Helander, J. Qiu, D. P. Puzzo, M. T. Greiner, Z. W. Liu, and Z. H. Lu, "Highly simplified phosphorescent organic light emitting diode with >20% external quantum efficiency at >10,000cd/m^2", *Applied Physics Letters* **98**(7), 073310 (2011).

[227] K. Müllen and U. Scherf, *Organic Light Emitting Devices - Synthesis, Properties and Applications*, Wiley-VCH, 1st ed. (2005).

[228] R. Meerheim, *Quanteneffizienz und Langzeitstabilität monochromer organischer Leuchtdioden*. PhD thesis, Technische Universität Dresden (2009).

[229] M. W. Shin, H. C. Lee, K. S. Kim, S.-H. Lee, and J.-C. Kim, "Thermal analysis of Tris (8-hydroxyquinoline) aluminum", *Thin Solid Films* **363**(1-2), pp. 244 – 247 (2000).

[230] J. H. Weaver and H. P. R. Frederikse, *CRC Handbook of Chemistry and Physics*, CRC Press, 88th ed. (2007).

[231] F. So and D. Kondakov, "OLEDs: Degradation Mechanisms in Small-Molecule and Polymer Organic Light-Emitting Diodes", *Advanced Materials* **22**(34), pp. 3762–3777 (2010).

[232] S. Nowy, W. Ren, J. Wagner, J. A. Weber, and W. Brütting, "Impedance spectroscopy of organic hetero-layer OLEDs as a probe for charge carrier injection and device degradation", in *Proc. SPIE*, F. So and C. Adachi, eds., *Organic Light Emitting Materials and Devices XIII* **7415**(1), 74150G, SPIE (2009).

[233] J. Drechsel, B. Männig, D. Gebeyehu, M. Pfeiffer, K. Leo, and H. Hoppe, "MIP-type organic solar cells incorporating phthalocyanine/fullerene mixed layers and doped wide-gap transport layers", *Organic Electronics* **5**(4), pp. 175 – 186 (2004).

[234] M. A. Baldo and S. R. Forrest, "Transient analysis of organic electrophosphorescence: I. Transient analysis of triplet energy transfer", *Phys. Rev. B* **62**, pp. 10958–10966 (Oct 2000).

[235] S. Reineke, *Controlling excitons: Concepts for Phosphorescent Organic LEDs at High Brightness*. PhD thesis, Technische Universität Dresden (2009).

[236] M. Thomschke, S. Reineke, B. Lüssem, and K. Leo, "Highly Efficient White Top-Emitting Organic Light-Emitting Diodes Comprising Laminated Microlens Films", *Nano Letters* **12**, pp. 424–428 (2012).

[237] T. Wagner, "Organische Leuchtdioden auf flexiblen Metallsubstraten", Diploma thesis, Hochschule für Technik und Wirtschaft Dresden (FH) (2006).

[238] P. Freitag, *White Top-Emitting OLEDs on Metal Substrates*. PhD thesis, Technische Universität Dresden (2010).

[239] P. B. Johnson and R. W. Christy, "Optical Constants of the Noble Metals", *Phys. Rev. B* **6**(12), pp. 4370–4379 (1972).

[240] H.-J. Hagemann, W. Gudat, and C. Kunz, "Optical constants from the far infrared to the x-ray region: Mg, Al, Cu, Ag, Au, Bi, C, and Al2O3", *J. Opt. Soc. Am.* **65**(6), pp. 742–744 (1975).

[241] http://www.sspectra.com/sopra.html, "Optical Data from Sopra SA", (may 2011).

[242] T. Fritz, J. Hahn, and H. Böttcher, "Determination of the optical constants of evaporated dye layers", *Thin Solid Films* **170**(2), pp. 249 – 257 (1989).

ABBREVIATIONS

AFM	atomic force microscopy
CIE	commission internationale de l'éclairage
CPE	constant phase element
CRI	color rendering index
EA	electron affinity
EBL	electron blocking layer
EL	electroluminescence
EML	emitting layer
EQE	external quantum efficiency
FWHM	full width half maximum
HBL	hole blocking layer
IP	ionization potential
ITO	indium tin oxide
I-V	current-voltage
LE	luminous efficacy
PL	photoluminescence
TE	transverse electric (s-polarization)
T_g	glass transition temperature
TM	transverse magnetic (p-polarization)
UPS	ultraviolet photoelectron spectroscopy
XRR	X-ray reflectometry

LIST OF CHEMICAL NAMES OF THE USED MATERIALS

Alq$_3$	Tris(8-hydroxyquinolinato)aluminium
BAlq$_2$	Bis(2-methyl-8-quinolinolato)-4-(phenyl-phenolato)aluminum-(III)
BPhen	4,7-diphenyl-1,10-phenanthroline
CuPc	Copper phthalocyanine
Cs	Cesium
F$_4$TCNQ	2,3,5,6-tetrafluoro-7,7,8,8-tetracyanoquino-dimethane
F6TCNNQ	2,2'-(perfluoronaphthalene-2,6-diylidene)-dimalononitrile
Ir(MDQ)$_2$(acac)	Iridium(III)bis(2-methyldibenzo-[f,h]quinoxaline)(acetylacetonate)
Ir(ppy)$_3$	Fac tris(2-phenylpyridine) iridium
MADN	2-methyl-9,10-bis(naphthalen-2-yl)anthracene
MeO-TPD	N,N,N',N'-tetrakis(4-methoxyphenyl)-benzidine
NDP-2	NOVALED p-type dopant 2
NET-18	NOVALED electron transport material 18
NHT-5	NOVALED hole transport material 5
NPB	N,N'-di(naphthalen-1-yl)-N,N'-diphenyl-benzidine
PTCDA	3,4,9,10-perylenetetracarboxylic dianhydride
Spiro-DPVBi	2,2',7,7'-tetrakis(2,2-diphenyl-vinyl)spiro-9,9'-bifluorene
Spiro-TAD	2,2',7,7'-tetrakis-(N,N-diphenylamino)-9,9'-spirobifluoren
Spiro-TTB	2,2',7,7'-Tetrakis-(N,N'-di-p-methylphenyl-amino)-9,9'spirobifluorene
TBPe	2,5,8,11-Tetra-tert-butyl-perylene
TCTA	4,4',4"-tris(N-carbazolyl)-triphenyl-amine
TPBi	2'2"(1,3,5-benzenetriyl) tris-[1-phenyl-1H-benzimidazole]
TPPhen	2,4,7,9-tetraphenyl-1,10-phenanthroline
W$_2$(hpp)$_4$	Tetrakis(1,3,4,6,7,8-Hexahydro-2H-pyrimido[1,2-a]pyrimidinato)ditungsten (II)
ZnPc	zinc-phthalocyanine

Acknowledgements

ERKLÄRUNG

Diese Dissertation wurde am Institut für Angewandte Photophysik der Fakultät Mathematik und Naturwissenschaften an der Technischen Universität Dresden unter wissenschaftlicher Betreuung von Prof. Dr. Karl Leo angefertigt.

Hiermit versichere ich, dass ich die vorliegende Arbeit ohne unzulässige Hilfe Dritter und ohne Benutzung anderer als der angegebenen Hilfsmittel angefertigt habe, die aus fremden Quellen direkt oder indirekt übernommenen Gedanken sind als solche kenntlich gemacht. Die Arbeit wurde bisher weder in Deutschland noch im Ausland in gleicher oder ähnlicher Form einer anderen Prüfungsbehörde vorgelegt.

Ich versichere weiterhin, dass bislang keine Promotionsverfahren stattgefunden haben.

Ich erkenne die Promotionsordnung der Fakultät Mathematik und Naturwissenschaften an der Technischen Universität Dresden vom 20.03.2000, in der Fassung der vom Fakultätsrat am 19.06.2002 und 12.07.2002 beschlossenen und mit Erlass des Sächsischen Staatsministeriums für Wissenschaft und Kunst vom 18.03.2003 genehmigten Änderungen gemäß Satzung vom 16.04.2003, sowie gemäß der Änderungssatzung vom 17.07.2008, an.

Michael Thomschke
Dresden, den 07.09.2012